Université catholique de Louvain
École Polytechnique de Louvain
Institute of Mechanics, Materials
and Civil Engineering

Titanic results: a numerical study of motion in the liquid bodies of a Saturnian icy moon

Doctoral dissertation presented by

David Vincent

in partial fulfilment of the requirements for the degree of

Docteur en Sciences de l'ingénieur

Thesis committee:

Prof. Véronique Dehant (Supervisor)	Université catholique de Louvain
Prof. Eric Deleersnijder (Supervisor)	Université catholique de Louvain
Dr. Özgür Karatekin	Observatoire Royal de Belgique
Prof. Vincent Legat	Université catholique de Louvain
Prof. Sandra Soares-Frazão (Chairperson)	Université catholique de Louvain
Prof. Gabriel Tobie	Université de Nantes

Louvain-la-Neuve, May 2020

Abstract

Titan, Saturn's largest moon, is a unique object in the Solar system inasmuch as it has a substantial atmosphere, a surface with a complex interplay of geological processes and an outer ice shell overlying a subsurface ocean. The climate on this icy satellite boasts a multiphase hydrological cycle where methane plays a role similar to that of water on Earth. Surface lakes and seas filled with liquid methane and ethane are found in the polar regions. The subsurface ocean, on the other hand, is filled with liquid water. This liquid layer lying beneath Titan's surface allows for the large surface deformation observed.

The first objective of this thesis was to adapt an Earth-based geophysical and environmental model, SLIM (www.climate.be/slim), to Titan's specific conditions in order to study the tidal motion in the surface lakes and seas. The modified model was applied to the largest lake in the southern hemisphere, Ontario Lacus, and the two largest seas, Kraken and Ligeia Maria, which are located in the northern hemisphere. The predicted surface elevation and velocity fields are part of the data needed to develop an exploration mission focusing on the surface lakes and seas of Titan. The normal modes of Ontario Lacus were also numerically studied. While resonantly forced modes could generate significant liquid motion, the natural periods are much shorter than the period of the astronomical forcings. Therefore, only atmospheric forcings could resonantly force the normal modes. Strong wind conditions corresponding to a stormy event are required to generate a surface elevation resulting

in significant shoreline variations.

Then, the model was used to study the tides of Titan's global subsurface ocean. To this end, the shallow water equations and the 3D hydrostatic equations under the Boussinesq approximation were modified in order to take into account the ice shell lying at the top of the ocean. The method was adapted to solve the equations on a sphere. The effects of the shell are represented by adding a surface friction and a surface pressure term. The shell decreases the ocean surface elevation and slows down the flow without modifying significantly the global patterns of these fields. The magnitude of these variations depends on the mechanical behaviour of the ice shell. Surface and bottom heat fluxes play a significant role in the liquid motion of the ocean. The interactions between the tidal motion and the thermally driven flow resulting from the surface heat flux were studied by means of the 3D version of SLIM. The surface heat flux significantly impacts the velocity field, both in terms of magnitude and orientation while the influence on the ocean's surface elevation is small. These results could be useful for astrobiologists paying attention to the ocean habitability and to validate hypotheses about Titan's internal structure.

Remerciements

J'aimerais tout d'abord remercier mes promoteurs, les professeurs Véronique Dehant et Eric Deleersnijder. Les connaissances d'Eric dans le domaine océanographique, et l'expertise astronomique de Véronique ont été des atouts tout au long de ma thèse. Ils m'ont poussé à approfondir chaque recherche entreprise et ont relu un nombre incalculable de fois mes écrits.

Je remercie tout autant Özgür Karatekin qui m'a encadré, aidé pour l'obtention des données et qui m'a mis en contact avec nombre de scientifiques travaillant sur Titan. Il m'a aussi été d'une grande aide de par ses connaissances sur le sujet et sa disponibilité. Merci également aux membres de mon jury de thèse pour leur lecture attentive et leurs commentaires constructifs.

Je tiens également à remercier de tout coeur Jonathan Lambrechts pour son travail dans l'ombre, notamment l'aide inestimable apportée face aux problèmes numériques et sa parfaite connaissance de SLIM. Sa disponibilité, sa bonne humeur et son support furent un soutient certain tout au long de ma thèse. Merci également à Valentin avec qui j'ai partagé un bureau durant 4 années, qui m'a encouragé, guidé et aidé tout au long de ma thèse. Je remercie aussi Pierre-Alexandre, Matthieu, Célestin, Philippe, Vincent, Alexandre, Ange, Nathan, Arthur et Alexis pour tout ces bons moments passés ensembles. Je tiens également à remercier les autres membres de l'équipe SLIM, tous les chercheurs et professeurs de MEMA, Astrid et tous les euleriens.

Cette longue liste de remerciements ne serait pas complète si je

ne mentionnais pas mes amis et ma famille, qui ont toujours été là pour moi, pour m'encourager et me changer les idées; Whisky; et surtout ma femme, Ariane, que je n'aurais sans doute pas rencontré sans ce doctorat. Elle m'a supporté quand mes travaux n'avançaient pas et que j'étais de mauvaise humeur, m'a encouragé à ne pas abandonner, et m'a entouré d'amour au quotidien. Whisky et elle m'ont grandement aidé à supporter le confinement, à rester calme et concentré durant cette période difficile.

Contents

Contents vii

1 Introduction 1
- 1.1 Titan . . . 3
- 1.2 Numerical modelling . . . 20
- 1.3 The SLIM model . . . 23
- 1.4 Scope of the thesis . . . 25

2 Developments in SLIM 33
- 2.1 Introduction . . . 34
- 2.2 Governing equations . . . 36
- 2.3 Discretisation and temporal schemes . . . 45
- 2.4 Application to the surface lakes and seas . . . 47
- 2.5 Application to the global subsurface ocean . . . 49
- 2.6 SLIM user interface . . . 63
- 2.7 Conclusion . . . 64

3 Modelling of Ontario Lacus tides 67
- 3.1 Introduction . . . 68
- 3.2 Ontario Lacus environment and characteristics . . . 71
- 3.3 Computational domain . . . 77
- 3.4 Results . . . 78
- 3.5 Discussion . . . 96
- 3.6 Applications and future missions . . . 102
- 3.7 Conclusion . . . 104

4 Normal modes of Ontario Lacus **107**
4.1 Introduction . . . 108
4.2 Method . . . 113
4.3 Astronomical forcings . . . 118
4.4 Normal modes . . . 119
4.5 Wind induced seiche . . . 123
4.6 Discussion . . . 128
4.7 Conclusion . . . 133

5 Modelling of Titan's northern seas tides **135**
5.1 Introduction . . . 137
5.2 Method . . . 142
5.3 Results . . . 150
5.4 Influence of the model parameters . . . 172
5.5 Discussion . . . 187
5.6 Applications and future missions . . . 194
5.7 Conclusion . . . 199

6 Modelling of Titan's subsurface ocean liquid motion **203**
6.1 Introduction . . . 205
6.2 Domain . . . 208
6.3 Initial and boundary conditions . . . 210
6.4 Results . . . 215
6.5 Influence of the parameters . . . 230
6.6 Discussion . . . 238
6.7 Conclusion . . . 244

7 Conclusions and perspectives **247**

Bibliography **265**

Acronyms

Cassini instruments	
CIRS	Composite InfraRed Spectrometer
ISS	Imaging Science Subsystem
SAR	Synthetic Aperture Radar
VIMS	Visible and Infrared mapping spectrometer

Model and methods	
API	Application Programming Interface
DG	Discontinuous Galerkin
DGFEM	Discontinuous Galerkin Finite Element Method
FEM	Finite Element Method
FVM	Finite Volume Method
GCM	Global Circulation Model
GSO	Global Subsurface Ocean
JUICE	JUpiter ICy moons Explorer
LPT	Lagrangian Particle Tracker
SLIM	Second-generation Louvain-la-Neuve Ice-ocean Model
SLIM2D	2D version of SLIM
SLIM3D	3D version fo SLIM
Tx	Titan flyby by Cassini (x denotes the numbering of the flyby)
TD	Titan Day

CHAPTER 1

Introduction

A common question in recent history is *"Is there life anywhere else in the vastness of space?"*. There are countless books, films and songs about such an extraterrestrial life. Historically, the first planet suspected to shelter life was Mars (this is why the word "Martian" is often used to refer to extra-terrestrial life). Indeed, observations of canals on its surface in 1877 by the astronomer Giovanni Schiaparelli led to the outbreak of legends about an intelligent extraterrestrial life on Mars which would have dug those canals. Nowadays, the existence of life on Mars is almost completely ruled out – at least on its surface – and the focus for searching life switched from Mars to other celestial bodies such as icy moons and exoplanets[1]. As far as we know, one (among other) essential condition to the emergence of life is the presence of liquid. In the solar system, one can find substantial amount of liquid on various planets and moons: Earth, Enceladus, Europa, Titan, Ganymede ... and,

[1] An exoplanet is a planet that is not part of our solar system.

as shown by recent observations (Orosei et al., 2018), on Mars. Nevertheless, most of these celestial bodies hide the liquid beneath their surface: only two of them have a significant amount of liquid bodies on their surface. The first one is well known as we live there: the Earth. Few have heard about the second one: Titan, the largest moon of Saturn. It has both surface lakes and seas filled with liquid hydrocarbons and a global subsurface water ocean.

This thesis aims at studying the motion of Titan's liquid bodies (i.e. both the surface lakes and seas and the global subsurface ocean). One purpose behind such studies is to suggest explanations for several observed phenomena such as shoreline variations, backscattering induced by lake surface roughness, appearance and disappearance of bright spots seemingly corresponding to solid ground on Cassini observations (the so-called "Magic Islands") and surface deformation – the latter being strongly influenced by the liquid motion in the global subsurface ocean. On Earth, this can easily be done by means of numerical modelling – whose results can be validated by measurements – and *in situ* or satellites observations. Nevertheless, on Titan, there is no way to get either *in situ* measurements or new observations from any spacecraft as Cassini recently dived into Saturn at the end of its mission. Consequently, the only way to get new information about Titan in the next years will be by analysing "old" data with new method(s) or using numerical models. For instance, M. Mastrogiuseppe, A. G. Hayes and their team successfully derived a bathymetry map of some lakes and seas with such methods (Hayes et al., 2016; Mastrogiuseppe et al., 2014, 2016, 2018a). Modelling tools are expected to play an important part in order to gain further insight about Titan but also to help planning and designing future exploration mission(s) of Titan. Indeed, except for an orbiter, a lot of information are needed to be able to predict/select the landing site (depending on the starting point of the descent). Furthermore, depending on the locomotion, data such as the wind and/or liquid velocity encountered could be needed in order to either engineer the lander motorisation or to predict its position as a function of time.

1.1 Titan

Titan was discovered in 1655 by the dutch astronomer Christiaan Huygens. The first spacecrafts to fly near Titan were Pioneer 11 and the Voyager I & II probes. Following their observations, a mission dedicated to the Saturnian system was launched in 1997: the Cassini mission. It was composed of a lander, Huygens, which landed on Titan on the 14^{th} of January 2005 and an orbiter, Cassini, which orbited around Saturn from the 11^{th} of June 2005 to the 15^{th} of September 2017. At first, Cassini mission was supposed to last 4 years but, due to happy circumstances, it outlived its initial duration by 9 years (see Fig. 1.2). Various projects were proposed to follow Cassini and study Titan in further details: Time (Lorenz et al., 2012), E2T (Mitri et al., 2014a), Titan sub (Hartwig et al., 2016), Oceanus (Sotin et al., 2017), Dragonfly (Turtle et al., 2017) . . . The latter was recently selected by the NASA as part of its New frontiers program. Its launch date is scheduled in 2026.

Titan is the second largest moon in the solar system, the largest one being Ganymede, a Jovian moon. Its orbital period around Saturn is 15.945 Earth days, which is close to its rotational period. Consequently, one can consider Titan as tidally locked as a first approximation. Indeed, the mean non synchronous rotation is of about $-0.024° \pm 0.018°$/year (Meriggiola et al., 2016). This results in length of day variations, polar motion and longitudinal libration due to the gravitational torque exerted by Saturn and the dynamic variation of the atmosphere (Coyette et al., 2018). Nevertheless, the impact of such variations on the attraction forces is insignificant when looking at the tidal motion and one can hence consider Titan as tidally locked in this respect. Like the Earth, Titan is an ellispoid with semi-major and semi-minor axes given by $a = 2575.15 \pm 0.02$ km, $b = 2574.78 \pm 0.06$ km, $c = 2574.47 \pm 0.06$ km (Zebker et al., 2009). A few characteristics of Titan are listed in Table 1.1.

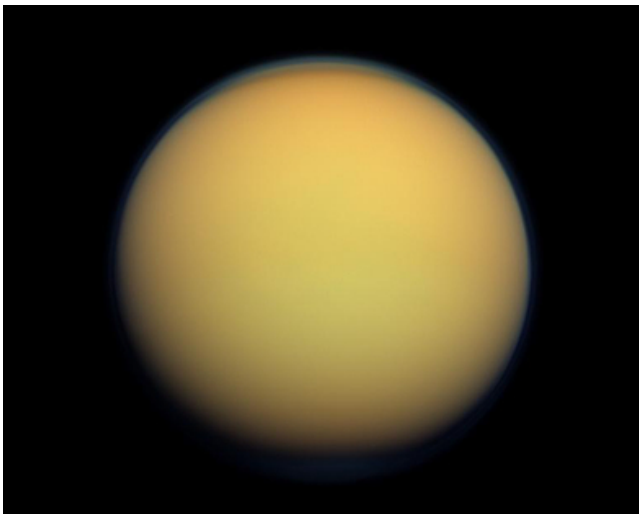

Fig. 1.1: View of Titan from the Cassini spacecraft (in the visible spectrum). The orange aspect of Titan is due to a thick haze mostly made of methane, ethane and nitrogen (image credit: NASA/JPL-Caltech/Space Science Institute).

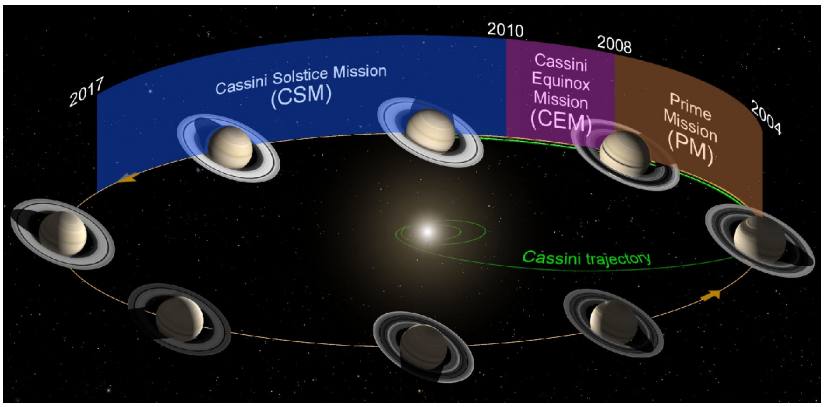

Fig. 1.2: Chronology of Cassini mission. The original mission was first extended by about 2 years (the so-called Equinox mission) and then by 7 years (the Solstice mission) (image credit: Manor-Chapman (2013)).

Table 1.1: Main characteristics of Titan compared with those of the Earth.

	Titan	Earth
Orbital eccentricity	0.0288	0.0167
Obliquity [°] [a]	0.3	
Obliquity [°] [b]	26.73	23.44
Average orbital speed [km/s]	5.57	29.78
Mean radius [km]	2574.73	6371
Volume [km^3]	7.16×10^{10}	1.08×10^{12}
Surface [km^2]	8.3×10^{7}	5.1×10^{8}
Mass [kg]	1.3452×10^{23}	5.972×10^{24}
Mean surface temperature [K]	93.7	288
Surface pressure [kPa]	146.7	101.325
Mean gravitational acceleration [m/s^2]	1.352	9.807

[a]: Obliquity relative to Saturn equatorial plan. This obliquity is relevant for the study of the tidal motion as it contributes to the tidal potential.
[b]: Obliquity relative to the Sun equatorial plan. This obliquity is relevant for a climate/solar illumination point of view.

1.1.1 Atmospheric conditions

Titan is the only natural satellite of the solar system which has a thick atmosphere[2]. The presence of an atmosphere on Titan was first assumed by the astronomer Josep Comas i Solá in 1903 and was confirmed in 1944 by Gerard Kuiper using a spectroscopic technique (Kuiper, 1944). In 1980, Voyager I revealed that the surface pressure was about 1.48 times larger than on Earth (see

[2]A thick atmosphere does not distinguish from a thin atmosphere by its total depth but by the gases that are present and their density. The larger the density is, the more thick the atmosphere.

Table 1.1). The major breakthrough regarding Titan's atmosphere came from the Cassini mission which was able to measure, among other things, the composition and the atmospheric conditions. The only *in situ* measurements of Titan atmospheric conditions were provided by the Huygens probe during its descent and at its landing site (see Fulchignoni et al., 2005) while Cassini instruments such as the CIRS[3] and the VIMS[4] were able to provide additional information through remote sensing. Unlike Mars, where surface water can be observed at large scales – but only in a solid state –, methane was observed in both gaseous, liquid, and solid state on Titan as a methane cycle similar to the water cycle on Earth takes place on Titan (Atreya et al., 2006). Most of the liquid methane is located in the surface lakes and seas (see Section 1.1.2). The atmosphere is mainly composed of nitrogen with a small amount of methane and a still smaller amount of other species (e.g. ^{40}Ar, ^{36}Ar, cyanogen, ethane) (Niemann et al., 2005) (for a detailed composition, see Table 1 in Cordier et al., 2009). The methane in the atmosphere can condense to form clouds (Toon et al., 1988; Griffith et al., 2000; Porco et al., 2005) which can lead to methane precipitation (Toon et al., 1988). In the high atmosphere, methane photolysis leads to the production of fast reacting radicals CH_3, CH_2, and CH. These radicals then react with atmospheric molecules such as nitrogen and hydrogen to form complex C_xH_y (mostly ethane, C_2H_6) and nitrile species (C–N–H) (Atreya et al., 2006).

In situ measurements of Huygens probe gave the vertical pressure, temperature, and wind speed profile along its descent but, in order to have a data map of these fields, one has to rely on models and remote measurements from Cassini spacecraft. The surface

[3]Composite InfraRed Spectrometer : it measures infrared energy from the surfaces, atmospheres, and rings of Saturn and its moons to study their temperature and compositions (Flasar et al., 2004).

[4]Visible and Infrared Mapping Spectrometer: it identifies the chemical composition of the surface, atmosphere, and rings of Saturn and its moons by measuring colors of visible light and infrared energy emitted or reflected (Brown et al., 2004).

temperature can be inferred from CIRS far infrared spectra while pressure field, precipitation and wind velocity have to be modelled. Jennings et al. (2009) and Cottini et al. (2012) both derived the surface temperature from CIRS data respectively from 2004 (right after the northern winter solstice) to 2008 (late northern winter) and from 2004 to 2010 (in the early northern spring). Their results are consistent with each other and with Huygens measurements. Seasonal variations were observed by both authors. Jennings et al. (2009) did not take into account the diurnal changes while Cottini et al. (2012) observed that the diurnal features disappeared at latitudes greater than $20-30°$ in the north and $30-40°$ in the south. Nevertheless, they took into account neither the data from latitudes greater than 60° nor the local influence of liquid bodies. Tan et al. (2015) established a formula describing the surface temperature as a function of the latitude and the time from January 2005 to December 2013 from Jennings et al. (2011) and Cottini et al. (2012) temperature profiles. The values predicted by this formula have to be used with caution as no variation with respect to the longitude was taken into account.

Several global circulation models (GCMs) (e.g. Tokano, 2008, 2009; Friedson et al., 2009; Lebonnois et al., 2012; Newman et al., 2011, 2016; Schneider et al., 2012) and mesoscale models (Soto and Rafkin, 2015; Charnay et al., 2015) were proposed in order to predict the atmospheric pressure, precipitation and winds. According to the GCMs, the atmospheric pressure variations are small at the surface and the winds are subject to significant spatial, seasonal and diurnal variations. Additionally, the wind speed may vary depending on the lake composition: if the seas are methane rich, the wind speed could be different than in the case of ethane-rich seas (Tokano, 2009; Lorenz et al., 2012). The tidal wind (i.e. the wind resulting from the diurnal astronomical forcing) has neither a preferential direction nor a specific time distribution while the wind due to the convergence of moist air over the lake area is directed offshore and can be stronger than the tidal wind (Tokano, 2009). According to Charnay (2014), the tidal winds are overesti-

mated by Tokano (2009) as the tidal forces induce mostly change in pressure, resulting in slower wind. Except in stormy conditions where it can reach up to 10 m/s, the predicted wind speed ranges from 0 to 2 m/s depending on the location and the season (Lorenz et al., 2012; Lorenz, 2013). Each of these models uses simplifying assumptions and none of them is fully consistent with observations (Schneider et al., 2012).

1.1.2 Surface lakes and seas

Due to the atmospheric conditions at Titan's surface measured by Voyager spacecrafts, the presence of liquid methane was evoked as soon as 1981 by, among others, Samuelson et al. (1981); Hanel et al. (1981). It led Sagan and Dermott (1982) and Dermott and Sagan (1995) to construct a pre-Cassini appearance of Titan's surface (which was unknown at that time) by conducting analyses of theoretical global surface ocean and disconnected seas and lakes on Titan's surface. Other features were also predicted on Titan: crater lakes (Lorenz, 1994), submerged impact craters (Lorenz, 1997) and cryovolvanic flows with pillow lava texture (Lorenz, 1996). Although such flows and crater lakes were not observed, the presence of surface lakes and seas was confirmed by Huygens and Cassini measurements (McEwen et al., 2005; Stofan et al., 2007). Cassini first detected possible surface lakes in the southern polar region of Titan's surface in 2004 (only some years later confirmed to be liquid) by means of the imaging science subsystem[5] (ISS) (McEwen et al., 2005). Its radar[6] showed dark patches, interpreted as lakes, in the northern polar region on the 22nd of July 2006, during the

[5]Imaging Science Subsystem: it takes pictures in visible, near-ultraviolet, and near-infrared light (see Porco et al., 2004).

[6]Radar: it maps the surface of Titan using a radar imager to pierce the veil of haze. It is also used to measure heights of surface features. The synthetic aperture radar observed Titan in 13.78 GHz Ku-band with a resolution ranging from 0.35 to 1.7 km (see Elachi et al., 2004).

flyby T16 (Stofan et al., 2007). These lakes and seas[7] are asymmetrically distributed with respect to the equator (Aharonson et al., 2009): there are many more lakes in the northern high latitudes where they are larger and deeper (Hayes et al., 2008, 2018). This asymmetry could be explained by the shorter and more intense southern summer induced by the obliquity of Saturn.

Various studies were carried out about Titan's seas and lakes: bathymetry (e.g. Hayes et al., 2010; Ventura et al., 2012; Mastrogiuseppe et al., 2014, 2018a,b; Lorenz et al., 2014; Hayes, 2016; Hayes et al., 2017), liquid composition (e.g. Brown et al., 2008; Cordier et al., 2009; Glein and Shock, 2013; Tan et al., 2013, 2015; Luspay-Kuti et al., 2015), dissipation due to friction in Titan's lakes and seas (e.g. Sagan and Dermott, 1982; Dermott and Sagan, 1995; Sears, 1995; Lorenz et al., 2014), tidal response (Tokano, 2010; Tokano et al., 2014; Vincent et al., 2016, 2018), normal modes (Dermott and Sagan, 1995; Tokano, 2010; Vincent et al., 2019) interactions with the atmosphere (Tokano and Lorenz, 2015, 2016), and phenomena such as the shoreline variations of Ontario Lacus (Turtle et al., 2011; Hayes et al., 2011) and transient features in the northern seas (Hofgartner et al., 2014, 2016) were studied.

The study of such lakes and seas belongs to a new scientific research field usually referred to as *extra-terrestrial oceanography*. Indeed, although the governing equations are similar to those of terrestrial oceanography, there are significant differences that need to be taken into account: extra-terrestrial surface seas or lakes involve regimes of temperature, pressure, composition, and physical environment (gravity, tidal forces, rotational, and orbital periodicities, etc.) that are not observed in Earth's oceans. Despite all the observations and the results of previous studies, there are a lot of uncertainties about some essential parameters such as the liquid density, the bathymetry, the attenuation of the forcing induced by the lake/sea's bottom deformation ... For instance, the bathymetry

[7]The largest liquid bodies are referred to as seas (Mare) and the others as lakes (Lacus), according to the nomenclature of the International Astronomical Union. It only reflects the size of the body.

of a lake was derived following two different approaches, resulting in depth variations up to 28 m. Consequently, sensitivity analyses are conducted with respect to several parameters.

1.1.2.1 Surface lakes and seas distribution

The surface lakes and seas of Titan cover 1.04×10^6 km^2, which represents about 1.3% of the moon surface. Most of them are located at latitudes higher than 60° (Aharonson et al., 2009) (see Fig. 1.3) although a few equatorial and mid latitudes dark spots are proposed as possible lakes (Griffith et al., 2012). 295 of these lakes, covering a combined surface of 1.36×10^5 km^2, are empty while there are 577 liquid-filled lakes, covering a combined surface of 2.33×10^5 km^2 (Hayes, 2016). Most of them consist of small sharp-edged depressions filled with liquid but there are also larger lakes such as Jingpo and Bolsena Lacus in the northern hemisphere and Ontario Lacus in the southern one. Besides these lakes stand three large Maria representing 80% of the liquid filled surface: Kraken Mare (5×10^5 km^2), Ligeia Mare (1.3×10^5 km^2) and Punga Mare (6.1×10^4 km^2) (Hayes, 2016). While Kraken Mare and Ligeia Mare are hydrologically connected by a strait, namely Trevize Fretum, (Sotin et al., 2012) (see Fig. 1.3) one can only assume a connection between Kraken and Punga Mare: the maria's surface elevation are similar (Hayes et al., 2017; Hayes, 2016) but no large canals were observed. Such a connection would therefore be made of small canals, shallow swamps, or underground flows. Kraken Mare is the largest sea identified on Titan, with an area of about $500,000$ km^2. It is centred at (68°N, 50°E) (Tokano, 2010) and it stretches from 55°N to 82°N (Lorenz et al., 2014). Two basins can be highlighted, Kraken 1 (in the north) and Kraken 2, linked by a strait named Seldon Fretum (see Fig. 1.3) and a set of small channels (Lorenz et al., 2014). The horizontal dimensions of Seldon Fretum are similar to those of the Gibraltar strait on Earth, about 17 km wide and 40 km long (Lorenz et al., 2014), but it is not the case of its depth. Ligeia Mare is located north-east of Kraken Mare:

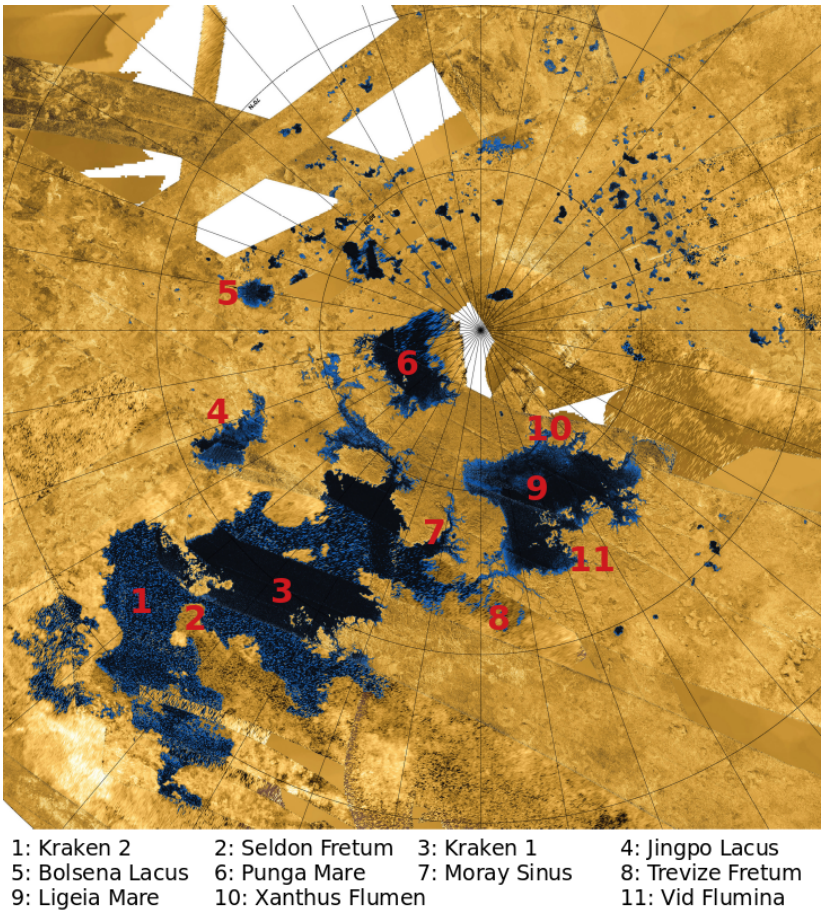

Fig. 1.3: Mosaic of Cassini radar images covering Titan northern hemisphere. (credit: NASA/JPL-Caltech/Agenzia Spaziale Italiana/USGS).

it is centred at (79°N, 112°E). Its maximal dimensions are about 420 by 350 km (Stofan et al., 2012). The Cassini radar altimeter also detected liquid filled canyons linked to Ligeia Mare in the northern region, near Xanthus Flumen, and south-eastern region, near Vid Flumina (Poggiali et al., 2016) (see Fig. 1.3). Transient features called "Magic Islands" were observed in Kraken Mare and Ligeia Mare (Hofgartner et al., 2014, 2016). They consist of areas which appear bright on some observations and dark on others.

Bright areas are consistent with solid ground while dark ones correspond to liquid. In Ligeia Mare, such phenomena were observed in regions centred at (78°N, 123°E) and (80°N, 111°E). They are best explained by ephemeral phenomena such as floating and/or suspended solids, bubbles, and waves while the diurnal phenomena, such as the tide, seem to be ruled out, the observations being all at nearly the same true orbital anomaly[8] (Hofgartner et al., 2016). In Kraken Mare, the phenomenon was observed at (73°N, 55°E). In this sea, the same explanations stand but the tides cannot be ruled out. The third sea, namely Punga Mare, is also the smaller. It is located north of Kraken Mare, near the north Pole. It is centred at (85.1°N, 339.7°W) and has a diameter of 380 km.

Ontario Lacus is the largest lake in the southern hemisphere, covering approximately an area of 200 × 70 km (Wall et al., 2010). It is centred at (72°S, 175°E). Ontario Lacus was flown over at least twice by each Cassini instrument (complete or partial flybys): ISS in 2004, 2005 & 2009, VIMS in 2007 & 2009, and radar in 2009 & 2010. It has the shape of a right footprint (see Fig. 1.4) and is named after Lake Ontario (one of the Great Lakes of North America). It is connected to a hydrological network (for example, in area N in Fig. 1.4) (Wall et al., 2010; Cornet et al., 2012) which can provide liquid hydrocarbons during and after precipitations. Several, quite different, morphologies were observed along the shoreline of Ontario Lacus: deeply incised bays, mountainous region, beaches ... (see Wall et al., 2010; Cornet et al., 2012, for further details). The two others significant lakes, Bolsena Lacus and Jingpo Lacus are located in the northern hemisphere. Bolsena Lacus is centred at (76°N, 10°W) and has a diameter of 101 km while Jingpo Lacus has a diameter of 240 km and is centred at (73°N, 336°W).

[8]The true orbital anomaly is the angle defining the position of Titan along its Keplerian orbit as seen from Saturn.

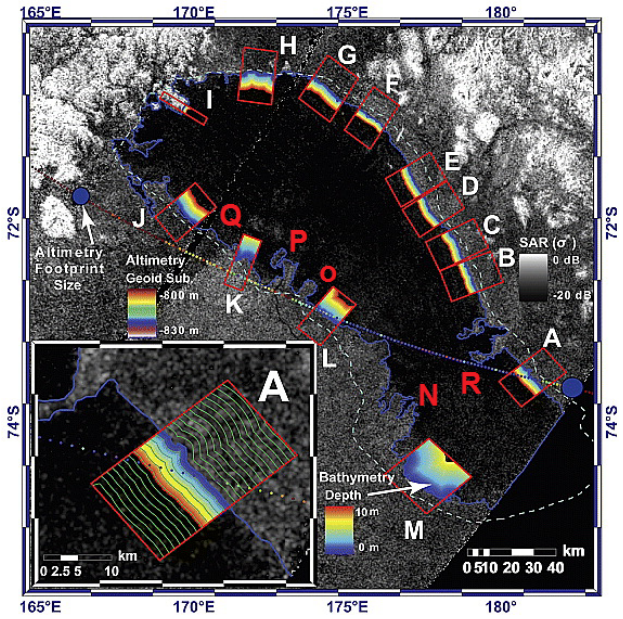

Fig. 1.4: Map of Ontario Lacus. Letters from A to M show the study areas of Hayes et al. (2010) which derived a nearshore bathymetry in these regions. The red letters, from N to R, are used in Chapter 3 to refer to particular areas (adapted from www.titanexploration.com; original image credit: Cassini Radar Science team, NASA/JPL/Caltech)

1.1.2.2 Liquid composition

Studies showed that the surface lakes and seas are not filled with pure methane but with a mixture of methane, ethane, nitrogen, and other low-molecular mass hydrocarbons (Mastrogiuseppe et al., 2014; Luspay-Kuti et al., 2015; Mitchell et al., 2015; Tan et al., 2013, 2015). The exact liquid composition varies between the lakes/seas. For instance, Ligeia Mare is much more methane rich than Ontario Lacus or Kraken Mare (Hayes et al., 2016; Le Gall et al., 2016). The VIMS identified liquid ethane in Ontario Lacus in 2008 while the identification of liquid methane on Titan's surface by means of this instrument is made difficult by the presence of methane in

the atmosphere (Brown et al., 2008). Using Cassini radar, (Mastrogiuseppe et al., 2014; Hayes et al., 2016; Le Gall et al., 2016) were able to predict the composition of some lakes and seas such as Ontario Lacus and Ligeia Mare. This method relies on analysing the dielectric constant and the loss tangent[9] of the lakes and seas: the proportion of methane, ethane and nitrogen is derived from the value of these parameters. Luspay-Kuti et al. (2015) and Mitchell et al. (2015) conducted laboratory experiments to study liquid properties such as evaporation rates and derived rough approximation of the lakes and seas composition. All these studies were able to predict the proportion of the major constituents such as ethane and methane but were not able to predict a detailed composition of the lakes and seas. To this end, models have to be resorted. Several models are available in the literature (see, e.g., Cordier et al., 2009; Tan et al., 2013, 2015; Glein and Shock, 2013). Cordier et al. (2009) and Tan et al. (2013, 2015) distinguished two types of lakes: the near-equator lakes and the high latitudes lakes. This distinction is the result of the temperature difference between the equator and the high latitudes. Cordier et al. (2009) established the composition by considering the lakes as non ideal solutions in thermodynamic equilibrium with the atmosphere. Nevertheless, this model is quite sensitive to uncertainties about thermodynamic data and other parameters: the relative standard deviations remain between 10% and 300% depending on the species considered (Cordier et al., 2012). Tan et al. (2013) also considered this equilibrium and used an equation of state to model the chemical system of the atmosphere. Tan et al. (2015) used the same model as Tan et al. (2013) and included the effect of multicomponent mixtures. Glein and Shock (2013) developed a van Laar model parametrised by using experimental phase equilibrium data. Cordier et al. (2009) and Luspay-Kuti et al. (2015) predicted an ethane-rich composition while Tan et al. (2013, 2015) predicted a methane-rich one. Nev-

[9]The loss tangent is the tangent of the loss angle. It is used to parametrise the electromagnetic energy dissipation inherent to a dielectric material.

ertheless, Tan et al. (2015) predicted that the composition varies seasonally: ethane and other heavy components would be present in larger quantities in winter than in summer. Glein and Shock (2013) also predicted a methane-rich composition but their results significantly vary with the mixing ratio of methane. If the mixing ratio of methane suggested by Voyager 1 was used, they would obtain an ethane-rich lake. The chemical models result in a liquid of similar density but there are some significant differences about the molecular viscosity: that predicted by Cordier et al. (2009) and Luspay-Kuti et al. (2015) is larger than that predicted by Tan et al. (2013) (respectively by a factor of 5 and up to 3). The lake also carries some solid particles like acetylene and high molecular weight organics produced by atmospheric photochemistry (see e.g. Lorenz et al., 2010, 2011; Lorenz, 2013) (Tan et al. (2013) showed that tholins and acetylene could be present in Titan's lakes). These particles modify the lake properties. Therefore, the liquid density and viscosity cannot be accurately derived from the lake composition.

1.1.3 Titan's internal structure

Titan is an icy moon. It is a class of natural satellites whose surface is composed mostly of water ice. The layers beneath the surface vary from one moon to another. As shown in Fig. 1.5, there is a liquid body on Titan other than the surface lakes and seas: a global subsurface ocean filled with liquid water lies beneath the icy surface of the moon. The latter is mostly composed of water ice and is therefore referred to as an icy shell. Lunine and Stevenson (1987) were the first to predict the presence of such an ocean, although it had been discussed by Consolmagno and Lewis (1978). Since then, the presence of a salt-rich or ammonia-rich water ocean has been supported by several observations and measurements such as Titan's obliquity, its surface motion, its gravity field and its topography (Rappaport et al., 2008; Nimmo and Bills, 2010; Iess et al., 2012; Hemingway et al., 2013; Lefevre et al., 2014; Baland et al.,

2011, 2014) and has been widely studied (see, e.g., Beuthe, 2008, 2015a,b; Fortes, 2012; Sohl et al., 1995, 2003, 2014). Beneath this ocean lies a layer of high pressure water ice and, beyond this layer, the core. Although the layers forming Titan are clearly identified, uncertainties remain about their thickness and properties. For instance, there are discrepancies between the ice Young modulus inferred from Cassini measurements and that obtained in laboratory (i.e., on Earth) (Nimmo, 2004). The models used to infer the thickness and properties of the internal layers are validated by comparison with properties inferred from Cassini measurements such as the mean moment of inertia (which was questioned by Hemingway et al. (2013), Baland et al. (2014) and Lefevre et al. (2014)), the second-degree gravity field coefficients, and Titan's mean density. The ocean's depth and density predicted can significantly vary depending on the model used. The commonly predicted depth ranges from several tens of kilometers to about 400 km. The ocean is dense: Baland et al. (2014) predicted a density between 1275 and 1350 kg/m^3, Sohl et al. (2014) studied two possible densities, 1150 and 1350 kg/m^3, while Coyette et al. (2018) considered that the ocean density may vary from 950 to 1350 kg/m^3. This range can be further constrained by using properties inferred from Cassini measurements such as the second degree tidal Love number k_2. Indeed, low densities are not consistent with respect to the value of k_2 derived by Iess et al. (2012). Densities lower than 1150 kg/m^3 are consequently disregarded.

1.1.4 Tidal forcing

There are numerous celestial bodies which can generate a tidal motion on Titan. Nevertheless, the forcing resulting from Titan's obliquity and its orbital eccentricity is much more significant. For instance, there is a ratio of $\mathcal{O}(10^{-6})$ between the solar tidal potential and those taken into account herein. Therefore, the solar gravitational tide and the tides due to other planets and moons are neglected (Sagan and Dermott, 1982). The period of the as-

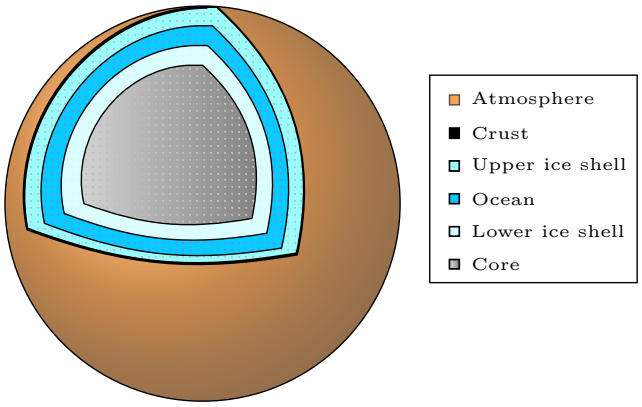

Fig. 1.5: Internal structure of Titan as seen by the scientific community. The thickness of each layer is not to scale for the sake of clarity.

tronomical forcing is 1 Titan day (TD), resulting in a diurnal tide exhibiting no spring-neap tide cycle. The forcing is given by the horizontal gradient of the tidal potential. The latter is given by the sum of two contributions: the potential due to Titan's orbital eccentricity (see Eq. 1.1) and the potential due to Titan's obliquity (see Eq. 1.2). The eccentricity potential is (Dermott and Sagan, 1995)

$$\phi_{ecc} = -\frac{GM_s}{a}\left(\frac{R_T}{a}\right)^2 3e$$
$$\Big(0.5(3\sin^2\theta\cos^2\lambda - 1)\cos(nt) + \sin^2\theta\sin(2\lambda)\sin(nt)\Big) \qquad (1.1)$$

where $G = 6.67259 \times 10^{-11}$ m^3/s^2/kg is the universal gravitational constant, $M_s = 5.685 \times 10^{26}$ kg is Saturn's mass, $a = 1.221865 \times 10^9$ m is the semi-major axis of Titan's orbit, $R_T = 2,574,730$ m is Titan's mean radius, $e = 0.0288$ is Titan's orbital eccentricity, $n = 4.5601 \times 10^{-6}$ s^{-1} is Titan's orbital angular velocity, t is the time measured from perikron (point on Titan's orbit closest to Saturn), θ is the colatitude and λ is the longitude. The potential due to the obliquity is (Tyler, 2008)

$$\phi_{ob} = \frac{3}{2}n^2 R_T^2 \theta_0 \sin\theta\cos\theta\,(\cos(\lambda - nt) + \cos(\lambda + nt)) \qquad (1.2)$$

where $\theta_0 = 5.34 \times 10^{-3}$ is the obliquity of Titan expressed in radian. The forcings resulting from Titan non synchronous rotation (NSR) have a much smaller magnitude. Consequently, the NSR forcings are disregarded when studying the tides of Titan's liquid bodies.

Due to the global subsurface ocean, the deformation of the icy shell and, hence, of the lakes and seas' bottom is much larger than the shape variation of a rigid Titan. Such deformation modifies the tidal forcing to which surface liquids respond, since the ice crust itself partly follows the changing potential. The uplifting of Titan surface reduces the tidal potential acting on the surface lakes and seas by $h_2 (\phi_{ecc} + \phi_{ob})$, where h_2 is the second degree radial displacement Love number, while the additional gravitational potential arising from the mass redistribution increases the potential by by $k_2 (\phi_{ecc} + \phi_{ob})$, where k_2 is the second degree tidal Love number. These effects are modelled by an attenuation factor, $\gamma_2 = 1 + \Re(k_2) - \Re(h_2)$ ($\Re()$ denotes the real part), applied to the tidal forcing (Lorenz et al., 2014; Tokano et al., 2014; Beuthe, 2015a,b), i.e. the forcing really applied to the surface lakes and seas is $\gamma_2 \nabla_h (\phi_{ecc} + \phi_{ob})$ where ∇_h is the horizontal del operator. The Love numbers depend on the internal structure of Titan and are particularly sensitive to the thickness, the rigidity and the rheological properties of the ice shell (e.g. Sohl et al., 2003; Lorenz et al., 2014; Tokano et al., 2014). As a consequence, γ_2 should be considered as a free parameter (Lorenz et al., 2014). Iess et al. (2012) and Durante et al. (2019) derived some values of k_2 from Cassini measurements by means of three analysis models while Sohl et al. (2003, 2014); Baland et al. (2014); Lefevre et al. (2014); Beuthe (2015a,b); Mitri et al. (2014b), among others, used models to reconstruct Titan's internal structure and compute the second degree Love numbers. As a result, different values can be found depending on the working hypotheses and the model used (see Table 1.2).

Beuthe (2015b) predicted values of k_2 matching with those computed by Iess et al. (2012). By setting the ice shell relative thickness in order to correspond with the value of k_2 obtained by Iess et al. (2012); Durante et al. (2019), the corresponding attenuation factors

Table 1.2: Real part of the Love numbers ($\Re(k_2)$ and $\Re(h_2)$) and attenuation factor (γ_2) corresponding to the presence of a subsurface ocean (as established by Sohl et al. (2003, 2014); Baland et al. (2014); Lefevre et al. (2014); Beuthe (2015b) from observations and measurements) found in the literature. k_2 and h_2 respectively are the second degree tidal potential Love number and the second degree radial displacement Love number.

Authors	$\Re(k_2)$	$\Re(h_2)$	γ_2
Sohl et al. (1995)	0.36	1.19	0.17
Sohl et al. (2003)[a]	$[0.39, 0.32]$	$[1.25, 1.05]$	$[0.13, 0.27]$
	$[0.39, 0.35]$	$[1.28, 1.15]$	$[0.12, 0.2]$
Nimmo and Bills (2010)	–	1.28	–
Iess et al. (2012)[b]	0.589 ± 0.075	–	–
	0.67 ± 0.09	–	–
	0.637 ± 0.112	–	–
Durante et al. (2019)	0.62 ± 0.067	–	–
Sohl et al. (2014)	0.437	1.29	0.147
Beuthe (2015b)[c]	$0.7 - 0.5$	$1.7 - 1.3$	$0 - 0.2$
	$0.7 - 0.41$	$1.7 - 1.2$	$0 - 0.21$

[a]: Various ice thickness and two ammonia concentrations.
[b]: Different analysis models.
[c]: Two crust densities and various relative thickness of the ice shell.

range from 0 to 0.21 depending on the density of the crust and subsurface ocean (See Fig. 5 in Beuthe, 2015b). Tokano et al. (2014) computed γ_2 for different internal structures and only retained those which satisfy the moment of inertia and the Love number k_2 predicted by Iess et al. (2012), which results in $\gamma_2 \in [0.1, 0.2]$ depending on the ice shell thickness. However, the value retained from the moment of inertia was obtained by having recourse to the hydrostatic assumption, which is questionable due to the significant degree-three signal observed in the gravity field (Hemingway et al.,

2013; Lefevre et al., 2014; Baland et al., 2014). All these models assume a thin and homogeneous crust. However, the crust could be non-homogeneous. There could be some clathrates outgassing methane in the atmosphere from time to time (Tobie et al., 2006). Such clathrates at the base of the ice shell might have a smaller shear modulus which would cause larger deformation of the shell and the Love number k_2 would be larger (Rappaport et al., 2008).

1.2 Numerical modelling

Some phenomena/mechanisms cannot be observed because they occurred in the past, at unattainable places, or at a too small or too large scale. In order to study them, scientists often have to resort to numerical modelling. Nevertheless, such an approach is not perfect as models are limited by their inherent nature. There are three main limitations: the hypotheses associated to the equations solved, the knowledge of the domain (initial and boundary conditions, composition, dimensions...), and the scales resolved. Indeed, for computer cost reasons, it is not possible to model each and every phenomenon that impacting the domain. For instance, an oceanic model which aims at modelling the global ocean circulation is not able to take into account small scale phenomena and has to model their impact on the larger scales by means of a closure scheme. Consequently, as useful as the models can be, it should be remembered they are only approximations of reality. « Essentially, all models are wrong, but some are useful » (Box and Draper, 1987).

Although numerical methods are increasingly used nowadays thanks to the creation of more and more powerful computers, these methods are not recent. In fact, one could trace them back to more than 2000 years ago. For instance, Babylonian astronomers, mathematicians in Seleucid Mesopotamia, and Greek astronomer Hipparchus (2nd century BC) used linear interpolation to fill the gaps in tables. These methods were on a rise with the introduction of calculus. Nevertheless, the computation relying on tables, it was of-

ten slow and tedious. Another rise in these methods was induced by the invention of modern computers. The first numerical modelling of geophysical fluid dates back to the 1940s (Cushman-Roisin and Beckers, 2011). Hansen (1956) was the first to create a model able to simulate regional storm surges and tide propagation in a two-dimensional model. It took ten additional years before the first general circulation model was developed (Bryan and Cox, 1967). For about 50 years, increasingly complex models emerged but most of them are based on structured grids using finite difference schemes. Recent improvements mainly concern the parametrisation of unresolved scales and limitations induced by the use of structured grids. Indeed, these grids suffer from significant drawbacks. A significant limitation is the difficulty to locally improve the spatial resolution. Although nesting techniques have been developed, they have their own drawbacks such as the numerical diffusion introduced (see, e.g., Brown et al., 2016). Structured grids also result in a staircase representation of the coastline which impacts the boundary currents. Such grids also suffer from the pole problem: the spatial discretization is higher near the poles, decreasing the maximum explicit time step.

In order to circumvent these limitations, new models based on unstructured meshes were developed. Such meshes allow to locally increase the resolution and are therefore better suited for capturing the complex geometry of the domains. They are also particularly well suited for spherical domains as they do not suffer from the pole problem. These models are not based on finite different schemes but rather use finite volume (FVM) or finite element (FEM) methods. The assets of these methods also lead to their main drawback: they have a lower computational efficiency due to the complexity of their topology. FVM are well suited for advection-dominated problems and are based on a low-order discretisation, resulting in a smaller computational cost than the FEM which are based on a high-order discretisation. Nevertheless, the latter allows a better representation of the solution by element and suffer from a smaller discretisation error.

Most of the modern models simulating large scale circulation or both small and large scale hydrodynamics are based either on FVM or FEM. Among the most known, a majority opts for the finite volume methods. This is the case of, among other, MPAS (Model for Precision Across Scales[10] Ringler et al., 2013), the model of Alfred Wegener Institute (Danilov, 2012), and MITGCM (MIT General Circulation Model[11], Marshall et al., 1997) which has the particularity of having already been applied to an extra terrestrial context as part of the study of Saturn atmosphere (Afanasyev and Zhang, 2018). The finite element methods are used by, among other, TELEMAC (open TELEMAC-MASCARET[12], Hervouet, 2007), FESOM (Finite Element Sea Ice-Ocean Model[13] Wang et al., 2008), and SELFE (Semi-implicit Eulerian-Lagrangian Finite Element[14], Zhang and Baptista, 2008), which is dedicated to coastal flows. A detailed review of the popular coastal models and concepts used in the United States is available in Fringer et al. (2019).

There are several finite element methods. Among them the discontinuous Galerkin (DG) is one of the most interesting as it combines the advantages of both FEM and FVM. Indeed, they are well suited for advection dominated problems (which is one of the advantage of FVM) (Bernard et al., 2007), locally conservative, they allow a high order accuracy, they benefit from the functional flexibility of FEM, and they do not require any stabilization. The discontinuity between the elements allows using hybrid meshes (i.e. with various element types or different degree of the basis functions (Kärnä, 2012)) and simplifies the multi-core parallel implementation (Seny et al., 2013, 2014). The DG method also suffers from drawbacks. For instance, the larger number of discrete unknowns results in a high storage and high computational cost. This method

[10] https://mpas-dev.github.io,
[11] http://mitgcm.org
[12] http://www.opentelemac.org
[13] https://fesom.de,
[14] http://www.stccmop.org/knowledge_transfer/software/selfe

is not widespread: one can cite as example Thetis[15] model (Kärnä et al., 2018) or the model developed by Conroy and Kubatko (2016). In this thesis, use and partially develop another model, SLIM, the Second-generation Louvain-la-Neuve Ice-ocean Model[16].

1.3 The SLIM model

SLIM, a project started in 1999, originally aimed at modelling coupled ice-ocean dynamics. It has been modified over the years and the ice component is presently frozen as it now focuses on modelling geophysical and environmental flows. One reason behind the project was to develop a model using the finite element method to take advantage of the unstructured meshes. Consequently, the first version of the model solved the depth-averaged shallow water equations using the continuous Galerkin method on various finite element pairs (Hanert et al., 2003; Le Roux et al., 2005). The model then evolved to use the discontinuous Galerkin method (Lambrechts et al., 2008a). Such methods are well suited for domains characterised by a complex geometry as unstructured meshes allows high topological flexibility and locally increasing the resolution. SLIM solves the one- (section-averaged), two- (depth-integrated) or three-dimensional hydrostatic shallow water equations under the Boussinesq approximation. Depending on the domain constraints, the user either solve the 1D, 2D or 3D equations. Section-averaged equations can be used to model the flow of river upstream parts showing small lateral variability such as the Scheldt (Gourgue et al., 2009; de Brye et al., 2010; de Brauwere et al., 2011b; de Brye et al., 2012) and the Mahakam (de Brye et al., 2011; Pham Van et al., 2016) rivers. 2D equations are able to predict the hydrodynamics of tidally-dominated flows such as the Great Barrier Reef (Lambrechts et al., 2008b; Thomas et al., 2014; Delandmeter et al., 2017), the Scheldt River and the Mahakam River but is not reliable

[15] http://thetisproject.org/
[16] http://www.climate.be/slim

in domains where there is a strong vertical shear or stratification (Delandmeter et al., 2015) or in domains where there is a steep bathymetry, strong exchange flows, and vertical stratification such as the Congo estuary (Le Bars et al., 2016; Vallaeys, 2018; Vallaeys et al., 2018, 2020). In such domains, the third spatial dimension is needed to properly model the hydrodynamics as more complex phenomena influence the flow. Consequently, a baroclinic version of SLIM, SLIM3D, has been developed. The equations are solved on prismatic elements extruded from an unstructured horizontal mesh (White et al., 2008a,b). The model was then enhanced to use the discontinuous Galerkin method (Comblen et al., 2010a; Blaise et al., 2010) and was further developed by Kärnä et al. (2013), Delandmeter et al. (2018) and Vallaeys (2018); Vallaeys et al. (2018, 2020).

Besides these hydrodynamic equations, SLIM can also solve the reactive transport equation (Gourgue et al., 2013; de Brauwere et al., 2014) and has a Lagrangian particle tracker (LPT) module (Thomas et al., 2014; Critchell and Lambrechts, 2016). Several wetting and drying algorithms were also developed to deal with tidal flats as part of the study of Mahakam river delta, Scheldt river estuary and Mekong river delta (Gourgue et al., 2009; Kärnä et al., 2011; Le et al., 2018, 2020). Other estuaries (Le Bars et al., 2016; Vallaeys et al., 2018, 2020), coral reefs areas (Legrand et al., 2006; Lambrechts et al., 2008b; Frys et al., 2020), which all have open boundaries, and enclosed domains, such as lake Tanganyika (Gourgue et al., 2007, 2011; Delandmeter et al., 2018), were also studied as part of the SLIM project.

Recently, SLIM has been applied to a domain covering the Florida Strait from the Gulf of Mexico to the Atlantic ocean in order to study the corral reefs connectivity (Frys et al., 2020). The depth-averaged version of SLIM is used to predict the hydrodynamics at large scale (the area is characterised by strong flows induced by the Gulf Stream) as well as at small scales (near the reefs and islands). The particle tracker module is used to predict the motion of corral larvae at and after spawn.

1.4 Scope of the thesis

The objective of this thesis is as follows:

> *Using the scarce available data and a numerical model to improve our knowledge of the motion of surface and subsurface liquid bodies of Titan, thereby helping design future exploration missions of this moon.*

Gaining further insight in the motion of Titan liquid bodies can only be achieved by means of numerical modelling as direct observations are impossible since Cassini's Grand Finale[17]. The motion predicted can be used by numerous scientists from various fields of research. For instance, the motion in the subsurface ocean is a key information for astrobiologists studying its habitability but it could also be used to gain further insight in the internal structure of Titan by allowing to validate hypotheses about the heat flux within the ocean. One reason for studying the liquid motion in the surface lakes and seas is to search for explanations of observed phenomena such as the "Magic Islands", shoreline variations, and solar glints. However, the main purpose is to provide some of the information requested for the planification and design of the future exploration mission(s). For instance, studying the lakes/seas temporal evolution of the heights and flows is useful for predicting areas to be avoided to prevent beaching of a landed spacecraft or for providing constrains for the design of a motorised exploration device. Indeed, the motor must be powerful enough to propel the device through the flow and wind encountered. The tidal flow can also be used to predict the path of a drifted capsule as a function of time and landing point by means of the Lagrangian particle tracker module.

The results could also be used to select/design the instruments of the future mission(s). The next observation mission, Dragonfly, will not focus on the surface lakes and seas as the timing corre-

[17]Cassini's Grand Finale is the final diving of Cassini into Saturn's atmosphere during which it disintegrated like a meteor, on the 15^{th} of September 2017.

spond to winter, and hence darkness, in the northern hemisphere and direct to Earth (DTE) communication are impossible in the high latitudes during winter (Lorenz et al., 2018). DTE communication with a lander being possible at lower latitudes, Dragonfly will land at the same location as Huygens so the wind profile measured during Huygens descent is relevant. The concept of a rotocraft was selected to facilitate the displacements while taking advantage of the dense atmosphere and low gravity. This mission will study prebiotic chemistry and extra terrestrial habitability at various locations of Titan but Dragonfly is unlikely to observe the surface lakes and seas. Therefore, the conclusions reached in this thesis regarding the instruments does not apply to this mission. Depending on the exploration mission, different data could be collected. An orbiter would not be well suited to provide data allowing a validation of the numerical results. Indeed, the vertical resolution of instruments such as a radar is too coarse to capture the predicted variations of the sea surface elevation. While an orbiter could measure the elevation of a specific point of Titan's surface, it would be complicated to isolate the liquid motion in the lake/sea from the deformation of Titan's surface as both phenomena are induced by the same forcing (and have, hence, the same period) and the amplitude of the surface deformation is several order of magnitude larger than the tidal range. Furthermore, the liquid motion in the surface lakes and seas does not result from the sole tides but is also induced by poorly constrained atmospheric forcings. An accurate knowledge of these forcings would be needed to model properly the resulting liquid motion, hence allowing comparison between model results and observations. An orbiter could also draw an accurate plan of the shoreline variations induced in a lake/sea over one Titan day. To this end, a high spatial resolution instrument able to detect accurately the presence of liquid (i.e., able to distinguish dry and wet areas for a small column of liquid) is required. While high resolution images of the Earth where provided by satellites, several complications arise when using the same instrument(s) on Titan. For instance, Titan's atmosphere is opaque to some wavelength

and the presence of methane in the atmosphere makes it harder to detect a small amount of liquid methane on the surface, which would decrease the spatial resolution of the instrument(s). Therefore, while an orbiter could measure the deformation of Titan's surface (which was achieved by Cassini), it would not be able to provide any data allowing validating the numerical results concerning the surface lakes and seas. To this end, a lander would be better suited. For instance, a floating capsule as well as a lander would be able to provide time series of the ocean elevation by means of a sonar/depth sounder, for the former, or a rangefinder, for the latter. A capsule could also measure the velocity field, liquid composition and atmospheric data such as the wind speed, air moisture, surface temperature ... While data about the velocity field are not useless, it is much more common to validate a model by comparing surface elevation time series at specific location. Indeed, the velocity field is much more sensible to poorly constrained parameters affecting a numerical model such as local variations of the bathymetry, bottom friction, atmospheric forcing (for instance, the wind orientation could be influenced by a cliff or a hummock) ... Measurements of the atmospheric data would allow to improve our model but would be useless for validation.

As part of this thesis, SLIM is modified and applied to the liquid bodies of Titan. This numerical model is based on the physical laws valid on Earth. It takes advantage of the state-of-the-art knowledge of Titan's liquid bodies while taking into account the uncertainties affecting the parameters. Predictions of the liquid motion in the surface lakes and seas can also be found in the literature as similar works were conducted in parallel with this thesis. The results presented in this thesis stand out by the number of parameters taken into account as well as by the wide range of values studied. While it allows us to constrain the impact of each of these parameters on the liquid motion, it did not result in a better range of their values. Therefore, the results presented are also subject to uncertainties and a safety factor should be used to design an exploration device while taking into account the worst case scenario prediction.

Besides the main goal, additional tasks were conducted to improve SLIM as a free and user-friendly model. An application programming interface (API) has been developed in collaboration with Dr. Jonathan Lambrechts, Dr. Valentin Vallaeys, and Dr. Philippe Delandmeter and post-processing scripts were developed to help analysing results.

1.4.1 Tides of the surface lakes and seas

In order to study the tidal motion in the surface lakes and seas of Titan, minor modifications are introduced (see Section 2.4.1). We first pay attention to Ontario Lacus, the largest lake in Titan's southern hemisphere. It had previously been studied by Tokano (2010). Our study takes advantage from a better representation of the shoreline and the recent bathymetry maps derived by Ventura et al. (2012) and Hayes (2016). Due to the uncertainties, a sensitivity study is conducted with respect to the bathymetry and the bottom friction, among other parameters. Tokano (2010) and our results, presented in Chapter 3, definitely rule out the tidal motion as the main source of the observed shoreline variations.

Our focus then switches toward two of the northern seas, Ligeia and Kraken Maria, as they are a designated target for oceanographic exploration on Titan. Indeed, they are the largest liquid bodies lying on Titan's surface, hence reducing the risk of missing the target and landing on dry ground. Another reason for paying attention to these seas is the unexplained phenomenon referred to as "Magic Islands". Once again, several parameters (bathymetry, bottom friction, depth of the straits, attenuation factor ...) are poorly constrained and a sensitivity analysis is thus conducted. Other aspects such as the liquid exchanges between the basins, the implications for future missions and the liquid motion in several specific areas (bay, canyons ...) are discussed (see Chapter 5).

1.4.2 Normal modes of Ontario Lacus

The tides being ruled out as a possible explanation for the shoreline variations, we focus on another hypothesis: a seiche could explain a significant variation of the surface elevation. To this end, we numerically study the barotropic normal modes of the lake using a mathematical approach based on Bernard et al. (2008). The method is well suited for domain with a complex geometry as it takes advantage of the geometrical flexibility of finite element methods. Nevertheless, it is impossible, using this approach, to predict the amplitude of the motion associated to the modes. Therefore, numerical simulations are conducted for arbitrary configurations likely to resonantly force some of the modes (see Chapter 4).

1.4.3 Tides of the global subsurface ocean

Finally, the liquid motion within the global subsurface ocean is studied. Although several studies about the tidal deformation of Titan exist, none of them focuses on the liquid motion within the ocean in itself, the latter being considered as a layer among others or the authors focusing on the energy dissipation without paying attention to the motion in itself. The main difficulties are raised by the fact that the shell also deforms due to the astronomical forcing. Depending on its properties, its deformation differs from the surface elevation of a free surface ocean, causing interactions between the ocean and the ice shell. In order to conduct simulations on such an ocean, significant modifications are applied to SLIM (see Section 2.5): the numerical implementation is modified to be able to solve the equation on a sphere and terms are added to the equations to take into account the impact of the ice shell. Due to the uncertainties about the depth of the ocean and the rheology of the ice shell, a sensitivity analysis with respect to these parameters is conducted. We also briefly study the interactions between the tidal flow and the flow generated by the heat fluxes at the top of the ocean for two configurations (see Chapter 6). To this end,

the baroclinic version of SLIM is modified similarly to its depth-averaged version (see Section 2.5.2.2).

Supporting publications

D. Vincent, O. Karatekin, V. Vallaeys, A.G. Hayes, M. Mastrogiuseppe, C. Notarnicola, V. Dehant, E. Deleersnijder, 2016, Numerical study of tides in Ontario Lacus, a hydrocarbon lake on the surface of the Saturnian moon Titan, *Ocean Dynamics*, 66: 461–482, doi: 10.1007/s10236-016-0926-2

D. Vincent, O. Karatekin, J. Lambrechts, R. D. Lorenz, V. Dehant, E. Deleersnijder, 2018, A numerical study of tides in Titan's northern seas, Kraken and Ligeia Maria. *Icarus*, 310: 105-126, doi: 10.1016/j.icarus.2017.12.018

D. Vincent, J. Lambrechts, O. Karatekin, T. Van Hoolst, R. H. Tyler, V. Dehant, E. Deleersnijder, 2019, Normal modes and resonance in Ontario Lacus: a hydrocarbon lake of Titan. *Ocean Dynamics*, 69: 1121-1132, doi: 10.1007/s10236-019-01290-2

D. Vincent, J. Lambrechts, O. Karatekin, T. Van Hoolst, R. H. Tyler, V. Dehant, E. Deleersnijder, Modelling of Titan's subsurface ocean liquid motion. *Icarus*, (In preparation)

C. Frys, A. Saint-Amand, M. Le Hénaff, J. Figueiredo, A. Kuba, B. Walker, J. Lambrechts, V. Vallaeys, **D. Vincent**, E. Hanert, High-resolution marine connectivity modelling in the Florida Coral Reef Tract, *Frontiers in Marine Science* (Submitted)

Public presentations

D. Vincent, O. Karatekin, V. Dehant, E. Deleersnijder, 2015 Numerical simulations of tides in Ontario Lacus. European geoscience Union - General Assembly, Vienna.
http://hdl.handle.net/2078.1/158392

D. Vincent, O. Karatekin, V. Dehant, E. Deleersnijder, 2016, Modelling of tidal flows between Titan's seas Kraken Mare and Ligeia Mare. Titan surface meeting, Paris.

D. Vincent, O. Karatekin, V. Dehant, E. Deleersnijder, 2016, Modelisation of tidal flows between Titan's seas Kraken Mare and Ligeia Mare. European geoscience Union - General Assembly, Vienna.
http://hdl.handle.net/2078.1/173566

D. Vincent, O. Karatekin, V. Dehant, E. Deleersnijder, Eric, 2017, Study of liquid exchanges between Titan's seas Kraken Mare and Ligeia Mare. European geoscience Union - General Assembly, Vienna.
http://hdl.handle.net/2078.1/185118

D. Vincent, O. Karatekin, V. Dehant, E. Deleersnijder, Eric, 2017, Modelling the tides of Titan's liquid bodies. TECLIM Seminar, Louvain-la-Neuve.

D. Vincent, O. Karatekin, J. Lambrechts, V. Dehant, E. Deleersnijder, 2018, Tides and eigenmodes of an idealized subsurface global ocean on Titan. European geoscience Union - General Assembly, Vienna.
http://hdl.handle.net/2078.1/196902

H. A. Le,X. H. D. Vu, J. Lambrechts, S. Ortleb, V. Vallaeys, **D. Vincent**, N. Gratiot, S. Soares Frazao, E. Deleersnijder, 2018, A new wetting – drying algorithm integrated in SLIM, with an application to the Tonle Sap lake, Mekong. European geoscience Union - General Assembly, Vienna.
http://hdl.handle.net/2078.1/196904

CHAPTER 2

Developments in SLIM

Abstract

The tides of Titan's liquid bodies are studied by means of an Earth-based numerical model, the Second-generation Louvain-la-Neuve Ice-ocean Model (SLIM, www.climate.be/slim). It has been developed to study the river-sea continuum and has been applied to numerous terrestrial domains. A 2D and a 3D version solving the depth-averaged shallow water equations and the 3D hydrostatic equations under the Boussinesq approximation, respectively, are available. The governing equations of each version are derived and the discretisation and temporal scheme used are presented. The model is slightly modified to take into account the specificities of Titan's extra-terrestrial environment while studying the tides of the surface lakes and seas. Besides these modifications, which concern the numerical implementation, several post processing tools and a user-friendly application programming interface are developed.

The subsurface ocean lying beneath an icy shell, they interact together. The equations solved are therefore modified to take into account the influence of the ice shell on the ocean. To this end, a surface pressure term and a surface friction term are added. The model is also modified to solve the equation on a spherical domain following a method previously developed within the SLIM project but which was no longer available.

2.1 Introduction

The state-of-the-art numerical model used is the Second-generation Louvain-la-Neuve Ice-ocean Model (`SLIM`, `www.climate.be/slim`). It has been developed by several PhD students, PhD graduates and Professors in order to study the river-sea continuum. It has been successfully applied to numerous domains on Earth such as Lake Tanganyika (Gourgue et al., 2007), the whole Great Barrier Reef (Lambrechts et al., 2008b), the Scheldt (de Brye et al., 2010), the Mahakam (de Brye et al., 2011), and Congo estuaries (Le Bars et al., 2016; Vallaeys et al., 2020) ... The 2D version (referred to as SLIM2D in this document) is sufficiently mature to be used by scientists who did not take part in the development. To facilitate the use of the model, a user-friendly application programming interface (API) was developed. Several wetting-drying algorithms were implemented in order to deal with tidal flats: an explicit algorithm was first developed (see Gourgue et al. (2009)); then an implicit one was developed (see Kärnä et al. (2011)). The latter is used to deal with the tidal flats while studying the tidal motion in Ontario Lacus. Recently, a third algorithm was developed and implemented by Le et al. (2020). Several modules were added to SLIM2D: a Lagrangian particle tracker module (Thomas et al., 2014), a passive or active tracer model (de Brauwere et al., 2011a), a sediment transport model (Gourgue et al., 2013; Van et al., 2016), and the Constituent oriented Age and Residence time Theory (CART) (de Brye et al., 2012). Tuomas Kärnä, Philippe Delandmetter, and Valentin

Vallaeys developed a 3D version (referred to as SLIM3D in this thesis). A sediment transport model associated to SLIM3D was developed by Delandmeter et al. (2015). Although it is also available trough the API, it is not mature yet and is still currently under development.

In this chapter, we briefly introduce SLIM and the modifications introduced to adapt the model to an extra-terrestrial domain. The governing equations are derived in Section 2.2. SLIM 2D and SLIM3D are based on different equations: the depth-averaged shallow water equations (see Section 2.2.1) and the 3D hydrostatic equations under the Boussinesq approximation (see Section 2.2.2), respectively. The temporal schemes and spatial discretisations implemented are briefly introduced in Section 2.3.

Depending on the domain studied, either SLIM2D or SLIM3D is resorted to. In order to study the liquid bodies of Titan, the models are modified accordingly. SLIM2D is resorted to to study the liquid motion in the surface lakes and seas as the hydrodynamic is expected to be mainly horizontal, the interactions with the atmosphere being ignored. To this end, the equations are not modified and only minor improvements are introduced (see Section 2.4.1). Modelling the liquid motion of the global subsurface ocean requires modifying the equations of both SLIM2D (see Section 2.5.2.1) and SLIM3D (see Section 2.5.2.2) as the ice shell interacts with the liquid motion. As we pay interest to a global ocean, the equations are solved on the sphere rather than on a horizontal mesh created by means of a geographic projection. To this end, a method previously developed within the framework of the SLIM project is resorted to and is implemented (see Section 2.5.1).

2.2 Governing equations

The developments presented in this section are based on Deleersnijder (2018). The governing equations of SLIM derive from the mass and momentum balances. The mass budget equation is

$$\frac{\mathrm{d}}{\mathrm{d}t}\int_{\Omega}\rho\,\mathrm{d}\Omega = 0 \tag{2.1}$$

where $\Omega(t)$ is a material volume (i.e. a finite-size control volume that is always made up of the same fluid parcels (Deleersnijder, 2018)). Using the divergence and Reynolds' transport theorems (see, e.g., Deleersnijder, 2019) allows transforming Eq. 2.1 into a volume integral. The latter must hold valid for any control domain. Therefore, its integrand must be zero, yielding the mass conservation equation

$$\frac{\partial\rho}{\partial t} + \nabla\cdot(\rho\boldsymbol{v}) = 0 \tag{2.2}$$

which is commonly referred to as the continuity equation. Assuming that the density variations are small with respect to a suitable reference value (a simplification commonly referred to as the Boussinesq approximation) leads to

$$\nabla\cdot\boldsymbol{v} = 0 \tag{2.3}$$

The momentum budget in a fluid flow is

$$\frac{\mathrm{d}}{\mathrm{d}t}\int_{\Omega}\rho\boldsymbol{v}\,\mathrm{d}\Omega = \int_{\Omega}\rho\boldsymbol{f}\,\mathrm{d}\Omega + \int_{\Gamma}\mathbf{T}\cdot\boldsymbol{n}\,\mathrm{d}\Gamma \tag{2.4}$$

where Ω is a material volume; Γ is the surface delimiting the material volume; $\boldsymbol{n}$ is its outward unit normal vector; $\boldsymbol{f}(t,\boldsymbol{x})$ is the acceleration induced by the volume forces; and $\mathbf{T}$ is the stress tensor associated to the contact forces. Applying the divergence and Reynolds' transport theorems (see, e.g., Deleersnijder, 2019) allows transforming Eq. 2.4 into a volume integral. The latter must hold

valid for any control domain. Therefore, its integrand must be zero, leading to the momentum conservation equation

$$\frac{\partial \rho \boldsymbol{v}}{\partial t} = \boldsymbol{f} - \nabla \cdot (\rho \boldsymbol{v}\boldsymbol{v} - \mathbf{T}) \tag{2.5}$$

The stress tensor can be parametrised as

$$\mathbf{T} = -p\mathbf{I} + \boldsymbol{\sigma} \tag{2.6}$$

where p is the pressure; $\mathbf{I}$ is the identity tensor; and $\boldsymbol{\sigma}$ is the viscous stress tensor. For a Newtonian fluid taking into account the Stokes assumption, it is given by $\boldsymbol{\sigma} = \rho\nu \left[\nabla \boldsymbol{v} + (\nabla \boldsymbol{v})^T - \frac{2}{3}\nabla \cdot \boldsymbol{v}\right]$ (ν is the kinematic viscosity). The only forces acting at a distance taken into account are the force of attraction exerted by Saturn and the weight $\boldsymbol{f} = \rho(\boldsymbol{g}^* + \boldsymbol{S})$ where $\boldsymbol{g}^*$ is the gravitational acceleration and $\boldsymbol{S}$ is the acceleration resulting from Saturn's attraction force. Applying Reynolds' averaging operator to these equations under the Boussinesq approximation ($\frac{\Delta\rho}{\rho_.} \ll 1$) and using a Fourier-Fick formula for the unresolved flux leads to the convective form of the momentum equation:

$$\begin{aligned}\frac{\partial \boldsymbol{v}}{\partial t} + \boldsymbol{v} \cdot \nabla \boldsymbol{v} = \frac{-1}{\rho_.}\nabla p + \frac{\rho}{\rho_.}(\boldsymbol{g}^* + \boldsymbol{S}) \\ - \nabla \cdot \left[-(\nu + \nu_t)[\nabla \boldsymbol{v} + (\nabla \boldsymbol{v})^T] + \frac{2}{3}k\mathbf{I}\right]\end{aligned} \tag{2.7}$$

where $\rho_.$ denotes the reference value for the density, ν_t is the eddy viscosity, and k is the turbulent kinetic energy. As Titan is rotating (and, hence, we work in a non-inertial framework attached to the moon), Coriolis ($\boldsymbol{a}_c$) and entrainment ($\boldsymbol{a}_e$) accelerations have to be taken into account.

The equation thus reads

$$\frac{\partial \boldsymbol{v}'}{\partial t} + \boldsymbol{v}' \cdot \nabla \boldsymbol{v}' + \boldsymbol{a}_c + \boldsymbol{a}_e = \frac{-1}{\rho_.} \nabla' p + \frac{\rho}{\rho_.}(\boldsymbol{g}^* + \boldsymbol{S}) - \nabla' \cdot \left[-(\nu + \nu_t)[\nabla' \boldsymbol{v}' + (\nabla' \boldsymbol{v}')^T] + \frac{2}{3} k \mathbf{I} \right] \quad (2.8)$$

where $'$ denotes the terms expressed in the mobile reference frame. For instance, $\boldsymbol{v}'$ is the relative velocity. The Coriolis acceleration is given by $\boldsymbol{a}_c = 2\boldsymbol{\Omega} \wedge \boldsymbol{v}'$ (where $\boldsymbol{\Omega}$ is Titan's rotation rate and $\wedge$ denotes the vector product) while the entrainment acceleration reduces to $\boldsymbol{a}_e = \boldsymbol{\Omega} \wedge (\boldsymbol{\Omega} \wedge \boldsymbol{x})$. The apparent gravitational acceleration is then defined as $\boldsymbol{g} = \boldsymbol{g}^* - \boldsymbol{\Omega} \wedge (\boldsymbol{\Omega} \wedge \boldsymbol{x})$, resulting in the following equation:

$$\frac{\partial \boldsymbol{v}'}{\partial t} + \boldsymbol{v}' \cdot \nabla \boldsymbol{v}' + 2\boldsymbol{\Omega} \wedge \boldsymbol{v}' = \frac{-1}{\rho_.} \nabla' p + \frac{\rho}{\rho_.}(\boldsymbol{g} + \boldsymbol{S}) - \nabla' \cdot \left[-(\nu + \nu_t)[\nabla' \boldsymbol{v}' + (\nabla' \boldsymbol{v}')^T] + \frac{2}{3} k \mathbf{I} \right] \quad (2.9)$$

Let us now introduce the concepts of reduced pressure $q(t, \boldsymbol{x}) = \frac{p(t,\boldsymbol{x}) - p_.(0)}{\rho_.} + gz$ (where $p_.(0)$ is the reference pressure at the altitude $z = 0$ (i.e. the geoid)) and buoyancy $b(t, \boldsymbol{x}) = -g\frac{\rho(t,\boldsymbol{x})}{\rho_.} + g$. These concepts pave the way for the scaling of the momentum equation and allows us to highlight a reference state at hydrostatic equilibrium. Substituting these concepts in Eq. 2.9 leads to the 3D hydrostatic equations under the Boussinesq approximation (the $'$ are dropped for the sake of simplicity):

$$\frac{\partial \boldsymbol{v}}{\partial t} + \boldsymbol{v} \cdot \nabla \boldsymbol{v} + 2\boldsymbol{\Omega} \wedge \boldsymbol{v} = -\nabla q - b\boldsymbol{e}_z + \frac{\rho}{\rho_.} \boldsymbol{S} - \nabla \cdot \left[-(\nu + \nu_t)[\nabla \boldsymbol{v} + (\nabla \boldsymbol{v})^T] + \frac{2}{3} k \mathbf{I} \right] \quad (2.10)$$

The eddy viscosity being significantly larger than the molecular one, the latter is discarded. Splitting the horizontal dynamics from the vertical yields to

$$\begin{aligned}\frac{\partial \boldsymbol{u}}{\partial t} + f_n w \boldsymbol{e}_x + f \boldsymbol{e}_z \wedge \boldsymbol{u} &= -\nabla_h q - \frac{\partial}{\partial z}\left(\boldsymbol{u}w - \nu_{t,v}\frac{\partial \boldsymbol{u}}{\partial z} - \nu_{t,v}\nabla_h w\right) \\ &\quad + \frac{\rho}{\rho_.}\boldsymbol{S} - \nabla_h \cdot \left(\boldsymbol{u}\boldsymbol{u} - \nu_{t,h}(\nabla_h \boldsymbol{u} + (\nabla_h \boldsymbol{u})^T) + \frac{2}{3}k\mathbf{I}\right) \\ \frac{\partial w}{\partial t} - f_n u &= -\frac{\partial q}{\partial z} + b - \nabla_h \cdot \left(w\boldsymbol{u} - \nu_{t,h}\left(\nabla_h w + \frac{\partial \boldsymbol{u}}{\partial z}\right)\right) \\ &\quad - \frac{\partial}{\partial z}\left(ww - 2\nu_{t,v}\frac{\partial w}{\partial z} + \frac{2}{3}k\right) \quad (2.11)\end{aligned}$$

where $\boldsymbol{u}$ is the horizontal velocity field, w is the vertical velocity, the subscript h denotes the horizontal part of the del operator, $\nu_{t,h}$ and $\nu_{t,v}$ are the horizontal and vertical eddy viscosity, and f and f_n comes from the f-plane approximation $2\boldsymbol{\Omega} = f\boldsymbol{e}_z + f_n\boldsymbol{e}_y$ where $\boldsymbol{e}_z$ and $\boldsymbol{e}_y$ are unit vectors pointing upwards and tangent to Titan in the local non-inertial cartesian basis, respectively. Resorting to dimensionless variables and operators allows highlighting terms multiplied by the ratio between the vertical and horizontal length scales, the so-called aspect ratio. For small aspect ratio flows, such terms can be neglected. Hence, the horizontal momentum equation reads

$$\frac{\partial \boldsymbol{u}}{\partial t} + \boldsymbol{u} \cdot \nabla \boldsymbol{u} + f\boldsymbol{e}_z \wedge \boldsymbol{u} = -\nabla_h q + \frac{\rho}{\rho_.}\boldsymbol{S} + \frac{\partial}{\partial z}\left(\boldsymbol{u}w - \nu_t \frac{\partial \mathbf{u}}{\partial z}\right) \quad (2.12)$$

The vertical momentum balance reduces to the hydrostatic equilibrium as a consequence of the smallness of the aspect ratio. In physical terms, the pressure-gradient force balances the weight of the fluid column.

$$\frac{\partial q}{\partial z} = b \quad (2.13)$$

The liquid density, which appears in the reduced pressure and buoyancy term, is computed as a function of temperature. It is

rewritten as the sum of a constant reference density $\rho_.$ and a deviation ρ', which is much smaller than $\rho_.$. Integrating Eq. 2.13 over the water column leads to the following expression for the pressure field

$$p = g\rho_.(\eta - z) + p_a + g\int_z^\eta \rho' \mathrm{d}\zeta \tag{2.14}$$

where p_a is the atmospheric pressure acting on the sea surface and η is the sea surface elevation.

The free surface equation can be obtained by integrating the continuity equation (Eq. 2.3) over the water column:

$$\frac{\partial \eta}{\partial t} + \nabla_h \cdot \int_{-h}^{\eta} \boldsymbol{u} \mathrm{d}z = 0 \tag{2.15}$$

Following a similar procedure, the equation describing the evolution of a tracer C is derived. It reads:

$$\frac{\partial C}{\partial t} + \nabla_h \cdot (\boldsymbol{u}C) + \frac{\partial (wC)}{\partial z} = \nabla_h \cdot (\mu_h \nabla_h C) + \frac{\partial}{\partial z}\left(\mu \frac{\partial C}{\partial z}\right) \tag{2.16}$$

where μ and μ_h respectively denote the vertical and horizontal eddy diffusivity.

2.2.1 Shallow water equations

The depth-averaged shallow water equations are derived by integrating Eq. 2.12 over the height of the water column under the impermeability conditions of the sea surface and bottom while taking into account the hydrostatic equilibrium (Eq. 2.13) and assuming the buoyancy term can be neglected (i.e. the density contrast or the water depth is small). The idea behind the impermeability conditions is that no fluid parcel is allowed crossing the surface. It reads $[(\boldsymbol{v} - \boldsymbol{v}^\Gamma) \cdot \boldsymbol{n}]_{\boldsymbol{x}\in\Gamma}$, where Γ is the impermeable surface, $\boldsymbol{n}$ is the unit normal vector to the latter and $\boldsymbol{v}^\Gamma$ denote the velocity of a point of the surface.

Using the outward unit normals to the seabed and to the surface shown in Fig. 2.1, the bottom and surface impermeability conditions read $[\boldsymbol{u} \cdot \nabla h + w]_{z=-h} = 0$ and $[\frac{\partial \eta}{\partial t} + \boldsymbol{u} \cdot \nabla \eta - w]_{z=\eta} = 0$. The

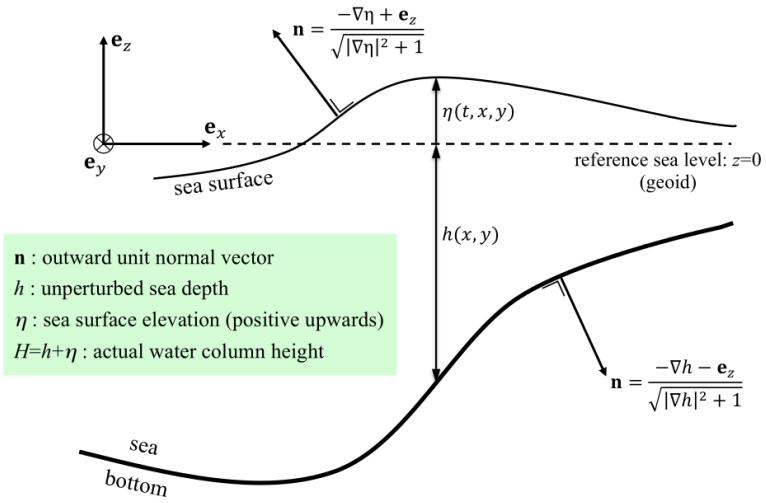

Fig. 2.1: Geometry of a standard domain. The water height column, H, is the sum of the unperturbed sea depth, h, and the sea surface elevation (positive upwards), η. The outward unit normal vector of the sea surface and bottom are drawn and their analytical formula is detailed. Figure courtesy of Deleersnijder (2018).

momentum equations resume in

$$\frac{\partial(H\overline{\boldsymbol{u}})}{\partial t} + H\overline{\boldsymbol{u}}\cdot\nabla\overline{\boldsymbol{u}} + f\boldsymbol{e}_z \wedge (H\overline{\boldsymbol{u}}) = -\frac{H}{\rho_.}\nabla_h p^a - gH\nabla_h\eta + \frac{\boldsymbol{\tau}^s - \boldsymbol{\tau}^b}{\rho_.} \\ -\nabla_h\cdot\left[H\nu_h[\nabla_h\overline{\boldsymbol{u}} + (\nabla_h\overline{\boldsymbol{u}})^T]\right] + H\boldsymbol{S} \tag{2.17}$$

where $\overline{\boldsymbol{u}}$ is the depth-averaged velocity, $\boldsymbol{\tau}^b$ and $\boldsymbol{\tau}^s$ respectively denote the bottom and surface stress, and ν_h is the 2D horizontal diffusivity. The continuity equation (Eq. 2.15) reads

$$\frac{\partial\eta}{\partial t} + \nabla\cdot(H\overline{\boldsymbol{u}}) = 0 \tag{2.18}$$

Dividing Eq. 2.17 by the water depth leads to the non conservative form of the depth-averaged shallow water equations (the symmetric part of the viscosity operator $\nu_h \nabla_h \overline{\boldsymbol{u}}^T$ is not implemented in the model):

$$\begin{cases} \dfrac{\partial \eta}{\partial t} + \nabla \cdot (H\overline{\boldsymbol{u}}) = 0 \\ \dfrac{\partial \overline{\boldsymbol{u}}}{\partial t} + \overline{\boldsymbol{u}} \cdot \nabla \overline{\boldsymbol{u}} + f \boldsymbol{e}_z \wedge \overline{\boldsymbol{u}} = -g\nabla\eta - \dfrac{1}{\rho_.}\nabla_h p^a + \dfrac{\boldsymbol{\tau}^s - \boldsymbol{\tau}^b}{\rho H} + \boldsymbol{S} \\ \qquad\qquad + \dfrac{1}{H}\nabla_h \cdot \left(H\nu_h [\nabla \overline{\boldsymbol{u}} + (\nabla \overline{\boldsymbol{u}})^T] \right) \end{cases} \tag{2.19}$$

Eddy viscosity and bottom friction in the shallow water equations respectively are parametrised by means of Smagorinsky's closure model (Smagorinsky, 1963) and empirical Earth-based formulas. The formulations used to model the bottom stress are commonly used on Earth. While Titan is a different environment (in terms of temperature, density, and pressure), there is no evidence pointing towards a significant modification of the phenomenological laws representing the turbulent flows. Consequently, the same approach as on Earth is implemented: the effect of a turbulent boundary layer at the bottom/top of the liquid bodies is modelled by means of a quadratic drag formulation (either the standard quadratic formulation or Chézy-Manning-Strickler's formulation).

When studying Titan's surface lakes and seas, the Chézy-Manning-Strickler's formulation (see, e.g., Lambrechts et al., 2008b) is used. Accordingly, the bottom stress is estimated as follows:

$$\boldsymbol{\tau}^b = \rho g n^2 \frac{|\overline{\boldsymbol{u}}|\overline{\boldsymbol{u}}}{H^{1/3}} \tag{2.20}$$

where $n \in [0.01, 0.075]$ sm$^{-1/3}$ is Manning's roughness coefficient (it is set to 0.03 sm$^{-1/3}$, which corresponds to a natural river bottom on Earth). One advantage of this formulation is the appearance of the mean gravitational acceleration which can, hence, be modified

accordingly. Manning's roughness coefficient depends on the surface material. While the bottom of dry lakes looks smooth at large scales, there is a lack of information about the surface material. Therefore, we selected a reference value corresponding to a natural river bottom on Earth and conducted sensitivity analysis with respect to this parameter. It is unlikely that the bottom of Titan's liquid bodies is uniform but information about the spatial variation of the roughness are lacking. On Earth, although the variations of the roughness are more easily constrained, they are not taken into account in most cases and implementing a uniform roughness is a last resort to which numerous models resort to. In this thesis, the same approach is used. In order to quantify the impact of a spatially variable roughness, simulations are conducted with a roughness coefficient randomly varying between 0.01 $\mathrm{sm}^{-1/3}$ and 0.06 $\mathrm{sm}^{-1/3}$ and between 0.02 $\mathrm{sm}^{-1/3}$ and 0.04 $\mathrm{sm}^{-1/3}$. The modifications induced by a spatial variation of the friction coefficient are expected to be small. Altaf et al. (2012) conducted numerical experiments to calibrate the depth and friction coefficient in the North Sea in order to improve the modelling of the tides. They concluded that depth adjustments have a far greater influence on the results than the spatial variations of the bottom friction (taking into account the latter does not reduce significantly the error with respect to the observations).

The standard quadratic formulation is used to model the bottom friction of the global subsurface ocean to facilitate the comparison with SLIM3D. In this case, the bottom stress reads:

$$\boldsymbol{\tau}^b = C_D \rho |\overline{\boldsymbol{u}}| \overline{\boldsymbol{u}} \tag{2.21}$$

where $C_D = 2.5 \times 10^{-3}$ is the bottom drag coefficient.

The surface stress term, which represents the effect of the wind, is modelled by means of an empirical Earth-based model. The wind-induced surface stress is

$$\boldsymbol{\tau}^s = C_{D_w} \rho_{atm} |\boldsymbol{u}_{10}|^2 \frac{\boldsymbol{u_{10}}}{|\boldsymbol{u_{10}}|} \tag{2.22}$$

with C_{D_w}, the wind drag coefficient; ρ_{atm}, the atmosphere density; and $\boldsymbol{u}_{10}$, the wind velocity 10 m above ground level (see, e.g., Drews, 2013). According to Drews (2013), C_{D_w} is about 1.2×10^{-3} on Earth lakes when $|\boldsymbol{u}_{10}] < 11$ m/s, which corresponds to the wind conditions expected on Titan (see Section 1.1.1).

The depth-averaged tracer equation is derived from Eq. 2.16 where the shear dispersion term is parametrised à la Fourier-Fick. The equation reads

$$\frac{\partial}{\partial t}(H\overline{C}) + \nabla_h \cdot (H\overline{\boldsymbol{u}}\overline{C}) = \nabla_h \cdot (H\kappa \mathbf{I} \cdot \nabla_h \overline{C}) \tag{2.23}$$

where κ is the horizontal diffusivity.

2.2.2 Baroclinic equations

The continuity equation, the three dimensional hydrostatic equations under the Boussinesq approximation, and an advection-diffusion equation of the temperature field are both implemented in SLIM3D. They read

$$\begin{cases} \dfrac{\partial \boldsymbol{u}}{\partial t} + \nabla_h \cdot (\boldsymbol{u}\boldsymbol{u} + \dfrac{\partial w\boldsymbol{u}}{\partial z}) = -f\boldsymbol{e}_z \wedge \boldsymbol{u} - \dfrac{g}{\rho_.}\nabla_h \displaystyle\int_h^\eta \rho' d\zeta \\ \qquad - g\nabla_h \eta + \nabla_h \cdot (\nu_h[\nabla_h \boldsymbol{u} + (\nabla_h \boldsymbol{u})^T]) + \dfrac{\partial}{\partial z}\left(\nu \dfrac{\partial \boldsymbol{u}}{\partial z}\right) \\ \nabla_h \cdot \boldsymbol{u} + \dfrac{\partial w}{\partial z} = 0 \\ \dfrac{\partial T}{\partial t} + \nabla_h \cdot (\boldsymbol{u}T) + \dfrac{\partial (wT)}{\partial z} = \nabla_h \cdot (\kappa_h \nabla_h T) + \dfrac{\partial}{\partial z}\left(\kappa \dfrac{\partial T}{\partial z}\right) \end{cases} \tag{2.24}$$

where T is the temperature field, w is the vertical velocity, $\rho' = \rho - \rho_.$ is the density deviation, ν and ν_h are the vertical and horizontal eddy viscosities and κ and κ_h are the vertical and horizontal eddy

diffusivities. The horizontal eddy viscosity is given by Smagorinsky's closure model (Smagorinsky, 1963). In terrestrial applications, the vertical eddy viscosity and diffusivity can be constant or determined either by the Pacanowski-Philander closure scheme (Pacanowski and Philander, 1981) or with the $k-\epsilon$ turbulence closure model GOTM (Burchard et al., 1999). In this thesis, the more basic approach is resorted to and Pacanowski-Philander's scheme is used. The symmetric part of the viscosity operator $\nu_{t,h}(\nabla_h \boldsymbol{u})^T$ is not implemented in the model. In the Earth-based version of SLIM3D, the density is a function of the temperature and salinity following the state equation of Jackett et al. (2006). Due to the lack of information about the "salinity" field in Titan's ocean[1], the salinity equation is not solved and the density is derived from the sole temperature field using a different function. For instance, in the subsurface ocean, the density is given by a linearisation of Kell (1975)'s formulation near a temperature of $T_0 = 282.75$ K: $\rho = \rho_. - 0.096(T - T_0)$ where $\rho_.$ is the reference density (it is the same as the reference value for the density in the hydrodynamic equations). As the temperature can vary spatially and temporally, the temperature field is simulated by an advection-diffusion equation (Eq. 2.16, 2.24) where the horizontal eddy diffusivity is evaluated by Okubo's formula (Okubo, 1971).

2.3 Discretisation and temporal schemes

SLIM relies on the discontinuous Galerkin finite element method (DGFEM) to solve the equations on an unstructured mesh. The 3D mesh is obtained by extruding a 2D mesh over the depth of the domain. Unstructured grids allow the user to refine the mesh at

[1]There is no salinity strictly speaking but there are mineral salts and/or ammonia playing the same role as the salinity on Earth. Although they play a similar role, their impact on the density cannot be modelled by the state equation of Jackett et al. (2006).

some particular places (in the vicinity of the shores or where the bathymetry gradient is the most significant) without significantly increasing the computational cost. They also have the advantage of circumventing problems specific to spherical domains such as the pole problem (the smaller grid spacing near the poles has a negative impact on the time step of an explicit model). Another asset of DGFEM is the high flexibility regarding the method spatial order: one can easily switch from first order elements to lower or higher order elements without modifying the source code of the model. The unknown fields and their spatial derivatives are discretised by means of the DGFEM. The numerical solutions are thus a piecewise polynomial function that can be discontinuous at the element interfaces. The inter-element fluxes are evaluated by means of either a Riemann solver (for further details, see Bernard et al., 2007) or a Lax-Friedrich solver, whose choice is left to the user discretion. This method is well suited for advection dominated problems as characteristic variables are upwinded across the element interface and does not suffer excessive numerical dissipation or oscillations. Moreover, it is highly parallelisable and local mass conservation is ensured. Several time-marching schemes are available depending on the model. In SLIM2D, implicit or explicit Runge-Kutta and Euler schemes and a multirate scheme developed by Seny et al. (2013) are available. In SLIM3D, the fast and slow propagating modes are solved separately. The splitting between internal and external modes, which is crucial regarding the computation time, is based on the approach of Higdon and de Szoeke (1997). The fast propagating gravity waves are simulated by means of the depth-averaged shallow water equations (Eq. 2.17) which are solved by means of an explicit Runge-Kutta scheme. The full 3D equations can be solved using the same numerical scheme or using an implicit scheme, allowing a larger time step. For further details about the mode splitting in SLIM3D, the reader is referred to (Vallaeys, 2018). The temperature is predicted by means of an advection-diffusion equation. In this equation, the temperature is the unknown while the velocity field is given by the continuity and momentum equations. The

latter required an *a priori* knowledge of the density field, which varies with the temperature. Both equations are thus coupled. In practice, the velocity field is computed at a transitional time step t^* using the 2D equations (following the mode splitting implemented). This velocity field, $\boldsymbol{u}^*$ is used in the advection-diffusion equation to predict the evolution of the temperature field over the whole time step, T^{n+1}. The density field is then computed from the temperature at t^{n+1}, which provides the density field required to compute the velocity field at t^{n+1}.

2.4 Application to the surface lakes and seas

The surface lakes and seas of Titan are filled with liquid hydrocarbons (mainly methane and ethane). Earth-based models are used in order to study the liquid motion within these liquid bodies. While the same physical laws apply on Titan, the extraterrestrial environment requires modifying some aspects of SLIM. Let us first ensure that the depth-averaged shallow water equations can be applied to the liquid bodies of Titan. Deriving Eqs. 2.19 and 2.11 from the mass and momentum budgets rests on three main assumptions. The first one is that the liquid behaves as a Newtonian fluid for which the Stokes assumption stands. Although the exact liquid composition is not known, the main constituents (methane, ethane, and nitrogen) are clearly identified. Separately, these constituents behave as Newtonian fluids. Furthermore, the dynamic viscosity of the liquid is $\mathcal{O}(10^{-3})$ Pa.s (Lorenz et al., 2010), which is the same order of magnitude as that of the water and the Reynolds number is $\mathcal{O}(10^8)$, which is similar to the Reynolds number observed in terrestrial domain such as Lake Ontario. Therefore, we assume the liquid also behaves as a Newtonian fluid. This allows computing the stress tensor as in Eq. 2.6. The second hypothesis is that the Boussinesq approximation stands, i.e. the density variations are small with respect to the mean density value. Tan et al. (2015)

predicted a maximum liquid density variation due to temperature changes of about 50 kg/m^3 for the temperature variations observed between 2006 and 2013 by Jennings et al. (2009, 2011), and by Cottini et al. (2012). The mean liquid density is at least one order of magnitude larger: depending on the model, it ranges from 547 kg/m^3 (Tan et al., 2015) to 662 kg/m^3 (Cordier et al., 2009). According to Cottini et al. (2012), the temperature diurnal variations are disappearing at latitudes greater than 40° in the south and 30° in the north. The liquid filled lakes and seas being located at higher latitudes and the tidal time scale being much smaller than that of the temperature variations observed by Jennings et al. (2009, 2011) and Cottini et al. (2012), the assumption that the density is constant can be resorted to. The last hypothesis is that the aspect ratio is small, implying that the hydrostatic assumption is valid. This assumption holds valid as the surface lakes and seas are shallow. For instance, Ontario Lacus' maximum depth is 58 m while the lake width is about 70 km and the deeper northern seas are expected to have a maximum depth of about 200 m (in Kraken mare) while their horizontal length scale is $\mathcal{O}(10^2)$ km. As the three assumptions hold valid, SLIM2D and SLIM3D can be resorted to to study the liquid motion of the surface lakes and seas.

2.4.1 Model modifications

In order to study the surface lakes and seas of Titan, the physical parameters hard-coded in the model had to be modified. The mean gravitational acceleration and the liquid density (used within the Chézy-Manning-Strickler scheme to predict the bottom friction) can now be provided by the user (the default value is set for terrestrial domain). The molecular viscosity being much smaller than the eddy viscosity, it is not taken into account in the model. A source term modelling the tidal forcing $\boldsymbol{S}$ is added to the momentum equation. The latter is due to Titan's obliquity and its orbital eccentricity (see Section 1.1.4). It is given by the product of the horizontal gradient of the tidal potential and an attenuation

factor γ_2, $\boldsymbol{S} = \gamma_2 \nabla_h \phi = \gamma_2 \nabla_h (\phi_{ecc} + \phi_{obl})$. This factor represents the impact of the deformation of Titan surface, which is induced by the same tidal potential. The resulting equations read:

$$\begin{cases} \dfrac{\partial \eta}{\partial t} + \nabla \cdot (H\overline{\boldsymbol{u}}) = 0 \\ \dfrac{\partial \overline{\boldsymbol{u}}}{\partial t} + \ \overline{\boldsymbol{u}} \cdot \nabla \overline{\boldsymbol{u}} \ + f\boldsymbol{e}_z \wedge \overline{\boldsymbol{u}} + g\nabla\eta \ = \dfrac{1}{H}\nabla \cdot (H\nu\nabla\overline{\boldsymbol{u}}) \\ \qquad\qquad\qquad\qquad\qquad\qquad\qquad\qquad + \dfrac{\boldsymbol{\tau}^s - \boldsymbol{\tau}^b}{\rho H} + \gamma_2 \nabla_h \phi \end{cases} \tag{2.25}$$

2.5 Application to the global subsurface ocean

First, let us ensure the governing equations of SLIM2D and SLIM3D are well suited to model the liquid motion within the global subsurface ocean. The first assumption is fulfilled as the ocean is filled with liquid water. The ocean is assumed vertically mixed as it is heated at its bottom and cooled down at its top. While some local density variations could occur due to variations in the composition or to the temperature gradient, they are expected to be small with respect to the mean density of the ocean (about 1200 kg/m^3). Therefore, the Boussinesq approximation holds valid. The aspect ratio could be more problematic. Titan has a radius of about 2575 km (from which the surface ice shell thickness has to be deducted) but the ocean depth is $\mathcal{O}(10^2)$ km. The resulting aspect ratio ranges from 1.9×10^{-2} for a 50 km deep ocean to 0.16 for an ocean depth of 400 km. Consequently, the assumption holds valid for a shallow ocean. For a somewhat deeper ocean, the assumption could be questionable but we consider it still holds valid as it remains one order of magnitude smaller than unity. As the three assumptions hold valid, SLIM2D ans SLIM3D can be resorted to to

study the liquid motion of a global surface ocean. In order to solve the equations on a sphere, the model is modified (see Section 2.5.1).

The ocean lying beneath an icy shell, they interact together. In order to model such interactions, the depth-averaged shallow water equations and the full 3D hydrostatic equations under the Boussinesq approximation are modified. The derivation of the additional terms is introduced in Section 2.5.2 and the resulting modifications of the hydrodynamic equations are presented in Sections 2.5.2.1 and 2.5.2.2, respectively.

2.5.1 Ocean discretisation

At the beginning of this thesis, despite the previous work of Comblen et al. (2009), the up-to-date version of SLIM was only able to solve equations on a flat domain. Thus, the user had first to project the domain using a geographic projection such as the stereographic or Universal Transverse Mercator (UTM) projection. Although this is of little inconvenience for small domains as the ones previously studied, this cannot be applied to a spherical domain as it would result in problems. For instance, as shown in Fig. 2.2, the same point is present at two locations on the mesh: once on the green line and once on the red line, leading to problems in computing the boundary fluxes and assembling the matrices. Consequently, projecting the domain is no longer a satisfactory solution and the equations have to be solved on a spherical domain. In order to perfectly model a spherical domain, one should use spherical triangles as elements. Nevertheless, it significantly increases the numerical complexity (for instance, the mapping is no longer linear) and SLIM is not able to use such elements. Hence, flat triangle elements are used as the error converges at the same rate as the discretisation error (Comblen et al., 2009). Various methods allowing solving equations on a sphere can be found in the literature. As part of this thesis, the approach developed by Comblen et al. (2009) is selected although it was no longer available in SLIM. The original idea is quite simple: DGFEM are based on flux exchanges at elements

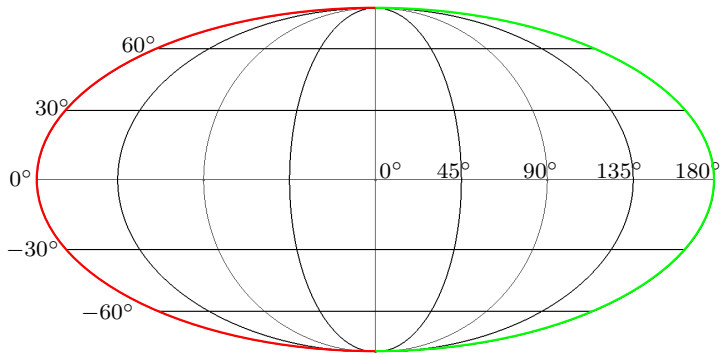

Fig. 2.2: Geographic projection of a spherical Titan (here, the Mollweide projection). Besides deforming the domain (a geographic projection can be accurate in angle and shape or in proportions of area), another drawback is that some physical points can appear twice, once on the green line and once on the red line.

interface. In order to solve an equation on a spherical surface, the outgoing flux at the boundary of an element has to be redirected in the tangent plane of the neighbouring element. The method, thus, consists in taking advantage of the geometrical flexibility inherent to the finite element method by means of a dialogue between a local and a edge-associated coordinate system (Comblen et al., 2009).

Comblen et al. (2009) developed his approach for 2D flat triangles, which is well suited for a 2D model such as SLIM2D. On the other hand, a 3D model requires a 3D discretisation of the domain. The meshes used by SLIM3D consist of triangular prisms. For flat domains such as the terrestrial ones on which SLIM3D is usually applied, the mesh is built by extruding the 2D flat triangles along the vertical coordinates. In order to create a spherical 3D mesh, the flat triangles are extruded along the vertical coordinates and the horizontal surfaces are then projected on spheres of decreasing radius. For each layer, the outgoing horizontal flux at a boundary of an element is redirected in the tangent plane of the neighbouring element of the same layer.

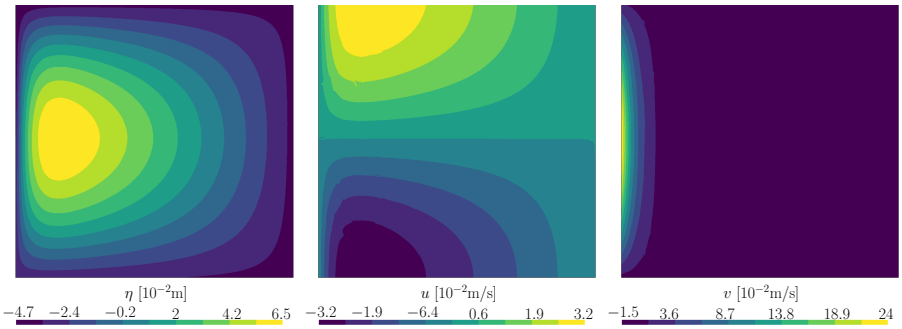

Fig. 2.3: Equilibrium state elevation and velocity fields planar components for the Stommel Gyre testcase.

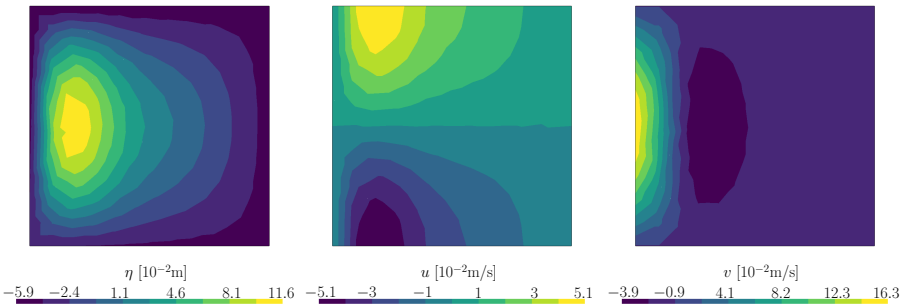

Fig. 2.4: Equilibrium state elevation and velocity fields planar components for the Munk Gyre testcase.

On a flat domain, the tangent planes of neighbouring elements are the same and the method should not modify the results. Therefore, the implementation is first tested on two planar testcases: the Stommel gyre and the Munk gyre testcases (see Stommel, 1948; Munk, 1950; Comblen et al., 2010b). In both cases, the flow is forced by a periodic wind stress $\boldsymbol{\tau} = 0.1 \sin(\pi \frac{y}{L}) \mathbf{e}_x$ inducing a clockwise circulation balanced by a linear dissipation with $\gamma = 10^{-6}$ s^{-1} (Stommel gyre) or by viscous dissipation with a constant viscosity $\nu = 10^4$ m^2/s (Munk gyre). The Coriolis effect is taken into account using the β-plane approximation, $f = f_0 + \beta y$ with $f_0 = 10^{-4}$ s^{-1}

and $\beta = 2 \times 10^{-11}$ m^{-1}s^{-1} corresponding to a mid-latitude domain in the northern hemisphere. In both testcases, the flow reaches a stationary state (see Figs. 2.3, 2.4) corresponding to the expected results.

The ability of a model to solve shallow water equations on a sphere can be assessed by several testcases available in the literature such as those created by Williamson et al. (1992). As this method was previously tested by Comblen et al. (2009), two testcases derived from those proposed by Williamson et al. (1992) are used to validate our implementation of Comblen et al. (2009)'s method. They respectively test the implementation of the shallow water equations and the passive tracer equation. The first test consists of a steady state solution of the non linear shallow water equations: the geostrophic balance. The initial velocity field and elevation respectively correspond to the solid body rotation speed and to the geostrophic height (see Williamson et al., 1992, for further details). The coriolis parameter is $f = 2\Omega(-\cos\lambda\cos\theta\sin\alpha + \sin\theta\cos\alpha)$ where θ is the latitude and λ is the longitude. It is ran with $\alpha = 0, 0.05, \frac{\pi}{2} - 0.05$ and $\frac{\pi}{2}$. The test is passed if the velocity and elevation fields do not change with time. The integral of the L2 norm of the error is a quadratic function of the spatial resolution. For a mean spatial resolution of 3×10^5 m, the error after 20 iterations is $O(10^{-8})$ m for the elevation field and $O(10^{-10})$ m/s for the velocity field.

The second testcase consists in advecting a cosine bell of passive tracer around the sphere. The hydrodynamics is given by the geostrophic balance (i.e. it is time independent) while the tracer field is predicted by solving the tracer equation with zero diffusion. The error is given by the difference between the initial bell and the bell after a complete rotation around the sphere. The error decreases quadratically as the mesh resolution increases. For a maximum length edge of 80 km, the maximum absolute error is 0.026, which is less than 3% of the initial value. Therefore, the implementation of Comblen et al. (2009)'s method for the tracer equation is considered successful.

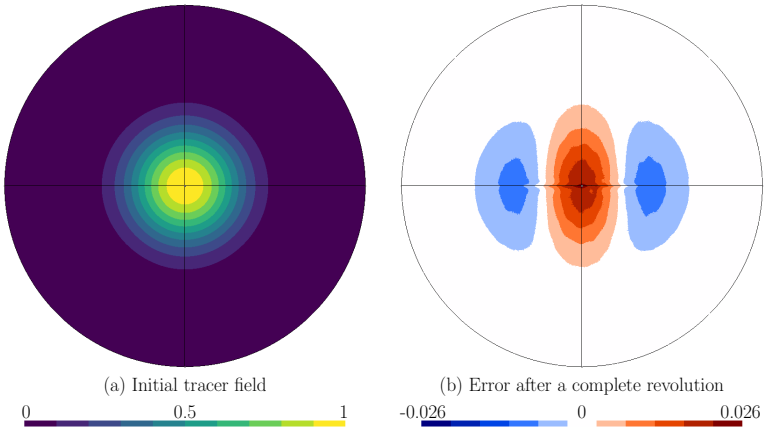

Fig. 2.5: (a) Tracer cosine bell at initial time and (b) difference between the initial condition and the tracer bell after a complete revolution.

These testcases are also conducted on 3D meshes in order to test the implementation of Comblen et al. (2009)'s method in SLIM3D. The results are similar and the implementation of the method is considered successful for both SLIM2D and SLIM3D.

2.5.2 Dynamics equations under a viscoelastic ice shell

The approach developed by Comblen et al. (2009) aims at solving the equations on a spherical domain. Nevertheless, the equations implemented in SLIM hold for an ocean with a free surface while Titan's global ocean is lying beneath an icy shell. Therefore, SLIM has to be modified to take into account the deformation of this ice shell. On the other hand, the deformation of the core of the moon is neglected (i.e. the bottom of the ocean is assumed to be rigid). The top shell influences the liquid motion in two major ways: an additional friction term takes place at the top of the ocean and the ice shell deformation results in a surface pressure term. Indeed, the

shell deformation can be predicted by means of membrane theory[2]. Following this theory, the main deformations of the shell are normal to its mid surface, which results in a normal pressure on the ocean. These effects affect both SLIM2D and SLIM3D equations although the modifications can be slightly different.

In order to compute the surface pressure term, we based our study on the simplified case of a spherical shell under internal pressure. In this case, the main stresses are circumferential and their is no shear stress (see Fig. 2.6). The circumferential stresses can be related to the internal pressure by computing the force equilibrium on one half of the sphere. For an elastic shell, the stress is a linear function of the strain while, for a viscous shell, it is a linear function of the strain rate. For a viscoelastic, both contributions are taken into account, the stress is hence a function of the strain and its time derivative. For a spherical shell, the circumferential strain are a function of the radial displacement. Using the stress-strain relation and the force equilibrium, the interface pressure can be written as a function of the shell's vertical uplifting and its time derivative. In accordance with the principle of action-reaction, the pressure acting on the bottom of the shell is the opposite of the pressure acting on the internal area of the shell.

The surface pressure acting on Titan's subsurface ocean is predicted by analogy with this basic case. The ocean's surface also deforms, resulting in a pressure which is a function of the difference between the ocean surface elevation and the shell vertical uplifting instead of depending on the sole shell vertical uplifting. The resulting surface pressure reads

$$p = a\rho g(\eta - \mathrm{w}_s) + b\rho g \frac{\partial(\eta - \mathrm{w}_s)}{\partial t} \tag{2.26}$$

where w_s is the vertical uplifting of the ice shell (positive upwards)

[2]The membrane theory is a particular case of the thin shell theory. It is appropriate for loads of large wavelength with respect to the shell thickness, which is the case for Titan. The adaptation of this theory for the study of the icy moons tidal deformation is available in Beuthe (2015a,b).

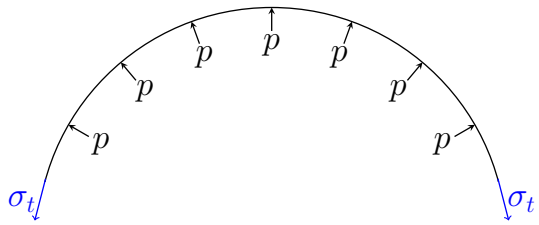

Fig. 2.6: Free body diagram of a spherical shell under an inner pressure p. According to the membrane theory, the shell can be represented by its mid-surface and the stresses are uniformly distributed along its thickness. The radial pressure p results in circumferential stresses σ_t.

(see Fig. 2.7) and a and b are phenomenological coefficients. In this case, the ocean pushes on the shell if the tidal bulge is larger than the vertical uplifting of the shell and vice versa. Regarding the computation of the top friction term, the tangential deformation of the ice shell is neglected as its amplitude is expected to be smaller than the vertical uplifting of the shell. Therefore, we do not model the tangential deformation of the ice shell but its effect is studied by varying the friction coefficient. Depending on the direction of the shell tangential deformation, the shear stress is larger (opposite direction with respect to the flow) or smaller (same direction as the flow). Both cases are studied by implementing a larger (resp. smaller) friction coefficient.

Various approaches are available to model the shell deformation (see Beuthe, 2008, 2015a,b; Fortes, 2012; Sohl et al., 1995, 2003, 2014, among others). Our development is based on the membrane approaches developed by Beuthe (2015a,b). He derived two approaches: the massless approach (see Beuthe, 2015a) and the massive approach (see Beuthe, 2015b). These approaches consist in extending the membrane theory of shells to viscoelastic shells with depth-dependent rheology. The membrane theory of shells is based on the idea of representing the 3D shell by a 2D mid-surface plan. It relies on several hypotheses:

- The shell is thin with respect to the horizontal length scale;

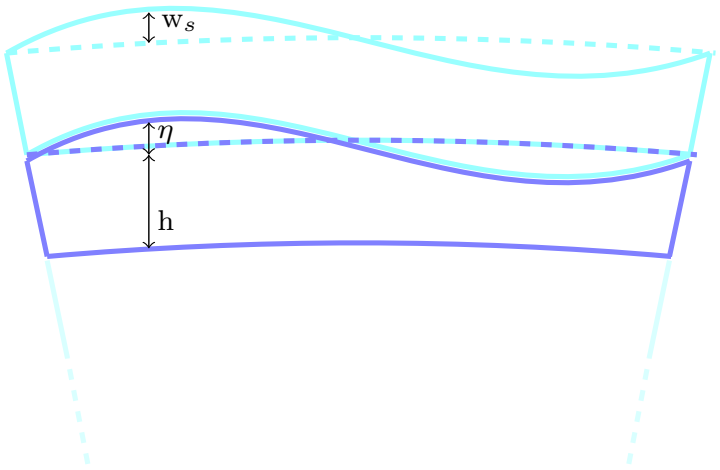

Fig. 2.7: Geometry of a part of the domain. w_s denotes the vertical uplifting of the ice shell (positive upawards), h is the unperturbed ocean depth, and η is the surface elevation (positive upwards). Light and dark blue represent the icy parts of the domain and the ocean, respectively. The dashed lines represent the unperturbed ocean/shell.

- The deformations are small;
- Straight lines normal to the mid-surface remain straight and normal to the mid-surface after deformation;

In the case of an icy moon's shell, additional simplifications can be made. First, the tidal deformation are of very long wavelength, half the circumference of the body, which mainly corresponds to extension and compression on a spherical shell. Bending and twisting are therefore disregarded, implying strains constant with respect to the depth. As the rheology varies with the depth, so do the stresses despite the constant strains. Second, a spherical symmetry is assumed in the shell properties (density and viscoelastic properties vary radially but not laterally). Beuthe (2015a,b) also imposed a free slip condition at the bottom of the shell, which means that the

shear stress vanishes at the interface. In the massless membrane approach, three additional approximations are made (which are not part of the massive membrane approach): the shell is assumed of uniform density and the density contrast between the ocean and shell is neglected (this is a modelling assumption), dynamical terms are neglected in the viscoelastic problem, and the thickness of the membrane is zero. In this thesis, we rely on the massless membrane approach derived by (Beuthe, 2015a) to predict the deformation of Titan's surface. Following this approach, the vertical uplifting of the ice shell can be related to the ocean elevation by the membrane spring constant Λ: $\eta = (1 + \Lambda)\mathrm{w}_s$. The massive membrane predicts a similar relation except for additional terms appearing: the compressibility correction (which vanishes if the crust is incompressible), the minor density correction (which vanishes if there is no density contrast between the shell and the ocean) and the dynamical correction term (which vanishes in the static limit). The membrane spring constant is generally dominant with respect to these terms (Beuthe, 2015b) and the massless membrane approach is a very good approximation for Titan (Beuthe, personal communication), hence we apply this approach.

The membrane spring constant varies with the ice shell rheology and the layers thickness, which are assumed to be latitude and longitude independent, resulting in a constant membrane spring constant. For a deformation of degree l, the membrane spring constant is given by $\Lambda = 2(l-1)(l+2)\frac{1+\overline{\nu}}{(l-1)(l+2)+1+\overline{\nu}}\frac{\overline{\mu}}{\rho g R}\frac{d}{R}$ where $\overline{\nu}$ is the effective Poisson's ratio, $\overline{\mu}$ is the effective shear modulus, and d is the ice shell thickness. The second degree deformation is, by far, the most significant as the forcing is mainly induced by Titan's obliquity and its orbital eccentricity, which correspond to degree 2. Other forcings such as those induced by other celestial bodies are much weaker and the nonsynchronous rotation forcing, if any, is at a much lower frequency than the diurnal forcing (as it should occur with a period similar to the viscous relaxation timescale of the ice shell (Wahr et al., 2009)) and would impact the ice shell on a timescale too large to be observed in this study. Therefore, we focus

on the deformation of degree two and neglect the others, resulting in $\Lambda = -\rho g 8 \frac{1+\overline{\nu}}{5+\overline{\nu}} \frac{\overline{\mu}}{\rho g R} \frac{d}{R}$. For an elastic rheology, $\overline{\nu} = \nu_E = 0.33$ and $\overline{\mu} = \mu_E = 3.5$ GPa (Beuthe, 2015a), resulting in a membrane spring constant $\Lambda = 0.055$. For a viscoelastic rheology, the effective Poisson's ratio and the effective shear modulus are complex. Their values can slightly vary with the configuration taken into account. In this thesis, their values correspond to the published results of Beuthe (2015a,b) which are obtained for a specific configuration: Titan is represented by a three-layer incompressible spherical body made of an infinitely rigid mantle, a subsurface ocean, and an ice shell made of two uniform layers. The shell's top layer is conductive and elastic whereas its bottom layer is convective and viscoelastic. In this case, Λ is a complex function of the relative thickness of the top layer and the ratio between the critical viscosity and the viscosity of the bottom layer, δ. Substituting w_s by $\frac{\eta}{1+\Lambda}$ in Eq. 2.26 leads to a complex formulation of the surface pressure. The hydrodynamic equations being solved in the temporal domain, the imaginary part of the surface pressure is disregarded. The (real) surface pressure term therefore reads $p = \rho g A \eta + \rho g B \frac{\partial \eta}{\partial t}$ where $A = \frac{\Lambda_r^2+\Lambda_r+\Lambda_i^2}{(1+\Lambda_r)^2+\Lambda_i^2}$ and $B = \frac{\Lambda_i}{(1+\Lambda_r)^2+\Lambda_i^2}$ are real parameters quantifying the elastic and viscous deformations of the ice shell which are function of both the real and imaginary part of the membrane spring constant, Λ (see Fig 2.8). The subscripts r and i respectively denote the real and imaginary part of the membrane spring constant.

Three mechanical behaviours of the bottom layer can be highlighted: $\delta \leq 0.1$ corresponds to an elastic-like bottom layer, $0.1 < \delta < 10$ corresponds to a critical bottom layer, and $\delta \geq 10$ corresponds to a fluid-like bottom layer. For elastic-like and fluid-like bottom layers, B is almost nil and A is constant with respect to δ (see Fig 2.8). For a critical behaviour, A decreases with δ while the closer the viscosity of the bottom layer to the critical viscosity, the larger B. Such different behaviours could have a significant impact on the tidal motion within the ocean. Therefore three configurations are studied: an elastic-like bottom layer ($\delta = 0.1$), a

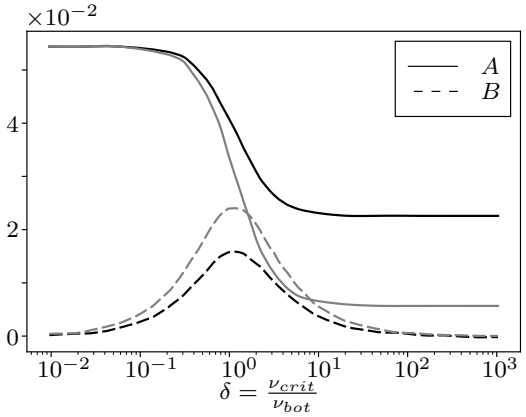

Fig. 2.8: A (full lines) and B (dashed lines) factors for a rheology based on Fig. 3 of Beuthe (2015b). The gray and black colors denotes a top layer representing 10% and 40% of the ice shell thickness, respectively.

viscoelastic like bottom layer ($\delta = 1$) and a fluid-like ($\delta = 10$) bottom layer. For each of these configurations, simulations are run for an elastic top layer making 10% and 40% of the shell thickness.

Beuthe (2015a,b) solved the equations in the frequency domain while our approach takes place in the temporal domain. Therefore, although the formulas derived by Beuthe (2015a,b) are resorted to to compute the surface pressure term, the approach is different. The modifications of the shallow water equations are presented in Section 2.5.2.1 and the corrections of the 3D hydrostatic equations under the Boussinesq approximation are introduced in Section 2.5.2.2.

2.5.2.1 Shallow water equations

The additional friction term can be modelled by doubling the friction coefficient as the friction at the top and bottom of the ocean are assumed to be similar. Introducing the surface pressure derived from the shell vertical uplifting predicted by the massless membrane approach in the shallow water equations results in

$$\left\{\begin{array}{lcl} \dfrac{\partial \overline{\boldsymbol{u}}}{\partial t} & + & \overline{\boldsymbol{u}} \cdot \nabla \overline{\boldsymbol{u}} \; + f \boldsymbol{e}_z \wedge \overline{\boldsymbol{u}} + g \nabla \left((1+A)\,\eta + B \dfrac{\partial \eta}{\partial t} \right) \\ & = & \dfrac{1}{H} \nabla \cdot (H \nu \nabla \overline{\boldsymbol{u}}) + \dfrac{\boldsymbol{\tau}^s - \boldsymbol{\tau}^b}{\rho H} + \gamma_2 \nabla_h \phi \\ \dfrac{\partial \eta}{\partial t} & + & \nabla \cdot (H \overline{\boldsymbol{u}}) = 0 \end{array}\right. \tag{2.27}$$

These additional terms modify the plane wave solutions admitted by the linearised version of the equations. We briefly study one of them, the Poincaré waves, in a 2D domain with no variation of the solution along the y axis and a constant bathymetry. In this case, a plane wave solution is of the form $\eta = \Re(Ee^{i(\omega t - kx)})$, $u = \Re(Ue^{i(\omega t - kx)})$, and $v = \Re(Ve^{i(\omega t - kx)})$ where E, U, and V are complex constants, ω is the angular frequency, and k is the wavenumber. In order to avoid a complex angular frequency, the solution is multiplied by a damping factor $e^{-\gamma t}$ as the additional pressure term damps the oscillations. Developing the equations following the same approach as that used to derive the dispersion relation of the Poincaré waves yields

$$\left\{\begin{array}{lcl} \gamma & = & 0.5 k^2 g h B \\ \omega^2 & = & f^2 + k^2 g h (1 + A - 0.25 B^2 k^2 g h) \end{array}\right. \tag{2.28}$$

The phase speed is $c_p = \frac{\omega}{k} = \sqrt{gh}\sqrt{(\frac{f^2}{k^2 gh} + 1 + A - 0.25 B^2 k^2 hg)}$, which is similar to the phase speed of Poincaré waves in a free surface ocean (it is identical if $A = B = 0$). For a 100 km deep ocean, the damping coefficient for long Poincaré waves is $\gamma \sim 10^{-8}$ s^{-1} and their phase speed is

$$c_p = 368\sqrt{(3.86 \times 10^{-3} + 1 + A - 5.4 \times 10^{-9} B^2)} \sim 370 \text{ m/s}$$

The terms $A - 5.4 \times 10^{-9} B^2$ represents the impact of the ice shell deformation on the phase speed. The elastic pressure term accelerates the plane waves while the viscous pressure term slows them

down. The effect of the elastic pressure term is identical for all planar waves as A is not multiplied by any factor. The viscous pressure term, on the other hand, affects more significantly small wavelength waves as B is multiplied by k^2 and the deeper the ocean, the larger the impact of this term. The factors A and B being $\mathcal{O}(10^{-2})$ (see Fig. 2.8), their impact on the phase speed is small. For each of the ocean configurations studied, the phase speed of long Poincaré waves within the subsurface ocean is larger than in a free surface ocean. Phase speed smaller than within a free surface ocean can be reached for short wavelengths or beneath a purely viscous ice shell.

2.5.2.2 Baroclinic equations

The surface pressure resulting from the ice shell deformation is the same as in the depth-averaged model. Unlike in the depth-averaged equations, the top friction cannot be modelled by doubling the friction coefficient. Instead, a top boundary condition consistent with friction is added, resulting in a boundary layer at the top of the ocean. The same friction parametrisation is used at the top and bottom of the ocean. The 3D hydrostatic equations under the Boussinesq equations then read:

$$\begin{cases} \dfrac{\partial \boldsymbol{u}}{\partial t} & + & \nabla_h \cdot (\boldsymbol{u}\boldsymbol{u} + \dfrac{\partial w\boldsymbol{u}}{\partial z}) = -f\boldsymbol{e}_z \wedge \boldsymbol{u} - \dfrac{g}{\rho_.}\nabla_h \displaystyle\int_h^\eta \rho' d\zeta \\ & - & g\nabla_h \left((1+A)\,\eta + B\dfrac{\partial \eta}{\partial t} \right) \\ & + & \nabla_h \cdot (\nu_h \nabla_h \boldsymbol{u}) + \dfrac{\partial}{\partial z}\left(\nu \dfrac{\partial \boldsymbol{u}}{\partial z} \right) + \gamma_2 \nabla_h \phi \\ \nabla_h \cdot \boldsymbol{u} & + & \dfrac{\partial w}{\partial z} = 0 \\ \dfrac{\partial T}{\partial t} & + & \nabla_h \cdot (\boldsymbol{u}T) + \dfrac{\partial (wT)}{\partial z} = \nabla_h \cdot (\kappa_h \nabla_h T) + \dfrac{\partial}{\partial z}\left(\kappa \dfrac{\partial T}{\partial z} \right) \end{cases} \tag{2.29}$$

2.6 SLIM user interface

As SLIM roots are well established (the unstructured grids are in use since the beginning of the project (Legrand et al., 2000; Hanert et al., 2003), the spatial discretisation has been relying on the discontinuous Galerkin method for more than ten years (Lambrechts et al., 2008a) ...), the next step is to facilitate the use of SLIM and to gather a community of users. In this perspective, a user friendly API has been developed. It aims at facilitating the set-up of a numerical simulation from the delimitation of the domain to the post-processing analysis of the results. To this end, all functionalities of SLIM base code are wrapped into Python modules. A defensive programming is implemented to avoid incompatible choices and consistent parameters default value are proposed although the user can set by himself the parameters value. Using this API allows running complex simulation(s) by means of compact scripts easily understandable, modified and shared. The user script is treated by the interface layer which calls the SLIM base code. The interface layer, which is the purpose of this section, is depicted in Section 3.4 of Vallaeys (2018). Therefore, it is only briefly introduced in this section. The interface is made up of four main modules: mesh generation, pre-processing, equations, and post-processing. The mesh generation module is optimised for terrestrial domain. Using the approach of Remacle and Lambrechts (2018), it generates a mesh on a sphere, based on shape-files, a standard file format for geographic information system softwares. This approach is not further developed in this section as it does not apply to Titan and it is developed in Vallaeys (2018).

Dealing with the data required by models is often the stumbling block for the user: data are available under different formats and the model usually requires a specific data format. The idea behind the pre-processing module is to rewrite the data into a SLIM-friendly format: the standard GMSH *".msh"* format or an adapted NetCDF format. The module requires the mesh and the associated geographic projection. From these files, the module creates

SLIM-formatted files by interpolating the data at the nodes of the mesh. Obviously, it is impossible to deal with all types of data. Therefore, the user may have to first interpolate the data and store them in module-friendly format such as a structured grid. The third module provides an easy access to SLIM2D and SLIM3D. For each of these models, the user has to provide the numerical domain (mesh, bathymetry ...) and the input data (gravity, density, wind, open boundary conditions, forcings ...). Depending on the equations, options such as the temporal scheme, the bottom friction model, a wetting-drying scheme ... are available. The user can solve the tracer equations (dissolved constituent, age concentration ...) along with the hydrodynamics or in offline mode, using the hydrodynamic data predicted by SLIM (or another model providing it is written in the SLIM format). Several tools are available in the post-processing module, allowing the user to analyse the results. The user can export time-series, perform a Fourier analysis, and use the Lagrangian particle tracker module.

2.7 Conclusion

SLIM is a well established model which has been used in various terrestrial domains. The depth-averaged and the full 3D version are both freely available and can easily be used thanks to the user friendly API. The spatial discretisation, temporal scheme, and the governing equations solved by the models are developed in Section 2.2.

Applying SLIM to an extra terrestrial domain required various modifications of the model. The first step is to ensure the equations are well suited. Regarding the surface lakes and seas, all assumptions hold. Concerning the subsurface ocean, the key question lies in the depth of the ocean. Indeed, the latter must be small with respect to the horizontal length scale. Using the radius as horizontal length scale results in an aspect ratio smaller than 0.16. Such a high value, although questionable, is not representative as it is associ-

ated to the upper bound of ocean depth found in the literature. For the reference depth of 100 km, the aspect ratio is about 0.04 which is deemed small enough. Judging the equations well suited for the various liquid domains encountered on Titan, the next step is to adapt these equations to the specific extra-terrestrial conditions. Only minor modifications are required to study the liquid motion of the surface lakes and seas. They are introduced in Section 2.4.1. Studying the global subsurface ocean required more numerous and complex modifications. An approach to solve the equations on a sphere has to be resorted to. It is depicted in Section 2.5.1. This approach was previously developed by the SLIM development team but it was no longer available. The ocean lying beneath an icy shell, its surface is not free as the shell deformation acts as an additional forcing and results in an extra friction source. This forcing is modelled by a surface pressure term added in the momentum equation (see Section 2.5.2).

These modifications can be used through the user friendly API which has been developed in parallel. This API aims at facilitating the usage of SLIM by means of intuitive Python modules. This allows users of various background to conduct complex numerical simulation(s) from the creation of the numeric domain to the post-processing of results. It also facilitates the development of the model as the developers can add and improve functionalities without making the simulation scripts obsolete.

The developments introduced in this chapter are used to conduct numerical simulations of the tides in the subsurface ocean and surface lakes and seas whose results are presented in the forthcoming chapters.

CHAPTER 3

Modelling of Ontario Lacus tides

This chapter is based on the following article[1]:

D. Vincent, Ö. Karatekin, V. Vallaeys, A.G. Hayes, M. Mastrogiuseppe, C. Notarnicola, V. Dehant, É. Deleersnijder, 2016, Numerical study of tides in Ontario Lacus, a hydrocarbon lake on the surface of the Saturnian moon Titan, *Ocean Dynamics*, 66: 461–482.doi: 10.1007/s10236-016-0926-2

A study of the impact of Titan surface deformation on the tidal motion is also included although the results were not published.

Abstract

In the context of the emergence of extra-terrestrial oceanography, we adapt an existing oceanographic model, SLIM

[1]Slight modifications were added in the chapter.

(www.climate.be/slim), to the conditions of Titan, a moon of Saturn. The tidal response of the largest southern lake at Titan's surface, namely Ontario Lacus, is simulated. SLIM solves the depth-averaged shallow water equations on an unstructured mesh using the discontinuous Galerkin finite element method, which allows high spatial resolution wherever needed. The impact of the wind forcing, the bathymetry, the deformation of Titan's surface and the bottom friction is also discussed.

The main tidal component, whose period is one Titan day, has an amphidromic point located near the centre of the lake and therefore consists in a wave rotating in the lake. The maximum tidal range is about 0.057 m and is reached in the southern part of the lake. The speed is larger nearshore where it can reach 0.036 m/s close to the shores depending on the geometry and the bathymetry. Except for these specific nearshore regions, the current speed is less than 0.005 m/s. As the sea surface elevation is small, tides can be ruled out as an explanation for the shoreline variations.

3.1 Introduction

In this chapter, we focus on one of Titan's surface lakes, Ontario Lacus. It is the largest lake in the southern hemisphere (with its centre at 72°S, 175°E.), covering approximately an area of 200 km $\times$ 70 km (Wall et al., 2010). Since its discovery, Ontario Lacus has been the subject of several publications focusing on morphology (Wall et al., 2010; Cornet et al., 2012), composition (Brown et al., 2008), bathymetry (Hayes et al., 2010; Ventura et al., 2012; Hayes, 2016; Mastrogiuseppe et al., 2018a), as well as tides (Tokano, 2010; Vincent et al., 2016) and normal modes (Vincent et al., 2019).

Differences between ISS images taken in 2005 (Rev009, L_s = 306° [2]) and in 2009 (T51, L_s = 355°) suggested possible shoreline variations (Turtle et al., 2011). Synthetic aperture radar (SAR)

[2]The planetocentric solar longitude, L_s, is the solar longitude of Saturn.

images from 2009 (T57, $L_s = 358°$ and T58, $L_s = 359°$) (see Wall et al., 2010; Hayes et al., 2011) gave additional support to the hypothesis of variations in lake volume and shorelines. Various phenomena were proposed to explain these variations. Tides were ruled out by Tokano (2010) as the tidal range is too small (see Section 3.4) and the images were not taken at low and high tides. Nowadays, the most common explanation involves evaporation/infiltration of surface liquid (Lunine et al., 2009; Turtle et al., 2011) as the observations took place during the southern summer, when evaporation was predicted to be the largest. Due to their low resolution, analysis of ISS images was inconclusive and the existence of seasonal shoreline variations remained questionable as the data are, within measurement error, consistent with no change at all (Cornet et al., 2012). Subsequent SAR images (T65 in 2010, $L_s = 5.5°$) suggested no significant shoreline changes in comparison with 2009 images. On the other hand, lacustrine features of the southern hemisphere seem to disappear between subsequent SAR observations (from 2007 to 2008/2009), corresponding to liquid evaporation or infiltration into the ground (Hayes et al., 2011; Hayes, 2016). Such observations tilt the balance in favour of shoreline variations taking place in Titan southern hemisphere (at least from 2007 to 2009). Ontario Lacus would likely experience a similar phenomenon although it could be less significant than the variations between 2005 ISS and 2009 SAR observations suggest.

Besides the shoreline, the parameter which has the most significant influence on the motion in the lake is its bathymetry map. Unfortunately, it is not possible to conduct measurements campaign on extra-terrestrial liquid bodies as it is done on Earth. Consequently, one has to rely on remote sensing to derive bathymetry maps. The first pieces of information about Ontario Lacus bathymetry came from T49, T57, and T58 observations (2008 and 2009) which were used by Hayes et al. (2010) to derive the bathymetry near the shoreline. Using SAR data from T65, Ventura et al. (2012) estimated the bathymetry over the whole lake. Their results indicate a maximum depth of about 30 m for a data map resolution of 256 pix/deg (i.e.,

about 0.17 km/pix). The most recent work from the Cassini radar team suggests that the lake could be even deeper than predicted by Ventura et al. (2012) (see Hayes, 2016; Mastrogiuseppe et al., 2018a)[3]. In this study, we consider all of above-mentioned bathymetries and quantify their influence on the tidal response. Besides the bathymetry, there are several other parameters that are not well known such as the exact lake composition, the roughness and the tidal deformation of Ontario Lacus bottom. We also quantify their influence on the tidal response.

Tokano (2010) was the first to conduct simulations of the tidal motion in Ontario Lacus. He used a 3D hydrostatic, baroclinic ocean circulation model based on structured grids. The spatial resolution of the grid was 10 km and, due to the lack of information at that time, he implemented a constant depth of 20 m. Due to the nature of the grid and the coarse resolution, the coastline was not well drawn. The only forcing taken into account was the astronomical forcing due to Saturn and the impact of Titan surface deformation was ignored. Taking advantage of recent works, we also conduct simulations of the tidal motion in Ontario Lacus using bathymetry maps derived from Cassini radar measurements. Our work stands out as the deformation of the lake bottom is taken into account and a sensitivity analysis with respect to the latter, the bottom friction, and bathymetry is conducted.

This chapter is organised as follows. Section 3.2 deals with Ontario Lacus environment and characteristics: atmospheric conditions, lake composition, and bathymetries are described. Section 3.3 presents the numerical domain. In Section 3.4, a reference case is studied and used as a basis for sensitivity analyses with respect to the bottom friction, bathymetry, and wind. Our results are discussed and compared with previous ones in Section 3.5, the implications for future missions are discussed in Section 3.6, and conclusions are drawn in Section 3.7.

[3]Although the bathymetry is derived following the method described in Mastrogiuseppe et al. (2018a), it was first published in Hayes (2016).

3.2 Ontario Lacus environment and characteristics

Ontario Lacus was flown over at least twice by each Cassini instrument (complete or partial flyby): ISS in 2004, 2005 & 2009, VIMS in 2007 & 2009, and radar in 2009 & 2010. It has the shape of a right footprint (see Fig. 3.1) and is named after Lake Ontario (one of the Great Lakes of North America). It is connected to a hydrological network (for example, in area N in Fig. 3.1) (Wall et al., 2010; Cornet et al., 2012) which can provide liquid hydrocarbons during and after precipitations. Several, quite different, morphologies were observed along the shoreline of Ontario Lacus: deeply incised bays, mountainous region, beaches ... (see Wall et al., 2010; Cornet et al., 2012, for further details).

3.2.1 Liquid composition

In the absence of *in Situ* measurements, the liquid composition can either be inferred from specific characteristics or by means of a chemical model. Based on the dielectric constant and the loss tangent of the liquid, Le Gall et al. (2016) predicted that Ligeia Mare is methane-rich. However, it does not imply that Ontario Lacus is methane-rich. Indeed, according to Glein and Shock (2013), higher temperatures cause liquid to lose methane and nitrogen and to gain ethane. CIRS measurements suggest that, at least during the summer, the lakes at 70°S (like Ontario Lacus) are about 1 K warmer than those at 70°N (Ligeia Mare is about 77°N) (Jennings et al., 2009). Using the value of loss tangent derived by Mastrogiuseppe et al. (2016), Hayes (2016) predicted a composition of 47% CH_4, 40% C_2H_6 and 13% N_2, which is much less methane rich than Ligeia Mare. The liquid composition can also be predicted by models (see Section 1.1.2.2). In this chapter, the composition predicted by Cordier et al. (2009) is adopted as a baseline: for a temperature

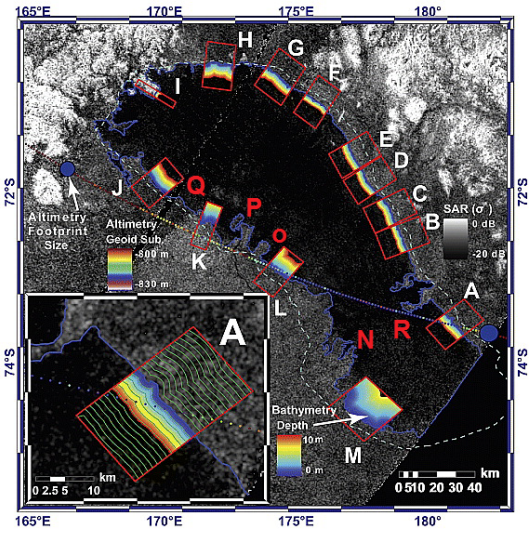

Fig. 3.1: Map of Ontario Lacus. Letters from A to M show the study areas of Hayes et al. (2010) who derived a nearshore bathymetry in these regions. The red letters, from N to R, are used in this chapter to refer to particular areas (adapted from www.titanexploration.com; original image credit: Cassini Radar Science team, NASA/JPL/Caltech).

of 90 K, Cordier et al. (2009)'s composition[4] results in a density of 662 kg/m^3 and a molecular viscosity of 1736×10^{-6} Pa.s, according to Lorenz et al. (2010). This molecular viscosity and density are larger than those predicted by Tan et al. (2013). According to the latter, the density is 547 kg/m^3 and the molecular viscosity is 5 times smaller. The lake carries some solid particles like acetylene and high molecular weight organics produced by atmospheric photochemistry (see, e.g., Lorenz et al., 2010, 2011; Lorenz, 2013) (Tan et al. (2013) showed that tholins and acetylene could be present in Titan's lakes). These particles modify the lake properties. Thus

[4]This composition is shown in Table 3 of Cordier et al. (2009). The main constituents and their lake mole fraction are C_2H_6 (7.64×10^{-1}), CH_4 (9.69×10^{-2}), C_3H_8 (7.42×10^{-2}), C_4H_8 (1.39×10^{-2}), N_2 (4.9×10^{-3}), Ar (5.01×10^{-6}), CO (4.21×10^{-7}) and H_2 (3.99×10^{-11}).

density and molecular viscosity cannot be accurately derived from the lake composition. Therefore, the impact of the lake composition is shortly discussed in terms of molecular viscosity and density within the range given by the models mentioned in Section 1.1.2.2 (i.e., a density ranging from 547 kg/m^3 to 662 kg/m^3 and a molecular viscosity ranging from 200×10^{-6} Pa.s to 2000×10^{-6} Pa.s).

3.2.2 Atmospheric conditions

According to Jennings et al. (2009), during the northern winter, the temperature at Ontario Lacus latitude (72°S) is more than 1 K lower than at the equator (93.56 K) while, at 72°N, it is more than 2 K lower than at the equator. Tan et al. (2015) established a formula describing the surface temperature as a function of latitude and time from January 2005 to December 2013 from Jennings et al. (2011) and Cottini et al. (2012) temperature profiles. The surface temperature variations between the northern and the southern end of Ontario Lacus (respectively 70°S and 74°S) are minimum (about 0.14 K) in January 2005 and increase almost linearly to reach about 0.26 K in December 2013. The temperature in the middle of the lake (at 72°S) is about 92.7 K in January 2005 and decreases almost linearly to reach about 90.3 K in December 2013. These absolute values have to be used with caution: the results do not take into account the local influence of the lake on the temperature (no variation as a function of the longitude was taken into account). In the light of the large timescale and the small magnitude of the surface temperature variations, their influence on the liquid density is not taken into account in the present study. The precipitation, evaporation, and atmospheric pressure variations are also disregarded. Indeed, the latter are small at the surface (see Section 1.1.1) and taking into account evaporation and precipitation would require coupling SLIM with a mesoscale atmospheric model and a longer study period, which is beyond the scope of this chapter. The uncertainties about the lake composition (which could influence the wind speed and orientation) make difficult to accurately predict the wind

conditions in the vicinity of Ontario Lacus. Modelling the impact of the wind on the liquid motion would, hence, also require coupling SLIM with a mesoscale atmospheric model. Therefore, we choose to discuss the response of Ontario Lacus to four hypothetical strong winds whose magnitude is consistent with GCMs predictions.

3.2.3 Bathymetry

An important ingredient of the model of Ontario Lacus is the bathymetry. Presently, bathymetries are available for a few lakes/seas: Ontario Lacus (see Ventura et al., 2012; Hayes, 2016; Mastrogiuseppe et al., 2018a), Ligeia Mare (see Mastrogiuseppe et al., 2014), Punga Mare (see Mastrogiuseppe et al., 2018b), and Kraken Mare (see Lorenz et al., 2014). This last one is computed from an empirical rule observed in terrestrial lakes' basin and adapted to Titan's seas from Ligeia Mare measured bathymetry.

Ventura et al. (2012) derived Ontario Lacus' bathymetry from the SAR data of the T65 flyby (January 12, 2010) using two approaches for backscattering description: a simplified semi-empirical model and a physically based one. Both methods rely on composition and seabed scattering properties and they return different results according to parameters such as the wind speed for the latter and the surface scattering for the former. The methodology used to derive this bathymetry is a combination of electromagnetic modelling and Bayesian approach to perform the inversion and obtain the lake optical thickness from SAR backscattering values. The conversion to physical depth is then obtained by using the loss tangent value as calculated in Hayes et al. (2010). In this work, we use the bathymetry returned by the second method with a wind speed of 0.7 m/s which results in a maximum[5] and a mean depths of respectively 28 m and 9.67 m (see Fig. 3.2(a)). This is the result which shows less extreme values and which best meets

[5]In this chapter, the words "maximum depth" refer to the maximum depth of the implemented bathymetry and not the maximum depth of the lake, which is a function of the spatial resolution of the data.

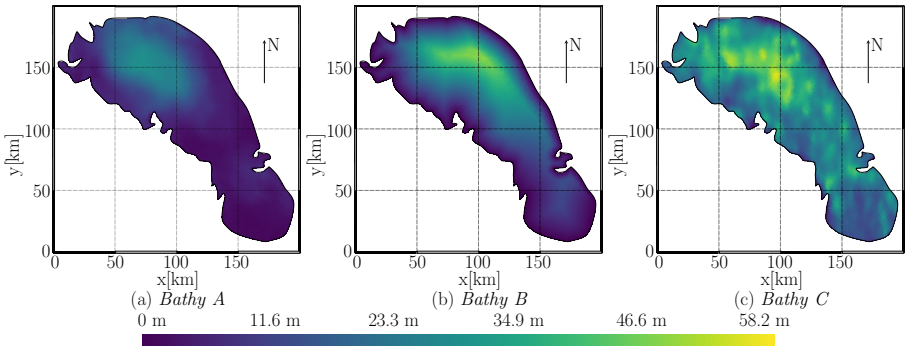

Fig. 3.2: Bathymetries of Ontario Lacus (in meters). Panel (a) is the bathymetry computed by Ventura et al. (2012) from SAR data. The bathymetry is smoothed to be coherent with the bottom of dry lakes. *bathy B* is shown in Panel (b) and *bathy C* is shown in Panel (c). Except at the shore, *bathy C* is deeper and presents more pits than *bathy A*. *bathy B* is also deeper than *bathy A* and is more accurate nearshore than *bathy C*.

the nearshore results obtained by Hayes et al. (2010). We obtain the implemented bathymetry shown in Fig. 3.2(a) by homogenising the physical depth in order to be coherent with the observed smoothness of bottom of dry lakes. It is referred to as *bathy A*.

The second bathymetry, namely *bathy B*, is obtained by extrapolating the mean bathymetry slopes presented in Table 1 of Hayes et al. (2010) (see also Fig. 3.1). Hayes et al. (2010) estimated the depth of the lake coastal areas from the local topography slopes obtained by means of the radar altimetry profile. This partial bathymetry is then used to determine the nearshore (i.e., < 15 km) imaginary component of the liquid complex index of refraction from SAR data of Titan flybys T57, T58 and T65 and altimetry observations (T49, $L_s = 352°$) (Hayes et al., 2010). Once the complex refractive index is known, it is used to estimate the local bathymetry slopes assuming uniform refractive properties throughout the lake (Hayes et al., 2010). It is the most accurate bathymetry in the region close to the shore (< 15 km) but the offshore depths are

given by an extrapolation of the nearshore slopes, which is inaccurate far from the shore. Consequently, we use *bathy B* to discuss the influence of the nearshore bathymetry and not to predict the tidal response of Ontario Lacus. The maximum and mean depths obtained are respectively 49.8 m and 15.8 m. The bathymetry map is shaped as *bathy A* but the maximum depth is larger and is not located at the same place than with *bathy A*. Due to its derivation, this bathymetry is much smoother than the two others.

The third bathymetry is also derived from SAR data. The Cassini radar altimeter data from flyby T49 (December 21, 2008) were used to calibrate the SAR backscatter (for further information about this method, see Hayes et al., 2014). Nevertheless, the T49 pass was the first over a liquid body on Titan and the default attenuator settings were overwhelmed. Consequently, Mastrogiuseppe et al. (2016) designed a model to recover the depths and absorptivity estimations in some saturated areas. The depths across the lake are then extrapolated from the SAR data. The bathymetry obtained is shown in Hayes (2016) and the method is described in Mastrogiuseppe et al. (2018a). This method is different from that of Ventura et al. (2012): instead of a model, an extrapolation method is resorted to for the derivation of the bathymetry. The results are consistent with the direct depths measured by altimetry from T49 flyby (see Mastrogiuseppe et al., 2016) but it is less accurate nearshore than *bathy B*. The implemented bathymetry is obtained by smoothing these data. This bathymetry is referred to as *bathy C* (see Fig. 3.2(c)). The maximum and mean depths obtained are respectively 58.2 m and 27.3 m, which is the same order of magnitude as with *bathy B* but is twice deeper than those predicted by Ventura et al. (2012). The deepest pit is located in the same region as in *bathy A* and *bathy B* but there are other smaller pits distributed over the lake (the small yellow/green spots offshore) which are not observed in *bathy A* and *bathy B*. *bathy C* is deeper than *bathy A* everywhere in the lake except at the shore: the dark blue areas nearshore are shallower. The bathymetry gradient offshore is more significant than in *bathy A* and *bathy B*.

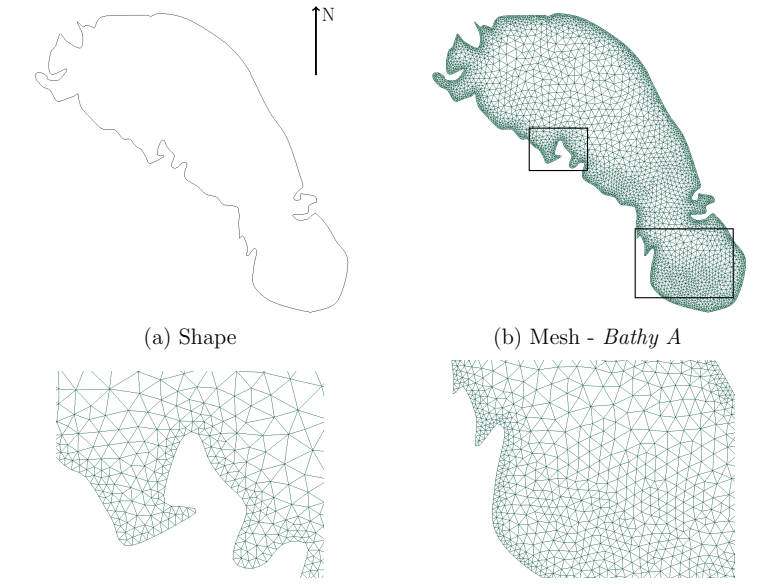

(a) Shape (b) Mesh - *Bathy A*

(c) Mesh resolution nearshore *Bathy A* (d) Mesh resolution offshore *Bathy A*

Fig. 3.3: Discretisation of Ontario Lacus using mesh-generation package GMSH: the coastline (Panel (a)) and the mesh used for *bathy A* (Panel (b)). Panel (c) shows the higher spatial resolution nearshore. Panel (d) shows the refinement in shallow regions in *bathy A*.

3.3 Computational domain

The tidal motion is predicted by means of SLIM, which is adapted to Titan conditions (see Chapter 2). An implicit Runge–Kutta scheme using a Newton–Raphson solver is resorted to, which allows time steps as large as 0.005 Titan Day (TD), $\sim$ 6890 s, to be used. This is far less time consuming than any multirate of explicit scheme as the temporal scale of the tides is large (1 TD). The shoreline contour, derived from radar images, is presented in Fig. 3.3(a) and the mesh used to implement *bathy A* is shown in Fig. 3.3(b,c,d).

The unstructured meshes are generated by means of GMSH (see Geuzaine and Remacle, 2009, `http://geuz.org/gmsh/`). It is one of the most widely used open source unstructured grid generator

and it can generate meshes on a sphere (for further details, see, e.g., Remacle and Lambrechts, 2018; Lambrechts et al., 2008a). We use fully unstructured meshes with a spatial resolution ranging from 1000 m to 5000 m. Three criteria of refinement are taken into account:

- The local element size is proportional to the celerity of the long surface gravity waves, $c = \sqrt{gh}$, as suggested by Henry and Walters (1993); Legrand et al. (2006);
- The mesh is refined nearshore to reach a high spatial resolution of 1000 m at the shores (see Fig. 3.3(c));
- The spatial resolution is increased where the bathymetry gradient is the largest and decreases with the distance to this point in order to avoid too many discontinuities between the elements.

These meshes allow us to represent as well as possible the coastline and the bathymetry and to be able to represent the small-scale phenomena occurring nearshore. For *bathy A* and *bathy B*, the local depth is smaller in the south and the spatial resolution is consequently increased in this region. There is no need for increasing the resolution elsewhere; these bathymetries being relatively smooth. The spatial resolution is locally increased offshore for *bathy C* (the spatial resolution offshore remaining larger than 3000 m). As a consequence, the number of triangles varies from one bathymetry to another: it ranges from about 6,400 to about 7,100.

3.4 Results

There are some significant differences between the Earth and Titan: the liquid properties and behaviour are different, the Coriolis term is smaller, the tidal forcing is larger than that due to the Sun and the Moon on Earth, and the mean gravitational acceleration is more than seven times smaller than on Earth. Some of these differences

can be shown by means of the Rossby number $Ro = \frac{U}{fL_h}$ and the temporal Rossby number $Ro_t = \frac{1}{fT}$ (see table 3.1) where f is the Coriolis parameter, $U \approx 10^{-2}$ m/s is the velocity scale predicted by our model, $L_h \approx 10^5$ m is the horizontal length scale, and $T =$ 1 TD is the time scale. Local Titan's rotation time scale f^{-1} is smaller than the advective time scale $\frac{L_h}{U}$, in a similar way to what is observed in Lake Ontario and in Earth's oceans. It is also smaller than the time scale, which is not the case in Earth's oceans or in Lake Ontario.

Table 3.1: Rossby (Ro) and temporal Rossby (Ro_t) numbers of Ontario lacus, Lake Ontario and Earth's oceans

	Ro	Ro_t
Ontario Lacus	3×10^{-2}	0.08
Lake Ontario[1]	5×10^{-2}	3.4
Earth oceans[2]	$\mathcal{O}(10^{-3})$	$\mathcal{O}(1)$

[1]: The observed speed is used to compute Ro (i.e., the wind and the barometric pressure changes are partially responsible for these currents).
[2]: For the M2 tide (principal lunar semi-diurnal tidal component) at mid-latitudes.

First, a reference simulation is achieved which allows us to conduct a sensitivity analysis for various bottom frictions, bathymetries, attenuation coefficients γ_2, and surface stresses. The attenuation factor is $\gamma_2 = 0.1$, Manning's roughness coefficient is $n = 0.03$ sm$^{-1/3}$ and *bathy C* is implemented because it is consistent with the direct depths measured by altimetry from T49 (Mastrogiuseppe et al., 2018a) and it is the most recent one.

3.4.1 Tidal response of Ontario Lacus

The astronomical forcing applied is shown in Fig. 3.4. It rotates clockwise with an exact period of 1 TD. At any time, the forcing is almost unidirectional over the lake. It has exactly the same magnitude in t^* and $t^* + 0.5$ TD but it is oriented in opposite directions. The maximum magnitude occurs 0.05 TD before perikron/apokron (points on Titan's orbit closest/farthest to Saturn), in the northern part of Ontario Lacus. The predicted local maximum/minimum at 0.25 TD after perikron/apokron are 16% and 13% weaker than their respective values at perikron/apokron. This forcing is slightly larger than that observed on Earth, at most 10^{-6} m/s^2 according to Wenzel (1997), while the minimum value, in the southern part of Ontario Lacus, is 2.46×10^{-6} m/s^2.

While studying the surface elevation of lakes and seas, it is common to study the tidal components. Indeed, the lake surface elevation at a point can be viewed as a sum of several components written as $\eta(t, x, y) = E(x, y)\cos(\omega t + \phi(x, y))$ where $E(x, y)$ is the amplitude[6], $\omega = 2\pi k/T$ is the angular period of the k^{th} component, and $\phi(x, y)$ is the tidal phase. On Titan, the first, second, third, and fourth tidal components respectively have a period of 1, 0.5, 0.33, and 0.25 TD. Fourier analysis shows that the diurnal component is responsible for more than 95% of the lake surface displacement, except at the amphidromic point of this tidal component where the liquid motion is due to the other tidal components, resulting in higher frequency oscillations. The amphidromic point is located in the centre of the lake, at (72.21°S; 175.27°E), see Fig. 3.5. The associated liquid motion consists of a clockwise rotating motion around the amphidromic point. The associated tidal range increases with the distance to this point. It is hence larger on the northern and southern shores than on the eastern and western ones (see Fig. 3.5 and Fig. 3.6), which matches with the evolution of the forcing magnitude and orientation during 1 TD. The maximum

[6]The amplitude of a tidal component is half of the tidal range which is the difference between high tide and low tide.

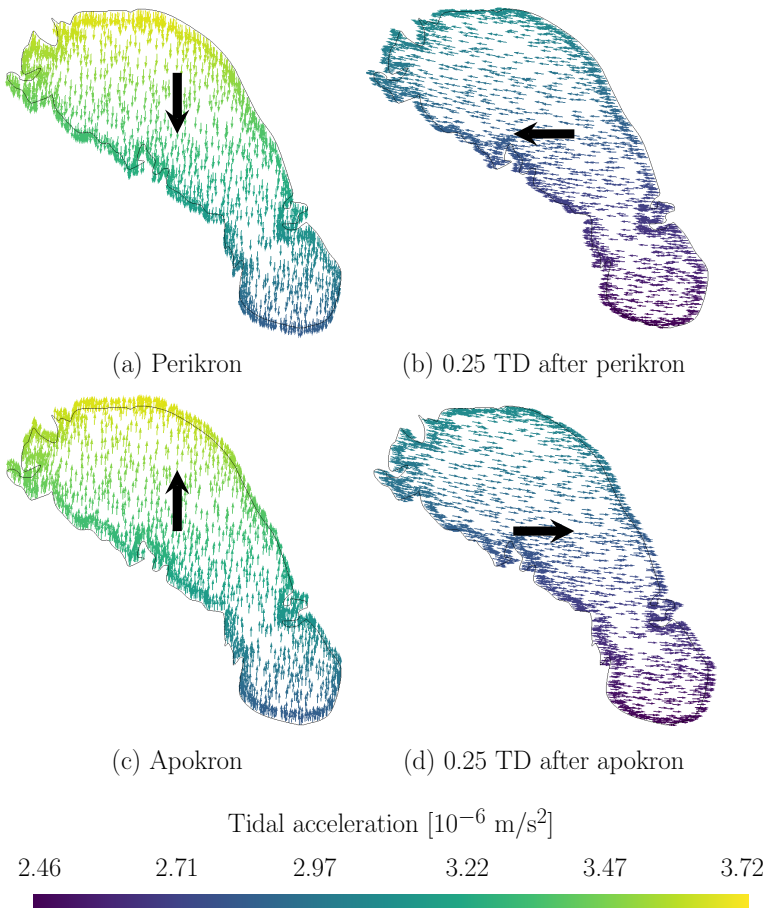

Fig. 3.4: Instantaneous maps of the acceleration caused by Saturn in Ontario Lacus at four different times (perikron, 0.25 TD after perikron, apokron and 0.25 TD after apokron)(the black arrows represent the mean direction). It rotates clockwise with an exact period of 1 TD and it is maximum in the northern part of the lake.

tidal range is 0.058 m and is located on the southern shore of the lake (see Fig. 3.5). The iso-lines have an ellipsoidal shape, which indicates interactions with the shoreline.

Fig. 3.6 shows the instantaneous surface elevation in Ontario

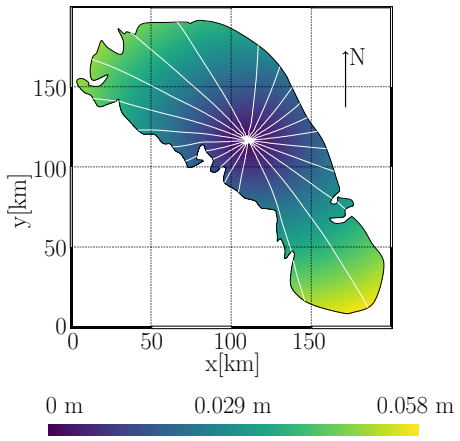

Fig. 3.5: Tidal range and phase (white lines, with a 15° spacing) of the 1^{st} tidal component in Ontario Lacus. The range is the difference between high tide and low tide. The cotidal lines (line of constant tidal phase) of the first component merge at the amphidromic point which is located at (72.21°S, 175.27°E). The cotidal lines show that the diurnal tide rotates clockwise. The tidal range increases with distance to the amphidromic point and is maximum (0.058 m) in the southern part of the lake.

Lacus at four orbital phases: perikron, 0.25 TD later, apokron, and 0.25 TD later. The clockwise rotation is noticeable. The maximum and minimum surface elevation are ±0.029 m and are respectively reached 0.08 TD before the instantaneous map shown in Fig. 3.6 (a) and Fig. 3.6 (c). Such a tidal response could generate dry area(s). With this bathymetry implemented, we do not detect dry areas but it does not mean that there is no tidal flats in Ontario Lacus. Indeed, such phenomenon could be generated out of the boundaries of this domain. For instance, the high tide floods some areas which are dry regarding to the geoid, but these areas are not included in the boundaries of Ontario Lacus as they are implemented. Given the weak shoreline slopes observed by Hayes et al. (2010) (it ranges from $0.5 - 2.7 \times 10^{-3}$), tidal flats are likely to exist but they should be relatively small (i.e. less than 100 m).

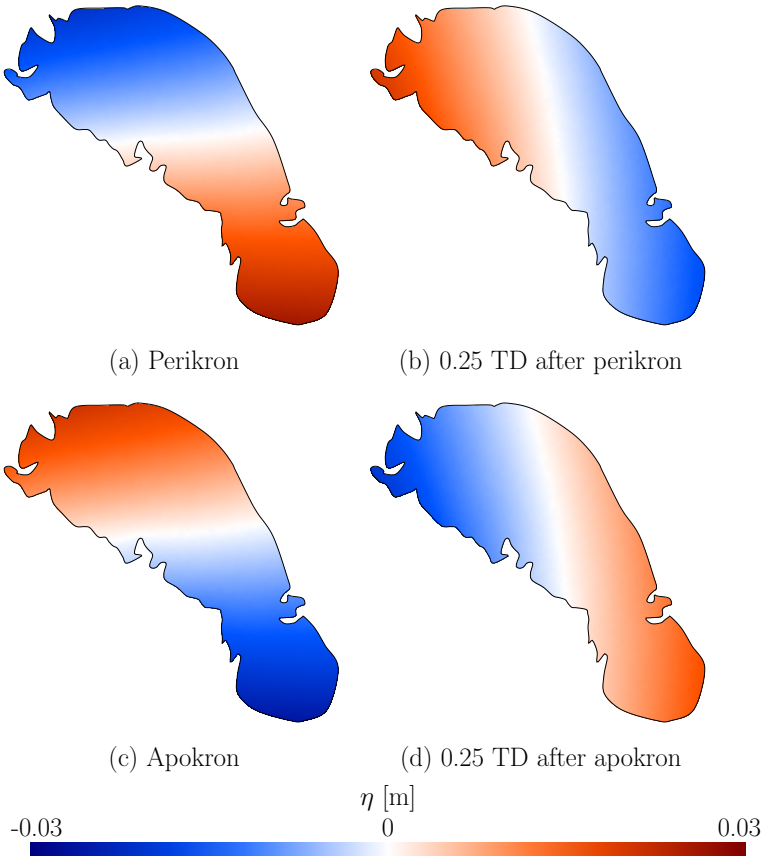

Fig. 3.6: Surface elevation (in meters) in Ontario Lacus at perikron (a), 0.25 TD after perikron (b), apokron (c) and 0.25 TD after apokron (d) with *bathy C* implemented. The tide is high in the southern part at perikron and rotates clockwise with an exact period of 1 Titan day. The maximum/minimum surface elevation respectively occurs 0.08 TD before perikron/apokron, in the south.

Fig. 3.7 demonstrates that the tidal currents are slower than 0.01 m/s except for some specific nearshore areas. The current magnitude is larger nearshore and, the larger the distance to the coast, the smaller the magnitude. A high speed is observed at

some specific nearshore convex regions like peninsula, cape, or the end of bays (this behaviour is particularly visible in Fig. 3.7 (a) and Fig. 3.7 (c)). Furthermore, the mean speed is higher when Titan is next to the apokron/perikron: the speed increases over the whole lake and the high-speed areas observed nearshore spread (see Figs. 3.7). Unlike the astronomical forcing, the tidal current is not always the same in t^* and $t^* + 0.5$ TD. For instance, for $t^* \in [0.325; 0.5]$ TD the maximum speed is larger in t^* than in $t^* + 0.5$ TD. The maximum speed, about 0.036 m/s, is predicted near area P (see Fig. 3.1), 0.43 TD after perikron. As the different figures in Fig. 3.7 show, the maximum current magnitude at a given time is located either in area P (Figs. 3.7 (a), (c)) or in area Q (Figs. 3.7 (b), (d)) but it does not have a constant magnitude over time. Such flow acceleration near headlands is also observed on Earth (e.g. in the Irish sea (see Figure 4 in Howarth, 2005), in the Baltic sea (see Figure 5.3 in Volkov, 2002), or in the North sea (see Figure 1.4 in the review from Otto et al., 1990)). The tidal current is globally directed from low to high tide. From 0.125 TD before perikron/apokron to 0.16 TD after perikron/apokron (i.e., during 0.57 TD), the flow forms a closed loop (see Figs. 3.7 (a) and (c)). Between these periods, the velocity field consists of helter-skelter currents. The closed loop spreads from the northern shore to the narrow part of the lake (areas N and R in Fig. 3.1). While the current is small in the closed loop (less than 0.007 m/s), it is significantly stronger nearshore where it forms a current parallel to the shore along the whole coastline. The flow associated with the diurnal component is mainly unidirectional and parallel (except near the northern and southern shores, where it is perpendicular) to the axis of the lake. In regions further from the coastline, this flow rotates on itself with a period of 1 TD (see Fig. 3.8).

Rotating shallow water waves such as long Kelvin waves and long Poincaré waves should not appear in Ontario Lacus. Indeed, the Rossby deformation radius $R = \frac{\sqrt{gh}}{|f|}$ (where the mean depth h is about 27.3 m in this case) is about 700 km which is larger

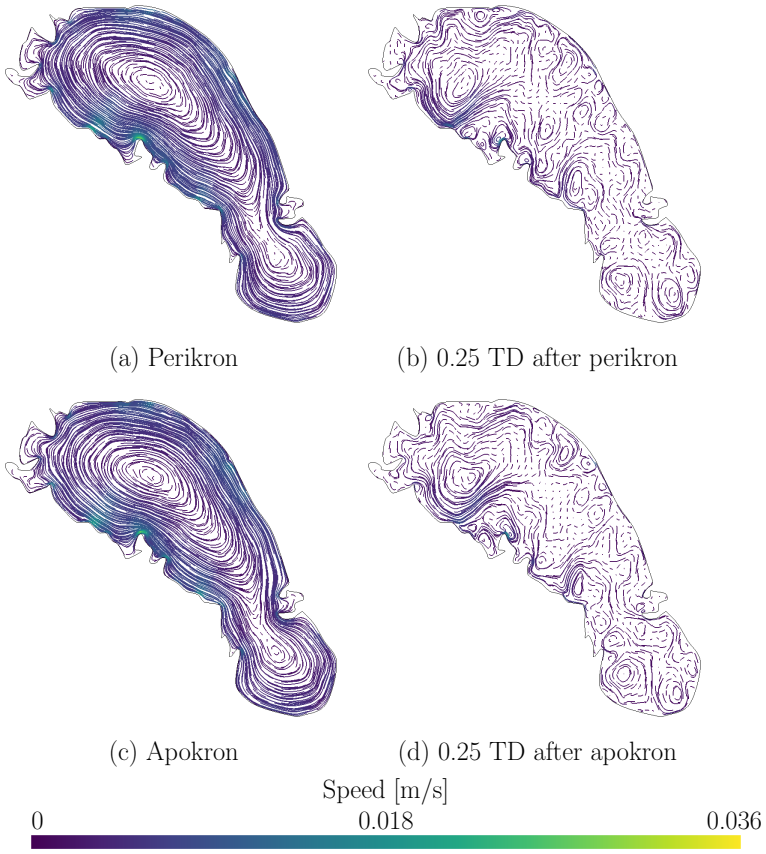

Fig. 3.7: Tidal current streamlines (the color scales with the magnitude, in m/s) in Ontario Lacus at perikron (a), 0.25 TD after perikron (b), apokron (c) and 0.25 TD after apokron (d). The current magnitude is maximum nearshore, at areas P and Q (see Fig. 3.1) and decreases with the distance to the shore.

than Ontario Lacus and makes Kelvin waves and long Poincaré waves impossible in this lake. For R larger than the characteristic length scale, the shallow water waves tend to be non dispersive as their phase speed tends to $c \approx \sqrt{gh}$. Such waves are referred to as external gravity waves and are little affected by Titan's rotation.

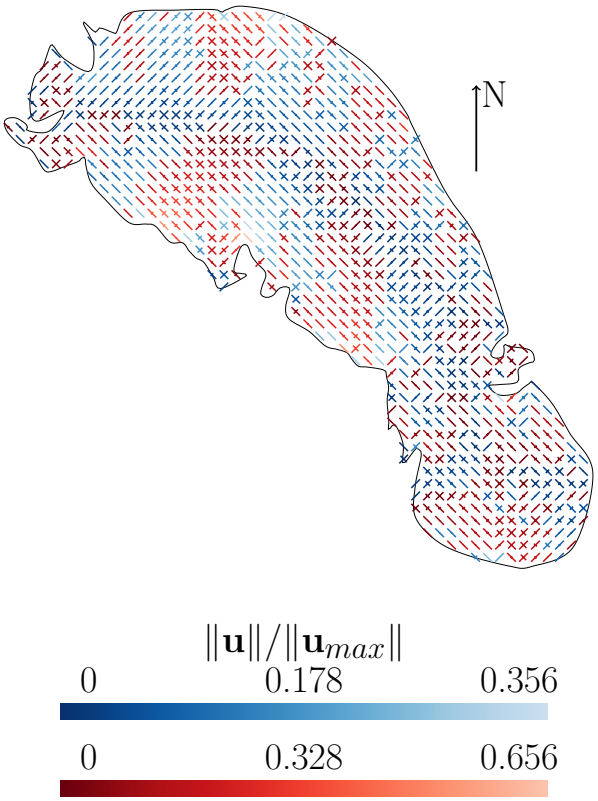

Fig. 3.8: Major and minor axes of the tidal ellipses of the 1^{st} component. The tidal ellipses represent the orientation of the tidal component of the current over a whole period. Red and blue ellipses respectively indicate an anti-clockwise/clockwise rotation while the color scales with the magnitude of the maximum velocity over 1 TD (i.e. 0.0359 m/s). The smaller the minor axes, the most unidirectional the flow is. The 1^{st} component can result in almost circular ellipses in the centre of the closed loop, and in the north western and southern part of the lake while the ellipses are almost linear nearshore.

Consequently, surface gravity waves of phase speed $c \approx 6$ m/s and with a time scale of about $33,000$ s (0.02 TD) could appear in Ontario Lacus.

3.4.2 Influence of model parameters

First, the results obtained with *bathy A* and *bathy B* are compared (in terms of tidal current and surface elevation) to each other and with respect to those predicted with *bathy C* implemented. Second, the impact of the bottom deformation and friction is studied by varying the attenuation factor γ_2 and Manning's coefficient.

3.4.2.1 Bathymetry influence

The bathymetry implemented does not have a significant impact on the tidal amplitude: the global behaviour is the same but modifications in the bathymetry can induce small local changes on the amplitude. The variations of the tidal range are smaller than 5%. However, depending on the bathymetry, dry areas can appear and disappear due to the tides (see Fig. 3.9 (a) and Fig. 3.9 (b)). They appear while the tide has been low in the southern part or in the northern part of Ontario Lacus. As discussed in Section 3.4.1, tidal flats could also occur out of the boundaries of this domain, which would increase the size of the areas that can be wet or dry due to the tides. The size and location of dry areas at low tide vary from one bathymetry to another. With *bathy A*, a dry area appears at the southern end of Ontario Lacus from 0.27 TD (right after Fig. 3.6 (b)) to 0.52 TD (right after Fig. 3.6 (c)) while, with *bathy B*, there are two of them: a narrow band appearing along the southern coastline and a dry area appearing in a bay at the northern end of Ontario Lacus. The narrow band appears on the south-eastern shore at 0.235 TD (soon before Fig. 3.6 (b)) and spreads along the shore reaching point N in 0.435 TD. This dry area has totally disappeared by 0.555 TD (soon after Fig. 3.6 (c)). The second dry area is much smaller: it appears at 0.73 TD and disappears by

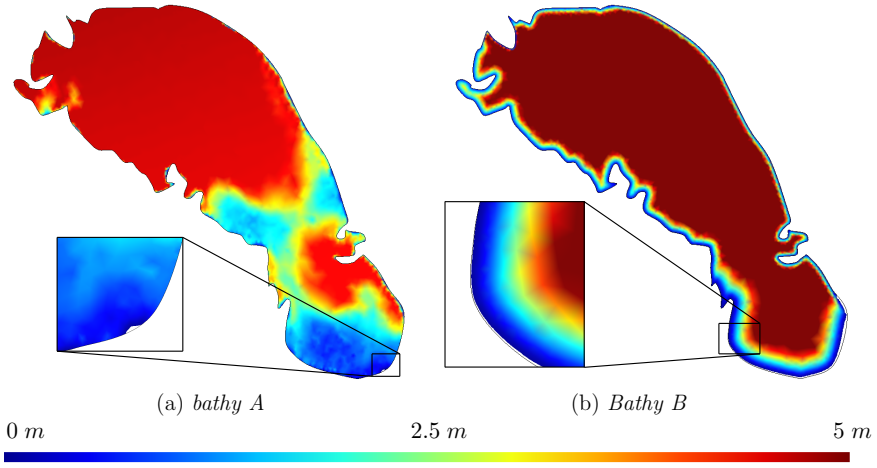

Fig. 3.9: Map of the total liquid depth (bathymetry + surface elevation) 0.335 TD after perikron respectively with *bathy A* (Panel (a)) and *bathy B* (Panel (b)) implemented. The depth is cropped at 5 m in order to highlight the dry areas generated by tidal motion and the areas where there is not much liquid remaining. Most of the dry areas are located in the south while shallow areas can also be found offshore and on the eastern and north-western shore for *bathy A*. With *bathy B* implemented, there are more dry areas and they are larger

0.985 TD. The differences in size and shape of such tidal flats between the bathymetries are due to the variations in terms of local depth (see Fig. 3.2) and in the bathymetry slope nearshore. For instance, Fig. 3.2 (b) shows that *bathy B* is shallower in its south-eastern part, which results in a narrow band of dry area along the shore (see Fig. 3.9 (b)) not observed with other bathymetries.

Modifications of the bathymetry have a significant impact on the current (see Fig. 3.10 and Fig. 3.11). While the main characteristics such as speed decreasing with distance to the shore, acceleration at some specific areas such as headlands and the closed loop in the northern part of the lake are still present, the magnitude and orientation of the velocity field are significantly different. With *bathy A* implemented, the current magnitude is globally smaller, although

it can be locally larger. For instance, the maximum speed (about 0.022 m/s), although smaller than with *bathy C* is located near another peninsula (near Point O, see Fig. 3.1), resulting in a speed locally larger than with *bathy C*. The speed is also locally larger near Points R and N (see Fig. 3.1). A wide area where the current is significantly larger than in the centre of the lake appear along the western shore of the lake (see, for instance, Figs. 3.10 (a) and (c)), between Points N and O (see Fig. 3.1). It corresponds with a shallower area (about 3 m depth) separating two deeper areas. In this shallow area, the current is unidirectional along the longitudinal axis of the lake: it is northward at perikron and southward at apokron. Due to this shoal area, the closed loop formed by the flow in the north is much smaller. Small circular flow patterns appear during transitions between perikron and apokron but they disappear quickly and are associated with a weak current magnitude.

With *bathy B* implemented, the maximum speed is also smaller, about 0.025 m/s, but it is located near the same headland as with *bathy C*. Similarly to the two other cases, the current magnitude is larger nearshore. Nevertheless, such high-speed areas can be found near other headlands as with the other bathymetries. For instance, at point N (see Fig. 3.1), the speed is significantly larger than with *bathy C*, which meets the results obtained with *bathy A*. The northern closed loop is shaped as with *bathy C* and another closed loop appears in the southern part of Ontario Lacus (see Figs. 3.11 (a) and (c)). This closed loop and the northern one appear and disappear together. During the transition between the clockwise and the anticlockwise closed loop, there is a short period during which the flow is almost unidirectional in Ontario Lacus (it is northward after perikron and southward after apokron). These results show that the nearshore bathymetry plays a significant part in the formation of local high-speed areas nearshore and can also modify the offshore flow patterns.

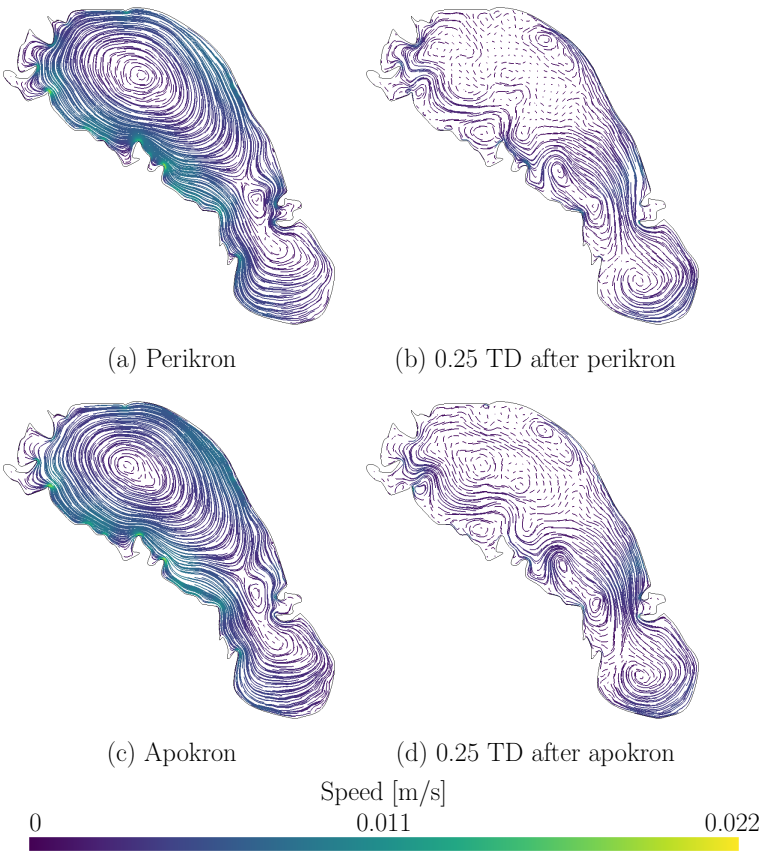

Fig. 3.10: Tidal current streamlines (the color scales with the magnitude, in m/s) in Ontario Lacus with *bathy A* implemented at perikron (a), 0.25 TD after perikron (b), apokron (c) and 0.25 TD after apokron (d). The current magnitude is maximum nearshore, at area O (see Fig. 3.1) and decreases with the distance to the shore except near area N where the flow speed is significant offshore. As with *bathy C*, a closed loop is noticeable in the north.

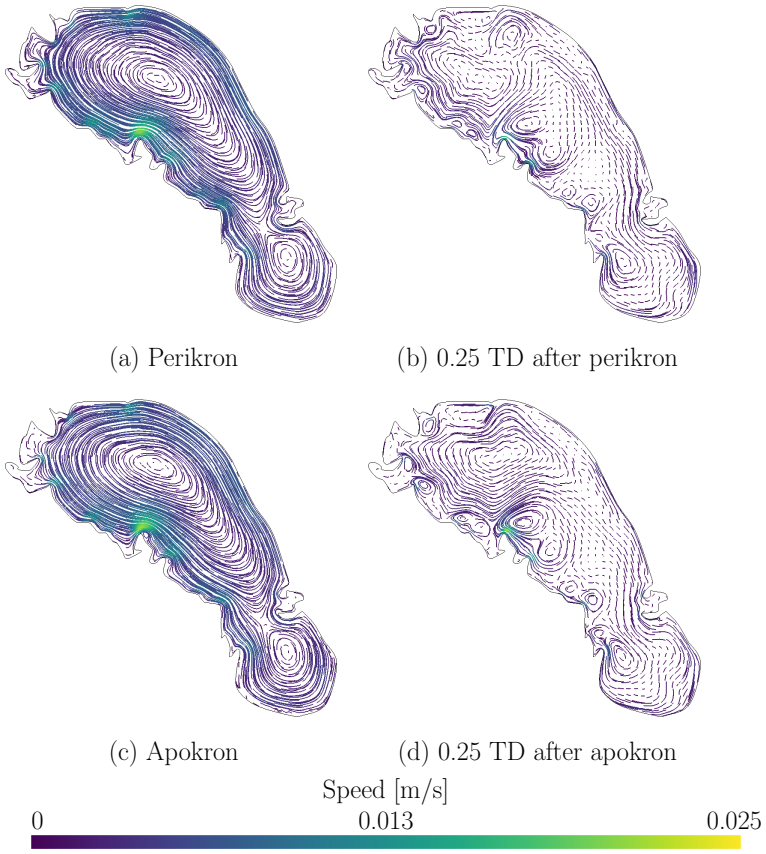

Fig. 3.11: Tidal current streamlines (the color scales with the magnitude, in m/s) in Ontario Lacus with *bathy B* implemented at perikron (a), 0.25 TD after perikron (b), apokron (c) and 0.25 TD after apokron (d). The current magnitude is maximum nearshore, at area O, and is significantly large at area H. The flow forms a closed loop in the north and a southern closed loop also appears at perikron and apokron.

3.4.2.2 Bottom friction influence

Common values of Manning's coefficient vary from 0.01 $sm^{-1/3}$ to 0.075 $sm^{-1/3}$ (which respectively correspond to smooth man-made channel and to flood plains with heavy brush on Earth). We study

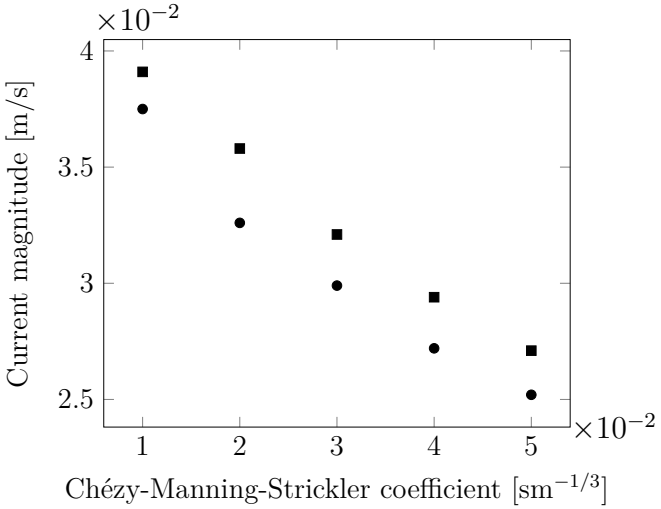

Fig. 3.12: Evolution of maximum current speed with respect to the Manning's friction coefficient at two different times: perikron (circle) and apokron (square). As expected, the speed decreases as the bottom friction increases.

values from 0.01 to 0.05 (which corresponds to natural channels with stones on Earth) by step of 0.01.

As expected, the flow slows down as Manning's coefficient increases (see Fig. 3.12). The high-speed areas along the shore shrink and the speed in these areas decreases faster than elsewhere in the lake while the bottom friction increases. The maximum speed is still reached nearshore but its location varies with Manning's coefficient. The elevation remains almost constant as n is modified (not shown): at a given time t^*, the difference is less than 0.3%.

3.4.2.3 Influence of Titan's surface deformation

As explained in Section 1.1.4, Titan's surface deforms due to the astronomical forcings. Such deformation damps the effect of these forcings on the surface lakes and seas, which is modelled by an attenuation factor, γ_2. We study the influence of this parameter

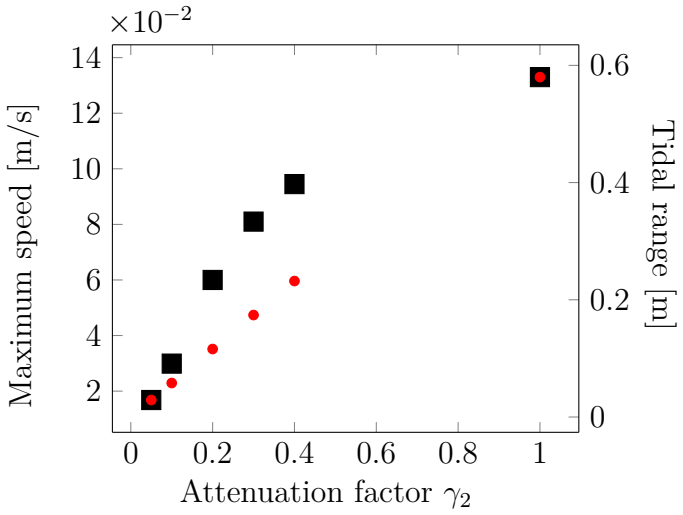

Fig. 3.13: Evolution of the maximum tidal range of the 1^{st} component (bullet) and of the maximum velocity (square) with respect to γ_2. The tidal range of the diurnal component increases linearly with the attenuation factor.

from 0.05 to 0.4. The tidal response of a fully rigid Titan (i.e. $\gamma_2 = 1$) is also studied as an upper bound.

Titan's surface deformation impacts neither the tidal phase, the shape of the corange lines, nor the flow orientation. It does impact the tidal range of the 1^{st} component, which increases linearly with respect to γ_2 (see Fig. 3.13), and the speed. The latter does not only increase but the areas where the speed is significantly larger than in the centre of the lake spread further from the shore as γ_2 increases. Although the maximum speed is still reached near Point P (see Fig. 3.1), the ratio between the speed nearshore and in the centre of the lake increases. This larger nearshore speed is observed along the shore of the northern part of the lake between Points N and Q and between Points H and B (see Fig. 3.1).

3.4.3 Wind orientation influence

In this section, we study the impact of the wind forcing on the surface displacements and currents. The wind is represented through the surface stress term $\boldsymbol{\tau}^s$ in Eqs. 2.19 and is modelled by Eq. 2.22. Tokano and Lorenz (2015) also studied wind-driven flows in Titan's sea. They discussed the wind-driven flows in Kraken and Ligeia Maria on a large time scale (1 Titan year) while neglecting the tides. They used the same ocean circulation model as in Tokano et al. (2014) and the wind speed and orientation were given by the GCM described in Tokano (2009). They showed that the wind-driven circulation is insignificant except from late spring to late summer in the north. They also showed that, if the wind is strong, a noticeable veering of the current takes place which is in line with the Ekman spiral theory.

Unlike Tokano and Lorenz (2015), we study wind-driven flows on a short time scale and the tidal forcing is taken into account so that the tidal flow interacts with the wind driven flow. In this context, extreme conditions[7] are implemented: four strong (1 m/s), unidirectional winds blowing during 1 TD. The impact of such winds is studied during the period during which it has been blowing and after. *Cases* 1 to 4, respectively, correspond to southerly, westerly, northerly, and easterly wind. We are aware that such hypothetical winds are unlikely but it allows us, despite the limitations due to the lack of direct observations, to assess how significant the impact of the wind forcing is on the regime of Ontario Lacus. Indeed, except at Huygens landing site, there is no *in situ* measurements of surface wind on Titan. Several studies predicted the wind by means of a GCM (see Section 1.1.1) but the time scale and the spatial resolution of such simulations are several orders of magnitude larger than those used in our model. In order to overcome this lack of information, a mesoscale model should be used to compute the surface stress but this is beyond the scope of the present study.

[7]Such a wind speed is strong in comparison with Titan standards: the wind is lower than 0.7 m/s most of the time.

The results show that the wind significantly impacts the flow and lake surface elevation. For instance, in *Case 1*, the high tide and the low tide surface elevation of the lake decrease respectively by 0.025 m and 0.044 m in the southern part of the lake, which results in a higher range in this region and a lower mean surface elevation, which cannot be neglected. This effect varies with the wind direction. Due to the wind, the surface elevation does not behave as a pure sinusoid and a constant value has to be added to the tidal components. This wind set-up can be larger than the surface elevation induced by the tidal forcing. For instance, in *Case 1*, this component is maximum in the south: 0.072 m, which is larger than the maximum tidal range. These extreme winds also increase the flow speed in specific locations (not shown). New high-speed areas appear near- and off- shore. The current magnitude, the size, and the location of these areas change with the wind orientation. For westerly and easterly wind (*Case 2* & *4*), the unidirectional high-speed area is oriented along the major axis of the lake and is directed to the left of the surface wind direction (northward for *Case 2* and southward for *Case 4*) which is an evidence of Ekman transport. This is not observed for northerly and southerly winds, which could be explained by the slender shape of Ontario Lacus. In these cases, (*Case 1* & *3*), there are several unidirectional high-speed areas: one in the north and one in the south of the lake (south of point G, see Fig. 3.1). They are much smaller and oriented along the wind direction.

The wind influence raises with the time: after 0.06 TD, the northern flow pattern is strongly modified and after 0.25 TD, it is replaced by small circular flow patterns around an unidirectional high-speed area which is strongly influenced by the wind direction. In these specific cases, the wind is the main driving force of the current and significantly influences the surface elevation. As soon as the wind stops blowing, its effects slowly decrease. Indeed, after 2 TD, the tidal elevation is maximum at the same location and time than without wind and the difference between the surface elevations is less than 5% (it is exactly the same after 4 TD). After 5 TD,

a closed loop reappears in the flow pattern and, after 7 TD, the pattern is the same as before the wind blew.

A depth-averaged model such as that used in this study suffers from a shortcoming for the simulation of wind-driven flows: the differences between the wind-driven flows near the lake surface and near the lake bottom cannot be simulated. Indeed, the flow is stronger near the surface and weaker near the lake bottom and the orientation can also differ due to phenomena such as the Ekman spiral. Nevertheless, this model allows us to study the main effects of wind and show that the wind-induced surface stress significantly modifies the flow patterns and the surface elevation. This is due to the low liquid density (about twice smaller than in Earth's ocean) and the large air density (about 4.5 times larger than at sea level on Earth).

3.5 Discussion

3.5.1 Parameters influence

The influence of the molecular diffusivity and the density is studied in the range given by the liquid composition found in the literature (see Section 3.2.1). The impact of their variation is insignificant (not shown). The attenuation factor is the only parameter which impacts significantly the surface elevation: the tidal range increases linearly with γ_2 while no effect on the tidal phase and shape of the corange line is observed. The velocity field, on the other hand, is significantly influenced by the bottom friction, attenuation factor, and bathymetry. Increasing $gamma_2$ speeds up the flow while it is slowed down all over the lake when the bottom friction is increased. This effect can be more significant in some areas, resulting in a variation of the distribution of high-speed areas. The velocity orientation can also change locally but the main pattern(s) remain(s) similar. The bathymetry influence on the flow is quite significant. Local circular flow patterns or small acceleration areas

can appear over the lake and the maximum speed can vary significantly. The results obtained with the three bathymetries show that the local depth significantly impacts on the velocity, as does the shape of Ontario Lacus: the maximum speed is observed near headlands and the speed is higher nearshore and where the lake is shallow. Consequently, an accurate shape, bathymetry, and value of γ_2 should be used to properly predict the velocity field while we can afford some discrepancy in liquid properties.

3.5.2 Shoreline variations induced by the tides

Although the shoreline variations due to the tides are difficult for Cassini to observe, it remains an interesting question. Depending on the bathymetry implemented, the size and the location of dry areas appearing at low tide vary. The largest are obtained with *bathy B*: with this bathymetry implemented, the dry areas spreads out to 0.12 km away from the south-western shore at low tide while the largest dry area predicted with *bathy A* implemented spreads out to 0.08 km away from the southern shore (see Fig. 3.9 (b)). These variations are those due to the low tide. By adding the dry areas flooded at high tide, one gets a variations of respectively 0.24 km and 0.16 km (providing the nearshore bathymetry slope are the same as the coastal shore). At point N (see Fig. 3.1), the tidal range predicted by means of our model is at most 0.058 m. Assuming the smaller slope from Hayes et al. (2011) (1.1×10^{-4}), it would result in 0.52 km length of land that could be submerged depending on the tide. Such variations remain much smaller than the observed recession (which are respectively $\sim$ 10 km in the south-west corner and about 20 km at point N (Turtle et al., 2011; Hayes et al., 2011)). These values are an upper bound: in order to observe such variations, the time lag would have to be exactly 0.5 TD. Consequently, tidally induced shoreline variations are very unlikely to be observed by Cassini.

In the light of the time lag between the 2005 ISS images and the 2009 SAR observations (94.67 TD) and between the 2005 and

2009 ISS images (87.17 TD), the difference in surface elevation is lower than the predicted tidal range and, although significant, the predicted tidal flats are much smaller than the observed shoreline variations. The wind could increase the size of the tidal flats but not enough to generate a 20 km length variation. Moreover, it would not explain the recession observed on both eastern and western shores. As a consequence, either other phenomena such as evaporation play a significant part in the shoreline recession (2005 ISS observations were made close to the mid southern summer while 2009 ISS and SAR observations are close to the vernal equinox) or the variations are due to the low spatial resolution of ISS observations in 2005.

3.5.3 Morphodynamic features in Ontario lacus

Morphodynamic features can take various forms which are generated by different forcings. These features and their main forcings can be classified as a function of temporal and spatial scales (see, e.g., De Vriend, 1991). The larger the timescale, the larger the spatial scale. While some phenomena occurring on Earth, such as climate change and sea level rise, are unlikely on Titan, others could generate similar morphodynamic features:

- Sea swell and turbulence could generate ripples
- The tidal cycle could generate sand banks.
- Shoals and shoreline modifications could occur due the liquid volume variations induced by the seasonal variability.
- Variations of the estuaries, tidal basins, and barrier coasts could be generated by long timescale phenomena.

The geomorphology of Ontario Lacus – which was studied by, among others, Wall et al. (2010); Cornet et al. (2012); Dhingra et al. (2018);

Birch et al. (2018) – shows evidence for active morphodynamic features taking place in the lake. Observing these features is a complex task as most of them are either too small (it is the case of the sea swell and turbulence impacting the ripples) or induced by very slow phenomena, such as the erosion modifying the coastal geomorphology. The only observed feature is the assumed shoreline variations induced by seasonal variations. While all these features are of interest and could take place in a study focusing on the geomorphology of the lake, they are out of the scope of the present chapter which focuses on diurnal phenomena. The diurnal tides could (depending on the bathymetry) generate dry areas nearshore but they are small and their apparition does not last. Sand banks could also locally appear in shallow areas due to sediment transport. Indeed, sediment transport likely takes place on Titan (Burr et al., 2006; Misiura and Czechowski, 2015) but, due to the lack of data, it is not possible to conduct realistic simulations of this phenomenon in Ontario Lacus (although theoretical studies would be justified).

3.5.4 Intercomparison with previous results and Lake Ontario

Numerical simulations of Ontario Lacus tidal response were performed by Tokano (2010). We compare the results of a simulation carried out for $\gamma_2 = 1$ to those of Tokano (2010). Our predictions have some similarities but there also are significant differences. In both simulations, the tidal amplitude is maximum in the southern part of the lake and the surface elevation is larger at apokron and perikron than 0.25 TD later. Nevertheless, our model predicts a maximum tidal range which is about three times larger than that predicted by Tokano (2010) (about 0.58 m instead of 0.2 m). Using an analytical approaches, Barnes et al. (2009) and Hayes et al. (2011) predicted a maximum tidal range of 0.4 m in the southern part of the lake, which is also larger. Tokano (2010) predicted a purely longitudinal motion along Ontario Lacus longitudinal axis while, according to our results, the tide rotates clockwise with an

exact period of 1 TD, which is consistent with the forcing. The current magnitude and orientation are also quite different: Tokano (2010) predicted a purely longitudinal current (along the longitudinal axis of the lake) with a maximum speed of about 0.003 m/s located offshore while the flow predicted by our model forms closed loop(s) and the maximum speed is located nearshore and can locally reach up to 0.036 m/s. This could be partially explained by the constant depth and the simplified shape used by Tokano. Indeed, the shallow areas and the headlands are poorly represented in Tokano (2010) while they have a significant influence on the velocity field. Comparing the spatially averaged speed at a given time is more satisfactory: that predicted by our model ranges from 0.001 m/s to 0.004 m/s, depending on the time period, which is of the same order of magnitude as the speed predicted by Tokano (2010). The temporal variation of the mean speed is strongly related to the speed near the headlands.

For a better comparison, a 20 m constant depth, a larger spatial resolution of 10 km and a quadratic bottom friction law was also implemented in order to be as close as possible to Tokano's simulations (not shown). Nevertheless, it remains an unstructured grid made of triangles while Tokano used a structured grid with equidistant grid points and the shape of the domain is simpler in Tokano (2010). Adopting a configuration similar to that of Tokano (2010) increases the similarities with his results. The maximum speed is smaller, about 0.001 m/s, and the orientation is significantly modified: it is unidirectional along the main axis of the lake during short periods and the transition, which occurs when the elevation bulge is on the eastern/western shore consists of a closed loop. The speed is maximum in the narrow part of the lake, near the headlands forming the narrowing. The elevation field is almost unaffected by this configuration: it still consists in a diurnal tide rotating around the same amphidromic point. The maximum is 0.284 m and is reached at the same time and location.

No additional information allows us to assess which model better represents the tidal motion in Ontario Lacus. The assets of our

model are: a higher spatial resolution allowing a better representation of the coastline and realistic bathymetry maps; although using the latter does not explain the difference in terms of tidal amplitude between the results. The main difference between the models is the fact that Tokano (2010) used a 3D hydrostatic, baroclinic ocean circulation model while we used a 2D hydrostatic, barotropic model. Therefore, he took advantage of the energy equation to take into account the solar heating in order to simulate seasonal effects. He isolated the diurnal motion from the long term seasonal variations to predict the tides. The model was also used to study the tidal motion in the northern seas (see Tokano et al., 2014) but the results vary significantly between Tokano (2010) and Tokano et al. (2014).

Lake Ontario, the terrestrial counterpart, is slightly larger (311 km $\times$ 85 km) and deeper (the mean depth is 86 m). It is located at a lower latitude and its longitudinal axis is almost perpendicular to the longitude axis. In Lake Ontario, the tidal range caused by the Moon and the Sun is less than 5 cm (NOAA, 2014), which is similar to that predicted by means of our model for Ontario Lacus, but the surface displacements increase significantly due to wind and barometric pressure changes (Hamblin, 1982; NOAA, 2014). The difference in the tidal range could be explained by the fact that the gravity on Titan and the Coriolis factor are smaller while the tidal potential is larger than that on Earth. Hamblin (1982) computed the tides in Lake Ontario by taking into account the forcing due to the Moon, the Sun and the wind, and compared his results with *in situ* measurements. He took into account the first four modes with a period of respectively 5.06 hr, 3.21 hr, 2.32 hr, and 1.705 hr. The periods are quite different from those observed in Ontario Lacus, which is due to the forcing: the orbital period of Titan around Saturn is much larger and we do not take into account the forcing due to the wind, the Sun and the other moons. He observed and predicted that the phase of the main mode progresses in a anticlockwise sense, which is the opposite of our results in Ontario Lacus. This is due to the fact that Lake Ontario is in the

northern hemisphere and Ontario Lacus is located in the southern hemisphere.

3.6 Applications and future missions

Unlike the northern seas, Ontario Lacus is not a designated target for a future mission. The lake is smaller, which increases the risk of landing on dry land, and does not provide the opportunity of exploring a wide range of latitudes and longitudes, hence reducing the ability to study the spatial variability of various data. The motion of a drifted capsule induced by the tidal flow would be very slow as shown by the simulation of its position as a function of time and landing site by means of the Lagrangian particle tracker module of SLIM (see Fig. 3.14): the maximum displacement after 3 TD is 1.8 km, near the headlands where the speed is maximum (see Fig. 3.14). Therefore, the wind is likely to act as a significant forcing regarding the path of a drifted capsule (both by modifying the liquid flow and by pushing the capsule in a specific direction). It would, hence, be interesting to couple SLIM with a mescosale atmospheric model in order to predict the resulting liquid motion. A motorised capsule would be better suited to prevent beaching and allow the capsule to travel long distances.

As discussed in Section 1.4, an orbiter is not well suited to measure time series of the surface elevation at a given point as the elevation is several order of magnitude smaller than the deformation of Titan's surface. The shoreline variations resulting from the tidal motion being small (at most 0.52 km), it would require a high resolution instrument to be able to observe them (for instance the spatial resolution of Cassini's radar was, at best, 300 m, which is to coarse). An optical camera can reach high resolution of the order of 0.1 m but the opacity of Titan's atmosphere in the visible spectra makes the use of such camera harder. If such observations were available, it could be of interest to conduct numerical simulations with a higher mesh resolution nearshore in order to better capture

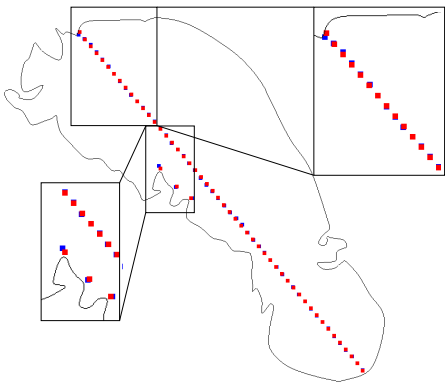

Fig. 3.14: Initial (in red) and final (after 3 Titan days, in blue) positions of the capsule for various sea landing sites along the main axis of Ontario Lacus and in the area where the speed is the largest. The tidal flow used to predict the paths is the one predicted in the reference case. The largest displacement (1.8km) occurs where the velocity is maximum.

the dry areas. Indeed, the nearshore mesh resolution enables the capture of dry areas of the order of 100 m but smaller dry areas are not captured. A lander would be better suited as it could provide a variety of data which would allow validating and improving our model. A capsule landing in Ontario Lacus could provide

- Time series of the sea surface elevation, at a given location (if it is supplied with an anchor) or at different locations, using a depth sounder/sonar;

- Time series of crucial atmospheric data such as the wind velocity, the surface temperature, and the "air moisture" at the lake surface. If the capsule is not anchored, an additional instrument able to measure the velocity of the capsule would be required;

- An analysis of the liquid composition and the vertical profile of density and temperature in the lake;

- Time series of the flow speed and orientation using a current meter.

A spacecraft landing near Ontario Lacus would be less well suited but could measure time series of the sea surface elevation at a given location using a rangefinder and could infer backscattering properties of the liquid.

In order to validate our model, time series of the elevation at various locations would be the most useful data as the velocity is highly sensible to poorly constrained local variations of the model parameters. Other data such as the liquid properties and the atmospheric forcings would allow us to improve our model. While these data could prove very useful, it would be more interesting to send such an exploration mission in the northern seas as the capsule could travel a longer distance, therefore allowing measuring the longitudinal and latitudinal variability of the atmospheric data and liquid composition and properties.

3.7 Conclusion

Titan is, with the Earth, the only celestial body of the solar system presenting large liquid bodies on its surface. In this paper, we studied Ontario Lacus, the largest lake in Titan's southern hemisphere. SLIM (www.climate.be/slim), a model solving the 2D depth-averaged shallow water equations by means of the discontinuous Galerkin finite element method, was adapted to Titan conditions (e.g. gravitational acceleration, tidal forcing) in order to simulate the tidal response of this lake. The influence of bathymetry, Titan's surface deformation, and bottom friction was studied through three different bathymetries and various attenuation factor and Manning's coefficient values. The influence of wind was roughly assessed.

Our model predicts a clockwise rotating tide with an exact period of 1 TD. The maximum tidal range (about 0.058 m) occurs in the southern part of the lake. At perikron, the tide is high in the

south. The current magnitude varies over the lake: it is maximum nearshore and decreases with the distance to the shore. The maximum is located next to headland(s), on the western shore, although its magnitude and location vary with the bathymetry implemented: it can reach up to 0.036 m/s while the speed offshore is smaller than 0.01 m/s. The flow forms a closed loop in the northern part of the lake. Despite many differences (e.g. gravitational acceleration, Coriolis factor, location, liquid properties, astronomical and wind forcing), our results exhibit similarities with the tides observed in Lake Ontario.

We studied the tidal response for the three bathymetries derived from Cassini data and conducted a sensitivity analysis with respect to the deformation of the lake's bottom and the bottom friction. All these parameters can significantly impact the current. Bathymetry variations induce some changes in current patterns and some local high-speed areas can appear or disappear. This effect is particularly significant in shallow areas. The bottom friction has a global effect: while it increases, the current speed decreases. The attenuation factor affects both the speed and surface elevation: their magnitude increases with the factor. Bathymetry and bottom friction both have a very small impact on elevation, although the bathymetry can significantly modify the appearance of dry areas of various shapes and sizes.

We studied four hypothetical winds which would be considered as weak reported to the terrestrial standards but are among the strongest predicted by means of GCMs on Titan (without taking into account the stormy events). Such unidirectional and strong winds are highly unlikely on Titan but their influence on the flow can be significant. Their impact strengthens with time when they are unidirectional and, in these particular cases, their effect continued to be felt after it died during 4 TD for the elevation, and during 7 TD for the current.

In the future, this model could be used to predict the tidal response of the sea where a capsule could land such as Ligeia Mare for the TiME (Titan Mare Explorer) capsule (Lorenz et al., 2012).

CHAPTER 4

Normal modes of Ontario Lacus

This chapter is based on the following article[1]:

D. Vincent, J. Lambrechts, Ö. Karatekin, T. Van Hoolst, R. H. Tyler, V. Dehant, & É. Deleersnijder, 2019, Normal modes and resonance in Ontario Lacus, a hydrocarbon lake of Titan, *Ocean Dynamics*,69: 1121-1132. doi: 10.1007/s10236-019-01290-2

Abstract

The normal modes of Ontario Lacus surface oscillations, the largest lake in Titan's southern hemisphere, are simulated and analysed as they are potentially of broad interest in a variety of dynamical researches. Tidal forces are too low in frequency to excite the (barotropic) normal modes

[1]Slight modifications were added in the chapter.

while broadband wind forcing likely spans the resonant frequencies. High wind speed, which could be encountered under episodic phenomena such as storms, would be required to significantly excite the normal modes. While the slower baroclinic normal modes could more easily be resonantly forced by the low-frequency tidal forces, addressing this issue demands unavailable information about the lake stratification.

4.1 Introduction

Titan, the largest moon of Saturn, is known for its surface lakes and seas filled with liquid hydrocarbons. The Cassini spacecraft, which had been investigating the Saturnian system from 2004 to 2017, detected a methane cycle similar to the hydrological cycle on Earth (Atreya et al., 2006) as well as surface lakes and seas filled with liquid hydrocarbons (mainly methane and ethane) (Stofan et al., 2007; Brown et al., 2008; Cordier et al., 2009). The distribution of these lakes and seas is asymmetric with respect to the equator (Aharonson et al., 2009): there are many more lakes in the northern hemisphere, where the largest liquid bodies are located (Hayes et al., 2008, 2018). The present work focuses on the largest lake of the southern hemisphere, Ontario Lacus. It is centered at (72°S, 176°E) and covers approximately an area of 200 km $\times$ 70 km (Wall et al., 2010). It exhibits well documented shoreline variations: Turtle et al. (2011) suggested that the differences between the ISS images taken in 2005 (on June 6, Rev09, $L_s = 306°$)[2] and 2009 (on March 27, T51, $L_s = 355°$) correspond to possible shoreline variations. This assumption is given additional support by synthetic aperture radar (SAR) images in 2009 (T57, $L_s = 358°$ and T58, $L_s = 359°$) (Wall et al., 2010; Hayes et al., 2011).

[2]The solar longitude of Saturn, L_s , is the angle between the Sun and Saturn and describes the season of Saturn and its moons.

Various attempts were made to understand and explain these variations. Tides were ruled out by Vincent et al. (2016) as the tidal range is too small. Nowadays, the most common explanation involves evaporation/infiltration of surface liquid (Turtle et al., 2011; Lunine et al., 2009) as the observations took place during the southern summer, when evaporation was predicted to be the largest. Due to their low resolution, analysis of ISS images was inconclusive and the existence of seasonal shoreline variations remained questionable as the data are, within measurement error, consistent with no changes at all (Cornet et al., 2012). Subsequent SAR images (T65 in 2010, $L_s = 5.5°$) suggested no significant shoreline changes in comparison with 2009 images. On the other hand, lacustrine features of the southern hemisphere seem to disappear between subsequent SAR observations (from 2007 to 2008/2009), corresponding to liquid evaporation or infiltration into the ground (Hayes et al., 2011; Hayes, 2016). Such observations tilt the balance in favour of shoreline variations taking place in Titan southern hemisphere (at least from 2007 to 2009). Ontario Lacus would likely experience such variations although they could be less significant than suggested by the variations observed between 2005 ISS and 2009 SAR images.

While the tidal motion of Titan's surface liquid bodies was the subject of several studies (see Tokano, 2010; Tokano et al., 2014; Vincent et al., 2016, 2018), the normal modes were only briefly investigated by Lorenz (1994), Dermott and Sagan (1995) and Tokano (2010). Dermott and Sagan (1995) used Merian's formula to investigate resonance phenomena in a hypothetical rectangular lake on Titan while Tokano (2010) calculated the period of a fundamental slosh in Ontario Lacus and Kraken Mare. Such modes need to be understood for a whole range of dynamical studies. Furthermore, they could form a signature that could be remotely sensed and, if they were observed, could possibly be used to infer lake characteristics such as the bathymetry. Indeed, detecting liquid motion associated with a natural period of the lake could give further insight into the bathymetry as the natural periods are related to the depth of the lake. Using such an inverse approach, one could, for in-

stance, gain an insight about the material/configuration properties of a wind-chime from the modes excited by broadband wind.

The resonant frequencies of barotropic modes[3] of a lake with complex shoreline and bathymetry such as Ontario Lacus can be bound by considering its geometry. The highest resonant frequencies would take place in a small cove, where a high-frequency slosh could occur. One can obtain a simple estimate of the lower bound from the period of a fundamental slosh[4] along the larger axis of the lake, of length L. This period is approximated by Merian's formula (Merian, 1828) for a rectangular domain: $T = \frac{2L}{\sqrt{gh}}$, where $g = 1.352$ m/s^2 is the mean gravitational acceleration and h is the mean depth of the lake. For Ontario Lacus, it results in a period much smaller than 1 Titan day (TD). Such modes could not be excited in the models of Tokano (2010) and Vincent et al. (2016) as the only forcing taken into account is that induced by the orbital eccentricity and Titan's obliquity, whose period is 1 TD. Other astronomical forcings with smaller magnitude that were not taken into account in previous studies or some atmospheric forcings could have a period matching those of the barotropic normal modes. Baroclinic modes could also resonate and generate significant liquid displacement within the lake but are not associated with large surface elevations. Furthermore, there is not enough information about the stratification of Ontario Lacus to study them properly. Therefore, we do not consider these modes.

[3]When studying the motion of liquid bodies, one can separate the signal between barotropic and baroclinic modes. The former concern the motion of a constant density liquid and are mostly external modes, i.e. approximately depth-dependent, while the latter differently impact each layer of various density, resulting in internal oscillations.

[4]A fundamental slosh is a normal mode with 1 node in the domain, i.e. it is the longest standing wave that can be observed in the domain.

We numerically study the normal modes of Ontario Lacus for two bathymetries available in the literature, that of Ventura et al. (2012) and that of Hayes (2016) and Mastrogiuseppe et al. (2018a)[5]. The bathymetries are derived from different data sets and using different methods. Ventura et al. (2012) used a model to derive the bathymetry from the SAR data of the T65 flyby (January 12, 2010) while Hayes (2016) and Mastrogiuseppe et al. (2018a) derived their bathymetry from the T49 flyby (December 21, 2008) by means of an extrapolation method. The methodology of Ventura et al. (2012) is a combination of electromagnetic modelling and a Bayesian approach to perform the inversion and to derive the lake optical thickness from SAR backscattering values. The conversion to physical depth is then achieved by using the loss tangent value as calculated in Hayes et al. (2010). Hayes (2016) and Mastrogiuseppe et al. (2018a) applied the method of Mastrogiuseppe et al. (2014) to the altimetry data from T49. This method consists in deriving the bathymetry from subsurface reflections in the Cassini radar altimeter. Nevertheless, T49 was the first pass over a liquid body and the default attenuator settings were overwhelmed, leading to saturation. Mastrogiuseppe et al. (2016, 2018a) used a radar altimetry simulator to recover the data over the saturated area, resulting in the bathymetry reported in Hayes (2016). A more detailed comparison of the methods is available in Section 2.3 of Vincent et al. (2016) while technical details are available in Ventura et al. (2012) and Mastrogiuseppe et al. (2014, 2016, 2018a). The lake shoreline considered is derived from T58/T59 flyby. It corresponds to the lowest level of the lake (see Fig. 4.1). Due to the complexity of Ontario Lacus' shoreline, unstructured grids are used to discretize the domain. It allows a better representation of the shoreline without significantly increasing the computational and memory costs.

[5]Although the bathymetry is derived following the method described in Mastrogiuseppe et al. (2018a), it was first published in Hayes (2016). We refer to this bathymetry as the bathymetry of Hayes (2016) throughout this article.

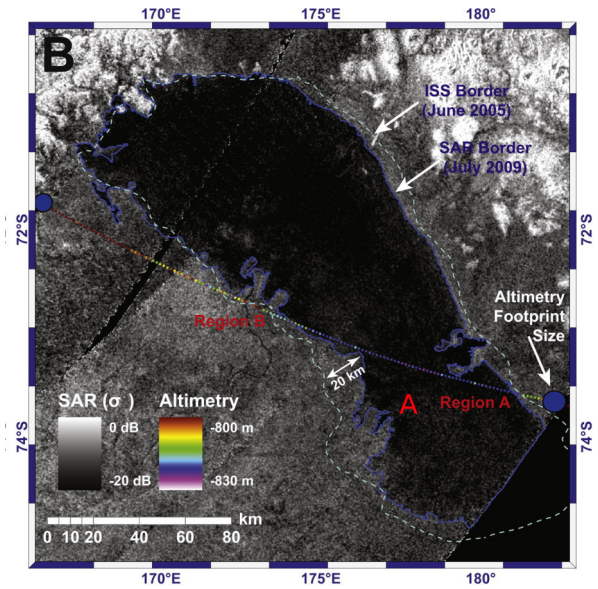

Fig. 4.1: Radar map of Ontario Lacus. The dashed line corresponds to the ISS shorelines from 2005. The red letter A denotes the area where the largest shoreline variations occurred. (Adapted from (Hayes et al., 2011); original image credit: Cassini Radar Science team, NASA/JPL/Caltech)[6]

The chapter is organised as follows: the method used to simulate the normal modes and periods of the lake is presented in Section 4.2. The periods of the various astronomical forcings acting on Titan are discussed in Section 4.3 and compared with the natural periods of Ontario Lacus in Section 4.4. Among the normal modes predicted, some of them stand out as they correspond to large area(s) with positive/negative sea surface elevation and could therefore be detected by an orbiter. They are briefly introduced in the same section. The liquid motion under arbitrary wind con-

[6]Reprinted from *Transient surface liquid in Titan's polar regions from Cassini*, 211, A. G. Hayes, O. Aharonson, J. I. Lunine, R. L. Kirk, H. A. Zebker, L. C. Wye, R. D. Lorenz, E. P. Turtle, P. Paillou, G. Mitri, and others, 655–671, Copyright (2011), with permission from Elsevier

ditions likely to excite some of these normal modes are studied in Section 4.5. Finally, the results are discussed in Section 4.6 and conclusions are drawn in Section 4.7.

4.2 Method

A normal mode (also called eigenmode) is a pattern of motion under which a system can freely oscillate following a perturbation of its equilibrium state. The frequency associated with the oscillation is called the normal frequency. The normal modes of a linear system form a complete basis set, i.e. any motion of the system can be described as a weighted sum of its eigenmodes. The motion associated with the excitation of a normal mode of a liquid body is called a seiche, which is defined by Baretta-Bekker et al. (1998) as "A standing wave occurring in lakes or semi-enclosed embayments as a result of some sudden disturbance. The topography of the basin determines the form and period of the different seiche modes that may occur.". These modes can be predicted from the linearised equations of motion.

Various methods allowing computing the eigenmodes of a liquid domain are described hereafter. For regular structured grids, the eigenmodes can be computed analytically by introducing a space Fourier mode in the discretised equations, leading to the dispersion relation which depends on the grid and numerical scheme (e.g. Sauter and Wittum, 1992). Another way to study the eigenmodes is to solve the stationary equations[7] for a range of angular frequencies (e.g. Webb, 2013). This allows predicting the frequencies associated with resonance and, hence, the normal periods and normal modes. Ontario Lacus has a complex shoreline and bathymetry which would require a high resolution structured grid to be properly captured. On the other hand, the geometrical flexibility of unstructured meshes allows one to locally increase the spatial resolution. This permits an accurate representation of the shoreline and bathy-

[7]These equations are obtained by separation of variables.

metry (see Fig. 4.2) whilst demanding less memory and computer time than calculations based on a structured mesh. The above-mentioned approaches being not easily applicable to unstructured grids, we use the alternative approach of Bernard et al. (2008), which is adapted to these grids. The key features of this method are laid out below. The modes are predicted from the linearised, frictionless, shallow-water equations:

$$\begin{cases} \dfrac{\partial \overline{\boldsymbol{u}}}{\partial t} & + \quad f\boldsymbol{e}_z \wedge \overline{\boldsymbol{u}} + g\nabla\eta = 0 \\ \dfrac{\partial \eta}{\partial t} & + \quad \nabla \cdot (h\overline{\boldsymbol{u}}) = 0 \end{cases} \tag{4.1}$$

where $\overline{\boldsymbol{u}}$ is the depth-averaged velocity (whose components along the x and y axes are $\overline{u}$ and $\overline{v}$, respectively); ∇ is the horizontal del operator; $f = 2\Omega \sin\theta$ is the Coriolis parameter ($\Omega = 4.5601 \times 10^{-6}$ s^{-1} is Titan's rotation rate and θ is the latitude); $\boldsymbol{e}_z$ is a unit vector pointing upwards in the local non-inertial Cartesian basis; $g = 1.352$ m/s^2 is the mean gravitational acceleration at Titan's surface; η is the surface elevation (positive upwards); and h is the reference height of the liquid column. One can rewrite this system as

$$\frac{\partial \mathbf{U}}{\partial t} + \nabla \cdot \mathbf{F}(\mathbf{U}) + \mathbf{S}(\mathbf{U}) = \mathbf{0} \tag{4.2}$$

where $\mathbf{U} = \begin{pmatrix} \eta \\ \overline{u} \\ \overline{v} \end{pmatrix}$ is the vector of unknowns, $\mathbf{F} = \begin{pmatrix} h\overline{u} & h\overline{v} \\ g\eta & 0 \\ 0 & g\eta \end{pmatrix}$ is the flux matrix and $\mathbf{S} = \begin{pmatrix} 0 \\ -f\overline{v} \\ f\overline{u} \end{pmatrix}$ is a vector related to the Coriolis force. These equations are discretised on an unstructured mesh following the discontinuous Galerkin finite element method (DGFEM): Eq. 4.2 is multiplied by a test function and integrated over the domain. Using a Riemann solver to compute the flux at the element interfaces, one obtains the semi-discrete discontinuous

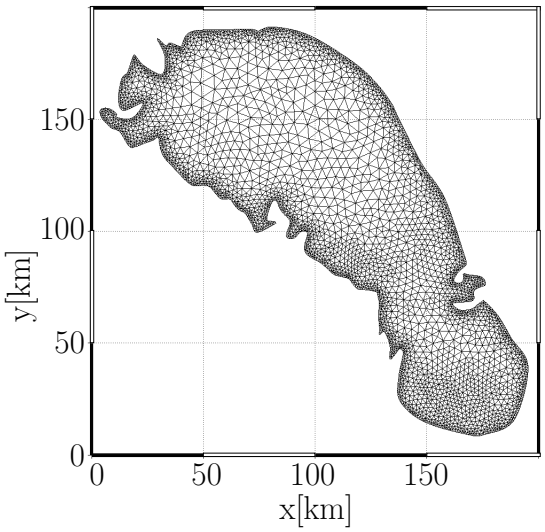

Fig. 4.2: Discretization of Ontario Lacus using mesh-generation package GMSH. The mesh is refined nearshore and where the bathymetry gradient is significant.

Galerkin (DG) formulation for a spatial piecewise discontinuous polynomial approximation $\mathbf{U}^p$

$$\frac{\partial \mathbf{U}^p}{\partial t} = \mathbf{L}\mathbf{U}^p \tag{4.3}$$

where $\mathbf{L}$ is the DG formulation of the linear shallow water space operator (see Bernard et al. (2008) for further details about this transformation). Finally, this linear operator transforms to

$$\frac{\partial}{\partial t}\mathbf{U}^p = \mathbf{M}^{-1}\mathbf{A}\mathbf{U}^p \tag{4.4}$$

where $\mathbf{M}$ is the mass matrix of the domain[8] and $\mathbf{A}$ is a matrix representing the spatial terms. $\mathbf{M}^{-1}\mathbf{A}$ is never assembled numerically as it would require a time and resource consuming inversion

[8]The mass matrix results from the integral of the product of the shape functions over each element of the domain.

of **M**. Consequently, the linear operator corresponding to the numerical equation is

$$\mathbf{M}\frac{\partial}{\partial t}\mathbf{U}^p = \mathbf{A}\mathbf{U}^p \tag{4.5}$$

This is a generalised eigenvalue problem whose complex eigenvalues, λ, satisfy the fact that $\mathbf{A}$-$\lambda\mathbf{M}$ is singular (i.e. the determinant is zero). The discrete solutions $\mathbf{U}^p$ are the real part of

$$\mathbf{U}^p = \mathrm{Re}\{\mathbf{X}^p(x,y)e^{\lambda t}\} \tag{4.6}$$

where $\mathbf{X}^p(x,y)$ is the eigenvector. These eigenvalues and the associated eigenvectors $\mathbf{X}^p$ can be computed using `eig` function of the `scipy.linalg` package of the python library (see Jones et al., 2001). Indeed, this is cheaper than inverting **M** and then multiplying **A** by $\mathbf{M}^{-1}$. Function `eig` uses the `ggev` routine from LAPACK and BLAS libraries. This routine performs a QZ decomposition (also called generalised Schur decomposition) to compute the eigenvalues and eigenvectors.

The eigenvalues should be purely imaginary as no dissipation term is present in Eqs. 4.1. However, they are actually complex (see Figs. 4.3). This is due to the dissipation introduced in the discrete equations by the Riemann solver used to deal with the spatial operators (Bernard et al., 2008). The real part of the eigenvalue quantifies this dissipation. For this application, the real parts of the eigenvalues range from 0 to 0.03 s^{-1} or 0.04 s^{-1}, depending on the bathymetry. The eigenmodes of interest in our analysis (they are represented by red dots on Fig. 4.3) correspond to eigenvalues whose real part is small (it is at most $\mathcal{O}(10^{-8})$ s^{-1}). The real parts of some eigenvalues are much more significant but they are associated with modes corresponding to numerical dissipation (i.e. without any physical meaning). The eigenvalues always come in complex conjugate pairs of same norms and dissipation. Therefore, they are characterised by the same frequency but with opposed directions of rotation. As the eigenvalues are complex, so are the eigenvectors. Both real and imaginary parts contribute to

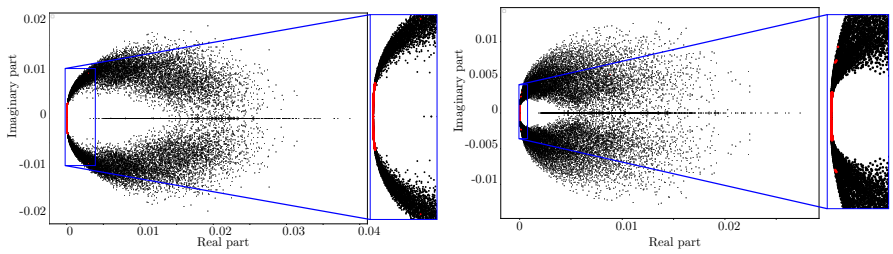

Fig. 4.3: Plot of the eigenvalues for the bathymetry of Hayes (2016) (left panel) and Ventura et al. (2012) (right panel). One can see the vertical symmetry of the plots corresponding to the fact that the complex eigenvalues always come with their complex conjugates. The resolved modes are coloured in red. They all correspond to eigenvalues whose real part is really small (it is at most $\mathcal{O}(10^{-8})$ s^{-1}).

the motion associated with the eigenmode. Indeed, eigenmode theory relies on the assumption that the solutions are periodic , i.e. $\mathbf{U}^p(x,y,t) = \mathrm{Re}\{\mathbf{X}^p(x,y)e^{j\omega t}\}$ where $j = \sqrt{-1}$, ω is the imaginary part of the eigenvalues and $\mathbf{X}^p(x,y) = \mathbf{X}^p_r(x,y) + j\mathbf{X}^p_i(x,y)$ are the eigenvectors – $\mathbf{X}_r$ and $\mathbf{X}_i$ respectively denoting the real and imaginary parts of the eigenvectors. For complex eigenvectors, the solution can be rewritten as

$$\mathbf{U}^p(x,y,t) = \mathrm{Re}\left\{\left[\mathbf{X}^p_r(x,y) + j\mathbf{X}^p_i(x,y)\right]\left[\cos(\omega t) + j\sin(\omega t)\right]\right\} \tag{4.7}$$

$$\Leftrightarrow \mathbf{U}^p(x,y,t) = \mathrm{Re}\left\{\left[\mathbf{X}^p_r(x,y)\cos(\omega t) - \mathbf{X}^p_i(x,y)\sin(\omega t)\right]\right. \tag{4.8}$$
$$\left. + j\left[\mathbf{X}^p_i(x,y)\cos(\omega t) + \mathbf{X}^p_r(x,y)\sin(\omega t)\right]\right\}$$

One can see that both the real and imaginary parts of the eigenvectors can contribute to the motion but there is a phase lag of $\frac{\pi}{2}$ between them.

The main drawback of the method used herein is that one mode is associated with each degree of freedom of the discrete equations, which results in an excessively large number of modes. Hence, both resolved and unresolved modes are obtained. The latter shorter

normal modes have a wavelength that is too short to be well represented on the mesh (i.e. the mesh resolution is not significantly smaller than the wavelength) or represent numerical noise. These modes have to be distinguished *a posteriori* from the resolved modes and are disregarded.

4.3 Astronomical forcings

In this section, the astronomical forcings that could resonantly force Titan liquid bodies are listed. Tokano (2010) and Vincent et al. (2016) studied the tidal motion induced by Titan's obliquity and orbital eccentricity. Other components of the tidally induced motion of the surface lakes and seas such as those induced by the Sun, planets of the solar system and Saturn's moons were neglected because they are much weaker (Sagan and Dermott, 1982; Tokano, 2010). Nevertheless, the forcings associated with these celestial bodies could, despite their small magnitude, excite a normal mode, resulting in a seiche through resonant amplification. Such phenomenon could generate a much larger liquid motion than the diurnal tidal motion. The most important of those tidal forcings arise through periodic perturbations in Titan's orbit induced by the other moons of Saturn and celestial bodies of the solar system, resulting in a variation of Titan's gravitational force acting on the surface lakes and seas. Such variations were studied by, among others, Vienne and Duriez (1991, 1992, 1995), who took into account perturbations induced by the Sun and by the other satellites of Saturn. The short-period variations predicted in these articles are listed in Table 4.1. Another way to detect a short period variation of the forcing acting on Titan is to study its position as a function of time, which is available in the HORIZONS Web-Interface (`https://ssd.jpl.nasa.gov/horizons.cgi`). We took into account two reference points while studying the position of Titan: Saturn and the solar system barycenter. In both cases, we study the evolution of the position with three different time steps: 1 day,

Table 4.1: Short period terms inducing perturbations of Titan orbital parameters larger than 10 km (a is the semi major axis, λ is the mean longitude, and $z = e\exp(i\overline{\omega})$ (where e is the eccentricity and $\overline{\omega}$ is the periapsis longitude of Titan) represents the eccentricity and pericentre of Titan) due to the Sun and other satellites of Saturn found in Vienne and Duriez (1991, 1992, 1995). The amplitude of the associated perturbations (amplitude smaller than 20 km are not specified) are shown in the third column and the mean depths required to develop a fundamental slosh are displayed in the fourth column.

Orbital parameter	Period (in days)	Amplitude [km]	Depth [m]
a	6.303	20.5	0.505
a	3.304		1.838
λ	6.303		0.505
z	15.945	81.7	0.0789
z	4.518		0.983

1 hour, and 1 min. Focusing on the days/months before the first ISS observation (6^{th} of June 2005), we do not detect any other periodic variations than those listed in Vienne and Duriez (1991, 1992, 1995). According to Hussmann et al. (2010), a resonance between Titan and Hyperion, which is not mentioned in Vienne and Duriez (1991, 1992, 1995)'s lists, can also be observed. This resonance has a period of 640 days and a libration amplitude of 36°.

4.4 Normal modes

A fundamental slosh is unlikely to develop as its period is much smaller than the periods corresponding to the astronomical forcings listed in Table 4.1. Indeed, the latter have time scales of days while Merian's formula (Merian, 1828) results in periods of 20.5678 hours for the bathymetry of Hayes (2016) (whose mean depth is about 27.33 m) and 34.56 hours for that of Ventura et al. (2012)

(whose mean depth is about 9.68 m). Inverting Merian's formula to get the depth needed to create a wave slow enough to correspond to the periods of the astronomical forcings results in mean depths of less than two meters (see Table 4.1), which does not correspond to the observations. Consequently, for a reasonable range of depths, none of the astronomical forcings' period corresponds to that of the fundamental slosh. Celestial bodies can also modify the length-of-day and polar motion of Titan due to the gravitational torque exerted on Titan and to the dynamic variations in the atmosphere (Coyette et al., 2018). Those rotation variations also influence the tides but are too small to affect significantly the tidal motion in Ontario Lacus. The resulting main atmospheric forcing is at annual, semi-anual, ter-annual and 1/4 annual periods, which is too long to resonantly excite a barotropic mode. Therefore, the rotation variations are not taken into account. Astronomical forcings could induce resonance phenomena other than sloshing. In order to study such phenomena, the eigenmodes of Ontario Lacus are computed following the method of Bernard et al. (2008), as described in Section 4.2. As one can see in Figs. 4.4 and 4.5, the periods of the astronomical forcings (in red) do not match with any of the lake natural frequencies. Nevertheless, as there are uncertainties about the bathymetries and as the latter have an impact on the period and shape of the normal modes, we also study the normal modes whose natural period is close (i.e. the difference is less than 2 hours) to that of the forcings but they correspond to unresolved modes. Consequently, astronomical forcing is not expected to excite significant barotropic normal modes in Ontario Lacus.

Various types of normal modes can develop in a lake such as Ontario Lacus depending on the relative importance of gravity, Titan's rotation speed, the depth of fluid column and its gradient. The variation of the Coriolis parameter is negligible over the lake, which is why Rossby waves are unlikely to be observed. The size of the lake being much smaller than the external Rossby radius of deformation ($R = \frac{\sqrt{gh}}{|f|} \sim 700$ km), most inertia-gravity modes

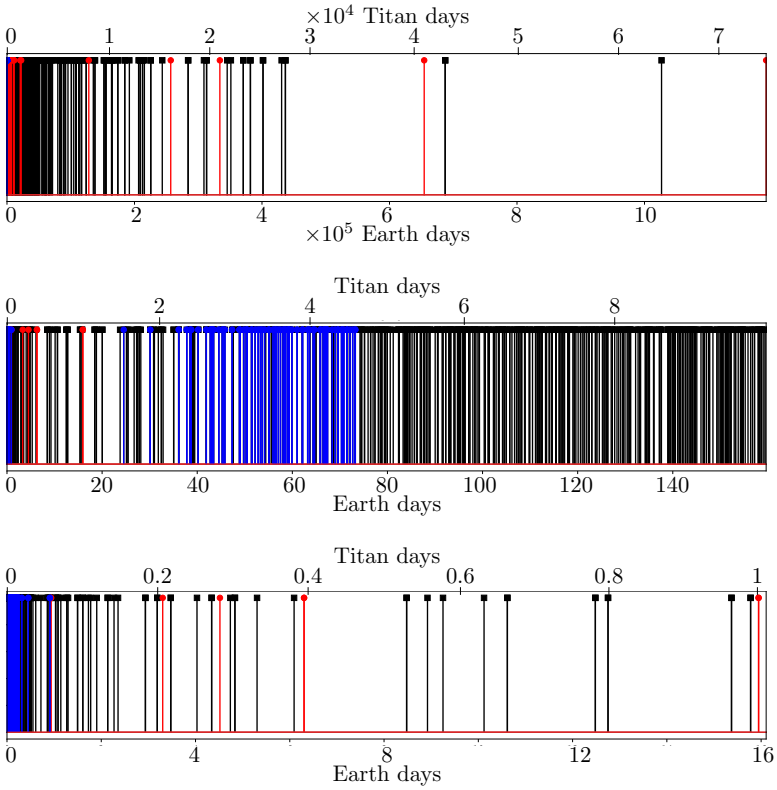

Fig. 4.4: Periods of the normal modes of Ontario Lacus with the bathymetry of Hayes (2016) with focus from 0 to 10 Titan days and from 0 to 1 Titan day. The red and blue dots respectively correspond to the periods of the astronomical forcings and the natural periods of the modes associated with large scale phenomena. The lower axis and the upper one of each subplot are graduated in Earth days and Titan days, respectively.

are little influenced by Titan's rotation. Nevertheless, some of the present numerical results point to the existence of normal modes bearing some similarities with Kelvin waves or topographic Rossby waves. These modes are localised along the shores of the lake, some of which can be associated with the areas where local variations in

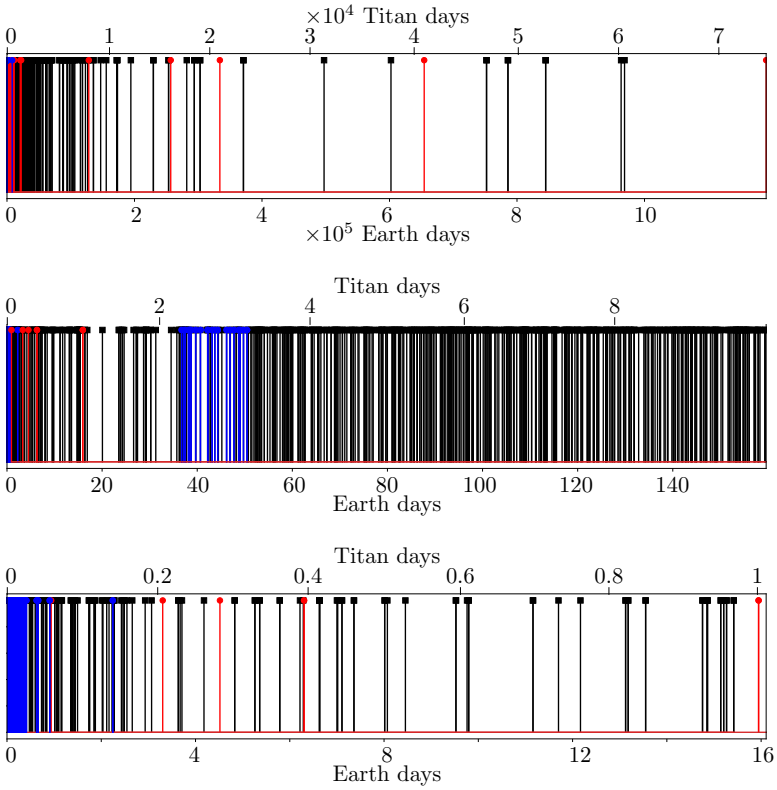

Fig. 4.5: Periods of the normal modes of Ontario Lacus with the bathymetry of Ventura et al. (2012) with focus from 0 to 10 Titan days and from 0 to 1 Titan day. The red and blue dots respectively correspond to the periods of the astronomical forcings and the natural periods of the modes associated with large scale phenomena. The lower axis and the upper one of each subplot are graduated in Earth days and Titan days, respectively.

the bathymetry are observed. Pure gravity waves are also obtained, mainly as sloshing modes. Some of them correspond to small oscillations in coves and bays while others correspond to the largest-scale oscillations calculated by the present method. For instance, a normal mode appearing as a fundamental slosh is observed for

both bathymetries (see the normal modes shown in Figs. 4.6 (d) and 4.7 (d)). The natural periods of these modes respectively are 21.829 hours and 53.876 hours, which is close to the period predicted by Merian's formula (Merian, 1828) (i.e. 20.5678 hours and 34.56 hours using the mean depth of the lake).

We only pay attention to the normal modes whose associated elevation variations covers a significant portion of the lake. For both bathymetries, some of the normal modes (both their real and imaginary parts as explained in Section 4.2) correspond to large scale variation of the lake surface elevation (see Figs. 4.6, 4.7). They are associated with limited dissipation, as shown by the smallness of the real parts of the eigenvalues: the maximum is $\mathcal{O}(10^{-8})$ s^{-1} (see the eigenvalues associated with the modes in Figs. 4.6, 4.7). The periods of the normal modes shown in Figs. 4.6, 4.7 are respectively 5.397, 7.555, 10.839 and 21.829 hours for the bathymetry of Hayes (2016) (Fig. 4.6) and 15.079, 15.904, 21.759, and 53.876 hours for that of Ventura et al. (2012) (Fig. 4.7). Such periods are small with respect to a Titan day – which is about 382.74 hours. Consequently, only phenomena characterised by a short time scale, such as atmospheric events, would be able to resonantly excite them. All of these modes correspond to sloshing modes and their natural period is close to the approximation given by Merian's formula (Merian, 1828).

4.5 Wind induced seiche

Although the amplitude of the motion associated with each normal mode cannot be theoretically predicted, it can be numerically modelled. Therefore, we conduct simulations under arbitrary wind conditions which could resonantly force the normal modes shown in Figs. 4.6(d) and 4.7(d). This allows estimating the order of magnitude of the liquid motion associated to these normal modes. To this end, we run simulations using SLIM2D. The initial conditions correspond to the tidal motion at perikron (see Chapter 3). The

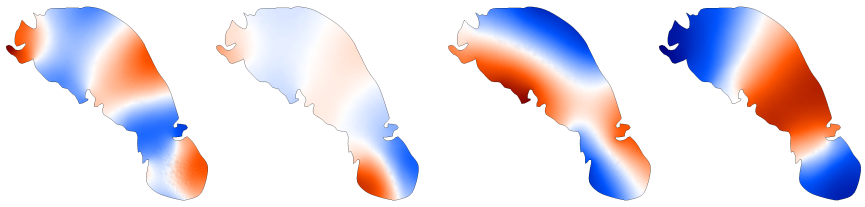

(a.1) Real part (a.2) Imaginary part (c.1) Real part (c.2) Imaginary part

(a) $\omega = 2.37\ 10^{-8} + 3.23\ 10^{-4} j\ \mathrm{s}^{-1}$ (c) $\omega = 3.55\ 10^{-9} + 1.61\ 10^{-4} j\ \mathrm{s}^{-1}$

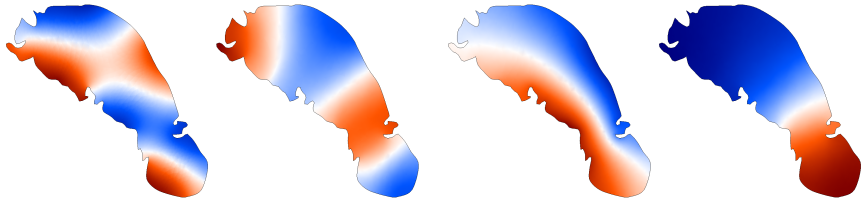

(b.1) Real part (b.2) Imaginary part (d.1) Real part (d.2) Imaginary part

(b) $\omega = 7.65\ 10^{-9} + 2.31\ 10^{-4} j\ \mathrm{s}^{-1}$ (d) $\omega = 6.52\ 10^{-10} + 8\ 10^{-5} j\ \mathrm{s}^{-1}$

Fig. 4.6: Real and imaginary parts of the lake surface elevation normal modes predicted with the bathymetry of Hayes (2016). The red areas correspond to lake surface elevation above the reference level while the blue areas correspond to a lake surface elevation below the reference level. By definition, the eigenvectors are defined up to a multiplying constant. Consequently, their amplitude has no meaning while the spatial patterns do. The vectors are chosen so that the square of their Euclidean norm is 1. The (small) real part of the eigenvalues is due to the numerical dissipation of the numerical scheme used.

surface stress corresponds to an unidirectional wind whose orientation remains constant over the time and space and whose period coincides with the natural period of the mode studied. The wind velocity, $\mathbf{u}_{\text{wind}}$, is given by

$$\mathbf{u}_{\text{wind}} = \begin{pmatrix} W \cos\theta_w |\sin(0.5\omega t)| \\ W \sin\theta_w |\sin(0.5\omega t)| \end{pmatrix} \tag{4.9}$$

where W is the wind speed, θ_w is the wind orientation with respect to the East, and ω is the angular frequency of the normal mode. The wind does not behave as a sinusoid but as the absolute

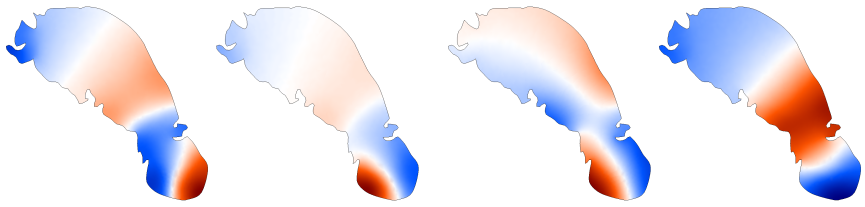

(a.1) Real part (a.2) Imaginary part (c.1) Real part (c.2) Imaginary part

(a) $\omega = 9.27\ 10^{-9} + 1.16\ 10^{-4} j\ \mathrm{s}^{-1}$ (c) $\omega = 2.53\ 10^{-9} + 8.02\ 10^{-5} j\ \mathrm{s}^{-1}$

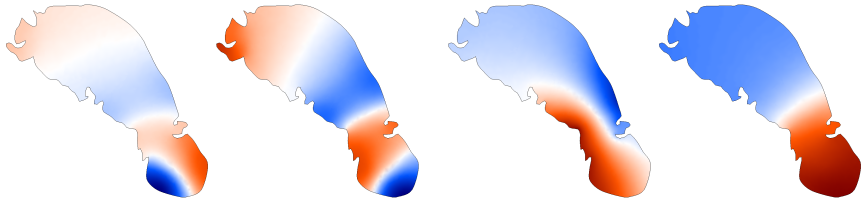

(b.1) Real part (b.2) Imaginary part (d.1) Real part (d.2) Imaginary part

(b) $\omega = 6.28\ 10^{-9} + 1.1\ 10^{-4} j\ \mathrm{s}^{-1}$ (d) $\omega = 2.92\ 10^{-10} + 3.24\ 10^{-5} j\ \mathrm{s}^{-1}$

Fig. 4.7: Real and imaginary parts of the lake surface elevation normal modes predicted with the bathymetry of Ventura et al. (2012). The red areas correspond to lake surface elevation above the reference level while the blue areas correspond to a lake surface elevation below the reference level. By definition, the eigenvectors are defined up to a multiplying constant. Consequently, their amplitude has no meaning while the spatial patterns do. The vectors are chosen so that the square of their Euclidean norm is 1. The (small) real part of the eigenvalues is due to the numerical dissipation of the numerical scheme used.

value of a sinusoid whose period is twice the natural period (see Figs. 4.8(b), 4.9(b) for $\theta_w = 220°$ and $\theta_w = 305°$, respectively). The simulations last 5 times the natural period of the normal mode studied. A sensitivity analysis with respect to the wind magnitude and orientation is conducted. We study the impact of these parameters for W and θ_w ranging from 1 m/s to 7 m/s (by increments of 1 m/s) and from 0° to 355° (by increments of 5°), respectively.

Figs. 4.8 and 4.9 show the elevation field predicted for a wind blowing along the main axis of the lake and almost perpendicularly to this axis (i.e. $\theta_w = 305°$ and $\theta_w = 220°$, respectively). These ori-

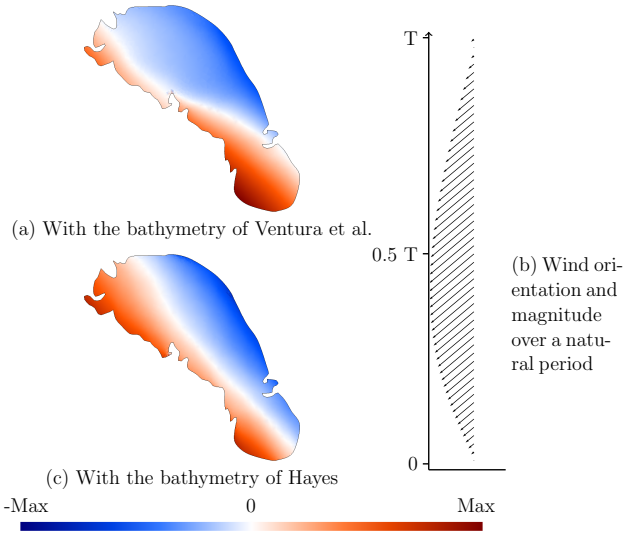

Fig. 4.8: Lake surface elevation of Ontario Lacus for time varying wind speed with a constant orientation of 220° with respect to the east for the bathymetry of Ventura et al. (2012) (a) and Hayes (2016) (c). The wind orientation and magnitude are shown in Panel (b). The amplitude of the lake surface elevation depends on the wind magnitude while its aspect (i.e. the areas where it is negative (in blue) and positive (in red)) remains the same.

entations are selected because they correspond to the largest lake surface elevation that can be reached ($\theta_w = 305°$) or to the largest positive lake surface elevation area along the south-western shore ($\theta_w = 220°$). For a wind orientation of 220° with respect to the east, the lake surface elevation is positive over the western shore of Ontario Lacus and negative along its eastern shore for both bathymetry (see Figs. 4.8(a) and (c)), which is similar to the shape of the real part of the associated normal modes (see Figs. 4.6(d.1), 4.7(d.1)). The maximum lake surface elevation varies with the wind speed and the bottom friction but it remains smaller than 30 cm. For a wind orientation of 305° with respect to the east, the lake surface elevation is positive in the southern part of Ontario Lacus and negative in

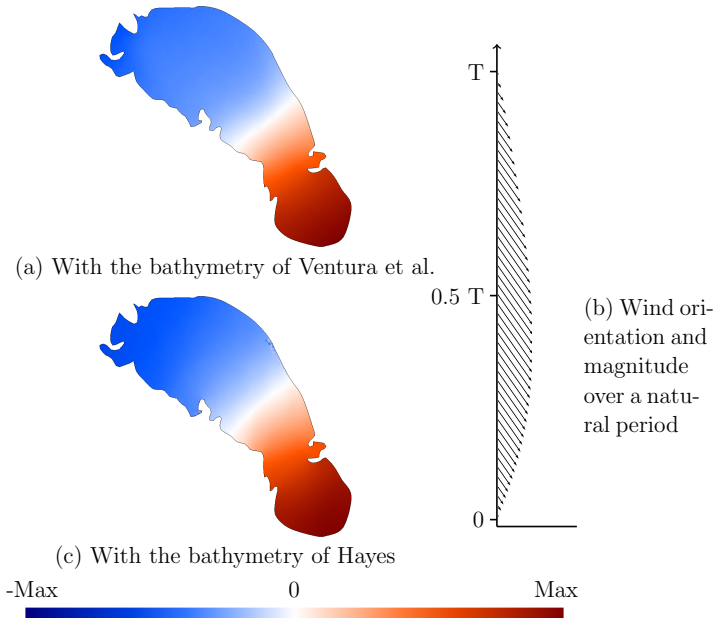

Fig. 4.9: Lake surface elevation of Ontario Lacus for time varying wind speed with a constant orientation of 305° with respect to the east for the bathymetry of Ventura et al. (2012) (a) and Hayes (2016) (c). The wind orientation and magnitude are shown in Panel (b). The amplitude of the lake surface elevation relies on the wind magnitude while its aspect (i.e. the areas where it is negative (in blue) and positive (in red)) remains the same.

the north for both bathymetry (see Figs. 4.9(a) and (c)), although the areas where the lake surface elevation is positive/negative and the maximum lake surface elevation slightly differ. The spatial patterns predicted are similar to the shape of the normal modes' imaginary part (see Figs. 4.6(d.2), 4.7(d.2)). The maximum lake surface elevation significantly varies with the wind speed and the bottom friction (see Fig. 4.10). For instance, the surface lake elevation at (74.43°S, 181.63°E), with the bathymetry of Hayes (2016), can reach up to 4 m after 5 natural periods for $W = 7$ m/s and a small bottom friction coefficient (see Fig. 4.10 (b)). Although

such a wind speed is likely to be observed on Earth, this corresponds to a stormy event on Titan. A more casual wind speed (i.e., $W = 1$ m/s) generates smaller lake surface variations (in terms of amplitude). For instance, Fig. 4.10 (a) shows that the lake surface elevation at (74.43°S, 181.63°E), with the bathymetry of Ventura et al. (2012), varies by less than 0.3 m. The sea surface elevation oscillates at the natural period of the mode but its minimum decreases during the first three periods and then increases, which is due to the tidal motion. The sea surface elevation predicted should not be viewed as an upper bound as stronger winds could occur or other modes could be excited in parallel with those studied.

4.6 Discussion

Due to the large discrepancy between the astronomical forcing periods and the natural periods of the lake, these forcings can be ruled out as a potential source of excitation of the normal modes. Indeed, although the natural periods critically depend on the bathymetry – as is shown by the variation between the two bathymetry maps implemented –, the modifications needed to get an overlap between the natural periods and those of the astronomical forcings are too large. For instance, the depth required to generate a fundamental slosh is not consistent with the observations (a simple approximation predicts a depth of less than 2 m, which is inconsistent with Cassini radar images). Indirect rocking by the tidal response of the global subsurface ocean would rock the lake at the same frequency (i.e. the tidal frequency) and so, is unlikely to generate resonant amplification in the lake. A resonant subsurface ocean could rock at different frequencies than the tidal frequency and hence resonantly force the lake but the liquid motion in the ocean widely varies with the parameter assumptions and there is no observation of such a phenomenon. The inability of astronomical forcings to resonantly force a normal mode is given support by the observations of Cassini. Although shoreline variations were observed, they

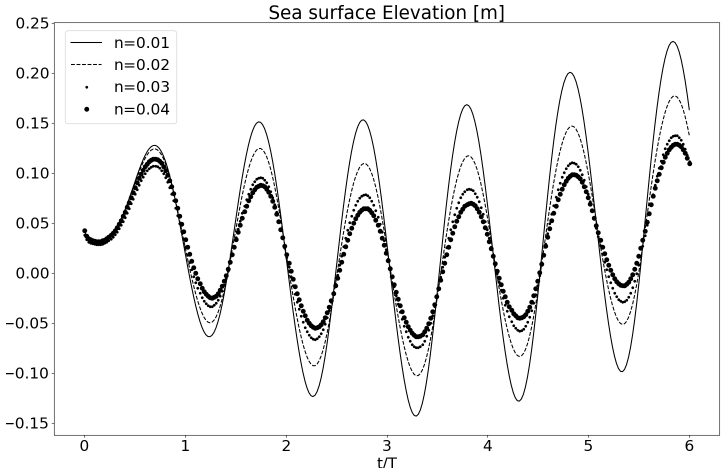

(a) $\mathbf{u}_{wind,max} = 1$ m/s, bathymetry of Ventura et al.

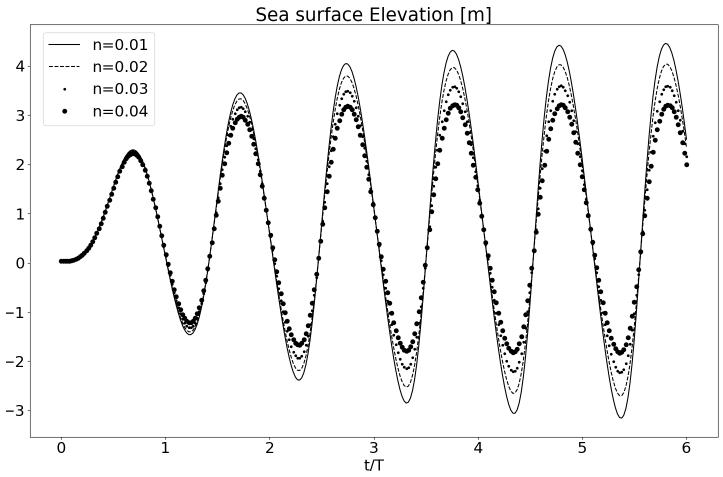

(b) $\mathbf{u}_{wind,max} = 7$ m/s, bathymetry of Hayes et al.

Fig. 4.10: Variation of the lake surface elevation at (74.43°S, 181.63°E) for a wind orientation of 305°. As expected the lake surface elevation increases with the wind speed while increasing the bottom friction results in smaller surface elevation. The decreasing minimum lake surface elevation in the southern part of the lake for a maximum wind speed of 1 m/s is due to the fact that the tidal motion is significant with respect to the wind induced liquid motion.

are claimed to be due to methane evaporation and/or infiltration. Indeed, the 2005 shoreline lies beyond the 2009 coastline except in the northwest corner but this could not compensate the negative sea surface elevation elsewhere in the lake. Furthermore, sloshing conserves volume and the slope in the fluid induced by an almost uniform retreat should be detectable by SAR.

Atmospheric forcing such as the wind could also resonantly force the normal modes of the lake. Annual and diurnal wind variations predicted by the global circulation models (GCM) are slow, at most 2 m/s, but, thanks to the density difference between Titan's atmosphere and the lake liquid, they can generate significant liquid motion in the northern seas (see Tokano and Lorenz, 2015). However, they are unlikely to resonantly force the lake due to their diurnal period. Shorter period travelling waves taking place in Titan's atmosphere are more likely to excite a normal mode in the lake. Such waves are predicted by, among others, Lebonnois et al. (2012). The frequencies of the dominant groups of waves are 5-7 cycles/Titan day and 10-12 cycles/Titan day (Lebonnois et al., 2012). The magnitude of the zonal and meridional wind associated with the travelling waves strongly varies with the altitude: from less than 1 m/s in the lower troposphere to more than 10 m/s in the stratosphere (see Figs. 15 and 16 of Lebonnois et al. (2012)). Hence, the magnitude of the forcing acting on the lake, which is a function of the wind velocity 10 m above the lake surface, should be very small[9] despite the significant density difference between the atmosphere and the lake. If the resulting forcing is strong enough to excite the normal modes, it would result in localised lake surface elevation variations near the shore. The amplitude of such variations, although presumably small, could be significant as compared with the tidal range. Mitchell et al. (2011) also predicted eastward propagating equatorially trapped Kelvin waves whose period and phase speed at the equator are about 8 days and 12 m/s, respectively,

[9]According to Lebonnois et al. (2012), the wind velocity associated with theses waves is less than 0.4 m/s near the surface (see Figs. 15 and 16 (a) of Lebonnois et al. (2012)).

and a slow westward propagating mode whose period and phase speed are about 100 days and 1 m/s, respectively. Those wave periods are much larger than the lake's natural periods. Furthermore, the lake is located at high latitudes, far from the equator. Hence, interactions between these waves and Ontario Lacus are unlikely. One-time events such as storms could result in stronger winds more likely to generate large amplitude liquid motion. Using a mesoscale model, Charnay et al. (2015) predicted that methane storms are accompanied by eastward gust front above the surface. The wind speed in these fronts can reach up to 10 m/s, which would be more than enough to resonantly force the normal modes of Ontario Lacus, depending on the gusts' spatial and temporal patterns. Such storms are characterised by the presence of convective clouds. The convection cells associated with such clouds are reported as able to generate significant seiches on Earth (see, for instance, the seiche in Rotterdam harbour described by De Jong and Battjes, 2004). Rodriguez et al. (2013) and Turtle et al. (2018) listed the cloud observations on Titan for over 13 years. Observations prior to the arrival of Cassini were made by means of Earth-based instruments until Cassini's VIMS and ISS could be used. Outbursts of large clouds at Titan's southern pole were observed almost continuously by Earth-based campaigns from December 2001 to December 2005 (Rodriguez et al., 2013). Afterwards, cloud activity in the south pole began to decline and the stormy activity disappeared after 2008 (Turtle et al., 2018). Consequently, during the period of large cloud outbursts, strong winds able to resonantly force the lake could have occurred in the vicinity of Ontario Lacus. Unfortunately, the observations of Ontario Lacus do not show lake surface elevation corresponding to the normal modes.

The lake bathymetry does influence the period and shape of the normal modes. The significant lake level change observed between 2005 and 2009 by Hayes et al. (2011) and Turtle et al. (2011) would, for instance, result in variations of the normal modes' shape and period. Hayes et al. (2011) predicted a lake level change of about 4 m over a period of 4 years. While studying the impact of such a

variation on all the normal modes would be complicated due to the absence of a bathymetry and coastline corresponding to the 2005 data, it is interesting to assess whether its impact on the normal modes is significant. To this end, Merian's formula (Merian, 1828) is resorted to to compute the period of a fundamental slosh within the lake for a bathymetry increased by 4 m (without modifying the coastline). It results in decreasing the fundamental slosh's period by 1.36 hours and 5.49 hours for Hayes (2016)'s and Ventura et al. (2012)'s bathymetries, respectively. The latter being more shallow, the natural periods are more sensitive to the lake level variation. Although significant, these differences are smaller than those observed between the normal periods for both bathymetries. Indeed, while the shape of the normal modes remains similar, the periods of similar modes can be significantly different, which can be explained by the significant depth variations (up to 38 m) between the bathymetries. The shape of a normal mode can therefore be considered rather insensitive to the bathymetry – but they can change with the shoreline. Consequently, if the lake is filled with methane precipitation or if another strong evaporation period took place, the shape and period of the normal modes would change.

The normal modes of Ontario Lacus, if excited to a sufficiently large amplitude, could be observed by future missions. Among the proposals discussed in the literature, some are better suited for this purpose than others. An orbiter such as Oceanus (see Sotin et al., 2017), could detect modes whose period is at least twice the sampling period, in accordance with the Nyquist-Shannon sampling theorem. The main limitation would be related to the amplitude that can be measured by a spacecraft instrument. The amplitude of the liquid motion associated to the normal modes is expected to be of the order of 10^{-1} m under astronomic forcings and no stormy wind conditions. Stormy wind conditions would increase the amplitude but the cloud outbursts associated with such an event could prevent observations, depending on the instrument used. A lake probe with an orbiter (such as the E2T, see Mitri et al., 2014a), a drifted capsule (similar to the TiME proposed for Ligeia Mare,

see Lorenz et al., 2012), a lander (such as the Dragonfly rotorcraft Lorenz et al., 2018), or a submarine (such as the Titan sub proposed for Kraken Mare, see Hartwig et al., 2016) would be better suited to observe normal modes without discrimination as to their period. Observations from a probe would be conditioned by its landing site and its ability to observe lake surface elevation. If it sinks in the lake, it could act as a tidal gauge and would be able to detect all the normal modes excited as well as the tides at aspecific location. On Earth, tidal gauges are accurate up to 10^{-3} m. Acoustic/radar tidal gauges rely on wave propagation within the liquid while the mean density and the atmospheric pressure are required to use a pressure tidal gauge. If the probe lands near the shores, it could use a laser rangefinder but it would have to use a wavelength to which the liquid is opaque. A lander would have the same advantages but would be able to study several areas. A floating platform or a surfaced submarine could also perform similar measurements and would offer the additional benefit of being able to conduct measurements at various locations. Using a sonar or a laser rangefinder would allow accurately measuring the lake surface elevation as a function of time. Such platforms would still be better suited if they were motorised as their localization and their spatial evolution could be forced instead of being driven by the fluid flow or wind stress.

4.7 Conclusion

Ontario Lacus has been the focus of various studies since its discovery. Although many aspects of the lake were studied, the normal modes were only briefly investigated by Tokano (2010). In this paper, we numerically predict the normal modes of the lake for the two bathymetries available in the literature. We use the method of Bernard et al. (2008) to compute the modes of the lake as this method allows us to use unstructured meshes to discretize the domain; hence, the spatial resolution can be increased to capture the coastline while keeping a reasonable computer cost.

The frequency of the tidal forces is too small to excite the (barotropic) normal modes, and a slosh between the northern and southern shores would require a fast propagation speed corresponding to a mean lake depth not met by the observations. Such low-frequency forcings could more easily resonantly force the baroclinic normal modes, but investigating this phenomenon requires unavailable information about the lake stratification. On the other hand, wind forcing could likely coincide with the resonant frequencies but it would require specific events such as a storm to generate wind strong enough to excite the normal modes significantly. The large scale normal modes predicted could be observed by an orbiter if they were excited, but it was not the case during the Cassini observations.

CHAPTER 5

Modelling of Titan's northern seas tides

This chapter reproduces the following article[1]:

D. Vincent, Ö. Karatekin, J. Lambrechts, R. D. Lorenz, V. Dehant, É. Deleersnijder, 2018, A numerical study of tides in Titan's northern seas, Kraken and Ligeia Maria. *Icarus*, 310: 105-126. doi: 10.1016/j.icarus.2017.12.018

Abstract

The tidal response of Titan's two largest northern seas, Ligeia Mare and Kraken Mare, is studied by means of a two-dimensional, depth-averaged, shallow water model, SLIM (www.climate.be/slim). Kraken Mare is formed of two

[1]Only minor modifications were made.

basins, the northern one being assumed to be linked by a single strait, Trevize Fretum, to Ligeia Mare. The tidal motions tend to be independent of each other in each basin (i.e., Ligeia Mare, Kraken 1 and Kraken 2) which results in sharp transitions in the straits. Our results are overall rather similar to those of Tokano et al. (2014), suggesting that a 2D model such as SLIM is adequate for modelling Titan's tides and, since it is (presumably) less computationally demanding, may be better for sensitivity studies. For instance, the maximum tidal range in Kraken and Ligeia Maria respectively are 0.29 m and 0.14 m, which is within the range predicted by Lorenz et al. (2014) although smaller by 0.07 m and larger by 0.04 m than the estimates of Tokano et al. (2014) (but it occurs at the same location). The tidal currents are faster (by about one order of magnitude) in the straits linking those Maria than in the basins themselves (with a maximum of 0.36 m/s in the strait linking Kraken 1 and Kraken 2, Seldon Fretum). A decomposition of the tidal history into different harmonic components is carried out. Except in specific areas such as the straits and the amphidromic point(s), the main tidal component has a period of 1 Titan Day. We also briefly study the eigenmodes of the northern seas whose period is close to the tidal period. Some eigenmodes have significant magnitudes (with respect to the magnitude of the modes elsewhere in the seas) in small bay(s) or near the islands of Kraken 2 and Ligeia Mare. But the contribution of these modes to the overall tidal motion is small.

A sensitivity analysis to poorly constrained parameters (bottom friction coefficient, depth of Trevize Fretum and attenuation factor – the latter is briefly discussed with respect to the values of the Love numbers found in the literature) is also conducted. The model parameters are seen to have a significant impact on the liquid exchanges between the basins and, consequently, on the tidal range and phase, fluid velocity and location of amphidromic point(s).

5.1 Introduction

Besides Earth, Titan is the only celestial body of the solar system on which liquid-filled surface lakes and seas were detected. Liquid hydrocarbon lakes and seas have been assumed to be present on Titan's surface since *Voyager 1* established that the surface conditions of this icy moon are close to the triple point of methane (Hanel et al., 1981; Samuelson et al., 1981). The Cassini spacecraft, which had been gazing at the Saturnian system from 2004 to 2017, observed a methane cycle similar to the hydrological cycle on Earth (Atreya et al., 2006). It also detected possible surface lakes in Titan's southern hemisphere in 2004 (only some years later confirmed to be liquid) by means of its ISS (McEwen et al., 2005), and surface lakes and seas[2] in the northern hemisphere in 2006 by means of its radar (Stofan et al., 2007). The distribution of these surface lakes and seas is asymmetrical with respect to Titan's equator (Aharonson et al., 2009): there are many more lakes and seas in the northern hemisphere, where they are larger and deeper (Hayes et al., 2008, 2018). The surface lakes and seas are not the only liquid bodies of Titan: a global subsurface ocean was also inferred from Cassini measurements. Lunine and Stevenson (1987) were the first to predict the presence of a global subsurface ocean on Titan, although it had been discussed by Consolmagno and Lewis (1978). Since then, this assumption has been supported by several observations and measurements such as Titan's obliquity, its gravity field and its topography (Rappaport et al., 2008; Nimmo and Bills, 2010; Baland et al., 2011, 2014; Hemingway et al., 2013; Lefevre et al., 2014) and has been widely studied (e.g. Sohl et al., 1995, 2003, 2014; Beuthe, 2015b). The global subsurface ocean results in significant deformation of the ice shell and, hence, of the lakes and seas bottom. Such deformation reduces the tidal forcings to which surface liquids respond, since the ice crust itself partly follows the changing potential. This effect is modelled by an attenuation factor, γ_2, ap-

[2]The distinction between lake (Lacus) and sea (Mare) is based solely on the size.

plied to the tidal forcing (Lorenz et al., 2014; Tokano et al., 2014; Beuthe, 2015b). This factor depends on the internal structure of Titan and is particularly sensitive to the thickness, the rigidity and the rheological properties of the ice shell (e.g. Sohl et al., 2003; Lorenz et al., 2014; Tokano et al., 2014). As a consequence, γ_2 should be considered as a free parameter (Lorenz et al., 2014).

In this study, we focus on two of the northern seas, Kraken Mare and Ligeia Mare. The former is the largest sea identified on Titan, with an area of at least $400,000$ km^2. It is centred at (68°N, 50°E) (Tokano, 2010) and it stretches from 55°N to 82°N (Lorenz et al., 2014). It is formed of two basins, Kraken 1 (in the north) and Kraken 2, linked by a strait named Seldon Fretum (identified by "A" in Fig. 5.1) and a set of small channels (Lorenz et al., 2014). It is about 17 km wide and 40 km long (Lorenz et al., 2014) which is similar to the dimensions of the Gibraltar strait on Earth. Ligeia Mare is located north-east of Kraken Mare: it is centred at (79°N, 112°E). Its maximal dimensions are about 420 by 350 km (Stofan et al., 2012). Recently, those seas were found to be linked by a strait, namely Trevize Fretum (identified by "B" in Fig. 5.1) (Sotin et al., 2012). The Cassini radar altimeter also detected liquid filled canyons linked to Ligeia Mare in the northern and south-eastern regions of this sea (Poggiali et al., 2016) (identified by "C" and "D" in Fig. 5.1). Transient features called "Magic Islands" were observed in Kraken Mare and Ligeia Mare (Hofgartner et al., 2014, 2016). In Ligeia Mare, such phenomena were observed in regions centered at (78°N, 123°E) and (80°N, 111°E). They are best explained by ephemeral phenomena such as floating and/or suspended solids, bubbles, and waves while the diurnal phenomena, such as the tides, seem to be ruled out, the observations being all at nearly the same true anomaly (Hofgartner et al., 2016). In Kraken Mare, the phenomenon was observed at (73°N, 55°E). In this sea, the same explanations stand but the tides cannot be ruled out. We study the tides induced by Saturn in the above-mentioned Maria and we pay special attention to specific areas such as Seldon and Trevize Fretum, the aforementioned liquid filled canyons, and

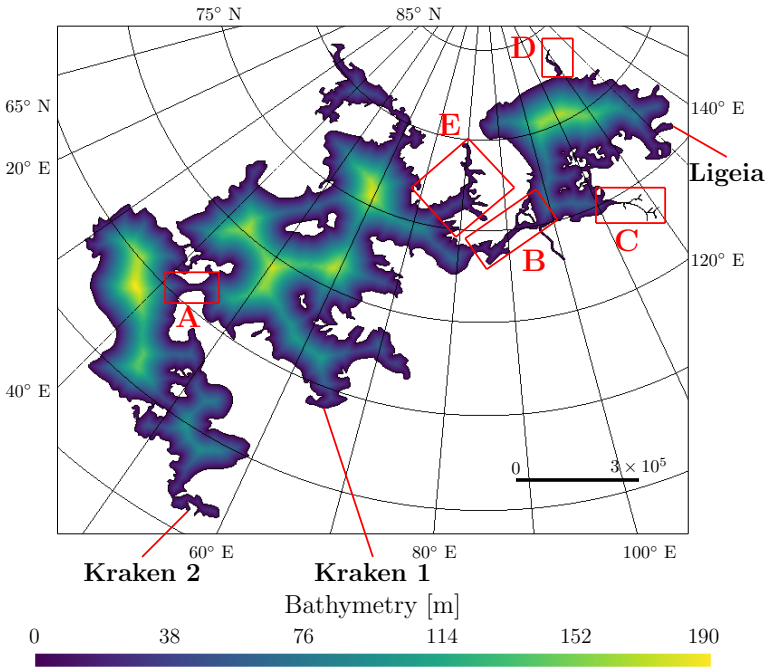

Fig. 5.1: Bathymetry map of Kraken and Ligeia Maria. The depth scales with the distance to the nearest shore, similarly to the bathymetry of Lorenz et al. (2014). The red letters refer respectively Seldon Fretum (A), Trevize Fretum (B), the canyons next to Vid flumina (C) and Xanthus Flumen (D), and Moray Sinus (E).

at the "Magic Islands" location.

Various studies were carried out about Titan's seas and lakes: bathymetry (e.g. Hayes et al., 2010; Ventura et al., 2012; Mastrogiuseppe et al., 2014; Lorenz et al., 2014; Hayes, 2016), liquid composition (e.g. Brown et al., 2008; Cordier et al., 2009; Glein and Shock, 2013; Tan et al., 2013, 2015; Luspay-Kuti et al., 2015), dissipation due to friction in Titan's lakes and seas (e.g. Sagan and Dermott, 1982; Dermott and Sagan, 1995; Sears, 1995; Lorenz et al., 2014), tidal response (Tokano, 2010; Tokano et al., 2014; Vincent et al., 2016), interactions with the atmosphere (Tokano and Lorenz,

2015, 2016), and phenomena such as the shoreline variations of Ontario Lacus (Turtle et al., 2011) and the transient features in the northern seas (Hofgartner et al., 2014, 2016). Among them, Tokano (2010); Lorenz et al. (2014); Tokano et al. (2014); Tokano and Lorenz (2015, 2016); Hofgartner et al. (2014, 2016) focused on the northern seas.

Tokano (2010) studied the tidal response of Kraken Mare using a 3D hydrostatic, baroclinic ocean circulation model based on a structured grid with a spatial resolution of 30 km. Due to the lack of information, he used a bathymetry scaling with the east-west distance from the closest shore (the maximum and minimum depth were respectively 500 m and 50 m) and the shoreline was not accurately represented (for instance, the connection with Ligeia Mare and the small channels near Seldon Fretum were ignored and Mayda Insula was considered to be an island). The impact of the ice shell deformation was not taken into account. According to his results, the tidal amplitude is minimum in the centre of the sea and increases with the distance to this point. He predicted a maximum tidal range (difference between high tide and low tide) of 4 m in the northern bay of Kraken 1 and he noticed that the tide rotates clockwise. The current is generally directed from places where the tide is low to places where the tide is high and its magnitude is maximum in Seldon Fretum (about 0.3 m/s) and offshore. Tokano (2010) took into account the seasonal effects through the solar heating: in winter, he predicted that the sea would be well mixed while it would be stratified in summer unless the evaporation cools down the sea surface. Lorenz et al. (2014) derived an analytical expression of the bathymetry and adapted Tokano (2010)'s results in order to take into account the surface deformation by multiplying the tidal amplitude by an attenuation factor γ_2. Tokano et al. (2014) improved the previous study of Tokano (2010): the bathymetry computed by Lorenz et al. (2014) was used, an attenuation factor $\gamma_2 = 0.1$ was implemented to represent the impact of the ice shell deformation and the spatial resolution was 5.2 km. Ligeia Mare and Kraken Mare were linked and the small channels next to Seldon

Fretum were considered as wide straits separated by islands (see Fig. 1 in Tokano et al. (2014)). The largest surface displacements predicted by the model were located in the south-eastern part of Kraken 2 and northern part of Kraken 1 with a maximum tidal range of 0.37 m. The crucial role of the (unknown) depth of Seldon Fretum was pointed out by Lorenz et al. (2014) as well as Tokano et al. (2014). According to the latter, changing the depth of Seldon Fretum from 6 m to 100 m completely changes the character of Kraken Mare tides. For instance, it results in a phase lag of 90° and an increase of the maximum tidal range of 17 cm.

In this work, we study the tidal response of Titan's northern seas by means of the state-of-the-art model SLIM, (`www.climate.be/slim`). It has already been used to predict the tidal response of a Titan lake, Ontario Lacus (see Vincent et al., 2016). SLIM solves the 2D depth-averaged shallow water equations on an unstructured grid (see Section 5.2.3), which allows an accurate representation of the shoreline and a higher resolution in the straits without the computational overhead of a regular but high resolution grid. We also focus on the tidally induced liquid exchanges between the basins. Various parameters are poorly constrained, notably the roughness of the bottom and the depth of the straits linking the basins of the Maria. Their impact(s) and that of Titan's surface deformation are quantified through a sensitivity analysis. We also briefly study the impact of the bathymetry by implementing a bathymetry similar to that displayed in Fig. 9a of Hayes (2016) in Ligeia Mare and by varying the slope of the bottom in Kraken Mare. Finally, the impact of the shape of the shoreline on the tidal response is studied by comparing our results with those obtained previously by means of other models. For the reference case, the bathymetry implemented scales with the distance to the shore (see Section 5.2.2) so that the maximum depth in Ligeia Mare is 170 m and the attenuation factor is set to $\gamma_2 = 0.1$, similarly to Tokano et al. (2014)).

The goal of this study is to discuss the tidal response of Kraken and Ligeia Maria. This could also be helpful in enhancing our understanding of observed transient events and for planning future

missions. Furthermore, being able to accurately predict the tidal response of the northern seas could allow assessing some parameters from future data. For instance, if we could measure accurately the sea surface elevation, we could infer the value of γ_2, which would give further insight into Titan's internal structure.

This chapter is organised as follows. Section 5.2 briefly describes the numerical model used, the forcings as well as the mesh and bathymetry implemented. In Section 5.3, the tidal response of the seas is studied, with a focus on the liquid exchanges between the basins, the volumetric flow rate through the main straits, the canyons of Ligeia Mare, Moray Sinus and the "Magic Islands" phenomenon. A sensitivity analysis to the attenuation factor, the depth of Trevize Fretum, the bathymetry scaling factor, the artificial bathymetry, and Manning's coefficient is conducted in Section 5.4. The results and implications for future missions are respectively discussed in Section 5.5 and 5.6. Conclusions are drawn in Section 5.7.

5.2 Method

The model is briefly introduced in section 5.2.3 (for further details, see Vincent et al., 2016). The tidal forcing applied is described in Section 5.2.1 while the computational domain, the bathymetry and the mesh are described in Section 5.2.2. The value of the parameters of the models which are likely to have a significant impact on the results are discussed in Section 5.2.4.

5.2.1 Astronomical forcings

The forcings taken into account are those induced by Saturn while those due to other moons and the Sun are neglected. Indeed, the latter is one order of magnitude smaller while the other moons are much smaller than Saturn, resulting in a smaller attraction potential. The ocean tidal loading due to the adjacent seas is neglected as suggested by Tokano et al. (2014). The tidal forcing is obtained

from the horizontal gradient of the tidal potential. As Titan is a tidally locked moon, the two main contributions to the astronomical forcing are that due to the orbital eccentricity (derived by Dermott and Sagan, 1995) and that due to Titan's obliquity (derived by Tyler, 2008), whose period is 1 Titan day (TD).

The ideal tidal forcing due to the horizontal gradient of the tidal potential would be completely effective on a totally rigid moon. Nevertheless, Titan is not rigid, it is even highly deformable compared to the Earth: the deformation of the ice shell above the global subsurface ocean is much larger than the deformation of the Earth's crust. The solid tides of Titan and the resulting sea bottom displacements are thus much more significant. The influence of such solid tides on the tidal potential can be modelled through the attenuation factor $\gamma_2 = 1 + \Re(k_2) - \Re(h_2)$ where $\Re(k_2)$ and $\Re(h_2)$ respectively are the real part of the second degree tidal potential Love number and the second degree radial displacement Love number (Sears, 1995; Sohl et al., 1995; Lorenz et al., 2014; Tokano et al., 2014; Beuthe, 2015b). This attenuation factor represents the fact that Titan's surface deformation reduces the tidal forcing to which surface liquids respond. It is consequently implemented as a factor multiplying the tidal forcing in the shallow water equations: the term representing the tidal forcing is $\gamma_2 \nabla_h \phi$ where ∇_h is the horizontal del operator and ϕ is the tidal potential. Love numbers k_2 and h_2 respectively characterize the ratio of the potential due to the ice shell deformation to the tidal potential and the ratio of the solid tides height to the height of an equilibrium ocean. Such a factor is also used to model solid Earth and ocean tides (e.g. Hendershott, 1972; Gordeev et al., 1977). Nevertheless, there are uncertainties about these Love numbers: they depend on the subsurface ocean thickness and density, on the rheological properties of Titan (Sohl et al., 2003), on the ice shell rigidity (Lorenz et al., 2014; Rappaport et al., 2008), and they vary linearly with the ice shell thickness (Sohl et al., 2003; Rappaport et al., 2008). Consequently, we decide to consider γ_2 as a free parameter (as recommended by Lorenz et al., 2014). The range of acceptable values of parameter γ_2 is

briefly discussed in Section 5.2.4. For the reference case, we choose $\gamma_2 = 0.1$ to match with Tokano et al. (2014).

5.2.2 Computational domain and bathymetry

We consider Ligeia and Kraken Maria independent from the other seas and lakes and without external fluid input due to hypothetical river(s). The shoreline contour is drawn from the radar mosaic shown in Lorenz et al. (2014). The resolution of these images varies depending on the location: from 1 to 2 km in Kraken Mare and from 0.3 to 1 km in Ligeia Mare (Lorenz et al., 2014). Particular attention is paid to Seldon and Trevize Fretum (respectively point A and B in Fig. 5.1). The latter is elongated (200 km, five times longer than Seldon Fretum) and narrow (about 15 km, 2 km less than Seldon Fretum). As recently discovered, there are liquid filled canyons in Vid Flumina (Point C in Fig. 5.1) and Xanthus Flumen (Point D in Fig. 5.1), near Ligeia Mare (Poggiali et al., 2016). Nevertheless, they are not included in our domain except for studying the tidal motion therein (see Section 5.3.3), as they do not impact the tides in the northern seas. At Vid Flumina location, the width of the implemented canyons is less than 1300 m, which is slightly larger than the observation of Poggiali et al. (2016) (they predicted a maximum width of 1000 m). Nonetheless, this value is only reached locally, at intersections, most of the canyons being narrower than 1000 m and the mean width is close to the value predicted by Poggiali et al. (2016) (700 m). Near Xanthus Flumen, there is a strait and a small widening before the start of the canyon. The canyon maximum width is about 6700 m (at the mouth of the canyon), which matches with the observations of Poggiali et al. (2016).

Due to the absence of *in situ* measurements, models have to be used to determine the chemical composition and, hence, the density of Titan's lakes and seas. The dominant compounds can be determined from physical properties inferred from Cassini measurements such as the loss tangent and the dielectric permittivity (see e.g. Le Gall et al., 2016; Hayes, 2016) and different models

are proposed (see e.g. Cordier et al., 2009; Glein and Shock, 2013; Tan et al., 2013, 2015; Luspay-Kuti et al., 2015). They all predicted that the seas and lakes are mainly composed of methane and ethane, other low-molecular-mass hydrocarbons, and nitrogen. Nevertheless, depending on the model or some parameters, the polar lakes and seas appear to be either ethane-rich or methane-rich, which modifies properties such as the liquid density and viscosity. Furthermore, the liquid composition varies with temperature (Glein and Shock, 2013). Consequently, the liquid composition can vary from one lake to another and over the year. For instance, according to Le Gall et al. (2016); Hayes et al. (2016), Ligeia Mare is methane rich and variations in backscattering between Ligeia Mare and Kraken Mare seems to suggest that Kraken Mare would have more ethane than Ligeia Mare, as assumed by Lorenz (2014). This could induce a density gradient in Trevize Fretum. Nevertheless, due to the sparse information about the composition of Kraken Mare, we do not take into account such density gradient in the present study. On the other hand, previous studies showed that small variations of the mean density have a negligible impact on the tidal response (Vincent et al., 2016). Regarding to the temporal variations of the liquid composition, those induced by daily modifications of the surface temperature are negligible, diurnal variations disappearing at latitudes higher than $20-30°$N (Cottini et al., 2012) while local variations induced by meteorological events are beyond the scope of this study, the associated time scale being much larger than that of the tides. Therefore, the density is assumed to be spatially and temporally constant in the northern seas. As the radar measurements (Hayes et al., 2016) and the independent microwave radiometry data (Le Gall et al., 2016) indicate quite clearly that methane dominates the composition (at least of Ligeia Mare), the density is set to 550 kg/m^3 in agreement with Tan et al. (2015).

A bathymetry profile along the T91 flyby (in Ligeia Mare) was derived from Cassini measurements by Mastrogiuseppe et al. (2014) and a bathymetry map of Ligeia Mare is displayed in Fig. 9a of Hayes (2016). Nevertheless, due to the opacity of Kraken Mare to the radar waves no bathymetry profile is available except in Moray Sinus. Consequently, no measured bathymetry is available for Kraken Mare. Lorenz et al. (2014) derived a hypothetical bathymetry with a simple bottom shape: a constant slope was assumed away from the shore. Nevertheless, due to variations in the shoreline contour, we cannot use this bathymetry. Consequently, we built our own bathymetry similarly to the method used by Lorenz et al. (2014) (see Fig. 2 in Tokano et al., 2014): the depth scales with the distance to the nearest shore (i.e., $depth = \alpha \times distance$), the scaling factor, α, being computed in such a way that the maximum depth in Ligeia Mare is the same as in Lorenz et al. (2014) (i.e. 170 m) (see Fig. 5.1). It results in small local variations of the bathymetry due to small modifications of the shoreline or the fact that an island is taken into account or ignored. For instance, the maximum depth of the implemented bathymetry is 189 m and is located in Kraken 2 instead of Kraken 1 according to the bathymetry of Lorenz et al. (2014). We briefly discuss to what extent an artificial bathymetry is justifiable in Section 5.4.4 by comparing our results with those obtained for a bathymetry of Ligeia Mare that mimics Fig. 9a of Hayes (2016).

5.2.3 Depth-averaged model

The numerical model used is the same as in Vincent et al. (2016): it is the Second-generation Louvain-la-Neuve Ice-ocean Model, SLIM. This model relies on the discontinuous Galerkin finite element method (DGFEM) to solve the 2D depth-averaged shallow water equations on an unstructured mesh. An implicit Runge-Kutta scheme using a Newton-Raphson solver is resorted to, which allows time steps as large as five thousandths of a Titan day ($\sim$ 6890 s) to be used. This method does not suffer from excessive numerical dissipa-

tion or spurious oscillations. Furthermore, it is highly parallelisable, local mass conservation is ensured and an efficient wetting-drying algorithm to deal with the tidal flats is implemented (Kärnä et al., 2011). Solving the equations on unstructured grids is another advantage of this method. Indeed, the mesh can be refined at places of particular interest (for example, in the vicinity of the shores or in the straits) without significantly increasing the computational cost. SLIM has already been successfully used to simulate tides in various terrestrial domains including the Scheldt estuary (e.g., de Brye et al., 2010), the Mahakam delta (e.g., de Brye et al., 2011), and the whole Great Barrier Reef (e.g., Lambrechts et al., 2008b). It was also used on Titan in order to study Ontario Lacus tidal motion (see Vincent et al., 2016).

Several assumptions are made in order to derive the governing equations solved hereinafter from the general mass and momentum conservation equations. First, density variations are disregarded, as explained in Section 5.2.2. Second, the maximum depth is about 189 m, which is much smaller than the horizontal length scale. Such a small aspect ratio is also observed in Seldon and Trevize Fretum. The aspect ratio being small, the hydrostatic approximation holds valid. Third, we neglect the atmospheric pressure gradient as we focus on tidal motion. These assumptions allow an integration over the depth resulting in the 2D equations solved by our model (see Eqs. 2.25). The interactions with the atmosphere are neglected: we take into account neither the precipitations, nor the evaporation, nor the wind stress.

The unstructured meshes are generated by means of `GMSH` (see Geuzaine and Remacle (2009)), which is one of the most widely used open source unstructured mesh generator. The spatial resolution in the seas ranges from 1 km to 12 km. We use three refinement criteria:

- The local element size is proportional to the celerity of the long surface gravity waves, $c = \sqrt{gh}$, as suggested by Henry and Walters (1993); Legrand et al. (2006);

- The mesh is refined near the shores;
- The spatial resolution is increased in Trevize Fretum and Seldon Fretum (the minimum grid size is still 1 km but the maximum grid size is 3 km in these areas).

5.2.4 Model parameters

Several parameters are likely to have a significant impact on the model results. A sensitivity analysis is conducted with respect to four of them: the attenuation factor γ_2, the bathymetry of Kraken Mare, the depth of Trevize Fretum H, and Manning's roughness coefficient n. The latter is studied within a range from 0.01 $\mathrm{sm}^{-1/3}$ to 0.06 $\mathrm{sm}^{-1/3}$, which respectively corresponds to smooth man-made channel and to natural channel with stones on Earth. The results are presented in Section 5.4.3.

As explained in Section 5.2.2, the bathymetry is not derived from measurements but is assumed to scale with the distance to the shore, the scaling factor, α, being set to reach the same maximum depth in Ligeia Mare as in the bathymetry map of Lorenz et al. (2014). However, there is no evidence to suggest that the scaling factor is the same in Kraken Mare. Consequently, we consider two additional cases: in case 1, we multiply the scaling factor by 2 (i.e., $depth = 2\alpha \times distance$) and, in case 2, we divide it by 2 (i.e., $depth = 0.5\alpha \times distance$). The former and latter cases are referred to as *bathy A* and *bathy B*. For *bathy B*, the maximum depth is 170 m and lies in Ligeia Mare; the maximum depth in Kraken 1 and Kraken 2 are 92 m and 95 m, respectively. For *bathy A*, the maximum depth in Kraken 1 and Kraken 2 are 365 m and 379 m, respectively. It results in significant modifications of the volume ratio between Kraken and Ligeia Mare. The variations of the tidal response induced by such modifications are detailed in Section 5.4.5. Furthermore, as pointed out by Tokano et al. (2014), the depth of Seldon Fretum (which is underconstrained) has a significant impact on the tidal current inside the strait. It is likely

that the depth of Trevize Fretum, which is also not well constrained, has a similar impact. Consequently, we consider the depth of this strait as a free parameter. We carry out simulations for four cases: the reference case and three constant depths. For the reference case, the depth increases with the distance to the shore, which results in a maximum depth of 15 m and a bottom profile which has the shape of a "$\vee$". The three other cases correspond to a bottom profile which has the shape of a "$\sqcup$" and whose depths respectively are 10 m, 20 m, and 50 m. The impact of this parameter is detailed in Section 5.4.2.

The attenuation factor value is a function of the Love numbers k_2 and h_2 which, in turn, depend on the internal structure of Titan. Unfortunately, the latter is poorly constrained, which results in uncertainties about these Love numbers. Iess et al. (2012) derived some values of k_2 from Cassini measurements by means of three analysis models while Sohl et al. (2003, 2014); Baland et al. (2014); Lefevre et al. (2014); Beuthe (2015b), among others, used models to reconstruct Titan's internal structure from observations and measurements such as the gravity field, the second degree tidal potential Love number k_2, and the moment of inertia. As a result, different values can be found depending on the working hypotheses and the model used (see Table 1.2). Beuthe (2015b) predicted values of k_2 matching with those computed by Iess et al. (2012) from observations. By setting the ice shell relative thickness in order to correspond with the value of k_2 obtained by Iess et al. (2012), the corresponding attenuation factors range from 0 to 0.21 depending on the density of the crust and subsurface ocean (See Fig. 5 in Beuthe, 2015b). Tokano et al. (2014) computed γ_2 for different internal structures and only retained those which satisfy the moment of inertia and the Love number k_2 predicted by Iess et al. (2012), which results in $\gamma_2 \in [0.1, 0.2]$, depending on the ice shell thickness. However, the value retained from the moment of inertia was obtained by having recourse to the hydrostatic assumption, which is questionable due to the significant degree-three signal observed in the gravity field (Hemingway et al., 2013; Lefevre et al., 2014;

Baland et al., 2014). All these models assume a thin and homogeneous crust. However, the crust could be non-homogeneous: there could be some clathrates outgassing methane in the atmosphere from time to time (Tobie et al., 2006). Such clathrates at the base of the ice shell might have a smaller shear modulus which would cause larger deformation of the shell and the Love number k_2 would be larger (Rappaport et al., 2008). In the light of the values found in the literature, we decide to study the tidal response for three additional values of γ_2: 0.05, 0.2, and 0.3 (see Section 5.4.1).

5.3 Results

In this section, we first describe the tidal response of Ligeia and Kraken Maria predicted by our model. For this purpose, we study the decomposition in different harmonic components as well as some of the northern seas eigenmodes. Then, we focus on some specific areas such as Trevize and Seldon Fretum, the canyons observed by Poggiali et al. (2016), Moray Sinus and the "Magic Islands" locations. The bathymetry is shown in Fig. 5.1, the attenuation factor is $\gamma_2 = 0.1$ and Manning's coefficient is set to 0.03 $\mathrm{sm}^{-1/3}$.

5.3.1 Tidal response of Kraken and Ligeia Maria

The tidal forcing (see Section 5.2.1) applied rotates anticlockwise with an exact period of 1 TD (not shown). It is not unidirectional over the seas. Indeed, there can be a significant difference in forcing orientation between Ligeia Mare and Kraken Mare or even between the southern and northern region of Kraken Mare. For instance, 0.25 TD after perikron/apokron (point of the orbit where Titan is nearest/farthest to Saturn), the angle between the direction of the forcing in the north-eastern and south-western regions can be larger than 90°. The forcing in t^* and $t^*+T/2$ has the same magnitude but it is oriented in opposite directions. In Ligeia Mare, the maximum is

about 3.59×10^{-7} m/s^2 and occurs 0.1 TD before perikron/apokron in the eastern part of the sea while, in Kraken Mare, it is about 5.46×10^{-7} m/s^2 and it occurs 0.145 TD after perikron/apokron in the south-eastern part of the southern basin.

The maximum/minimum sea surface elevation (η) is ± 0.145 m. It occurs 0.31 TD after perikron/apokron in the south-eastern part of Kraken 2 (see the video in the additional content of Vincent et al. (2018), available at https://doi.org/10.1016/j.icarus.2017.12.018), 0.165 TD after the maximum forcing magnitude, which is directed south-westwards. The maximum/minimum sea surface elevation in Kraken 1 is ± 0.115 m and occurs 0.18 TD before perikron/apokron at the north-western end of the basin. In Ligeia Mare, the maximum/minimum is ± 0.07 m and occurs 0.05 TD before perikron/apokron at the eastern shore of Ligeia Mare. The sea surface elevation in Kraken 2 and Ligeia Mare can be positive/negative over the whole basin, which suggests strong liquid exchanges through the straits (see Section 5.3.2). It lasts longer in Ligeia Mare (about 0.2 TD) than in Kraken 2 (where the sea surface elevation is positive/negative over the whole basin during respectively 0.095 TD and 0.06 TD) and does not occur in Kraken 1 due to the presence of the amphidromic point. The period of time during which the elevation is positive over the whole basin is not the same as that during which it is negative which suggests that the volumetric flow rate going through Seldon and Trevize Fretum is not the same at t^* than at $t^* + T/2$. The fact that the tidal motion is independent in each basin results in strong sea surface elevation gradient in the straits. This gradient is larger in the small channels near Seldon Fretum (the maximum is about 2.22×10^{-5}) than in Seldon and Trevize Fretum where it can respectively reach about 1×10^{-5} and 7×10^{-6}. The gradient increases and decreases twice on a tidal cycle and can be very small during some short periods of time (see, for example, the sea surface elevation in the video in the additional content of Vincent et al. (2018)).

While studying the sea surface elevation of seas, it is common to study the tidal components. Indeed, the sea surface elevation

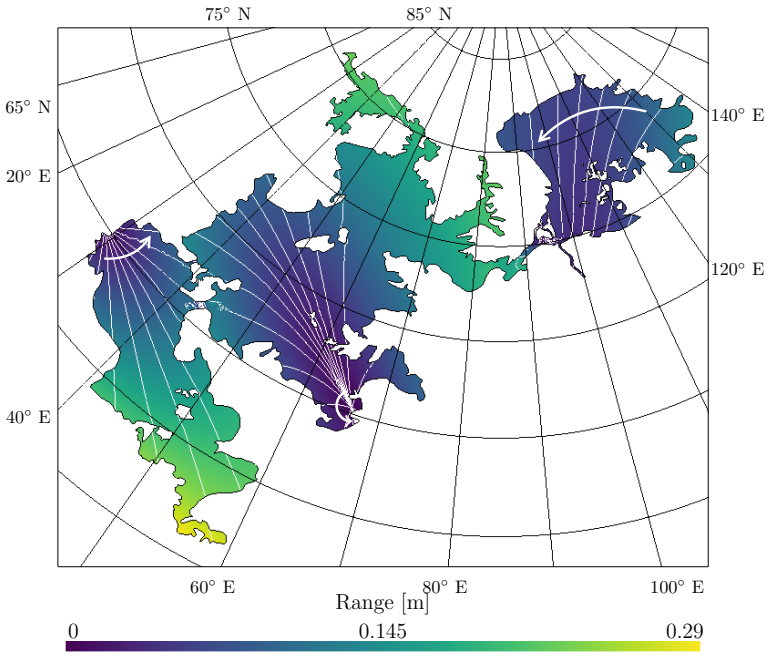

Fig. 5.2: Tidal range (in m) and tidal phase (white lines, with a 15° spacing) of the first tidal component (whose period is 1 TD) in Kraken and Ligeia Maria. The white arrows show the direction of the diurnal tide. The tidal range is the surface elevation difference between high tide and low tide. There is an amphidromic point in Kraken 1 (at 65.213°N, 66.459°E) but not in Kraken 2 or Ligeia Mare. The tidal phase at each end of Seldon and Trevize Fretum are not the same, which results in strong transition in the straits. This is also observed for the tidal range. Such phenomenon suggests independent tidal motion in each basin. The tidal range is maximum in the south-eastern part of Kraken 2.

at a point can be viewed as a sum of several components written as $\eta(t,x,y) = E(x,y)\cos(\omega t + \phi(x,y))$ where $E(x,y)$ is the amplitude[3], $\omega = 2\pi k/T$ is the angular period of the k^{th} component, and $\phi(x,y)$ is the tidal phase. On Titan, the first, second, third, and

[3]The amplitude of a tidal component is half of the tidal range which is the difference between high tide and low tide.

fourth tidal components respectively have a period of 1, 0.5, 0.33, and 0.25 TD. Fourier analysis shows that the first tidal component (whose period is 1 TD) is responsible for more than 90% of the sea surface motion, except for some small areas in the straits and at the amphidromic point of the first tidal component (see Fig. 5.2). The second and fourth components are significant in the straits (see Table 5.1) but can be neglected elsewhere while the third component is significant in Trevize Fretum and where the tidal range due to the first tidal component is weak (i.e. near the amphidromic point and in the south-western part of Kraken 2 (see Fig. 5.2)). The other tidal components are insignificant in comparison to the aforementioned components. In the small straits near Seldon Fretum, the tidal range of the second and fourth tidal components are larger than that of the first one. Nevertheless, it remains small (at most 0.017 m for the second). The fact that the amplitude of the others components is significant with respect to the first one in these straits is due to the small amplitude of the latter at this location (see Table 5.1). In the remainder of this paper, unless otherwise specified, the expressions "tidal range" and "tidal phase" refer to the range and phase of the first tidal component. An amphidromic point of the first tidal component is located in the south-eastern part of Kraken 1, at (65.21°N, 66.47°E) (see Fig. 5.2). At this location, the most significant component is the third one but the resulting tidal range remains weak: at most 2.5×10^{-3} m. As a consequence, the diurnal tide in this basin rotates around this point and the tidal phase ranges from $-180°$ to $180°$. There is no such point in Ligeia Mare or Kraken 2. In Ligeia Mare, the tidal phase is larger than $-86°$ and smaller than $19°$ while, in Kraken 2, it ranges from $-208°$ to $-52°$. In both basins, the cotidal lines (lines of constant tidal phase) are not rectilinear, which is due to the friction which is higher in the vicinity of the shoreline and islands as the sea is shallower at these locations.

Fig. 5.2 shows that, in Kraken 2, the tidal range increases with the distance to a point on the south-western shore and is maximum (0.288 m) at the south-eastern end. In Kraken 1, the tidal range

Table 5.1: Maximum amplitude of the first tidal component and ratio between the amplitude of the other tidal components and that of the first tidal component. In the basins, these values are computed at three points: (80°N, 110°E) in Ligeia Mare, (70°N, 50°E) in Kraken 1, and (62.5°N, 40°E) in Kraken 2. In the straits, they are computed where the relation $\frac{comp2}{comp1}$ is maximum

Comp	Period [TD]	Ligeia Mare[c]	Kraken 1[d]	Kraken 2[e]	Seldon Fretum	Trevize Fretum	Small channels
1[a]	1	2.7	2.3	5.6	1.8	0.8	0.1
2[b]	0.5	1%	1%	1%	96%	62%	378%
3[b]	$\frac{1}{3}$	2%	4%	3%	3%	18%	58%
4[b]	0.25	0%	0%	0%	21%	10%	118%
5[b]	0.2	0%	1%	1%	1%	1%	48%
6[b]	$\frac{1}{6}$	0%	0%	0%	4%	1%	54%
7[b]	$\frac{1}{7}$	0%	0%	0%	1%	1%	34%

[a]: Amplitude of the diurnal tidal component expressed in 10^{-2} m
[b]: Amplitude of the tidal component expressed as a percentage of the amplitude of the first tidal component
[c]: at (80°N, 110°E)
[d]: at (70°N, 50°E)
[e]: at (62.5°N, 40°E)

increases with the distance to the amphidromic point and, hence, is higher on the northern shore (maximum: 0.225 m) than in the middle and southern part of the sea. The corange lines (lines of same tidal range) have an ovoid shape with their longitudinal axis parallel to the maximum width direction and whose centre is located at the amphidromic point. In Ligeia Mare, it increases with the distance to a point located on the southern shore of the sea, east of the Ligeia outlet of Trevize Fretum and is maximum (0.14 m) in the south-eastern part of the sea. The tidal motions remain in-

dependent of each other in each basin. Indeed, a transition takes place in each strait linking the basins. This transition is sharper in the straits linking Kraken 1 and Kraken 2 than in Trevize Fretum. In the former, there are buffer areas where the tidal range is smaller than elsewhere in the strait, which results in sharp transition in its phase. In the latter, the transition is smoother for both tidal range and phase although it does not take place at the same location (the transition of tidal phase occurs much closer to Ligeia Mare than that of the tidal range). This suggests that, to a large extent, the tidal motion in Kraken 1 and Ligeia Mare can be represented by a sloshing wave mode. Indeed, in these basins, the tidal phase is nearly uniform over large geographical areas while there are strong variations (sometimes by about 180°) over the straits connecting those basins with Kraken 1 (see Fig. 5.2).

The speed is maximum in the straits such as Trevize Fretum, Seldon Fretum, the small channels next to the latter, and the strait north of Mayda Insula (see Fig. 5.3). Except for these specific locations, the largest speed is observed nearshore but the fluid velocity is one order of magnitude smaller than in the straits (about 0.027 m/s). In Seldon Fretum, the fluid speed has two maxima located in the middle of the straits, 0.364 m/s and 0.355 m/s, which occur respectively 0.06 TD after perikron/apokron while the speed is the lowest (0.08 m/s, which remains larger than everywhere else in the seas, excluding the straits) 0.15 TD before perikron/apokron. The current is mainly unidirectional toward Kraken 1 or 2 depending on the period of time (see Fig. 5.4(a, b, c, d, e, f)). The transition between two unidirectional flows occurs when the fluid speed at this location is the weakest. Once the flow is unidirectional, it accelerates to reach its maximum speed and then decelerates until it starts turning again. In Trevize Fretum, the maximum speeds, 0.235 m/s and 0.234 m/s, occur respectively 0.3 TD after perikron/apokron in the southern part of Trevize Fretum while the speed is the lowest (about 0.065 m/s) 0.07 TD after perikron/apokron. As in Seldon Fretum, the flow is mostly unidirectional (see Fig. 5.4(g, h, i, j, k, l)) and turns when its speed is

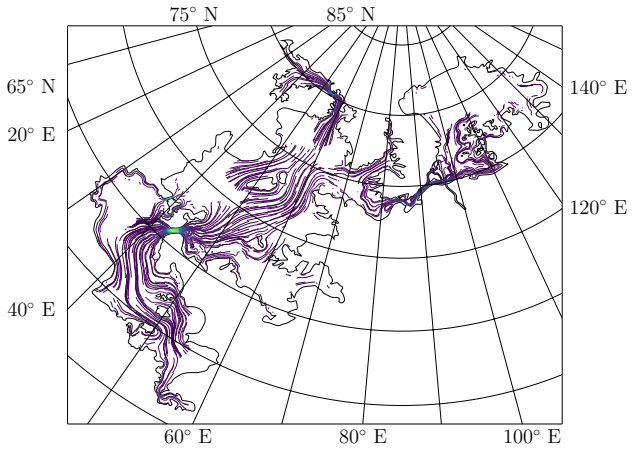

(a) Perikron

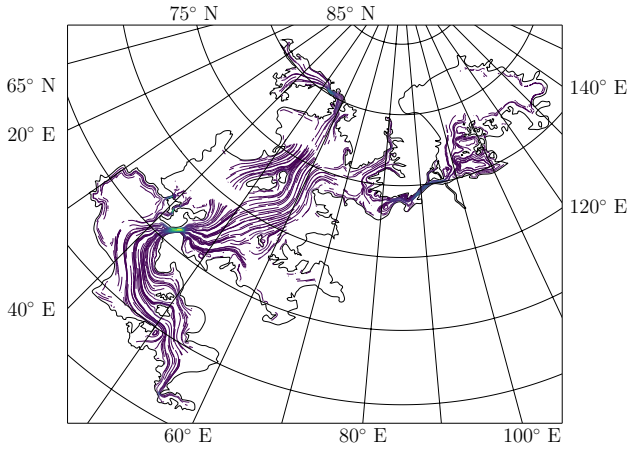

(b) Apokron

Fig. 5.3: Tidal current streamlines at perikron (a) and apokron (b). The empty areas correspond to areas where the predicted velocity field magnitude is smaller than 0.001 m/s. At these periods, the main current pattern is a flux going from the south-eastern part of Kraken 2 toward the north of Kraken 1 and from Moray Sinus toward Ligeia Mare (Panel (b)) or in the opposite direction (Panel (a)).

the weakest. The period of time during which the flow is unidirectional is longer in Trevize Fretum than in Seldon Fretum. These periods of time are concomitant with each other as long as the flow is unidirectional in Seldon Fretum.

The fact that the current is almost unidirectional in Seldon and Trevize Fretum is also shown in Fig. 5.5: the tidal ellipses[4] of the main tidal component are nearly rectilinear at these locations, which means that there is a fast transition between the two main velocity orientation at a given point. Elongated tidal ellipses also occur elsewhere in the Maria but the velocity is much smaller. At locations where the flow speed is smaller than 0.001 m/s (for instance, in the western part of Kraken 2, the south western part of Kraken 1, and the northern part of Ligeia (see Fig. 5.3)), the ellipses are near circular which indicates that the flow velocity rotates over 1 TD instead of being nil during the transition between two directions. The orientation of the flow and, hence, of the tidal ellipses depends on the location. In the straits, the ellipses are aligned with the main axis of the strait while, in their vicinity, they point at the nearest outlet of the strait. Offshore, where the speed is larger than 0.001 m/s, the main axis of the ellipses is aligned with the streamlines at perikron/apokron (see Fig. 5.3).

The tidal forcing studied in this paper does not seem to generate resonance in the northern seas (at least during the 15 TD studied). Nevertheless, it does not mean that normal modes of the northern seas could not be excited by other phenomena. In order to study the eigenmodes, we perform a discrete modal analysis of the Discontinuous Galerkin solution of the linear shallow water equations following the method of Bernard et al. (2008). The eigenvalues and eigenvectors are computed by means of the `linalg.eig` function of `scipy` package of python which solves the generalised eigenvalue problem $M\frac{dU}{dt} = AU$ where M is the mass matrix, A is the discontinuous Galerkin discretisation of the linear shallow water space

[4] A tidal ellipse is the locus of the end of the velocity vector associated with one tidal component over a tidal period at one point.

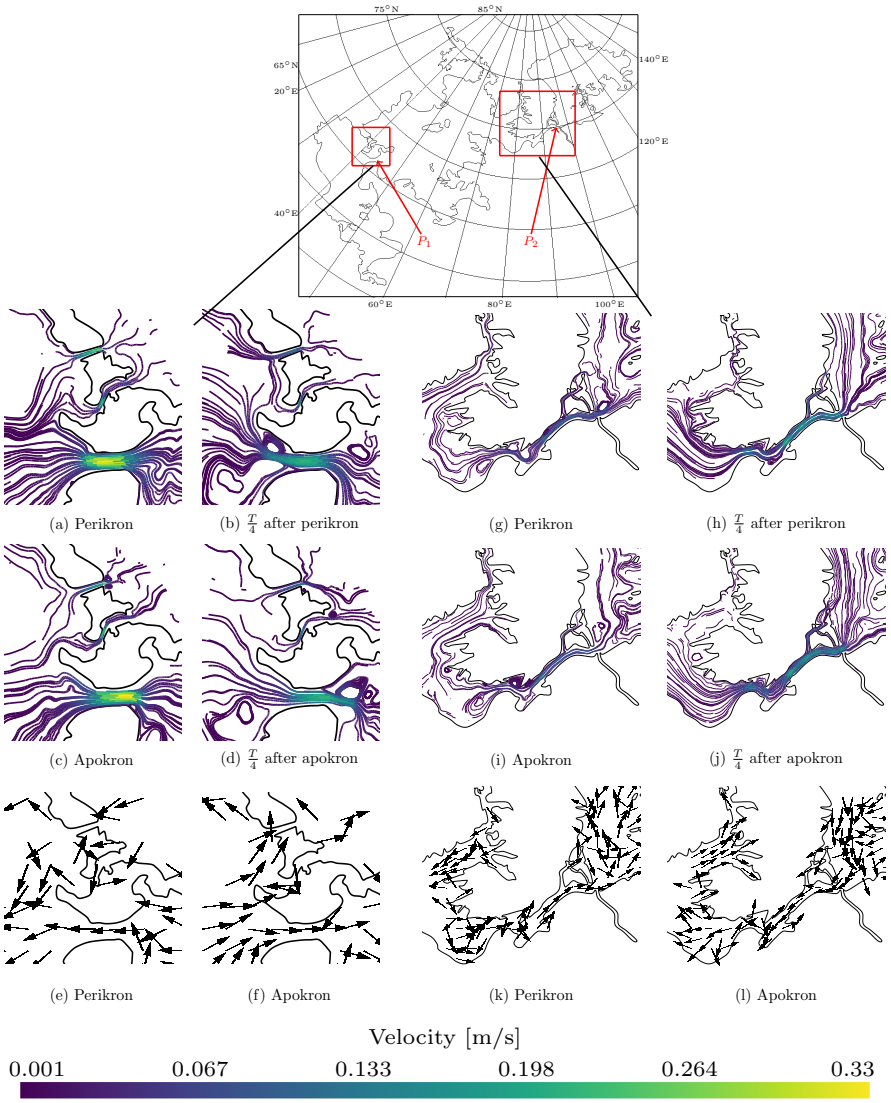

Fig. 5.4: Streamlines (a, b, c, d, g, h, i, j) and orientation (e, f, k, l) of the tidal current (in m/s) in Seldon and Trevize Fretum at four times of day: perikron (a, e, h), $T/4$ after perikron (b, i), apokron (c, f, j), and $T/4$ after apokron (d, k). The fluid speed is maximum (0.364 m/s) in Seldon Fretum 0.06 TD after perikron. The other areas where the speed is high are, in first instance, the other straits and, in second instance, the nearshore regions corresponding to specific shapes in the shoreline such as cape, peninsula and bay. The velocity in the strait is unidirectional for most of a Titan day (see Panels (e, f, k, l)).

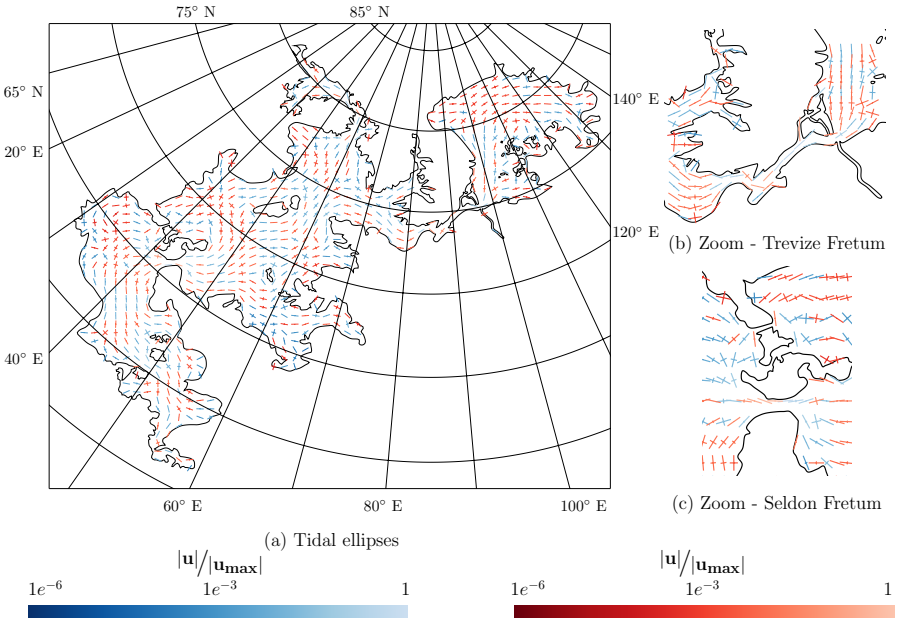

Fig. 5.5: Major and minor axes of the tidal ellipses in the northern seas (Panel (a)), Trevize Fretum (Panel (b)) and Seldon Fretum (Panel (c)). The tidal ellipses represent the orientation of the first tidal component of the current over a whole period. Red and blue ellipses respectively indicate an anti-clockwise/clockwise rotation while the color scales with the magnitude of the maximum velocity over 1 TD. The smaller the minor axis, the more elongated the ellipses, and the more unidirectional the velocity.

operators for the domain, and $U = (\eta, u, v)$ is the solution. The natural periods range from 2.55×10^{-3} TD to $15,171$ TD. Nevertheless, most of the eigenmodes (90%) have a period smaller than 25 TD. Some of the eigenmodes have a period close to 1 TD but these eigenmodes consist of localised modifications of the sea surface elevation in some of the small bays, along the northern shore of Ligeia Mare or near the islands of Kraken 2 and Ligeia Mare. These localised phenomena do not play a significant role in the global tides of the northern seas and these eigenmodes are not no-

ticeable while looking at the tidal motion. Some of the eigenmodes correspond to phenomena such as coastal trapped waves or funnel shaped waves but their resonance frequency is not excited by the tides. A complete discussion of the northern seas eigenmodes is of interest but beyond the scope of this chapter.

In Kraken 1, 2, and Ligeia Mare, the Rossby radius of deformation ($R = \frac{\sqrt{gh}}{f}$ where $g = 1.352$ m/s^2 is the mean gravitational acceleration at Titan's surface, h is the depth, and f is the Coriolis parameter) ranges are $[91.3, 1776.3]$ km, $[98.5, 1938.2]$ km, and $[93.5, 1655.3]$ km, respectively. These values are larger than the characteristic length scale of the basins except for areas near the shore where the seas are shallower. This means that rotating shallow water waves such as Kelvin waves could appear near shore, R being smaller than the characteristic length scale at these locations. Other coastal trapped waves such as the edge waves could occur in the northern seas while continental shelf waves are ruled out because there is no shelf. Some of the eigenmodes of the northern seas correspond to such coastal trapped waves but they are not excited by the tidal forcing as their periods are much smaller than the tidal period. Such coastal trapped waves could appear due to other forcings such as the wind but this is beyond the scope of this chapter. Furthermore, the evolution of the sea surface elevation over one tidal period does not show evidence for any coastal trapped waves (see the video of the tidal motion over 1 TD in the additional content of Vincent et al. (2018)). Such waves are, hence, unlikely, unless they have a period smaller than 0.05 TD ($\sim 6.9 \times 10^4$ s) (which is the numerical time step) or larger than 0.5 TD ($\sim 6.9 \times 10^5$ s) or they occur on a really small spatial scale. Topographic planetary waves could occur if $|\nabla_h H| \geq H R_0$ (LeBlond and Mysak, 1978) where H is the depth, $R_0 = R \tan \theta_0$ (R is Titan's radius and θ_0 is the latitude), and $|\nabla_h H| \sim 0.002$ is the bathymetry gradient. This condition being never encountered with the bathymetry implemented, such waves are not expected. Offshore, the shallow water waves phase speed tends to $c = \sqrt{gh}$ and

to be non dispersive. In Trevize and Seldon Fretum, capillary waves could occur – thus tidal current could generate surface roughness detectable in radar observations. Other phenomena, which could not be detected by spacecraft instrument, such as surface gravity waves and turbulence, could also occur in these seas and might play a role in the transfer of energy and momentum to these waves.

It is noteworthy that the system of two basins connected by a channel is a classic Helmholtz oscillator. A terrestrial example of such behaviour is the identification of a $48-72$ hours periodicity in currents through the Straits of Mackinac, between the Great Lakes, Michigan and Huron (Anderson and Schwab, 2013). The two major Kraken basins and Seldon Fretum form an analogous system. The natural period can be calculated (Eq. 8 of Anderson and Schwab (2013)) from the channel cross-section ($A_c \sim 0.2$ km^2, for ~ 10 m depth), the area of the basins ($A_{K1} \sim 2.4\times10^5$ km^2 and $A_{K2} \sim 1.3\times 10^5$ km^2), the channel length $l = 40$ km, and the mean gravitational acceleration $g = 1.352$ m/s^2 as $T = 2\pi\sqrt{\frac{l}{A_c g\left(\frac{1}{A_{K1}}+\frac{1}{A_{K2}}\right)}}$. With these values, the predicted period is about 8.8 Earth days. As this period is not an integer divisor of the tidal period, it would take several tidal cycles to observe any resonance phenomena with the tides. The Ligeia-Trevize-Kraken system has an even longer period (about 18.7 Earth days) and would be more heavily damped by the long tortuous channel, so the Helmholtz mode is insignificant there. Other possible resonance phenomenon could be the quarter wavelength resonance. The latter can be observed on shelves in the Earth ocean. The speed of long waves is given by $c \sim \sqrt{gh}$. For a tidal period of 1 TD (about 15.95 Earth days), the resulting quarter wavelength width ranges from 283 km nearshore up to 5500 km at the maximum depth. This increase is not linear. For instance, the quarter wavelength width is higher than 1400 km at 1.7 km offshore. Consequently, such resonance phenomenon is unlikely in Titan's northern seas.

Table 5.2: Location of potential amphidromic point(s) for the various values of the parameters. γ_2 is the attenuation factor, H is the depth (constant) of Trevize Fretum, α is the scaling factor for the bathymetry, and n is Manning's coefficient. The reference case (bold text) corresponds to $\gamma_2 = 0.1$, $n = 0.03$ sm$^{-1/3}$, and a bathymetry scaling with the distance to the shore.

	Amphidromic Point in Kraken 1	Amphidromic Point in Kraken 2
$\gamma_2 = 0.05$	(64.06°N, 65.102°E)	-
$\gamma_2 = 0.1$ [a]	(**65.213°N**, **66.46°E**)	**-**
$\gamma_2 = 0.2$	(67.391°N, 64.197°E)	(64.171°N, 32.143°E)
$\gamma_2 = 0.3$	(68.418°N, 62.529°E)	(63.897°N, 33.905°E)
$H = 10$ m	(66.695°N, 62.16°E)	-
$H = 20$ m [b]	(70.056°N, 44.491°E)	-
$H = 50$ m [b]	-	-
$n = 0.01$ sm$^{-1/3}$	-	-
$n = 0.02$ sm$^{-1/3}$	(65.032°N, 63.27°E)	-
$n = 0.04$ sm$^{-1/3}$	(66.57°N, 65.686°E)	(64.302°N, 31.032°E)
$n = 0.05$ sm$^{-1/3}$	-	(63.927°N, 33.202°E)
$n = 0.06$ sm$^{-1/3}$	-	(63.721°N, 34.711°E)
2α [c]	(67.347°N, 48.643°E)	-
0.5α [d]	(70.3506°N, 57.958°E)	(63.15°N, 38.5°E)

[a]: Reference case (i.e. γ_2=0.1 and no bathymetry modification).
[b]: In these cases, the maximum elevation occurs in Ligeia Mare
[c]: In this case, the bathymetry in Kraken Mare is computed with a scaling factor doubled.
[d]: In this case, the bathymetry in Kraken Mare is computed with a scaling factor divided by 2.

Table 5.3: Sea surface elevation (η), tidal current (u), tidal range ($\Delta\eta$), maximum volume variation (ΔV), and liquid exchanges through a strait (q) over one Titan day for the various values of the parameters. γ_2 is the attenuation factor, H is the depth (constant) of Trevize Fretum, α is the scaling factor for the bathymetry, and n is Manning's coefficient. S, T, L, K1, and K2 subscripts respectively refer to Seldon Fretum, Trevize Fretum, Ligeia Mare, Kraken 1, and Kraken 2.

γ_2	0.05	**0.1**[a]	0.2	0.3	
η_{max} [m]	0.086	**0.145**	0.247	0.342	
$\|u\|_S$ [m/s]	0.242	**0.364**	0.523	0.64	
$\|u\|_T$ [m/s]	0.172	**0.235**	0.32	0.385	
$\Delta\eta_{max}$ [m]	0.168	**0.288**	0.492	0.678	
ΔV_L [km^3]	1.8	**2.5**	3.6	4.6	
ΔV_{K1} [km^3]	6.2	**8.9**	12.3	14.8	
ΔV_{K2} [km^3]	5.9	**9.2**	13.7	17.1	
q_S [km^3/TD]	21.103	**32.749**	48.712	60.661	
q_T [km^3/TD]	7.523	**10.501**	14.642	17.847	
	$H = 10$ m	$H = 20$ m[b]	$H = 50$ m[b]	2α [c]	0.5α [d]
η_{max} [m]	0.143	0.162	0.223	0.179	0.099
$\|u\|_S$ [m/s]	0.357	0.342	0.434	0.269	0.258
$\|u\|_T$ [m/s]	0.202	0.304	0.211	0.273	0.219
$\Delta\eta_{max}$ [m]	0.285	0.331	0.446	0.352	0.192
ΔV_L [km^3]	3.9	10.8	15.7	3.4	1.2
ΔV_{K1} [km^3]	8.6	8.2	7.6	14.6	2.7
ΔV_{K2} [km^3]	9	8.8	11.24	13.4	3.3
q_S [km^3/TD]	32.071	30.955	39.714	47.193	11.806
q_T [km^3/TD]	16.133	44.151	63.488	14.343	4.385
n [sm$^{-1/3}$]	0.01	0.02	0.04	0.05	0.06
η_{max} [m]	0.184	0.165	0.129	0.118	0.11
$\|u\|_S$ [m/s]	0.595	0.448	0.293	0.241	0.203
$\|u\|_T$ [m/s]	0.523	0.332	0.178	0.144	0.12
$\Delta\eta_{max}$ [m]	0.354	0.326	0.258	0.235	0.22
ΔV_L [km^3]	6	3.6	2	1.6	1.3
ΔV_{K1} [km^3]	14.5	11.6	6.9	5.6	4.7
ΔV_{K2} [km^3]	12.74	11.3	7.4	6.2	5.2
q_S [km^3/TD]	43.834	39.677	26.763	22.267	18.946
q_T [km^3/TD]	22.854	14.574	7.987	6.413	5.352

[a]: Reference case (i.e. γ_2=0.1, $n = 0.03$ sm$^{-1/3}$ and standard bathymetry).
[b]: The maximum elevation occurs in Ligeia Mare.
[c]: The bathymetry of Kraken Mare is computed with a scaling factor doubled.
[d]: The bathymetry in Kraken Mare is computed with a scaling factor twice smaller.

5.3.2 Fluid exchanges between the basins

In this sub-section, we focus on the tidally induced fluid exchanges between Ligeia Mare and Kraken Mare and between both basins of Kraken Mare. There are much more liquid exchanges between both basins of Kraken Mare than between Kraken Mare and Ligeia Mare: the maximum volumetric flow rate through Seldon Fretum is about twice larger than in Trevize Fretum (see Fig. 5.6) and the total volumetric flow rate through Seldon Fretum (in one way or another) over one Titan day is 32.7 km^3/TD while it is 10.5 km^3/TD in Trevize Fretum. The former matches the semianalytic estimate of Lorenz et al. (2014); they considered a wedge-like volume of liquid of $10 - 30$ km^3 in each half period. Fig. 5.6 shows that there is an asymmetry in the flow rate through both straits: it does not behave as a sinusoid. Indeed, the behaviour of the volumetric flow rate is not the same at its maximum and at its minimum. This is due to the fact that the flow rate in the straits does not only depend on the velocity but also on the sea surface elevation at this location. For instance, in Trevize Fretum, the flow rate increases faster after its minimum than it decreases after its maximum (the slope of the graph is steeper). This can be linked to the fact that the sea surface elevation is positive in Trevize Fretum when the volumetric flow rate is maximum. This larger total depth of liquid results in a slower decrease of the volumetric flow rate when the velocity decreases. Despite this asymmetry, the daily average is nil. The volumetric flow rates explain the smaller volume variation in Ligeia Mare. Indeed, the latter is about three times larger in both basins of Kraken Mare than in Ligeia Mare (see Fig. 5.7). Consequently, there is a strong correlation between volume variation in Kraken 1 and Kraken 2: the volume variation is maximum in one basin soon after/before the minimum in the other and vice versa (see Fig 5.7). This can be explained by the fact that the tidal forcing magnitude is more significant in the surroundings of Seldon Fretum than near Trevize Fretum and by the shape of the straits: Trevize Fretum is much more elongated than Seldon Fretum and the small channels

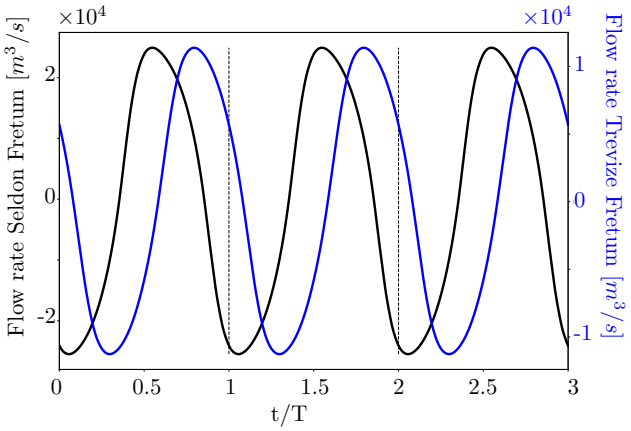

Fig. 5.6: Volumetric flow rate through Seldon (black line) and Trevize Fretum (blue line) over three Titan days. In Seldon and Trevize Fretum, it is respectively positive toward Kraken 1 and Ligeia Mare. The total volumetric flow rate through the former is about three times larger than that through the latter. The net difference over 1 TD is 0 km^3.

next to Seldon Fretum allow additional liquid exchanges.

The volume variation of each basin behaves as a sinusoid whose period is 1 TD. Although being significant, the volume variation is quite weak with respect to the volume of the basins. Indeed, for this bathymetry, the total volume of Ligeia Mare, Kraken 1 and Kraken 2 are respectively about 4500 km^3, 13000 km^3 and 7200 km^3 while the maximum volume variations over a Titan day predicted by our model with these parameters are about 2.5 km^3, 8.9 km^3, and 9.2 km^3, respectively.

We also study the fluid exchanges between the basins and Maria over a period of time of 150 TD (about 6.55 Earth years or 0.22 Titan years) by means of a passive tracer: the tracer concentration is set to 1 in Ligeia Mare and Kraken 2 and to 0 in Kraken 1. This means that wherever the tracer is larger than 0 in Kraken 1 (or smaller than 1 in the others basins), there is some liquid originating from the adjacent basin(s). Such volumes grow over time. They

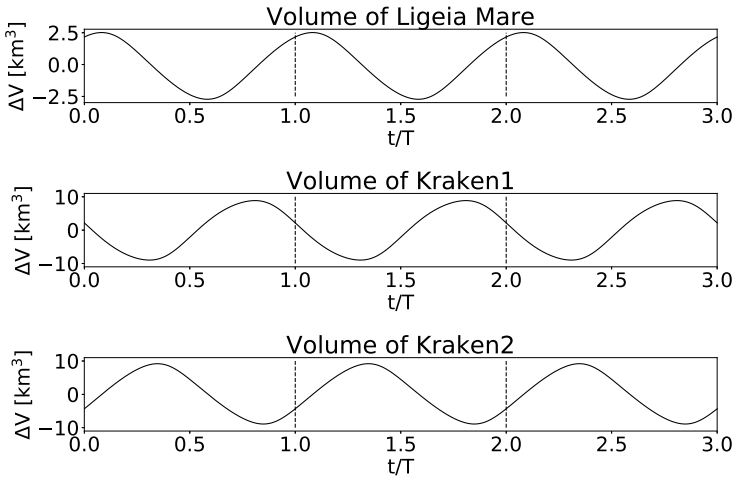

Fig. 5.7: Volume variation in the basins of Kraken and Ligeia Maria over three Titan days. The variation is larger in both basins of Kraken Mare than in Ligeia Mare and the total variation of each basin over a Titan day is nil.

grow faster in Kraken Mare than in Ligeia Mare. For instance, after 150 TD, at least 1% of the liquid at one location is originating from another basin in most of Kraken Mare (see Fig. 5.8 (a)). The areas where this is not the case are almost enclosed bays such as that west of Mayda Insula. On the contrary, in Ligeia Mare, there are some traces of liquid originating from Kraken Mare only in the southern part of the sea, near Trevize Fretum. If we look at higher thresholds, we can see that the liquid exchanges between Ligeia Mare and Kraken Mare remain confined to Trevize Fretum and the small channels at Ligeia outlet. On the other side, there is a wide area (about half of the basin) in both basins of Kraken Mare where at least 5% of the liquid is originating from the other basin, which is due to the much more significant liquid exchanges through Seldon Fretum (see Fig. 5.8 (b)). The area where at least 10% of the liquid is originating from the other basin remains located near Seldon Fretum in Kraken 1 while it spreads over the western part of Kraken

2 (see Fig. 5.8 (c)). This can be due to the smaller volume of liquid and smaller area of Kraken 2 (about 54% of the volume of Kraken 1). Unless a precipitation event (which is unlikely in Kraken 2 and in the southern region of Kraken 1) or an evaporation rate peak (which seems to occur during the spring) occurs, our model gives a good approximation of the tidally induced liquid exchanges between the basins of Kraken Mare. Indeed, the density driven circulation predicted in Seldon Fretum by Tokano and Lorenz (2016) are either insignificant (for the thermally forced circulation) or at least one order of magnitude smaller (see Fig. 14a of Tokano and Lorenz (2016)) than the tidally induced flow (for precipitation/evaporation driven flows). Furthermore, the former occurs on a much larger time scale than the diurnal time scale of the tides. On the other hand, there could be a more significant difference in composition between Ligeia and Kraken Maria (Lorenz, 2014). As the shape of the strait almost reduces the tidal flow to a back an forth motion, a significant density gradient in the strait could modify the flow in Trevize Fretum and, hence, the liquid exchanges. But studying this is beyond the scope of the present chapter. Furthermore, other factors could modify these results. For example, in the case of a pure tidal flow in and out of Ligeia Mare through Trevize Fretum, the same parcel of liquid is washed back and forth and the net mixing is small: a parcel of liquid comes through the channel and sits at the mouth, then is sucked back through. However, if there is, for instance, a strong wind-generated gyre in Ligeia Mare, then whatever Kraken Mare liquid is hosed out of Trevize Fretum into Ligeia Mare is quickly swept away and mixed into Ligeia Mare, and what is sucked back into Trevize Fretum is now mostly Ligeia Mare liquid, not the previously Kraken parcel. Consequently, we can only assess that the variation of liquid composition observed in Moray Sinus (Hayes et al., 2011) with respect to Kraken Mare cannot be explained by tidally induced liquid exchanges over a time scale smaller than 150 TD. This variation could be related to liquid exchanges with Ligeia Mare over a much longer period or to liquid exchanges interacting with wind gyre(s) (or similar phenomenon)

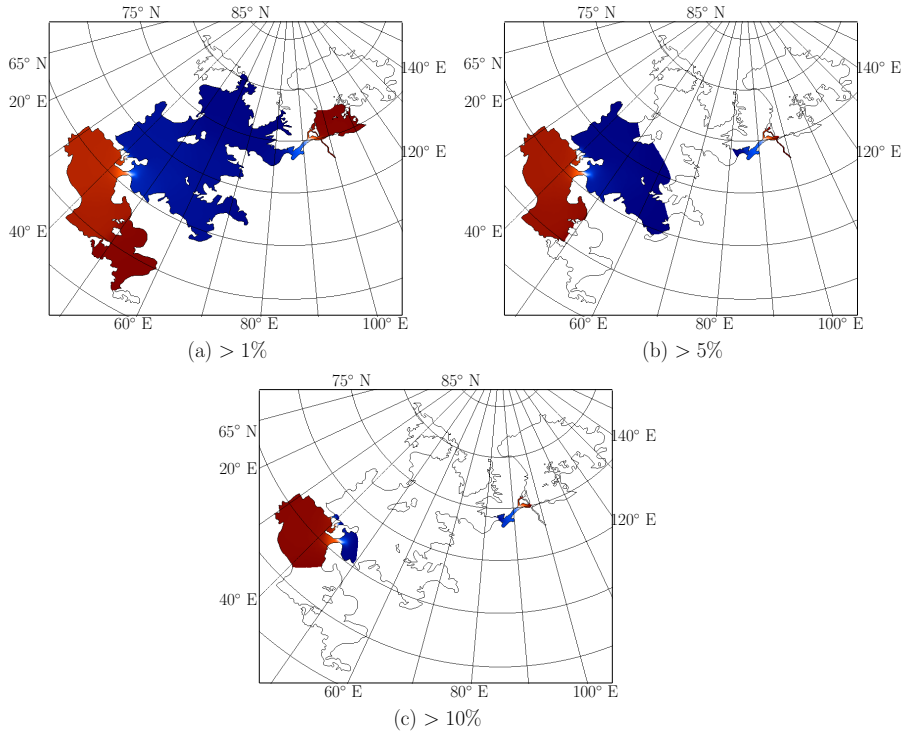

Fig. 5.8: Tracing experiment to illustrate the fluid exchanges between the basins of the northern Maria. The coloured areas are the regions where at least 1% (Panel (a)), 5% (Panel (b)), and 10% (Panel (c)) of the liquid comes from the adjacent basin(s) after 150 TD. The mixing of Ligeia Mare is very slow while it is fastest in Kraken 2.

at one (at least) of Trevize Fretum outlets.

5.3.3 The canyons of Ligeia Mare

In this section, we investigate the tidal current and sea surface elevation in the canyons studied by Poggiali et al. (2016). We show that the tides do not play a significant role in filling these canyons. As no information is available about the liquid depth in these canyons, the bathymetry is derived similarly to that of Ligeia Mare. Near

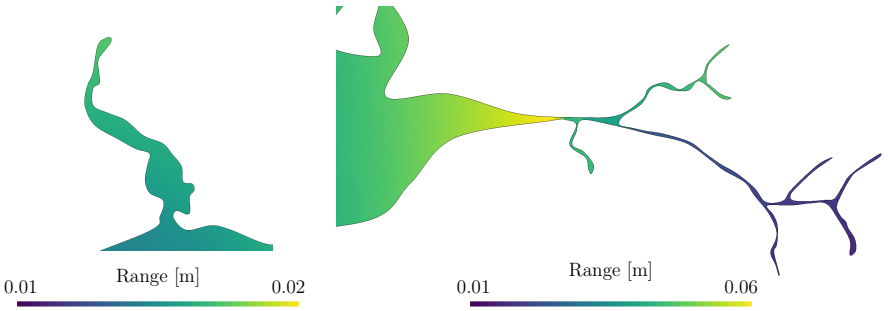

(a) Tidal range - Xanthus Flumen (b) Tidal range - Vid Flumina

Fig. 5.9: Tidal range in canyons near Xanthus flumen (a) and near Vid Flumina (b) for the reference case. The areas shown in these figures correspond to red rectangles D and C in Fig.1.

Vid Flumina, it results in a maximum depth of 2.3 m, the mean depth being about 1 m while the maximum depth is about 6.5 m near Xhantus Flumen. This bathymetry does not take into account the slope of the bottom of the canyons, the latter being unknown: Poggiali et al. (2016) predicted that the liquid surface is at the same level as in Ligeia Mare with an error of about 0.7 m.

The maximum sea surface elevation in the canyons is about 0.034 m, which does not significantly modify the liquid depth at this location and cannot be detected by any Cassini instrument. At the time of the flyby analysed by Poggiali et al. (2016) (T91, at a true anomaly of 69°), the tide was high in the canyons: the sea surface elevation was between 0.009 m and 0.02 m in the canyons near Vid Flumina while it was between 0.027 m and 0.031 m in those located next to Xanthus Flumen. Unfortunately, such variations are too small to be observed by means of the radar whose precision along the vertical axis is about 0.7 m (Poggiali et al., 2016). There is no discontinuity between the tides in the canyons and in Ligeia Mare: the liquid motion in the canyons is induced by the tides of Ligeia Mare. In both canyons, the only significant tidal component is the first harmonic (see Fig. 5.9). The maximum velocity in the canyons near Vid Flumina is 0.064 m/s and occurs at the mouth of

the dendritic network, where the canyon is narrow. Except for this location and at the mouth of the southern canyon, the speed is lower than 0.04 m/s. In the canyon near Xanthus Flumen, the speed is lower than 0.012 m/s. In the light of such predictions and as we do not take into account the slope in the canyon, it is highly unlikely that the presence of liquid in these canyons is due to the tides. Nonetheless, those conclusions may be put into question if there are significant discrepancies between the bathymetry implemented in the numerical model and the real bathymetry.

5.3.4 Moray Sinus and the "Magic Islands" phenomenon

In this section, we detail the tidal response of the northern seas in regions where transient features were observed and in a bay west of Trevize Fretum, Moray Sinus. The "Magic Islands" phenomenon was observed both in Kraken and Ligeia Maria. Nevertheless, Hofgartner et al. (2016) suggested that, in Ligeia Mare, the phenomenon is independent from the diurnal tide. Consequently, it is not of a particular interest to study accurately these areas.

In Kraken Mare, the "Magic Island" was observed at (73°N, 55°E) between T91 and T104 flybys. The true anomaly of Titan during these flybys was 69° and 246° respectively, which correspond to a variation of 177°, almost half a Titan day. Consequently, diurnal phenomena such as the tides cannot be ruled out. In this area, tidal components other than the diurnal one are not significant and, hence, can be disregarded. The sea surface elevation variation between both flybys is about 0.1 m, which is too small to explain the phenomenon. The tidal currents in this area are weaker than 0.029 m/s (the maximum occurs near the shores of the nearby island).

Other phenomena related to the tides such as sediment/solid body transport could explain the "Magic Island" in both seas. Burr et al. (2006); Misiura and Czechowski (2015) showed that sediment transport could be an active process on Titan and the suspended

load is the main means of transport in Titan's rivers. Suspended sediments could locally increase the turbidity of an area, resulting in variations of the sea backscattering properties. Unfortunately, conducting a study of sediment transport in the northern seas would require unavailable data such as an exhaustive list of the rivers, their discharge, the sediment load, and the sediment characteristics. While a study of the various plausible scenarii could be of interest in the areas where the "Magic islands" were observed, it is beyond the scope of this thesis. Another explanation could be local variations of the sea surface roughness. This could be studied by means of a wave model such as SWAN (Simulating WAves Nearshore, see Booij et al. (1997)). Coupling SWAN with SLIM would allow studying the waves in the northern seas and more specifically in the areas of interest. Such a model would also require an *a priori* knowledge of the surface wind at the time of the observations as the wind is a key parameter when studying wave generation and propagation. Using SWAN to predict the sea surface roughness would allow validating/rejecting this explanation. This approach has the advantage of requiring no additional data – the surface wind can be predicted by means of a mesoscale model – and can therefore be conducted without waiting for data from another exploration mission. Coupling SWAN with SLIM is a complex task which is beyond the scope of this thesis[5].

In Moray Sinus, the bathymetry is amphitheater-shaped with a maximum depth (45 m) at the inlet. The main tidal component is diurnal and the tidal range ranges from 0.17 to 0.225 m. The flow is really weak except in the narrow part at the northern end of Moray Sinus where it can reach 0.058 m/s. In both areas, no capillary waves are expected, the tidal flow being too small.

[5]A PhD student of the SLIM research group recently started working on this coupling. The results are encouraging but the model has not been modified to be applied on Titan, yet.

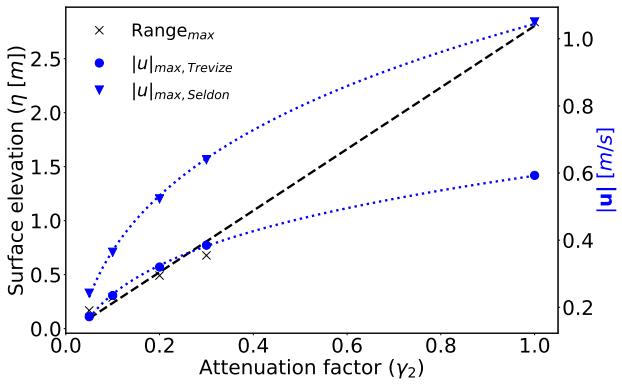

Fig. 5.10: Maximal tidal range (cross, in m) and maximum fluid speed in Trevize (circle, in m/s) and Seldon (triangle, in m/s) Fretum as function of the attenuation factor γ_2. The dashed and dotted lines are respectively a linear and a quadratic mean square root approximation.

5.4 Influence of the model parameters

In this section, a sensitivity analysis to the poorly constrained parameters γ_2, the depth of Trevize Fretum, the bathymetry of Kraken Mare, and the bottom friction is conducted. We also present our results when a bathymetry mimicking that shown in Fig. 9a of Hayes (2016) is used in Ligeia Mare. The main results are summarised in Table 5.2 and Table 5.3. The reference values are $\gamma_2 = 0.1$, $n = 0.03$ sm$^{-1/3}$, and a bathymetry scaling with the distance to the shore, which corresponds to the results presented in Section. 5.3.

5.4.1 Influence of the attenuation factor γ_2

We discuss the influence of the attenuation factor γ_2 on the tidal response in Ligeia and Kraken Maria. In order to take into account the wide range of values of Love numbers found in the literature (see Section 5.2.1), we study γ_2 for values ranging from 0.05 to 0.3.

The maximum tidal range is an increasing function of the attenuation factor within the studied range (see Fig. 5.10). The maximum surface elevation (and tidal range) occurs at the same location and at the same time (0.31 TD after perikron) whatever the value of γ_2 (see the video entitled "Northern_seas_sse_gamma2" in the additional content of Vincent et al. (2018)), which is not the case for the maximum speed. Indeed, although the latter remains located in Seldon Fretum, the time slightly varies with γ_2: the higher γ_2, the later the maximum speed occurs (there is a time lag of 0.045 TD between $\gamma_2 = 0.05$ and 0.3). The opposite is observed in Trevize Fretum: the higher γ_2, the earlier the maximum speed occurs in the strait. In Seldon and Trevize Fretum, the maximum speed behaves like a square root with respect to γ_2: it increases and seems to tend toward a constant value (see Fig. 5.10). The increase is larger in Seldon Fretum than in Trevize Fretum: the maximum speed is respectively multiplied by 2.64 and 2.24 between $\gamma_2 = 0.05$ and 0.3. This may be interpreted as follows: at some point, the geometry of the strait prevails the tidal forcing concerning the maximum speed. In the seas, the speed also increases with γ_2 but it remains of the same order of magnitude whatever the value of γ_2 except at some specific locations such as capes, peninsula, islands or smaller straits. The flow orientation can change locally when γ_2 varies but the global patterns of the flow remain identical.

The most significant changes induced by γ_2 variations are the modifications in the phase and range of the first tidal component. For instance, for $\gamma_2 \geq 0.2$ a second amphidromic point appears (see Fig. 5.11 (b)). It is located in the south-western part of Kraken 2. The existence and the position of such amphidromic points are clearly related to the value of γ_2. Between $\gamma_2 = 0.05$ and $\gamma_2 = 0.3$, the amphidromic point moves by about 201 km in Kraken 1 while, between $\gamma_2 = 0.2$ and $\gamma_2 = 0.3$, it moves by about 37 km in Kraken 2. In Kraken 1, the amphidromic point moves north-westwards as γ_2 increases except for the transition between $\gamma_2 = 0.05$ and $\gamma_2 = 0.1$ where it moves north-eastwards. In Kraken 2, it moves south-eastwards (see Table 5.2). As a consequence of this displacement,

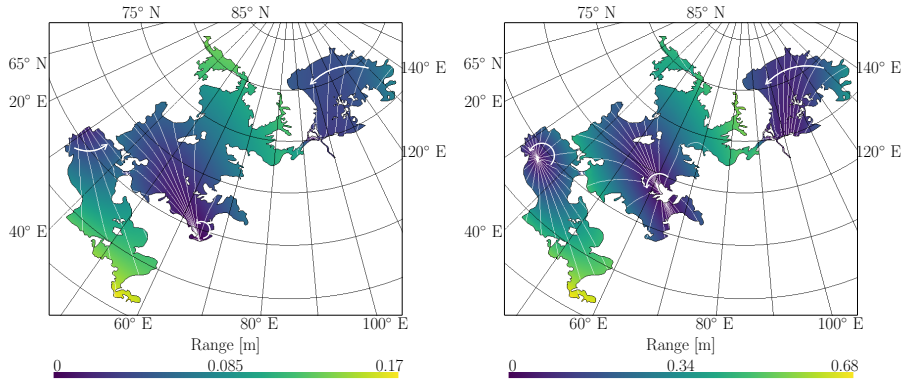

(a) Tidal range and phase for $\gamma_2 = 0.05$

(b) Tidal range and phase for $\gamma_2 = 0.3$

Fig. 5.11: Tidal range (in m) and tidal phase (white lines, with a 15° spacing) in Kraken and Ligeia Maria for $\gamma_2 = 0.05$ (a) and $\gamma_2 = 0.3$ (b). The white arrows show the direction of the diurnal tide. The maximum tidal range remains located in the south-eastern part of Kraken 2 but increases with respect to γ_2. The displacement of the amphidromic point in Kraken 1 is noticeable likewise the one which appears in Kraken 2. It results in an increase of the tidal range on the southern shore of Kraken 1.

the tidal range can locally decrease although γ_2 is increasing. The shape of the corange lines does not change with γ_2: it remains an ovoid centred on the amphidromic point. Consequently, their orientation locally varies with γ_2 as the amphidromic point moves. It also results in much stronger variations (in tidal range and phase) in the strait linking both basins of Kraken Mare. The variations of the tidal phase and displacement of these amphidromic points are due to a side effect of the variation of γ_2: the resulting modifications of liquid exchanges and, hence, the volume variation of each basin (see Fig. 5.13). Indeed, if we look at an enclosed basin (i.e. without liquid exchange with others basins), there is no variation of the tidal phase or amphidromic point displacement when γ_2 varies.

Variations of γ_2 strongly modify the amount of liquid exchanges between the basins through Seldon and Trevize Fretum, see Fig. 5.12.

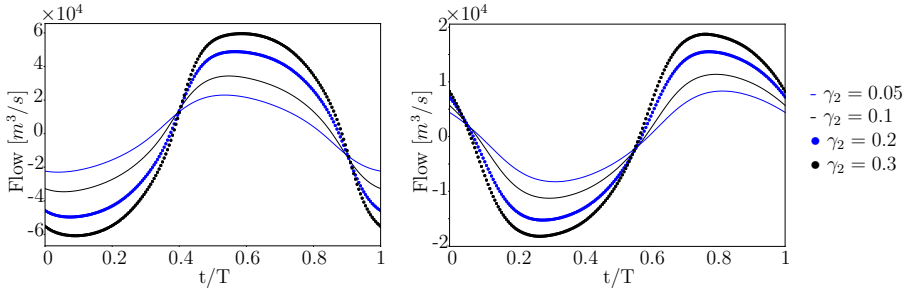

(a) Seldon Fretum (b) Trevize Fretum

Fig. 5.12: Volumetric flow rate through Seldon (a) and Trevize Fretum (b) over one Titan day for γ_2 ranging from 0.05 to 0.3. In Seldon and Trevize Fretum, it is respectively positive toward Kraken 1 and Ligeia Mare. In each strait, the volumetric flow rate increases with γ_2 and a small time lag appears.

The volumetric flow rate over a Titan day is respectively multiplied by 2.87 and 2.37 between $\gamma_2 = 0.05$ and $\gamma_2 = 0.3$ (see Table 5.3) and it does not reach its maximum at the same time of the day, which is consistent with the behaviour of the velocity field. These effects are also noticeable when looking at the volume variation over the basins (i.e, Kraken 1, Kraken 2 and Ligeia Mare): the larger γ_2, the larger the volume variation (see Fig. 5.13). For instance, the maximum volume variation in Kraken 1, Kraken 2 and Ligeia Mare are multiplied by 2.37, 2.89, and 2.55 between $\gamma_2 = 0.05$ and $\gamma_2 = 0.3$. A small time lag in volume variation is also observed between each value of γ_2. Except for $\gamma_2 = 0.05$, for which it occurs in Kraken 1, the maximum volume variation occurs in Kraken 2 (Fig. 5.13).

These results allow us to assess that the attenuation factor has not only an impact on the surface elevation and the velocity (magnitude and orientation) at a given point but it also affects the tidal phase and the global behaviour of the tides in the northern seas. This proves that the deformability of Titan's surface has a significant influence on the tides in the northern seas.

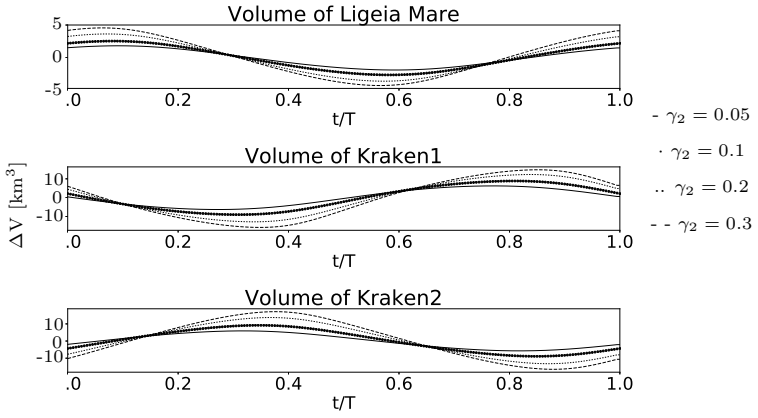

Fig. 5.13: Variation of volume in both basins of Kraken Mare and Ligeia Mare over one Titan day. In each basin, a time lag appears and the maximum volume variation rises when γ_2 increases.

5.4.2 Influence of the depth of Trevize Fretum

Following the work of Tokano et al. (2014) who investigated the influence of the depth of Seldon Fretum on the tidal response of the northern seas, we study the tidal response of the Maria for three additional constant depths of Trevize Fretum: 10 m, 20 m, and 50 m which are referred to as *Trevize A*, *Trevize B*, and *Trevize C* (the maximum depth in the reference case is 15 m). Indeed, Tokano et al. (2014) established that modifying the depth of Seldon Fretum results in a phase lag (up to 90°), modifications of the flow in the strait, displacement of the amphidromic point observed in Kraken 1, and variations of the liquid exchanges between both basins of Kraken Mare.

As shown in Table 5.3, for $H = 10$ m, there is no significant variation in sea surface elevation (and, hence, in tidal range) and fluid speed with respect to the reference case except in Trevize Fretum where the maximum speed decreases by 0.033 m/s. The maximum sea surface elevation and tidal range remain located in the south-eastern part of Kraken 2 and occur at the same time (see

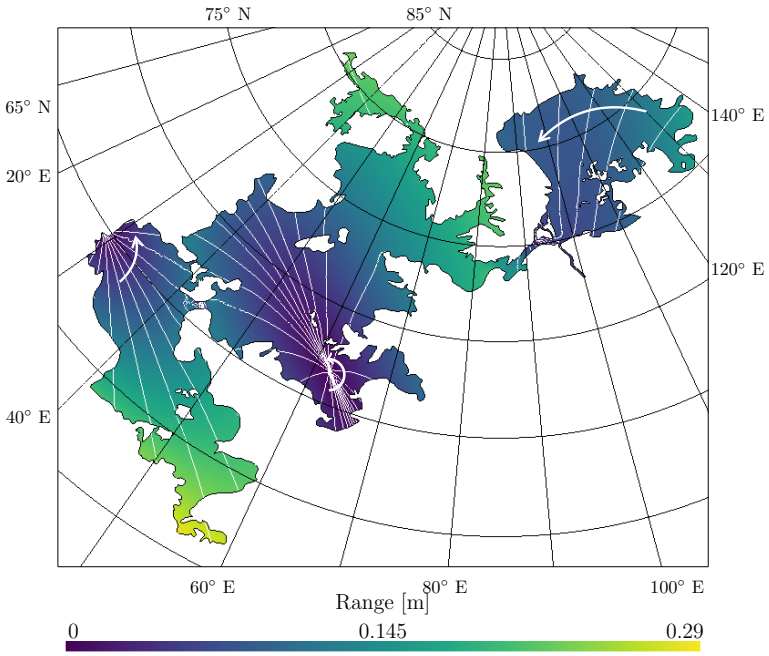

Fig. 5.14: Tidal range (in m) and tidal phase (white lines, with a 15° spacing) in Kraken and Ligeia Maria for $H = 10$ m. The white arrows show the direction of the diurnal tide. The latter rotates anticlockwise and the amphidromic point in Kraken 1 moved with respect to its location for the reference case. The location and value of the maximum tidal range do not change significantly with respect to the reference case.

Fig. 5.14). The main variation is a small displacement of the amphidromic point in Kraken 1 (it moves north-westwards by about 103 km), which does not impact significantly the shape of the corange lines.

For $H = 20$ m and $H = 50$ m, there are much more variations with respect to the reference case. First, although the sea surface elevation remains high in the south-eastern part of Kraken 2 (about 0.136 m for *Trevize B* and 0.151 m for *Trevize C*) at the same time, this is no longer the maximum. Indeed, η is maximum in the eastern part of Ligeia Mare respectively 0.02 TD and 0.16 TD

before perikron. As a consequence, the maximum tidal range also occurs in the eastern part of Ligeia Mare, at the location where the local maximum in Ligeia Mare was previously reached, and there are significant modifications of the tidal phase (see Fig. 5.15 (a) and 5.15 (b)). The modifications mainly take place in Kraken 1 and Ligeia Mare. Indeed, in Kraken 2, the tidal range at a given point change by less than 0.01 m and the lag in the tidal phase is small, about 6°-7°. In contrast, in Kraken 1, modifications of H involve a large displacement of the amphidromic point north-westwards: this point moves by 430 km with respect to the benchmark for $H = 20$ m (it is located in the south-western region of Kraken 1) and, for $H = 50$ m, there is no amphidromic point in Kraken 1 (the shape of the lines of constant tidal phase seems to imply that it would be located somewhere on the land, south of Mayda Insula). For *Trevize C*, the tidal phase pattern suggests that, to a large extent, the tidal motion in each basin can be represented by a sloshing wave mode. Indeed, the tidal phase is nearly uniform over large geographical areas while there are strong variations (sometimes by about 180°) over the straits connecting those basins (see Fig. 5.15 (b)). The displacement of the amphidromic point explains the modifications of tidal range and phase observed in Kraken 1, i.e. the tidal range decreases on the northern shore and increases on the southern shore of the basin. In Ligeia Mare, increasing the depth of Trevize Fretum results in a larger tidal range. For *Trevize C*, the tidal range in Ligeia Mare is larger than everywhere else in Kraken Mare. This observation holds for *Trevize B* except for the south-eastern part of Kraken 2 (where the tidal range is maximum in the benchmark). In Trevize Fretum, the transition is different for $H = 20$ m: the tidal range is smaller in the strait than at both outlets. This phenomenon is not observed with *Trevize A* and *C*. The other main difference in this strait occurs for $H = 50$ m. Indeed, for such a depth, the tidal phase in Kraken 1 and Ligeia Mare are continuous. It means that the tidal motion in Ligeia Mare is no longer independent from that in Kraken 1. Indeed, for the benchmark, *Trevize A*, and *Trevize B*, the tidal phase in Ligeia Mare respectively is about $-70°$, $-52°$,

and $-5°$ which is significantly smaller than the tidal phase in the northern part of Kraken 1 (about 100°, 100° and 115°) while, for $H = 50$ m, the tidal phase in Ligeia Mare is about 75° and increase toward Kraken 1 (but there is no transition observed in Trevize Fretum). The fact that the tides in Ligeia Mare and Kraken 1 are no longer independent can also be observed by looking at the sea surface elevation (see the video entitled "Northern_seas_sse_50m" in the additional content of Vincent et al. (2018)): for the reference case and *Trevize A and B*, there is a significant elevation gradient in both Seldon and Trevize Fretum while such a gradient is only observed in Seldon Fretum for *Trevize C*.

The depth of Trevize Fretum has a small influence on the fluid velocity out of the straits. Indeed, although some local variations in current orientation can be observed, the global patterns remain the same (not shown). The speed increases offshore in Ligeia Mare for *Trevize B and C*, which is consistent with the sea surface elevation. The latter being doubled, the liquid transport is more significant and the same applies to the fluid speed. In Trevize Fretum, the speed exceeds that of the reference case only for *Trevize B* (see Table 5.3).

The modification of Trevize Fretum depth logically results in variations of liquid exchanges between the basins. In Seldon Fretum, there is almost no variation for *Trevize A* while for *Trevize B* and *C*, a time lag of about 0.06 TD appears and the maximum volumetric flow rate respectively decreases and increases by 5.5% and 21.3% (see Fig. 5.16). The impact on the volume variation of Kraken 2 is similar: almost no variation for $H = 10$ m and a time lag and a decrease/increase of maximum volume variation for $H = 20,\ 50$ m of respectively 4.7% and 22.4%. As expected, modifying the depth of Trevize Fretum has a significant influence on the flow crossing this strait. A significant increase of the volumetric flow rate and a time lag can be observed for all implemented depths of Trevize Fretum. The maximum volumetric flow rate respectively represents 154%, 420%, and 605% of the volumetric flow rate going through Trevize Fretum in the reference case for *Trevize*

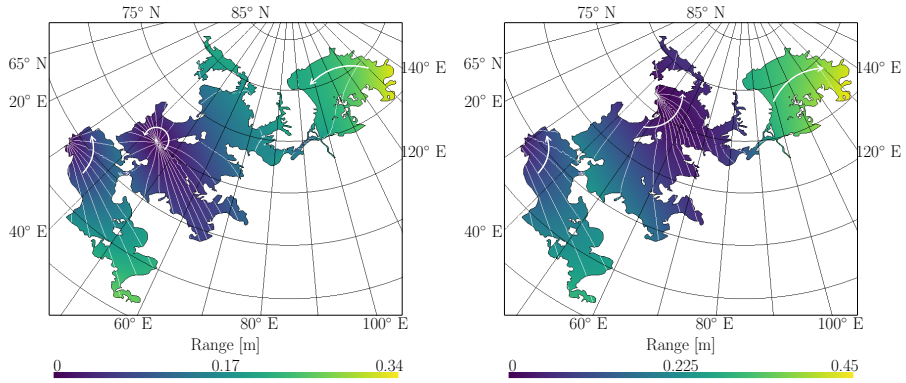

(a) Tidal range and phase for $H = 20$ m

(b) Tidal range and phase for $H = 50$ m

Fig. 5.15: Tidal range (in m) and tidal phase (white lines, with a 15° spacing) in Kraken and Ligeia Maria for $H = 20$ m (a) and $H = 50$ m (b). The white arrows show the direction of the diurnal tide. For $H = 20$ m, there is a significant displacement (about 425 km) of the amphidromic point: it is now located near the western shoreline of Kraken 1 (70.06°N, 44.49°E). For $H = 50$ m, there is no amphidromic point in any basin of the Maria and no tidal phase transition through Trevize Fretum. In both case, the tidal range is now maximum in the eastern part of Ligeia Mare although it remains high in the south-eastern part of Kraken 2.

A, B and *C*. The maximum volumetric flow rate is not a linear function of the depth. This implies that the liquid exchanges between the basins would be constant if the strait was deeper than a certain limit (which is larger than 50 m). This result was also observed in Seldon Fretum by Tokano et al. (2014). Despite the fact that the volumetric flow rate crossing Trevize Fretum increases with the depth of the strait, this is not the case for the maximum volume variation of Kraken 1. Indeed, the latter slightly decreases when the depth increases and is smaller than the reference case for each *Trevize*. For *Trevize A, B,* and *C*, the volume variation in Kraken 1 represent about 97%, 93%, and 86% of ΔV for the reference case (see Table 5.3). As shown in Fig. 5.17, the major impact of H on

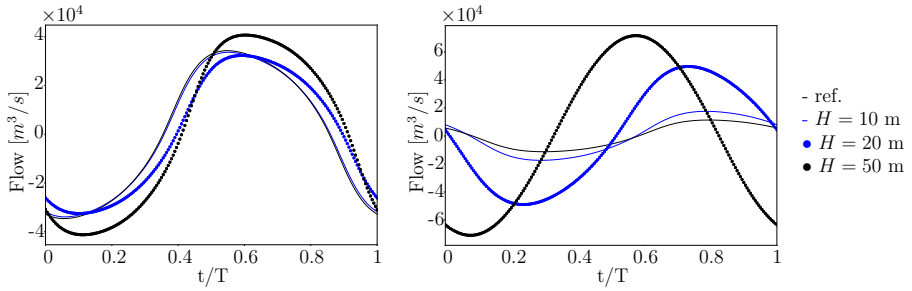

(a) Seldon Fretum (b) Trevize Fretum

Fig. 5.16: Volumetric flow rate through Seldon (a) and Trevize Fretum (b) over one Titan day for the reference case and the three depths implemented. In Seldon and Trevize Fretum, it is respectively positive toward Kraken 1 and Ligeia Mare. The volumetric flow rate in Seldon Fretum is less sensitive to this parameter than that in Trevize but it still increases and is lagged when H varies. The volumetric flow rate in Trevize Fretum increases with H and a time lag appears.

the volume variation in Kraken 1 is a time lag (much more significant than that observed for the volumetric flow rate in Trevize Fretum). The latter increases with the depth of the strait and can reach up to about 0.55 TD. A significant time lag is also observed in Ligeia Mare. It is the only basin of the Maria where the volume variation significantly increases with H: ΔV increases respectively by a factor 1.57, 4.28 and 6.24 with respect to the reference case for *Trevize A, B* and *C*.

The time lag and modifications of volume variation resulting from the various depths also cause change in the period of time during which the sea surface elevation is positive or negative over a whole basin. There are some changes in Kraken 2: the period of time can last slightly longer (at most 0.135 TD) and a small time lag can be observed (at most 0.055 TD) but they remain minor in comparison to the variations in Ligeia Mare. Indeed, in this Mare, the period of time during which the elevation is positive (negative) over the whole domain lasts longer and longer when H

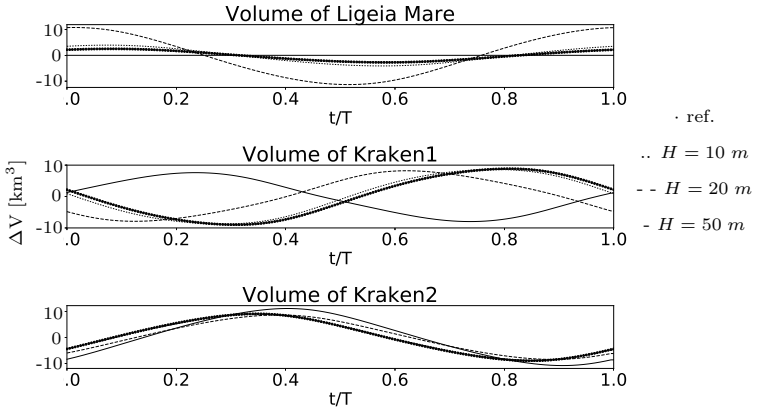

Fig. 5.17: Variation of volume in the basins of Kraken and Ligeia Maria over one Titan day. The impact of H on the volume variation is weak in Kraken 2 while it results mostly in time lag in Kraken 1. In Ligeia, the maximum volume variation increases by a factor of about 6 between $H = 50$ m and the reference case.

is increased: in contrast to the reference case, these two periods of time combined last longer than half a Titan day for *Trevize A, B,* and *C* (respectively 0.535, 0.83 and 0.9 TD). For *Trevize A* and *Trevize B* the period of time ends 0.02 TD later than for the reference case and start earlier (respectively 0.045 and 0.19 TD) while, for *Trevize C*, the period of time starts and ends earlier (respectively 0.395 and about 0.19 TD.

5.4.3 Influence of the bottom friction

We study the influence of the bottom friction on the tidal response in Ligeia and Kraken Maria by varying Manning's roughness coefficient, n. The values studied range from 0.01 to 0.06 $\mathrm{sm}^{-1/3}$, which correspond to artificial and natural bottom with stones on Earth respectively. As it can be seen in Table 5.3, the flow slows down as Manning's coefficient rises. A time lag also occurs: for $n \geq 0.03$ $\mathrm{sm}^{-1/3}$ the maximum speed in Trevize and Seldon Fre-

tum are respectively reached earlier and later than for the reference case while their is no global behaviour for $n \leq 0.02$ sm$^{-1/3}$. As the volumetric flow rate decreases through Seldon and Trevize Fretum, the same also applies to the volume variation of each basin. As was seen before, the latter has a significant impact on the position of the amphidromic point and can modify the sea surface elevation accordingly. For instance, for $n = 0.04$ sm$^{-1/3}$, there is an amphidromic point both in Kraken 1 and 2 while for $n = 0.01$ sm$^{-1/3}$, there is no amphidromic point (see Table 5.2). Modifying n thereby results in changes of the tidal range and phase almost everywhere in the Maria: the tidal range decreases as n increases and, in Kraken Mare, it can locally change due to the displacement of the amphidromic point. Nevertheless, the maximum remains located at the same place and occurs at the same time.

The impact of a spatially varying bottom roughness is also studied. To this end, two numerical simulations are conducted with Manning's roughness coefficient randomly varying between 0.0001 and 0.06 sm$^{-1/3}$ and between 0.02 and 0.04 sm$^{-1/3}$, respectively. In the first case, the maximum elevation is smaller, by 0.015 m, and occurs slightly later. The main patterns of the velocity field are not impacted but the speed can locally increase/decrease, depending on the local value of Manning's coefficient. The maximum speed can therefore be observed at a different location and time. The liquid exchanges decrease slightly but the variations are smaller than those observed between the liquid exchanges predicted for two constant values of Manning's coefficient. In the case of n randomly varying between 0.02 sm$^{-1/3}$ and 0.04 sm$^{-1/3}$, there is no significant variations of the liquid exchanges and sea surface elevation with respect to a uniform $n = 0.03$ sm$^{-1/3}$. The speed can locally increase/decrease depending on the local roughness coefficient but the differences are small and do not impact significantly the daily flow in the straits.

5.4.4 Influence of the artificial bathymetry

As explained in Section 5.2.2, a bathymetry map of Ligeia Mare is available in the literature (see Fig. 9a of Hayes (2016)). We hereby discuss to what extent an artificial bathymetry is justifiable by comparing our results obtained for the reference case to those predicted by our model when a bathymetry mimicking the bathymetry map shown in Fig. 9a of Hayes (2016) is implemented. Although the maximum depth is of the same order of magnitude for both bathymetries, there is a feature similar to a seamount near $80°N$ and Ligeia Mare is much deeper near the shore according to the bathymetry map of Hayes (2016), resulting in a higher total volume of the sea. Increasing the total volume of Ligeia Mare results in a significant modification of the liquid exchanges with Kraken Mare: the daily flow crossing Trevize is doubled. This results in almost no variation in Kraken 2: the maximum tidal range is increased by 0.008 m, there is a small phase shift in the western part of the basin, and the maximum volume variation slightly decreases. In Kraken 1, the maximum volume variation decreases by 22% and it occurs sooner in the tidal period. As seen previously, such modifications result in a displacement of the amphidromic point. The latter is now located 233 km westwards of its location in the reference case. In Ligeia Mare, there is a significant increase of the maximum tidal range (by 0.07 m, leading to a tidal range of 0.21 m) and maximum volume variation (it is doubled) but the tidal motion remains similar. The velocity orientation can vary locally but its magnitude is globally smaller, except in Trevize Fretum where it increases.

Modifying the bathymetry of Ligeia Mare (and, hence, increasing its total volume) results in variations with respect to our reference case, the main one being a significant modification of the flow through Trevize Fretum and, hence, of the volume variation in Ligeia Mare and Kraken 1. Regarding the tidal motion, the main modification is the shift of the amphidromic point in Kraken 1. Nevertheless, the global tidal motion remains similar to that of the reference case: the tidal motions remain independent of each

other in each basin and the main flow keeps its global orientation. Consequently, we consider the artificial bathymetry as justifiable for the simulation of Titan's northern seas as part of a sensitivity study.

5.4.5 Influence of the bathymetry scaling factor

Due to the uncertainties in the bathymetry, we also conduct a study of the influence of Kraken Mare overall depth. To this end, we create two additional bathymetries *bathy A* and *bathy B* (see Section 5.2.4).

As expected, modifying the total volume of Kraken Mare basins results in modifications of the volume variation and, hence, the flow through Seldon and Trevize Fretum and the tidal phase. Diminishing/increasing the overall depth of Kraken Mare results in a reduction/rise of the tidal range, volume variation and daily flow rate through the straits. These effects are more significant in Kraken 1 and 2 and in Seldon Fretum than in Ligeia Mare and Trevize Fretum (see, for instance, the values in Table 5.3). For instance, with *bathy B*, the tidal range decreases by 9 cm at its maximum while it decreases by less than 2 cm in Ligeia Mare. As pointed out previously, modifications of the volume variation result in significant modifications of the tidal phase in the basins. For *bathy A*, it results in a shift of the amphidromic point of 334 km westwards while the pattern of the tidal phase remains similar in Kraken 2 and Ligeia Mare; although the value of the tidal phase at a given location varies (see Fig. 5.18 (a)). For instance, the maximum sea surface elevation occurs 0.055 TD later than in the reference case. For *bathy B* on the other hand, the amphidromic point shifts by 271 km northwestwards in Kraken 1 and a second amphidromic point appears in Kraken 2 (see Fig. 5.18 (b)) which results, among other things, in a maximum sea surface elevation occurring 0.075 TD sooner than in the reference case.

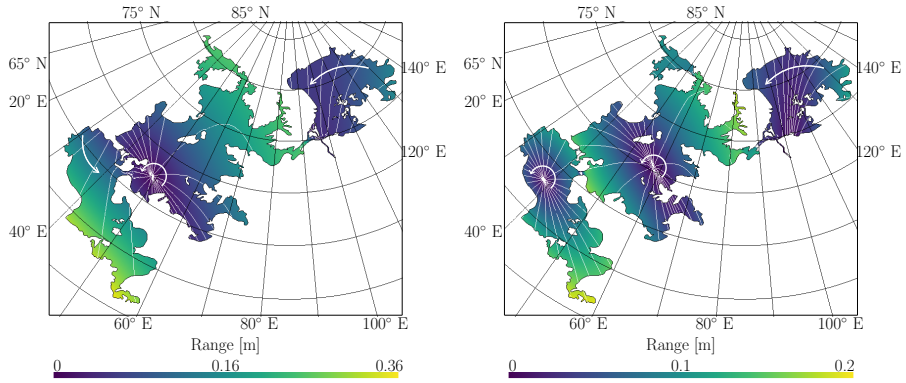

(a) Tidal range and phase for *bathy A*

(b) Tidal range and phase for *bathy B*

Fig. 5.18: Tidal range (in m) and tidal phase (white lines, with a 15° spacing) in Kraken and Ligeia Maria for *bathy A* (a) and *bathy B* (b). The white arrows show the direction of the diurnal tide. The maximum tidal range remains located in the south-eastern part of Kraken 2. The displacement of the amphidromic point in Kraken 1 is noticeable likewise the one which appears in Kraken 2.

Using *bathy A* or *bathy B* can also result in local variations of the flow orientation (although the global patterns remain similar) and magnitude: the maxima remain located in the straits but they occur at different moments of the day. The maximum speed respectively increases/decreases for *bathy A*/*bathy B*.

Those results allow us to conclude that modifying significantly the total volume of Kraken Mare has a significant effect on the liquid exchanges between the basins and, hence, on their volume variation and tidal phase but the tidal motions remain independent of each other in each basin and the main flow keeps its global orientation.

5.5 Discussion

5.5.1 Influence of the model parameters

Due to uncertainties about the specific environment of Titan, various parameters of the model are poorly constrained. Some of them such as the mean density are not considered here (Vincent et al. (2016) showed that their influence on the tides is not significant) while others such as the attenuation factor and Manning's roughness coefficient are discussed in this section. In addition to these parameters, the influence of the depth of Trevize Fretum and the overall bathymetry of Kraken Mare, which are unknown to this day, are also discussed.

The depth of Trevize Fretum has a significant impact on the tidal response of the Maria. Indeed, modifying the depth of this strait results in variations of the sea surface elevation, fluid velocity, and tidal phase and range in both Ligeia Mare and Kraken Mare. The results obtained with the four depths (three constant depths and the reference case) show that the volume variation of Kraken 2, Ligeia Mare, and, to a lesser extent, Kraken 1 significantly varies with the depth of Trevize Fretum. Tokano et al. (2014) reached similar conclusions about the depth of Seldon Fretum: it significantly impacts the volume variation of both basins of Kraken Mare. They also observed the same induced variations: displacement of the amphidromic point(s), local modifications of the sea surface elevation, modification of the speed in the straits, and time lag up to 0.25 TD.

As explained in Section 5.2.1, solid tides attenuate the liquid tides in the surface seas, which is taken into account in this work by means of an attenuation factor γ_2. The tidal range linearly varies with γ_2 while the fluid speed in the straits behaves as a square root with respect to γ_2 (see Fig. 5.10). Changing γ_2 also results in displacement of amphidromic point(s) in both basins of Kraken Mare (but not in Ligeia Mare). Nevertheless, this seems to be a phenomenon induced by another effect: when γ_2 increases, the volumetric flow rates through Seldon and Trevize Fretum and

the volume variation in each basin also rise, which influences the location of the amphidromic point(s) and the tidal phase and range.

The bathymetry of Kraken Mare mostly impacts the tidal motion in Kraken Mare but it also slightly impacts that in Ligeia Mare. Modifying the scaling factor used to compute the bathymetry (see Section 5.2.2) results in displacement and/or appearance of amphidromic points in both Kraken Mare basins, which can be related to the significant variation of the flow rate in the straits linking the basins. The tidal range, maximum volume variation, and flow through the straits increase with the scaling factor.

The influence of the bottom friction is related to the value of Manning's coefficient: for $n \geq 0.03$ sm$^{-1/3}$, the fluid velocity decreases as n increases while for smaller values, no clear pattern can be observed. The consequences of this modification are mostly significant in the straits such as Trevize and Seldon Fretum. It results in variations of the liquid exchanges between the basins of the Maria. As seen previously, such variations induce significant displacement of amphidromic point(s) (leading to the appearance/disappearance of such points) and local modifications of the sea surface elevation and tidal range. For instance, the maximum sea surface elevation decreases by 0.035 m between $n = 0.03$ sm$^{-1/3}$ and $n = 0.06$ sm$^{-1/3}$ (see Table 5.3). Similar effects are observed for a random distribution of Manning's roughness coefficient. Depending on the range of the coefficient variations, the impact can vary. If small variations are assumed (i.e. by less than 0.01 sm$^{-1/3}$ with respect to 0.03 sm$^{-1/3}$), the flow can locally speed up/slow down but without impacting significantly the liquid exchanges between the basins or the sea surface elevation. Larger variation of the roughness coefficient (between 0.0001 sm$^{-1/3}$ and 0.06 sm$^{-1/3}$), results also in local variations of the velocity field but the latter are more significant, hence impacting the liquid exchanges between the basins, which results in a phase lag and local variations of the sea surface elevation. In both cases, the variations with respect to a uniform roughness of 0.03 sm$^{-1/3}$ are smaller than those predicted by varying the roughness coefficient over the whole domain.

Consequently, in order to accurately predict the tides of the northern seas, one would need an accurate knowledge of the straits linking the seas: the depth and the roughness of the bottom both have a significant impact on the liquid exchanges between the basin and, therefore, on the tides of the northern seas. The internal structure of Titan and rheology properties of the layers need also to be accurately known in order to predict as accurately as possible the value of γ_2. An accurate bathymetry is not needed to predict the global picture but is necessary to predict the local flow velocity and the local flow patterns. Depending on the goal of the study, an artificial bathymetry similar to the one used in this chapter is justifiable. Nevertheless, such an artificial bathymetry could be improved if a nearshore bathymetry similar to that derived by Hayes et al. (2010) in Ontario Lacus was available. Indeed, previous results show that, at least in Ontario Lacus, the tidal response computed with such a bathymetry is close to the tidal response predicted with a bathymetry derived from the SAR data (see Vincent et al., 2016).

5.5.2 Density variation between the basins

Although the value of the mean density does not significantly impact the model results, spatial or temporal variations of the density would significantly modify the liquid motion due to the resulting density gradient. Local variations could be induced by meteorological events such as precipitation and evaporation or due to the vertical profile of the absorption of sunlight. Such phenomena were previously studied by Tokano and Lorenz (2016). According to their results, the flow in the straits linking the basins of the northern seas is weaker (by about one order of magnitude) than that induced by the tides while it can be larger in the middle of the basins depending on the light extinction coefficient. Such phenomena are independent from the tides and are either episodic or associated with much longer time-scale. The liquid motion induced by the density gradient could therefore be regarded as constant when studying the tidal motion as it does not modify the tidal forcing nor the parameters

of this model. The tidal forcing, on the other hand, could increase the mixing between the areas of different density, hence modifying the density gradient. This would be very slow. An estuary could also result in a density gradient if the river liquid composition is different. Due to the lack of information about the rivers discharge, it is not possible to predict the estuaries characteristics based on the terrestrial classification (i.e. salt-wedge, fjord, slightly stratified, vertically mixed, and freshwater estuaries), although vertically mixed estuaries could likely be ruled out due to the slow tidal flow. Therefore, the influence of a river on the liquid motion should be studied on a case-by-case basis.

There could also be a liquid composition difference between Ligeia Mare and Kraken Mare due to surface temperature variation with the latitude (Lorenz, 2014). Such a liquid composition variation between Kraken Mare and Ligeia Mare, if exists, would result in a significant density gradient and imply that the tidal mixing between Ligeia Mare and Kraken Mare is too weak to overcome the precipitation/evaporation forcing difference between those seas. The gradient would significantly modify the flow in Trevize Fretum and, hence, the liquid exchanges between Ligeia Mare and Kraken Mare. Such density counterflows are also encountered on Earth (e.g. in the Strait of Gibraltar). Paradoxically, the resulting mixing could be more significant than the tidal mixing but would not be strong enough to prevent the liquid composition difference. It could explain the smaller liquid opacity in Moray Sinus with respect to the rest of Kraken Mare. The tides can be studied apart from this phenomenon as it does not modify the tidal forcing nor the parameters of this model. While the tidal motion is not influenced by such a density gradient, it would significantly modify the velocity field in the area and it should be taken into account to study the global liquid motion in this area. To this end, an *a priori* knowledge of the present density spatial distribution is needed. Such data are not available. Therefore, the mean density of each basin could be used as initial condition but it would require lengthy and costly numerical simulations to reach an equilibrium solution

and the latter could differ from the reality due to the lack of data about the precipitation/evaporation events and the influence of the delimitation between the basins in the initial condition.

5.5.3 Shoreline

We implement the shoreline from radar images. Nevertheless, the whole shoreline is not mapped in high resolution which makes it difficult to accurately draw it. Moreover, the radar interprets some shallow areas as dry ground. This results in uncertain shorelines. For instance, our implementation differs from Tokano et al. (2014) in various respects:

- Trevize Fretum is implemented as an elongated (200 km) narrow (15 km) strait with small channels near Ligeia outlet instead of a set of short (150 km) and narrow (20 km) straits.
- The link between both basins of Kraken Mare next to Seldon Fretum is represented by two narrow channels instead of a wide connexion with two small islands.
- We take into account some islands ignored by Tokano et al. (2014): in the southern part of Ligeia Mare, the middle of Kraken 2, and the east of Kraken 1 (see Fig. 1 in Tokano et al. (2014))

The interpretation of Lorenz et al. (2014) is different from both ours and Tokano's: the global shape of the shoreline and the islands of Lorenz et al. (2014) are closer to that used by Tokano et al. (2014) but our implementation of Seldon and Trevize Fretum is closer to that of Lorenz et al. (2014) than to that of Tokano et al. (2014). Such variations of the shoreline are doubly important because our bathymetry (as well as Tokano's) depends on the distance to the shore. Consequently, taking into account an island or ignoring it can significantly modify the bathymetry. Additionally to this effect, the shape of the seas can locally generate high speed currents (near

a cape or a peninsula) and the shape (width and length) of a strait has a significant impact on the liquid exchanges between the basins. In order to enhance the quality of our predictions, a more accurate map of the northern seas shoreline would be needed. Unfortunately, this requests another mission as Cassini dived into Saturn few years ago.

5.5.4 Comparison with previous results

The tidal response of Ligeia and Kraken Maria has already been studied by means of numerical simulation by Tokano (2010) and Tokano et al. (2014). In this section, we compare our results obtained for the reference case with the predictions of Tokano et al. (2014). First of all, we list the discrepancies between our model and that used by Tokano et al. (2014). Then, we compare our results.

In terms of model design, the main difference is that Tokano et al. (2014) used a 3D baroclinic ocean circulation model while we use a 2D barotropic shallow water model. Nevertheless, although Tokano's model is better suited to study complex interactions, it is usually not necessary to have recourse to a 3D model to predict the tidal response of a sea. There are also some minor discrepancies in the shoreline of the Maria which results in local variations of the bathymetry. For instance, in Seldon Fretum, the depth scales with the distance to the shore and the maximum is about 16 m while Tokano et al. (2014) implemented a constant depth of 12 m and the shape of the straits slightly varies (see Section 5.5.3). Despite these discrepancies, the main parameters are similar: the same forcing is applied, $\gamma_2 = 0.1$, and the depth scales with the distance to the shore.

In both simulations, the tides propagate in the same direction (i.e. anticlockwise in Kraken 1, westwards in Ligeia Mare between perikron and perikron + 0.25 TD ...), there is a sharp transition in sea surface elevation in the strait linking both basins of Kraken Mare (η is positive at one outlet and negative at the other at perikron and 0.25 TD later), and an amphidromic point is observed

in Kraken 1 in the same area (the small variation of position could be due to the modification of volume variation in this basin (it has a significant influence on the position of such a point, see Section 5.4.2)). The tidal range predicted in each Mare is maximum at the same location as in Tokano et al. (2014) although it is slightly smaller (0.29 m instead of 0.37 m) in Kraken Mare and slightly larger (0.14 m instead of 0.1 m) in Ligeia Mare. This could be due to the difference in the shape of the small channels near Seldon Fretum (Tokano et al. (2014) implemented it as a wider connection, resulting in larger liquid exchanges between both basins of Kraken Mare) and Trevize Fretum and/or to the fact that the bathymetry of Seldon Fretum is significantly different. This can be seen by comparing the maximum volume variation of each basin: almost the same magnitude is predicted in Ligeia Mare (2.5 km^3 versus about 2 km^3 for Tokano et al. (2014)) while we predict a smaller one in both basins of Kraken Mare. The sea surface elevation at perikron and 0.25 TD after perikron are close to those predicted by Tokano et al. (2014) but there are also some differences: η is high/low at the same locations but the magnitude can vary locally. For instance, the elevation predicted by our model at perikron is smaller in the south-eastern part of Kraken 2 and can be slightly larger in the eastern part of Ligeia Mare. The tidal currents predicted by both models are also similar: it is small offshore and maximum in the strait where it can reach 0.36 m/s and 0.14 m/s according to our model and to Tokano et al. (2014) (for a depth of 12 m). This could be explained by the different characteristics of Seldon Fretum. In the straits, the velocity is directed toward the area where η is the smaller. In conclusion, our results are close to those of Tokano et al. (2014). Although some discrepancies can be observed, they can be linked to the differences between the models, particularly to the variations in the shape and depth of the two main straits, Trevize and Seldon Fretum. Both models have their advantages, that of SLIM being the higher resolution used to represent the shoreline, the wide range of parameters values studied, and the use of tracers to study the liquid exchanges.

We are not able to validate our model by comparison with *in situ* data due to their non-existence. While our results compare well with those published by Tokano et al. (2014), the latter were not validated either. Both models are based on the state-of-the-art knowledge of Titan and take into account the uncertainties by conducting sensitivity analyses with respect to the poorly constrained parameters. Nevertheless, they both use a bathymetry scaling with the distance to the shore. While it seems to be a good approximation based on the measured bathymetry of the surface lakes and seas, it cannot explain the fact that the SAR failed to detect the bottom echo in Kraken Mare (except in Moray Sinus). As demonstrated by our sensitivity analysis, the bathymetry significantly influences the tidal motion. Therefore, a totally different bathymetry could invalidate our results. Similarly to Tokano et al. (2014), we adapted an Earth-based model to Titan's specific conditions assuming that the same phenomenological laws apply. Nothing leads to believe that such an assumption does not stand but, just as Cassini mission invalidated the assumption (based on Voyager's data) of a deep ocean of hydrocarbon near Titan's equator[6], a future mission could disprove this assumption.

5.6 Applications and future missions

As discussed previously, there are a few parameters which remain poorly constrained. One way of improving our model is to get additional data in order to constrain these parameters. Unfortunately, Cassini reached the end of its life and fell into Saturn during its "Grand Finale". Consequently, providing further data about Titan requests to plan further mission(s). So far, various proposals were discussed: a drifted capsule (TiME, see Lorenz et al., 2012), an orbiter and a lake probe (E2T, see Mitri et al., 2014a), a submarine (Titan sub, see Hartwig et al., 2016), and an orbiter (Oceanus, see

[6]This assumption was based on the amount of methane in Titan's atmosphere and on the distribution of liquid bodies on Earth.

Sotin et al., 2017). Among these missions, several (Lorenz et al., 2012; Mitri et al., 2014a; Hartwig et al., 2016) plan to send a vehicle in the northern seas. In order to organise such missions, various above-mentioned results are of high interest: the tidal range is of interest in knowing whether a floating capsule like the Titan Mare Explorer (or related European proposals) could be grounded and refloated from the beach or a tidal flat over a tidal cycle; a particle tracking model can predict the position of a capsule as a function of time and landing time and position; the tidal flow is of interest in order to size the propulsion system of a boat/submarine that should overcome the current in Trevize/Seldon Fretum or to assess over what fraction of the tidal cycle a submarine could or could not sail through the straits.

As a preliminary study, we take advantage of the Lagrangian particle tracker (LPT) module of SLIM to predict the path of a drifted capsule as a function of time and landing sites. The latter were selected arbitrarily and are located either offshore in the three basins or in the straits (see Fig. 5.19(a)). In order to represent the impact of the capsule sea landing time, a capsule lands at each time step (i.e., each 0.005 TD) in each location. The simulation is conducted over three tidal cycles. The predicted paths are a good approximation of the tidally induced motion. The density gradient would modify the liquid motion, hence impacting the paths, but it is not taken into account as the timescale of the phenomena responsible for such a gradient is much longer. Its effect could be modelled by adding a constant velocity field (predicted by a 3D model and corresponding to the specific season or the density variations between the basins) to the tidal flow. The wind is expected to significantly modify the path of the capsule, not only by modifying the velocity field but also by pushing the capsule in a direction that could differ from the flow orientation. This could be modelled by adding the acceleration resulting from this force in the cinematic equations of the LPT and coupling SLIM with a mesoscale atmospheric model. In this case, using SLIM3D would be a significant asset as the surface velocity could differ significantly from the

depth-averaged velocity, which is not the case for the tidal motion. Indeed, the tides being a barotropic phenomenon, the velocity field is not expected to vary significantly with the depth except near the sea bottom, where a boundary layer due to the friction develops.

The capsules positions at different periods are shown in Fig. 5.19. The displacement of the capsules which landed in the middle of the basins is small, less than 1 km over 3 TD except for the capsule located in the south-eastern part of Kraken 1 which moves by 1.1 km. The capsules which landed in the straits follow a longer path but they remain trapped in the straits or near their outlets (see Figs. 5.19(b,c,d)). These capsules follow a back and forth path due to the tidal flow. Only a few percentage can reach the straits' outlets and none of them is able to significantly go far from these outlets over the 3 TD period studied. In the light of these results, a motorised capsule seems better suited than a non-motorised one as it would allow traveling larger distances over a reasonable time and avoiding being trapped in the vicinity of the straits.

Future exploration missions could improve significantly the general knowledge of Titan. Among the observations/data that could be provided, some of them would be useful to validate or improve our model:

- An orbiter could theoretically detect the tides of the surface seas with a precision altimeter and provide a map of the sea surface elevation as a function of time. Such observations on Earth were able to constrain internal processes in the oceans such as the tidal dissipation (e.g. Egbert and Ray, 2000). Nevertheless, the thick atmosphere of Titan makes things harder due to its opacity to some wavelengths. Reaching the high vertical resolution requested to observe the tidal motion (whose tidal range is smaller than 0.7 m) is therefore unlikely;

- An orbiter could theoretically provide images in the visual band of the surface lakes and seas. Such images could be

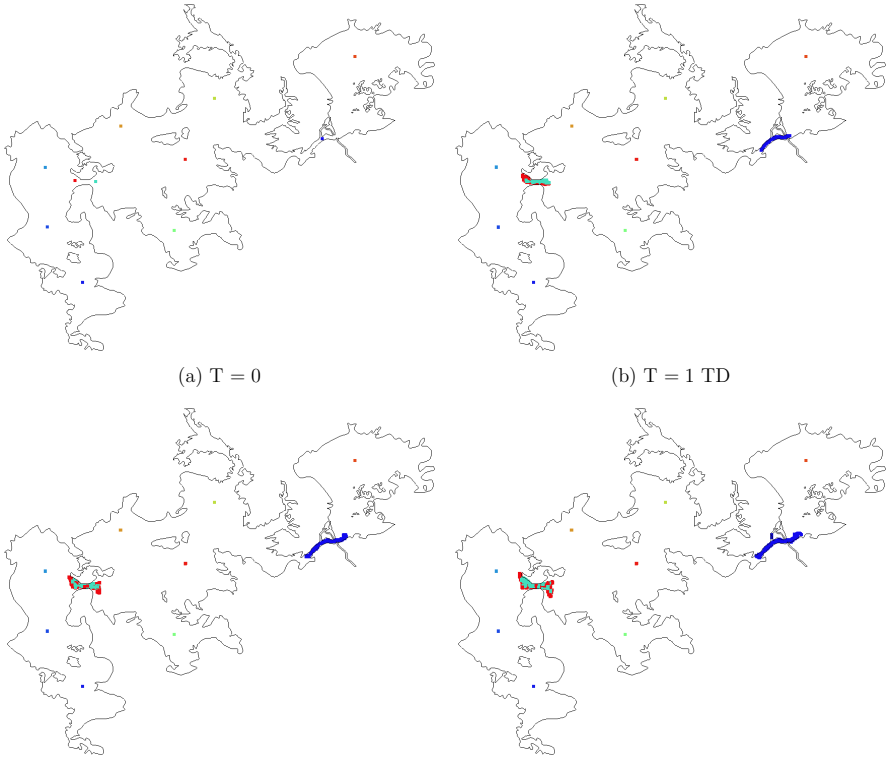

(a) T = 0 (b) T = 1 TD

(c) T = 2 TD (d) T = 3 TD

Fig. 5.19: Sea landing positions of the capsule (a), and their positions 1 TD (b), 2 TD (c), and 3 TD (d) later. The capsules are coloured as a function of their landing site. The latter were selected arbitrarily. A capsule lands every 0.005 TD at each location.

used to predict the surface flow of the sea (see, e.g. Delandmeter et al., 2017) by means of Particle Image Velocimetry (Chen, 2011) or by Global Optimal Solution (Tseng et al., 2012). Once again, the opacity of Titan's atmosphere makes things harder and could prevent an orbiter from making high resolution observations in the visual specter;

- An orbiter could isolate the crustal response to constrain γ_2 by means of altimetry/gravimetry;

- A sounder could constrain the bathymetry of the northern seas (presently, details on Kraken are particularly lacking) with a high resolution. If we pay interest to the global behaviour, a structured grid of $2-3$ km resolution would be enough but a higher resolution would be needed in Seldon and Trevize Fretum and in specific areas such as Moray Sinus or at the "Magic Islands" emplacements. To this end, there are at least two relevant kinds of sounder:
  - A radar system, operating from orbit (or from an aerial platform) could possibly detect a discontinuity in dielectric constant;
  - An acoustic sounder (depth sounder/sonar) on a vehicle on/in the sea would detect a discontinuity in acoustic impedance (e.g. Arvelo and Lorenz, 2013).

  A sharp change in composition or temperature could yield detectable reflections to either type of instrument, but in each case the reflection at such a liquid-liquid interface would likely not be so severe as to suppress the echo from the much stronger dielectric/acoustic contrast between liquid and the solid seabed;
- A lander with a view of the shoreline could constrain the tidal motion at some specific locations supplying time series of sea surface elevation and velocity at these points;
- A submarine or a floating capsule could constrain the liquid composition and the stratification of the surface seas and study the tidal current;
- A submarine or a floating capsule could provide time series of the elevation by means of a sonar/depth sounder and time series of the velocity field by means of a current meter;
- A buoy similar to the Argo float is a compromise between a submarine and a floating capsule as it could provide the same

data as a submarine (i.e. density and temperature vertical profile as well as time series of surface elevation and velocity) but would be easier to design. Its main drawback is that it is driven by the flow instead of being able to move in a specific direction.

Such data/observations could be used to constrain the parameters or to validate our model. To this end, time series or spatial variations of the sea surface elevation are better suited as they are less sensitive to small scale variations of the model parameters. The diurnal variation of the signal should then be extracted to remove the influence of atmospheric forcings such as the wind. If such a time series was obtained by an orbiter, an additional analysis should be conducted to isolate the tidal motion of the surface seas from the deformation of Titan's surface. This would be complicated as both phenomena have the same period. It would be easier if a time series of the surface elevation was measured in parallel. Future observation missions could also provide data that could be used as input(s) for other model(s) or/and to study accurately local phenomena. For instance, providing the flow velocity, sea surface elevation, temperature and composition along a line joining the shore of Ligeia (Kraken) Mare away from the outlet/inlet of the strait would allow one to study Trevize Fretum accurately (i.e. with a high resolution mesh) by means of a 3D oceanographic model.

Unfortunately the next mission planned, Dragonfly, will land near the equator and will not get close to the northern seas as direct to Earth communication will be impossible in high northern latitudes during the mission. Therefore, an exploration mission focusing on the northern seas is not expected before decades.

5.7 Conclusion

Hydrocarbon filled liquid bodies have been known to exist on Titan's surface since Cassini radar observations from 2006 (Stofan et al., 2007). In this paper we study the tidal response of the

two largest seas, namely Kraken Mare and Ligeia Mare, which are linked by a strait called Trevize Fretum. To do so, we use SLIM (`www.climate.be/slim`), a model previously adapted to Titan conditions (Vincent et al., 2016). A sensitivity analysis with respect to various poorly constrained parameters such as the bottom friction, the depth of Trevize Fretum, the overall depth of Kraken Mare, and the attenuation factor due to the sea bottom tidal deformation is conducted. This study brings further insight in the liquid exchanges between the basins and the influence of these parameters on the tidal response of the northern seas.

Our model predicts an independent tide, with an exact period of 1 TD (Titan Day), in each basin of Kraken Mare and Ligeia Mare. In the northern basin of Kraken Mare, the diurnal tide rotates anticlockwise around an amphidromic point located in its south-eastern part. The tidal phase suggests that, to a large extent, the tidal motion in Kraken 1 and Ligeia Mare can be represented by a sloshing wave mode. Indeed, in these basins, the tidal phase is nearly uniform over large geographical areas while there are strong variations over the straits connecting those basins with Kraken 1. The maximum tidal range (about 0.29 m) is located in the south-eastern part of the southern basin of Kraken Mare and occurs 0.31 TD after perikron (high tide)/apokron (low tide). The fluid speed is one order of magnitude larger in Trevize and Seldon Fretum than offshore in Kraken or Ligeia Mare. The maximum speed in each strait is 0.24 and 0.36 m/s, respectively. No resonance phenomenon is observed in the northern seas. Some of the seas eigenmodes correspond to coastal trapped waves or to funnel shaped resonance but their periods are much smaller than the tidal period. The maximum volume variation in both basins of Kraken Mare are about three times larger (respectively 8.9 km^3 for the northern one and 9.2 km^3 for the southern one) than that of Ligeia Mare (about 2.5 km^3). These results are overall rather similar to those of Tokano et al. (2014), suggesting that a 2D model is adequate for modelling many aspects of Titan's tides and may be better for parametric studies since it is less computationally demanding than a 3D model.

We study the influence of Trevize Fretum depth, the bathymetry scaling factor α, the attenuation factor γ_2, and the bottom friction. They have a significant influence on the tidal response of each basin, mainly by modifying the liquid exchanges between the basins. Indeed, modifying the depth of Trevize Fretum logically leads to changes of the liquid exchanges through the strait. The bottom friction has an impact on the speed: as the bottom friction increases, the speed decreases (and consequently the liquid exchanges through the straits). Increasing γ_2 (and thereby the forcing) results in larger liquid exchanges. The bathymetry scaling factor modifies the volume ratio between Kraken Mare and Ligeia Mare as well as the total amount of liquid in Kraken Mare which, in turns, modifies the liquid exchanges. Such variations lead to the displacement of amphidromic point(s) in both basins of Kraken Mare, significant time lag, and can modify the location at which the tidal range is maximum.

CHAPTER 6

Modelling of Titan's subsurface ocean liquid motion

Abstract

An ocean filled with liquid water lies beneath the icy surface of several Jovian and Saturnian moons. In such an ocean, the currents are driven by the tidal forcing (1), the deformation of the ice shell lying at its top (2), and the temperature gradient resulting from the surface and bottom heat fluxes (3). The flow induced by (1) and (2) can be modelled by a 2D depth-averaged model while (3) generates horizontal and vertical density variations whose effects can only be captured by means of a 3D baroclinic model.

We study the tides of Titan's subsurface ocean and the impact of the ice shell on the liquid motion by means of

the Second-generation Louvain-la-Neuve Ice-ocean Model, SLIM (www.climate.be/slim). The impact of the ice shell lying at the top of the ocean is modelled by a surface friction term and a surface pressure term. The latter is a function of the difference between the ocean elevation and the vertical uplifting of the shell and the time derivative of this difference. The results are compared to the tidal motion of a similar ocean with a free surface, which consists of two tidal bulges rotating around Titan. The associated velocity field consists of two gyres, separated by an area of high speed flow, whose center follows a sinusoidal path centred on the equator. A viscoelastic ice shell slightly decreases the surface elevation, by 3%, and the speed, by 5%, without significantly modifying the spatial patterns of these fields. The depth of the ocean and the mechanical behaviour of the ice shell being poorly constrained, a sensitivity analysis is conducted. The depth significantly modifies the velocity field while its impact on the elevation field is small. The mechanical behaviour of the ice shell influences both the elevation and velocity fields in terms of magnitude but does not modify the spatial patterns of these fields.

The influence of the surface heat flux is studied by means of the 3D baroclinic version of SLIM. The heat fluxes derived from Titan's topography by Kvorka et al. (2018) are used as surface boundary condition for the temperature equation while a constant bottom heat flux is implemented. Its value is computed assuming that the heat balance of the ocean is at equilibrium. These boundary conditions are responsible for density variations, hence impacting the hydrodynamic of the ocean. The resulting flow interferes with the tidal flow, modifying significantly the spatial patterns of the velocity field as well as the speed. The impact of the surface heat flux being much more significant than that of the shell mechanical behaviour, future studies should focus on modelling accurately the surface and bottom heat fluxes while discrepancies about the mechanical behaviour of the shell can be tolerated.

6.1 Introduction

Several celestial bodies of the solar system hide a liquid layer beneath their surface. Such a liquid layer modifies the magnetic field, ability to deform, and shape of the celestial body. The layer can be filled with molten metal (Mercury and Earth), liquid hydrogen (Jupiter, Saturn, Neptune, and Uranus), or liquid water with ammonia and/or minerals (Europa, Titan, Ganymede, Enceladus, and Mimas). The latter are categorised as icy satellites (or icy moons), a group of natural satellites of the gaseous planets of the Solar system with a near spherical shape and which are mostly made of ice. In this chapter, we pay interest to Titan's subsurface ocean as part of a study of Titan's liquid bodies (see Vincent et al., 2016, 2018, 2019).

Lunine and Stevenson (1987) were the first to predict the presence of a global subsurface ocean on Titan, although it had been discussed by Consolmagno and Lewis (1978). Since then, the presence of an ocean has been supported by several observations and measurements such as Titan's obliquity, the gravitational tides, and electric signals (see, e.g., Rappaport et al., 2008; Béghin et al., 2010; Nimmo and Bills, 2010; Iess et al., 2012; Hemingway et al., 2013; Lefevre et al., 2014; Baland et al., 2011, 2014). While the presence of a global subsurface ocean is asserted, its depth and liquid composition remain an open question. Several models were developed to derive the internal structure of Titan. Although they differ about the predicted depth and density of the ocean, their results can be used to bound these characteristics: the depth and density range from less than 100 km to 400 km and from 950 kg/m^3 to 1350 kg/m^3, respectively. The low densities (less than 1100 kg/m^3) do not correspond to the value of k_2 derived by Iess et al. (2012) and are therefore disregarded. The presence of such a liquid ocean despite the low surface temperature (about 93 K) implies the existence of at least one heat source. The first that comes to mind is the flux of radiogenic heat from Titan core. The second one is the heat produced by momentum dissipation within the ocean,

which depends, among other things, on the flow velocity and the roughness of the ocean surface and bottom. There is therefore a correlation between the ocean motion and its liquid state.

Several aspects of the subsurface oceans such as the tidal heating and dissipation, hydrothermal plumes, heat transfer and its implication on topography were studied (see, e.g., Sears, 1995; Sohl et al., 1995; Chen et al., 2010, 2014; Goodman and Lenferink, 2012; Beuthe, 2016; Hay and Matsuyama, 2017, 2019; Kvorka et al., 2018; Matsuyama, 2014; Matsuyama et al., 2018; Soderlund et al., 2014; Tyler, 2014; Vance and Goodman, 2009). At first, the ocean was considered as a layer among others within studies of Titan's internal structure (see, e.g., Sears, 1995; Sohl et al., 1995) but, over the last ten years, several studies have focused on the global ocean itself. Goodman and Lenferink (2012) used a general circulation model (the MIT GCM) to study local radial hydrothermal plumes induced by the spatial variations of the bottom heat flux within Europa's ocean. Hay and Matsuyama (2017, 2019) solved the Laplace tidal equations by means of a finite difference scheme to study the tidal dissipation while other authors focusing on the same topic such as Beuthe (2016), Matsuyama (2014), and Matsuyama et al. (2018) expanded the solution in spherical harmonics and solved the system to compute the unknown spherical harmonic coefficients. The first models do not take into account the self-attraction and loading as well as the interaction between the ocean and the solid regions (see, e.g., Sears, 1995; Tyler, 2008, 2014; Chen et al., 2014; Hay and Matsuyama, 2017). Such effects modify the tidal potential acting on the ocean as well as the dissipation due to the friction at the top of the ocean and the surface pressure induced by the shell. Matsuyama (2014) was the first to model such effects. He assumed a rigid ice shell at the top of the ocean. Nevertheless, the ice shell is far from rigid. Depending on the deformation time scale, it behaves as an elastic, a viscoelastic, or a fluid material, which could have a significant impact on the interactions between the ocean and the ice shell. For instance, a viscoelastic shell does not deform instantly, resulting in a time lag between the almost

immediate ocean response and the ice shell deformation. Such simulations were conducted recently by Matsuyama et al. (2018) and Hay and Matsuyama (2019). In order to take into account the ice shell, they added a surface friction term at the top of the ocean and a surface pressure term computed from a pressure potential decomposed in spherical harmonics.

In this chapter, we numerically study the liquid motion within the global ocean of Titan by means of the state-of-the-art numerical model SLIM (`www.climate.be/slim`). It was previously used to study the tides of the surface lakes and seas (Vincent et al., 2016, 2018). SLIM solves either the 2D depth-averaged shallow water equations (see Section 2.2.1) or the 3D hydrostatic equations under the Boussinesq approximation (see Section 2.2.2). SLIM2D is used to study the tides of the ocean and conduct a sensitivity analysis with respect to poorly constrained parameters such as the depth of the ocean and the mechanical behaviour of the ice shell. To this end, the model is modified to take into account the influence of the latter on the ocean (see Section 2.5.2). SLIM3D is used to study the interactions between the tidal flow and the flow induced by the surface and bottom heat fluxes. The results can be used to further constrain the heat fluxes and internal structure of Titan by comparison with the observations. Gaining further insight into the flow of a subsurface ocean could also prove helpful for astrobiologists studying the habitability of such oceans.

The chapter is organised as follows. The internal structure of Titan is briefly described in Section 6.2 and the numerical boundary conditions are detailed in Section 6.3. In Section 6.4.1, the tidal response of a free surface and a subsurface ocean are compared. The liquid motion induced by the heat fluxes at the top and bottom of the ocean is discussed in Section 6.4.2. A sensitivity analysis with respect to the ocean depth and ice shell mechanical behaviour is then conducted (see Section 6.5). The results are discussed in Section 6.6 and conclusions are drawn in Section 6.7.

6.2 Domain

The internal structure of Titan has been widely studied (see, e.g., Sears, 1995; Beuthe, 2008, 2015a,b; Dunaeva et al., 2016; Fortes, 2012; Sohl et al., 1995, 2003, 2014; O'Rourke and Stevenson, 2014; Barr et al., 2010; Baland et al., 2011, 2014; Tobie et al., 2012; Nimmo and Bills, 2010; Mitri et al., 2014b; Lefevre et al., 2014; Castillo-Rogez and Lunine, 2010). The general consensus is a structure consisting of a core, a high-pressure ice layer, a global subsurface ocean filled with liquid water, and an outer ice shell (see Fig. 1.5). The composition and thickness of each layer is open to debate as no direct measurements are available to constrain them accurately. Indeed, to this day, most of the data constraining the internal layers are provided by means of numerical models based on thermodynamic and/or solid mechanic laws. These models are validated by comparison with properties inferred from Cassini measurements such as the mean moment of inertia, the second-degree gravity field coefficients, and Titan mean density. Using models to derive the internal structure of Titan has several drawbacks:

- The wide range of parameters needed to run the models results in uncertainties in the composition and thickness of each layer;
- The data used for the validation are subject to measurement errors/provided by other models. For instance, the moment of inertia is questioned by Hemingway et al. (2013), Baland et al. (2014), and Lefevre et al. (2014);
- The structure predicted can be significantly different depending on the model used. For instance, the ocean could be as deep as 400 km (Lefevre et al., 2014; Mitri et al., 2014b) or could be shallow, less than 100 km (Baland et al., 2014).

Depending on the data used to validate the model and the model itself, the results vary significantly, both in terms of layer configu-

ration and combination of these configurations. The configurations predicted for each layer are briefly introduced hereafter:

Core: Three compositions can be found in the literature 1) a mixture of rock and iron, 2) silicates, and 3) a mixture of rock and ice.

Mantle: Most of the models agree with the presence of an ice-rock mantle at the top of the core but differ about its thickness and composition.

High pressure ice: A few models consider a uniform water-ice shell lying beyond the mantle but most of the models differentiate this layer between a high-pressure ice(s) layer, a global subsurface ocean and an outer ice shell. Depending on the temperature and pressure conditions (and, hence, the model), the crystalline structure[1] of the high-pressure ice is Ice II, Ice III, Ice V, or Ice VI (or a combination of these structures).

Global ocean: The bulk of the ocean is liquid water in which salts, volatiles and/or ammonia are dissolved. Depending on the model and assumptions, the depth and density of the ocean respectively range from less than 100 km (Baland et al., 2014) to 400 km (Lefevre et al., 2014; Mitri et al., 2014b) and from 1100 kg/m^3 (Sohl et al., 2003; Nimmo and Bills, 2010; Fortes, 2012, e.g.) to 1350 kg/m^3 (Mitri et al., 2014b; Fortes et al., 2007; Baland et al., 2011).

Outer icy crust: All models predict the crystalline structure of the ice shell to be Ice Ih. Depending on the model, the shell is assumed homogeneous or made of several sub-layers of various mechanical properties. Additional features such as methane clathrates can also be included.

[1]The crystalline structure of water ice changes with the temperature and pressure. Ice Ih corresponds to frozen water for terrestrial standard conditions but there are more than 18 types of crystalline structure. Depending on the conditions, the crystal can be hexagonal (Ice Ih), rhombohedral (Ice II), tetragonal (Ice III, Ice VI), monoclinic (Ice V), cubic ...

In this chapter, we consider a thin icy crust lying above a subsurface ocean whose density is initially uniform. The ocean bottom is assumed to be static (i.e., it does not deform). Therefore, $\gamma_2 = 1$, there is no pressure boundary term, and the layers beneath the ocean do not impact the tidal motion (the static assumption is discussed in Section 6.6.1). A uniform density is a good approximation when studying the tidal motion as the tides are not significantly impacted by the mean density. Vertical density variations can be disregarded as a stratified ocean is unlikely. Indeed, the ocean is heated at its bottom by the radiative heat flux and cooled down at its surface. Such boundary conditions are favourable for vertical mixing. On the other hand, horizontal density variations could occur if the top and bottom heat fluxes are not uniform. The impact of the horizontal density gradient is disregarded in the study of the tidal motion. Its impact on the liquid motion is then studied by means of SLIM3D (which takes into account both the density gradient and the tidal forcing). In this model, the density is a function of the sole temperature field, which is predicted by means of an advection-diffusion equation coupled to the hydrodynamic equations (see Section 2.2.2 for further details).

6.3 Initial and boundary conditions

In this section, we describe and discuss the initial conditions and the surface and bottom boundary conditions for the temperature and momentum equations.

The initial temperature field is derived from the melting temperature at the bottom of the ocean (281 K). It is assumed to be uniform in the meridional and zonal directions and to vary linearly with the depth, the temperature decreasing with the depth to reach 281 K at the bottom of the ocean.

In order to predict the temperature field, boundary conditions at the top and bottom of the ocean are requested. The top boundary condition that is implemented is the surface heat flux predicted

by Kvorka et al. (2018). They derived two heat fluxes taking place at the top of the ocean from the topography of Titan (see Fig. 6.1). This approach is based on the fact that the observed shape of Titan differs from the hydrostatic reference ellipsoid by several hundred meters. The variations of the gravity field associated with these shape differences are small, indicating a high degree of compensation in the shell. The compensation takes the form of spatial variations of the shell thickness or of its density. The former and the latter can respectively be explained by spatial variations of the heat flux at the boundaries or by the accumulation of dense hydrocarbon clathrates in the shell. Kvorka et al. (2018) modelled the melting/crystallization process at the water-ice interface and the resulting mechanical response of the ice shell. Using their results, they were able to constrain the heat flux associated with the large scale processes (small scale processes were disregarded because of the lack of information). In this chapter, the surface heat fluxes predicted when erosion is neglected (see Fig. 6.1) are used as surface boundary condition. The two cases derived by Kvorka et al. (2018) are considered: an axisymmetric model including only the even zonal spherical harmonics and a model including all harmonics up to degree 6. Using only even zonal spherical harmonics, Kvorka et al. (2018) predicted an axisymmetric heat flux ranging from about 7.5×10^{-3} W/m^2 at the poles to about 5.5×10^{-3} W/m^2 at the equator (see Fig. 6.1(a)). Using all spherical harmonics up to degree 6 results in a heat flux ranging from less than 2×10^{-3} W/m^2 to more than 10^{-2} W/m^2 (see Fig. 6.1(b)). Both heat fluxes are used as boundary condition to constrain the sensitivity of the ocean with respect to the surface heat flux.

According to Choblet et al. (2017), the heat flux at the bottom of the ocean ranges from 5×10^{-3} to 40×10^{-3} W/m^2, depending on the core properties, and varies spatially significantly due to the high pressure ice shell. Indeed, the radiogenic heat flux melt the ice at the bottom of the latter. This water is transported to the ocean by hot convective plume conduit, resulting in a non uniform bottom heat flux. Conducting a sensitivity analysis with respect to

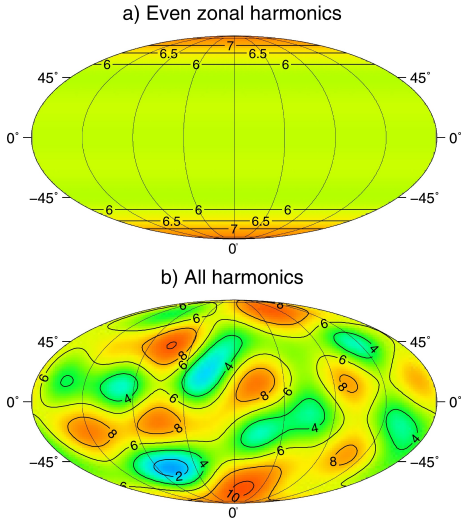

Fig. 6.1: Heat fluxes at the top of the ocean derived by Kvorka et al. (2018) from Titan's long-wavelength topography. Image credit: Kvorka et al. (2018)

the value and spatial distribution of the bottom heat flux is impossible as there are an infinity of configurations and no information available to favour one of them. Therefore, we resort to a good practice that consists in assuming the heat balance of the ocean to be at equilibrium. The implemented bottom heat flux is assumed uniform and its value, about $6 \times 10^{-3}\mathrm{W/m^2}$, is computed such that the surface integral of the ingoing flux at the bottom of the ocean is the same as the surface integral of the outgoing flux at its top. This hypothesis is discussed in Section 6.6.2.

The temperature field resulting from the bottom and surface heat fluxes is not uniform and, hence, so is the density. The density gradient associated to the temperature field generates a thermally driven flow which is independent from the tidal flow, although both flows interact. The timescale associated with the thermally driven flow being much larger than 1 TD, we implement initial conditions corresponding to the steady solution predicted when the tidal forc-

ing is ignored and the surface and bottom heat fluxes are used as boundary conditions (see Section 6.4.2). The steady solution is predicted by taking into account the initial temperature field depicted above (the initial density is computed from the initial temperature field by using the linearisation of Kell (1975)'s formulation, see Section 2.2.2). The initial temperature and density fields could be non uniform in the meridional and zonal directions due to the spatial distribution of a realistic bottom heat flux[2]. Nevertheless, a uniform bottom heat flux being implemented in this model, the horizontal variations of the initial temperature and density fields are disregarded to be consistent. Using the predicted steady solution as initial condition, simulations of the liquid motion are conducted by taking into account both the tidal forcing and the bottom and surface heat fluxes.

Our model is sensitive with respect to parameters such as the thickness and rheological properties of the ice shell. Although the derivation of the surface heat flux is based on the fact that the shell thickness can vary spatially, such variations are not taken into account while computing the impact of the shell deformation on the liquid motion. Taking into account such variations would require a much more elaborate model than the membrane approach (which assumes an axisymmetric shell). The thickness variations being small with respect to the shell thickness, at most $\mathcal{O}(200)$ m according to Kvorka et al. (2018), disregarding them while modelling the impact of the shell deformation seems to be a good simplification.

A boundary layer develops at the top and bottom of the ocean due to the friction with the ice layers. In SLIM2D, the effect of these boundary layers is modelled by a quadratic formulation (see Eq. 2.21). The hydrodynamic equations being integrated over the depth, the boundary layers act on the depth-averaged velocity and

[2]The surface heat flux is also responsible for temperature and density variations in these directions. This part of the study aims at predicting the impact of two different surface heat fluxes on the density, which is why a horizontally uniform initial temperature/density is consistent regarding the surface heat flux.

their effect can be summed, which is the same as summing the friction coefficients. The approach differs in 3D. In 3D terrestrial domain, the friction coefficient is computed from the inversion of the Prandtl-Karman law of the wall: this law is used to predict the current friction velocity which is then used to compute the friction coefficient corresponding to this velocity (see, e. g., Kärnä et al., 2013) for further details). To this end, the user has to provide parameters of the boundary layer such as the bottom roughness length, and the vertical coordinates where the current friction velocity is defined. As such parameters are unknown in Titan's subsurface ocean, the friction coefficients are given by the user instead of being computed. We implement the same friction coefficient (2.5×10^{-3}) at the top and bottom of the ocean as there is no indication of a significant roughness variation between the top and bottom surfaces. The physicochemical nature of the water could differ between the top and bottom of the ocean due to the higher pressure, which could result in small differences in the boundary layer. The impact of the friction coefficient on the tidal motion is therefore briefly studied in Section 6.5.2 for various uniform friction coefficients. The liquid properties such as the density and the molecular viscosity could vary due to the temperature spatial variations, resulting in spatial variations of the boundary layer and, hence, of the friction coefficient. Such variations are not taken into account in this model as their magnitude is small. Indeed, the predicted surface temperature variations are smaller than 1 K (see Section 6.4.2) which results in small variations of the density and viscosity that would result in small variations of the friction coefficient[3].

[3] A small, local, variation of the friction coefficient is not expected to significantly modify the liquid motion. It does not mean that the impact of the density variations on the liquid motion can be disregarded. Indeed, it is the density gradient that impacts the liquid motion. The impact of a gradient differs from the impact of the local variations of a parameter whose gradient does not appear in the equations.

6.4 Results

In this section, we first describe the tidal response of a free surface global ocean (see Section 6.4.1.1). The impact of the ice shell on the tides is then studied for a viscoelastic shell (see Section 6.4.1.2) and the results are compared to the tidal motion of a free surface ocean. We also briefly study the impact of the surface heat flux on the liquid motion (see Section 6.4.2). Unless otherwise specified, the results are obtained for the reference case which consists of a 100 km deep ocean. The drag coefficient for a free surface ocean is $c_D = 2.5 \times 10^{-3}$, which is the value commonly used in Earth-based model. The reference subsurface ocean lies beneath a viscoelastic ice shell whose elastic upper layer makes 10% of its thickness (see Sections 2.5.2, 6.4.1.2). The associated drag coefficient is doubled as friction also occurs at the top of the ocean, leading to $c_D = 5 \times 10^{-3}$. For the sake of clarity, some results are shown on a domain which is a Mollweide projection of the sphere (see Fig. 6.2). This is a pseudocylindrical projection conserving the area but not the angle. Using this projection allows showing both hemispheres in one figure.

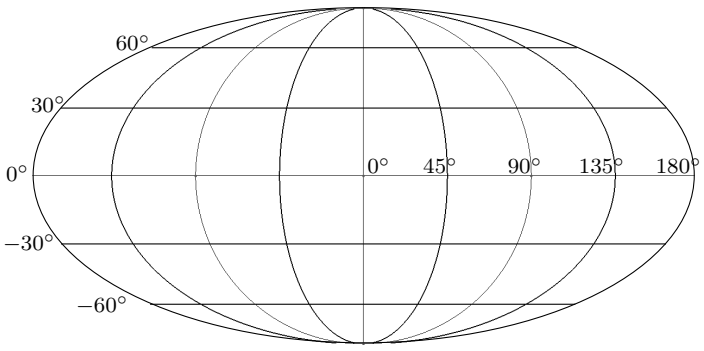

Fig. 6.2: Mollweide projection of a spherical Titan. This is an equivalent projection, i.e. the angles are not conserved.

The Rossby and Reynolds number associated with the tidal flow are $\mathcal{O}(10^{-4})$ and $\mathcal{O}(10^{10})$, respectively. The latter is similar to the

range observed in Earth's ocean for the M2 tide while the Rossby number is one order of magnitude smaller. It implies that the inertial forces are less significant with respect to the Coriolis force on Titan although their ratio with respect to the viscous forces is similar to that observed on Earth. These numbers slightly varies with the parameters but by less than one order of magnitude (except between a 400 km deep and a 50 km deep ocean).

6.4.1 Tidal motion

The external tides[4] being a 2D phenomena, SLIM2D is used to predict the tidal motion of a free surface and a subsurface ocean.

6.4.1.1 Free surface ocean

The elevation field mainly consists of two antipodal bulges and two antipodal troughs. Depending on the period, these bulges/troughs are separated or linked by an area of positive/negative surface elevation. The elevation at a point and its antipodal counterpart is the same and, at a same location, the elevation at t^* is the opposite of its value at $t^* + 0.5$ TD. These bulges/troughs rotate eastwards around Titan in 2 TD, resulting in a tidal period of 1 TD. At perikron, the troughs are circular and centred at (3.22°S, 0.51°W) and (3.22°N, 179.49°E) while the bulges are linked at the poles, forming a ring of positive elevation separating the troughs (see Fig. 6.3(a)). The transition between the circular troughs observed in (see Fig. 6.3(a)) and the circular bulges shown in (see Fig. 6.3 (c)) starts about 0.125 TD after perikron/apokron and lasts about 0.255 TD. The transition occurs as follows: the troughs start extending themselves in the meridional direction and the ring starts shrinking in the same direction at the poles (see Fig. 6.3(b)) until the troughs form a ring of negative surface elevation separating the two circular bulges resulting from the shrinking of the positive elevation ring observed

[4]Unless otherwise specified, the tides discussed are the external tides. We refer to them as tides.

at perikron. They are fully formed about 0.380 TD after perikron. The bulges keep rotating around Titan until 0.125 TD after apokron, when they start extending themselves to form a ring of positive elevation between two troughs. The maximum/minimum elevation, ±8.89 m, is reached in the centre of the bulges/trough 0.345 TD after apokron/perikron.

The main tidal component is the diurnal one, with an associated tidal range of 17.8 m (see Fig. 6.4). Other components are not significant as the range associated with is, at most, $\mathcal{O}(10^{-4})$ m. A central symmetry with respect to Titan's center can be observed in the tidal range of the diurnal component. In the hemisphere ranging from 90°W to 90°E, there are two amphidromic points, at (51.8°N, 0°E) and (58.5°S, 0°E), and two local maxima at (1.69°S, 32.2°W) and (2°S, 32.5°E). These maxima are linked by a peanut-like shaped area of large tidal range marked out by the amphidromic points in the north and in the south. These outstanding areas are encircled by a ring of constant tidal range (about 8.3 m) parallel to the 90°E and 90°W meridians. Therefore, the tidal range is larger at the equator than at the poles, except near the aforementioned meridians. There is no symmetry with respect to the equator: the southern amphidromic point is located at higher latitudes than the northern one. This also influence the shape of the high tidal range area which spreads further southwards than northwards. This asymmetry with respect to the equator is due to the obliquity of Titan. Similar patterns can be observed on the other side of Titan, but their location is different due to the central symmetry: the amphidromic points and the maxima are located at (58.5°N, 180°E), (51.8°S, 180°E), (1.69°N, 147.8°W), and (2°N, 147.5°E), respectively. The tidal phase is also symmetric with respect to the centre of Titan. For the hemispheres centred on the 0° and 180° meridian, the tidal phase is an odd function of the longitude (i.e. the phase at longitude $\lambda_{ref} + \lambda$ is the opposite of the phase at a longitude $\lambda_{ref} - \lambda$, where λ_{ref} is the longitude of the meridian at the centre of the hemisphere). The tidal phase of the circle formed by the 90°E and 90°W meridians, which corresponds to the ring of

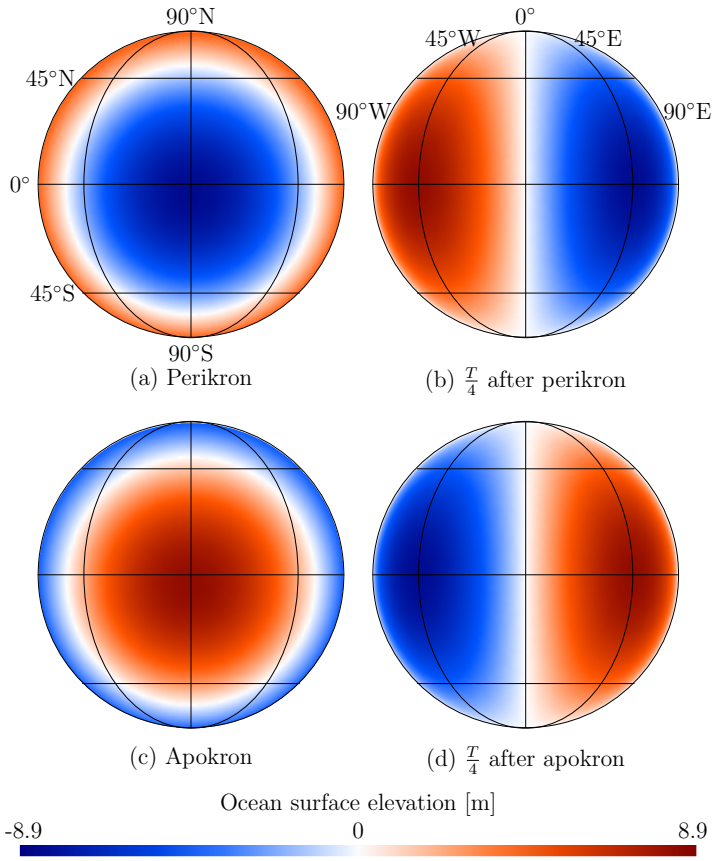

Fig. 6.3: Elevation field at (a) perikron, (b) 0.25 TD after perikron, (c) apokron, and (d) 0.25 TD after apokron for a 100 km deep free surface ocean. It consists of two antipodal bulges/troughs rotating eastwards around Titan.

constant tidal range, is nil. It is negative from 0°W to 90°W and from 90°E to 180°E.

The velocity field is made of two antipodal gyres separated by a ring of unidirectional high speed flow (see Fig. 6.5). One of the gyres rotates clockwise while the other rotates anticlockwise so that the

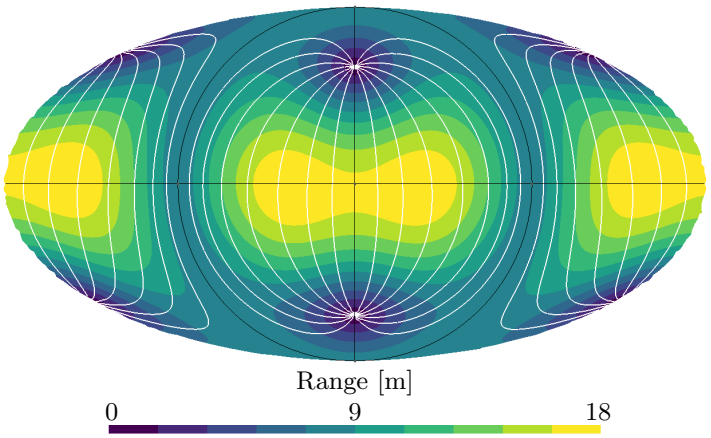

Fig. 6.4: Tidal range (in m) and phase (white lines, with a 22.5° spacing) of the main tidal component for a 100 km deep free surface ocean. The 90°E and 90°W meridians correspond to a tidal phase of 0°. There are four amphicromic points located at (58.5°N, 180°E), (51.8°S, 180°E), (51.8°N, 0°E), and (58.5°S, 0°E).

ring of high speed flow is a prolongation of each gyre. The gyres move westwards with their centre following a sinusoidal path of small amplitude around the equator (see Fig. 6.6). For instance, at perikron, the gyres are centred at (0.844°S, 107°E) and (0.742°N, 73°W), which is slightly after a local extrema of the sinusoid. It takes 1 TD for each gyre to turn around Titan, whose diameter corresponds to three times the wavelength of the sinusoidal path. The maximum speed, which is reached 0.4 TD after perikron, is 1.35×10^{-2} m/s which is two orders of magnitude larger than the speed observed in the gyres. In the gyres, the speed is slower than 5×10^{-4} m/s and decreases towards their center.

6.4.1.2 Subsurface ocean

The effects of the ice shell lying at the top of the ocean are modelled by a surface pressure term and by doubling the friction coef-

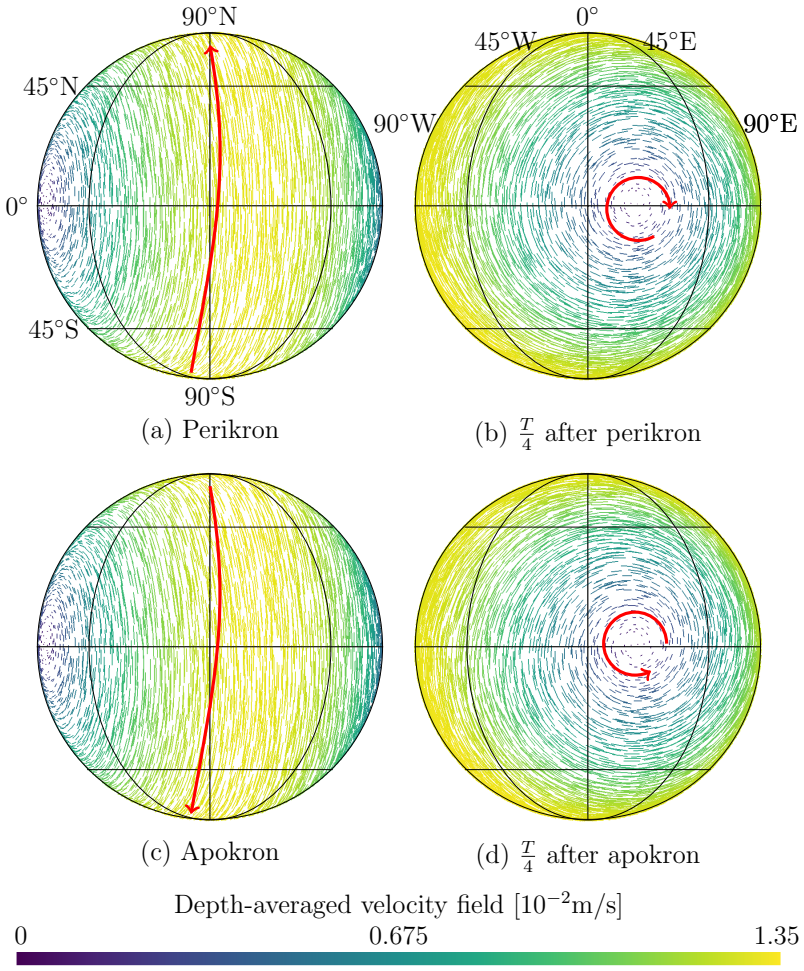

(a) Perikron (b) $\frac{T}{4}$ after perikron

(c) Apokron (d) $\frac{T}{4}$ after apokron

Fig. 6.5: Velocity field at (a) perikron, (b) 0.25 TD after perikron, (c) apokron, and (d) 0.25 TD after apokron for a 100 km deep free surface ocean. The global direction of the velocity field is marked by a red arrow. The velocity field consists of two gyres separated by a ring of high speed current.

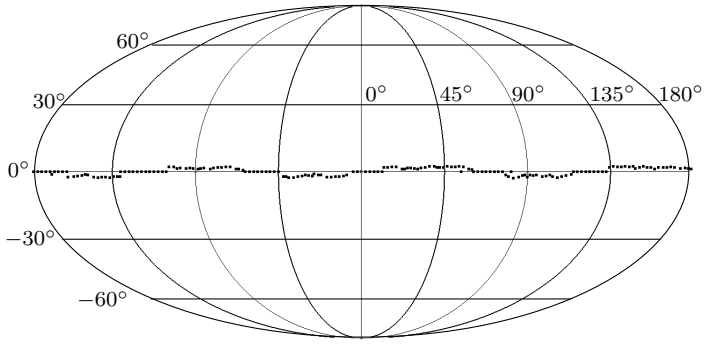

Fig. 6.6: Position of the gyres centres at each time step (i.e. 200 times per period) for a 100 km deep free surface ocean. The center follows a sinusoid whose amplitude is about 1° and whose wavelength is $\frac{2}{3}\pi R$, where R is the radius of Titan.

ficient. As explained in Section 2.5.2, this pressure term is given by $p = \rho g A \eta + \rho g B \frac{\partial \eta}{\partial t}$ where A and B quantify the elastic and the viscous deformations of the ice shell, respectively. These factors depend on the model used to predict the shell deformation as well as the shell configuration implemented (i.e. its thickness, whether it is homogeneous or made of several layers of different mechanical behaviour, the rheology ...). As explained in Section 2.5.2, our approach is based on the work of Beuthe (2015a,b). Therefore, an ice shell made of two layers corresponding to the published results of Beuthe (2015a,b) is implemented. It consists of a conductive-elastic top layer and a convective-viscoelastic bottom layer. A and B are functions of the top layer relative thickness and the ratio between the critical viscosity[5] and the viscosity of the bottom layer. A sensitivity study with respect to these factors is conducted in Section 6.5.3. In this section, the liquid motion of a 100 km deep ocean lying beneath a 70 km thick shell whose top layer represents 10% of its thickness and whose bottom layer is at the critical state

[5]The critical viscosity is the value of the viscosity maximising the imaginary part of the shear modulus.

(i.e. $\delta = 1$ in Fig. 2.8) is studied. This configuration results in A and B factors of the same order of magnitude, meaning that the elastic and viscous deformations are equally significant. The liquid motion predicted is compared to that of a 100 km deep free surface ocean.

The impact of the ice shell on the elevation and velocity fields is noticeable. The maximum surface elevation is smaller by 0.29 m. This decrease integrally results from the diurnal tidal component whose range diminishes by 0.58 m. Therefore, the difference between the elevation of a free surface ocean and that of a subsurface ocean is similar (in terms of shape) to the elevation field itself: it also consists of two bulges/troughs rotating around Titan. This field ranges from -0.29 to 0.29 m. The difference is negative/positive where the elevation is negative/positive and the larger the amplitude of the elevation, the larger the difference. While the value of the diurnal tidal range is affected by the ice shell, this is not the case of its spatial patterns: no variation of the position of the amphidromic points is observed (see Fig. 6.7) and the iso-contours have the same shape (this is not the case in Fig. 6.7 because the scale is the same as in Fig. 6.4, for comparison purpose). The phase of the diurnal component is also subjected to modifications (although it cannot be seen by comparing Figs. 6.4 and 6.7): the shell induces a phase lag which is maximum near the amphidromic point (up to $\pm 1.4°$) but is less than $0.1°$ over the rest of the domain (see Fig. 6.8). The tidal motion under an ice shell is therefore slightly delayed/ahead with respect to that of a free surface ocean depending on the location. Except for this small phase lag, the elevation field is similar. The global patterns are the same and their position at each time step does not vary significantly.

The ice shell slows down the tidal flow. The decrease is not constant over the domain and time: it is larger than 1×10^{-4} m/s in the ring of high speed flow while it is less than 5×10^{-5} m/s near the gyres. The maximum difference (7.16×10^{-4} m/s, which represents 5.3% of the velocity at this location) coincides with the time and location of the maximum speed (0.4 after perikron in both

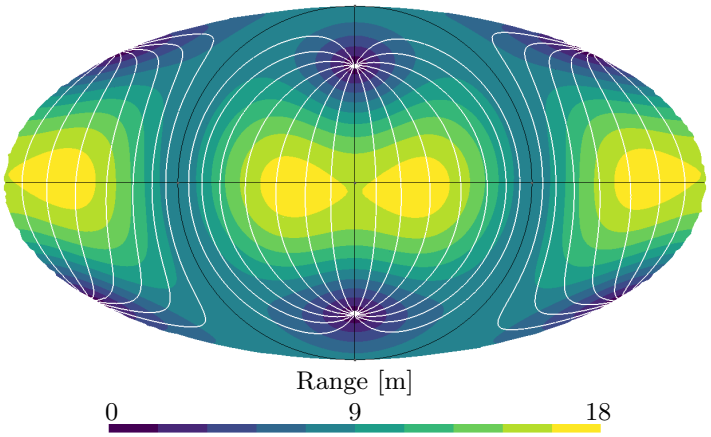

Fig. 6.7: Tidal range (in m) and phase (white lines, with a 22.5° spacing) of the main tidal component for a 100 km deep subsurface ocean lying beneath a viscoelastic ice shell. There are four amphicromic points located at (58.5°N, 180°E), (51.8°S, 180°E), (51.8°N, 0°E), and (58.5°S, 0°E).

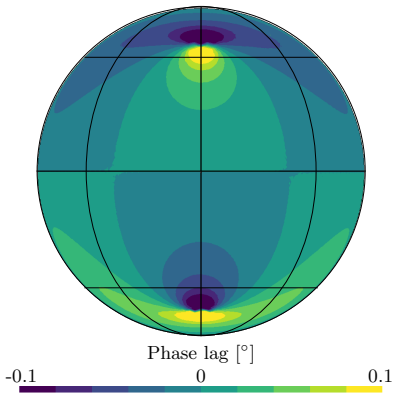

Fig. 6.8: Difference between the phase of the diurnal tidal component of a subsurface and a free surface ocean. The scale is saturated beyond 0.1°. The maximum phase lag is 1.4° and is located near the amphidromic points.

cases). Similarly to its effect on the elevation field, the shell does not impact the global patterns of the flow: it consists of two gyres whose center follows the same path (see Fig. 6.6).

6.4.2 Thermally driven flow

Spatially varying bottom/surface heat fluxes can generate a significant motion in a liquid body. For instance, despite the ice covering the bottom and top of Europa's subsurface ocean, significant liquid motion induced by the bottom heat flux is predicted therein (see, e.g., Goodman and Lenferink, 2012). We therefore study the impact of the surface heat fluxes derived by Kvorka et al. (2018) on the liquid motion in Titan's ocean. This approach is first applied to the zonal heat flux derived by Kvorka et al. (2018) (see Fig. 6.1(a), hereafter referred to as *case A*) and then to the more elaborate flux derived by the same authors (see Fig. 6.1(b), hereafter referred to as *case B*). For each flux, we describe the stationary solution used as initial condition. The interactions with the tidal flow are then highlighted by comparison with the reference subsurface ocean.

The zonal heat flux tends to decrease the vertical temperature gradient. The surface temperature is slightly smaller (about 0.1 K) at the poles, where the heat flux is maximum. Such a heat flux results in a surface elevation which is negative at latitudes higher than 45° with a minimum (-0.13 m) located at the poles. At smaller latitudes, the elevation is positive, but one order of magnitude smaller, and reaches its maximum (0.026 m) at the equator (see Fig. 6.9(a)). The depth-averaged flow consists of a zonal eastward flow with two gyres centred at the poles. The maximum speed is 1.75×10^{-3} m/s, which is one order of magnitude smaller than the tidal flow. The 3D velocity field varies with the depth in terms of magnitude and orientation. At the bottom and top of the ocean, it consists of a zonal eastward flow but the magnitude is smaller at the bottom (7.6×10^{-3} m/s instead of 1×10^{-2} m/s) while, 50 km below the surface, the flow consists of a zonal westward flux. The velocity is slightly larger (1.1×10^{-2} m/s) 25 km below the surface than at the

surface due to the friction term.

In *case B*, the vertical temperature gradient also decreases due to the surface heat flux: the bottom temperature is about 282.7K while the surface temperature ranges from 282.66 K to 282.83 K. The latter is minimum at the north pole, increases towards the equator, and decreases from the equator to the south pole, where it reaches a local minimum. This minimum is warmer than that reached at the north pole due to the asymmetry of the heat flux. Similarly to *case A*, the elevation is maximum (0.118 m) at the equator but the minima are not located at the poles and an asymmetry can be observed between the southern and the northern hemispheres. The minima are located at (82.2°N; 136.6°W) and (78.6°S; 43.8°E), i.e. closer to the pole in the northern hemisphere. The elevation is also smaller at this location: -0.427 m while it reaches -0.161 m near the south pole (see Fig. 6.9(b)). The depth-averaged flow is similar to that predicted in *case A* although the maximum is slightly smaller, 1.14×10^{-3} m/s. While the 3D flow was almost always parallel to the equator in *case A*, it is no longer the case due to the longitudinal variation of the heat flux. The surface flow is globally eastward and larger in the northern hemisphere (up to 6.32×10^{-2} m/s) than in the southern (the maximum is 5 times smaller). 75 km beneath the surface and at the bottom, the flow is westward and larger near the location of the minimum surface elevation (up to 3.2×10^{-2} m/s).

In both cases, the heat flux generates a surface elevation two order of magnitude smaller and a depth-averaged flow one order of magnitude smaller than those induced by the tidal forcing. Therefore, the impact on the elevation field is expected to be small although an asymmetry appears as the heat flux increases the elevation at the equator and decreases it at the poles. The velocity field, on the other hand, could be significantly modified in terms of orientation. Indeed, although the thermally driven flow is slower, it is almost unidirectional and could, hence, impact the orientation of the flow resulting from the interactions between the tidal and thermally driven flows.

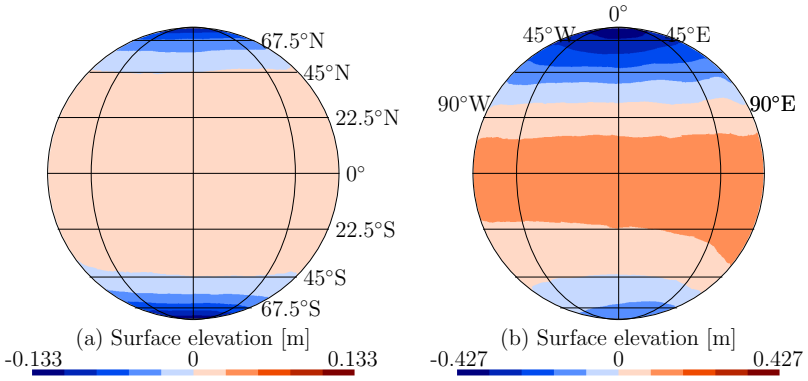

Fig. 6.9: Ocean surface elevation generated by the zonal (a) and elaborate (b) heat fluxes predicted by Kvorka et al. (2018). In both cases, the elevation is negative near the pole and maximum near the equator. The elaborate heat flux is responsible for larger elevation variations and is not symmetric with respect to the equator.

Taking into account both the tides and the thermally driven liquid motion does not influence significantly the temperature field (with respect to the purely thermally driven motion) nor the range and phase of the diurnal component (with respect to the tidal motion). The surface elevation is almost identical to that of a subsurface ocean without surface heat flux except for an asymmetry in the surface elevation scale: in terms of absolute value, the maximum is larger than the minimum (by 0.03 in *case A* and by 0.2 in *case B*). This is due to the positive surface elevation generated near the equator by the thermally driven liquid motion: adding this positive surface elevation increases both the maximum and minimum elevation at this location, resulting in the asymmetry.

In *case A*, several aspects of the depth-averaged velocity field are similar to the reference case. Indeed, it consists of two gyres, separated by a high speed flow, whose center rotates around Titan following a sinusoid centred on the equator. However, the maximum speed is slightly smaller, occurs 0.09 TD sooner, and the

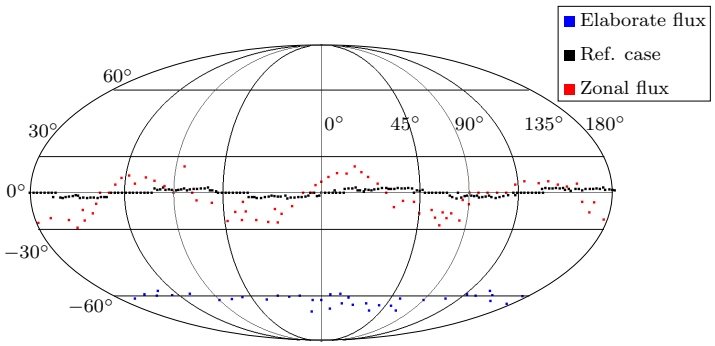

Fig. 6.10: Position of the gyres centres at each time step (i.e. 200 times per period). Blue, black, and red dots respectively denote *case B*, the reference case, and *case A*. The centres are located at higher latitudes when the thermally driven flow is taken into account.

amplitude of the sinusoid is much larger (see Fig. 6.10). For instance, at perikron, the gyres are centred at (10.6°N, 77.2°W) and (1.49°S, 104°E), which is further from the equator than any position predicted in the reference case. The 3D flow differs significantly from the depth-averaged one (see Fig. 6.11). The maximum speed at the surface is 1.31×10^{-2} m/s. It is slightly larger in the upper layers of the ocean, due to the smaller effect of the surface friction, and then decreases with the depth. The maxima of each layer are not located in the same area and are not oriented in the same direction, which explains why the depth-averaged speed is smaller. The spatial patterns are significantly different from those of the depth-averaged velocity and differ from one layer to another. At the surface, the velocity field consists of two gyres centred near the poles (see Fig. 6.11(e, f, g, h)). Their centre follows a circular path around the poles, completing a revolution in 1 TD. The maximum velocity in each hemisphere is close to these points and also rotates westwards around the poles. The main flow is directed from one maximum to another (see Fig. 6.11(a, b, c, d)). It is therefore north-eastward west of the maximum located in the northern

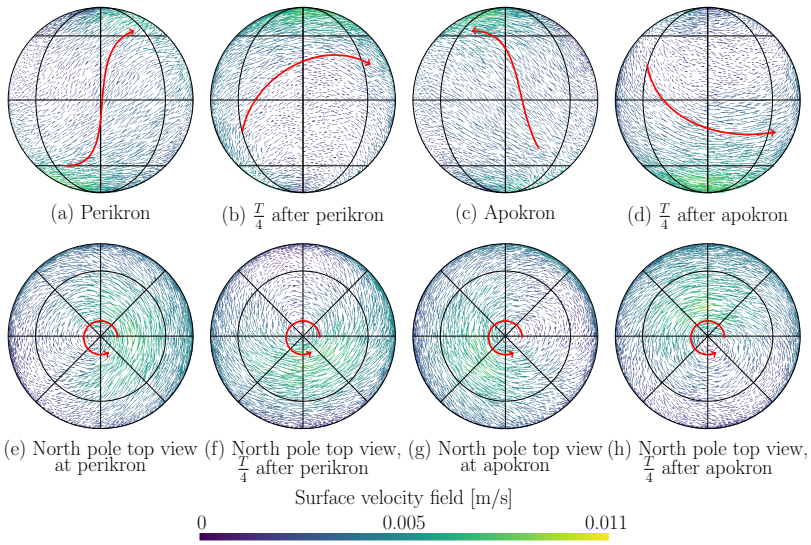

Fig. 6.11: 3D velocity field at the surface of the ocean for a zonal surface heat flux. For Panels (a), (b), (c), and (d) the north/south pole is at the top/bottom of the image, which is centred on the 0° meridian. Panels (e), (f), (g), and (h) correspond to a top view of the north pole with the 0° meridian at the bottom of the image. The meridians/parallels are represented in black, with a 45° spacing. The surface velocity consists of two gyres whose centres are located near the poles and two high speed areas adjacent to these gyres. The global flow orientation is illustrated by a red arrow.

hemisphere and south-eastward east of this point. The velocity orientation changes with time as the high speed areas rotate around the poles due to the tidal forcing. Similar patterns are observed 25 km deeper and at the bottom of the ocean although the gyres are not centred at the same location. The orientation can locally vary making the flow less unidirectional. 50 km below the surface, the patterns are also similar but the flow is oriented in the opposite direction.

In *case B*, the depth-averaged velocity field differs significantly

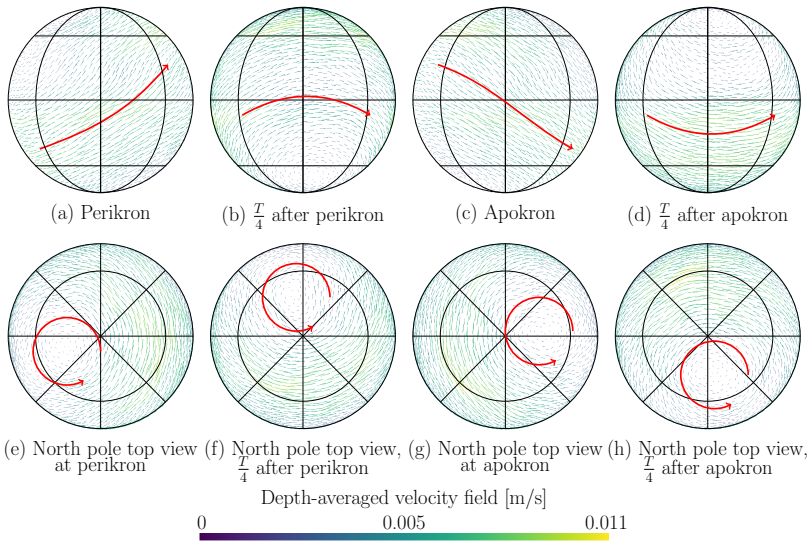

Fig. 6.12: Depth-averaged velocity field for an elaborate surface heat flux. For Panels (a), (b), (c), and (d) the north/south pole is at the top/bottom of the image, which is centred on the 0° meridian. Panels (e), (f), (g), and (h) correspond to a top view of the north pole with the 0° meridian at the bottom of the image. The meridians/parallels are represented in black, with a 45° spacing. The depth-averaged velocity consists of two gyres whose centres are located near the poles and follow a sinusoidal path centred on the 60°S meridian. The global flow orientation is illustrated by a red arrow.

from the tidally driven flow. While the maximum speed is 1.1×10^{-2} m/s, which is of the same order of magnitude, the spatial patterns are totally different (see Fig. 6.12). Although the main patterns of the depth-averaged velocity field consist of two gyres, the latter are located at much higher latitudes and their center moves westward following a sinusoidal path centred on high latitude meridians (see the path of the southern gyre in Fig. 6.10). For instance, at perikron, the centres are located at (65.4°N, 74.9°W) and (54.3°S, 104°E). Therefore, depending on the position of the gyres,

the flow is either south-eastward or north-eastward. For instance, on the 0° meridian, the flow is north-eastward when the southern gyre is located in the eastern hemisphere and south-eastward when the southern gyre is located in the western hemisphere. The 3D flow also differs from the depth-averaged flow. Similarly to *case A*, the speed is maximum a few kilometres beneath the surface due to the surface friction. Depending on the location, the speed can increase with the depth as the maximum speed of the various layers are not located in the same area. Near the surface, the flow is globally eastward and two gyres are located near the poles while, near the bottom, the flow is globally westward with its orientation varying with time between north-westward and south-westward. The speed is significantly larger in the northern hemisphere than in the southern one at the top and at the bottom of the ocean, which can be related to the thermally driven velocity field.

6.5 Influence of the parameters

Various parameters used in these simulations are poorly constrained. Therefore, a sensitivity analysis with respect to the depth, friction coefficient, and mechanical behaviour of the ice shell (by modifying A and B factors) is conducted.

6.5.1 Influence of the free surface ocean depth

Depending on the model used to study the internal structure of Titan, the depth of the ocean varies from less than 100 km to a few hundreds of kilometres (see Section 6.2). Therefore, the influence of the depth on the tidal motion is studied. This study is conducted on a free surface ocean in order to decouple the impact of the ocean depth from that of the ice shell. The depths taken into account are 50, 75, 100, 150, 200, 250, 300 and 400 km. The lower and upper bounds correspond to the depth predicted by Baland et al. (2014) and Mitri et al. (2014b); Lefevre et al. (2014).

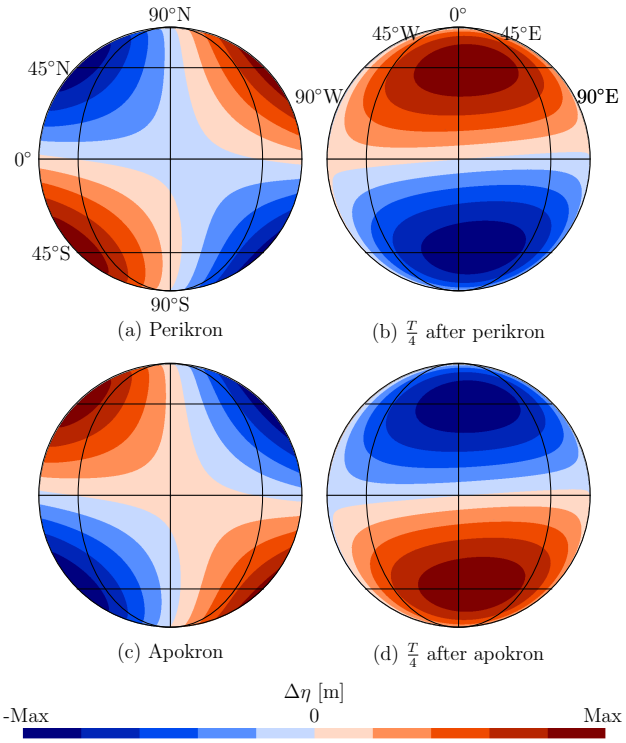

(a) Perikron (b) $\frac{T}{4}$ after perikron

(c) Apokron (d) $\frac{T}{4}$ after apokron

Fig. 6.13: Difference between the surface elevation of a 100 km deep ocean and deeper or more shallow ocean ($\Delta\eta$). The spatial patterns at (a) perikron, (b) 0.25 TD after perikron, (c) apokron and (d) 0.25 TD after apokron are similar while the amplitude (which is symmetric with respect to 0) varies with the depth. The maximum difference is 1.74×10^{-2} m, 2.67×10^{-2} m, 3.24×10^{-2} m, 3.62×10^{-2} m, and 4.53×10^{-2} m for 150, 200, 250, 300, and 400 km deep oceans, respectively. In the case of more shallow ocean, the spatial patterns are identical but the difference is of opposite sign (the maximum being 4.7×10^{-1} m and 1.71×10^{-2} m for 50 and 75 km deep oceans, respectively).

Varying the ocean depth results in modification of both the elevation and velocity fields magnitude while the spatial patterns of these fields are not modified. The difference between the surface elevation of a 100 km deep ocean and the elevation of a deeper or more shallow ocean is shown in Fig. 6.13. The global patterns of this field are similar for each depth studied – for 50 and 75 km deep oceans, the field is of opposite sign. Although the maximum surface elevation does not vary with the depth, the magnitude of this difference does increase with the depth (see Fig. 6.14). This can be explained by the fact that the ocean depth does not affect the range of the diurnal tidal component but impacts its phase. The larger the depth difference, the larger the phase variations and, hence, the larger the magnitude of the difference between the elevations. The phase lag increases with the depth (but not linearly) to reach about 2° for a 400 km deep ocean. For an ocean more shallow than 100 km, the elevation variation is of opposite sign and is larger than for an ocean deeper than 100 km. Besides these variations, high frequency oscillations can also be observed in a 50 km deep ocean. Two tidal components stand out as their associated range are more than one order of magnitude larger than others (although 4 orders or magnitude smaller than the range associated to the diurnal component). The period and amplitude of these components are $\frac{1}{55}$ TD and $\frac{1}{56}$ TD and 4.04×10^{-3} m and 4.94×10^{-3} m, respectively. Both mean and maximum speeds decrease with the depth (see Fig. 6.14). However, the speed reduction is not large enough to compensate the larger depth, resulting in an augmentation of the mean liquid transport (by 101 m^2/s between a 100 km and a 400 km deep ocean).

6.5.2 Influence of the friction

The influence of the friction on the tidal motion is studied by varying the quadratic friction coefficient in SLIM2D. Therefore, it is not possible to isolate the effects of the top surface friction from those of the bottom surface friction. Three uniform friction coef-

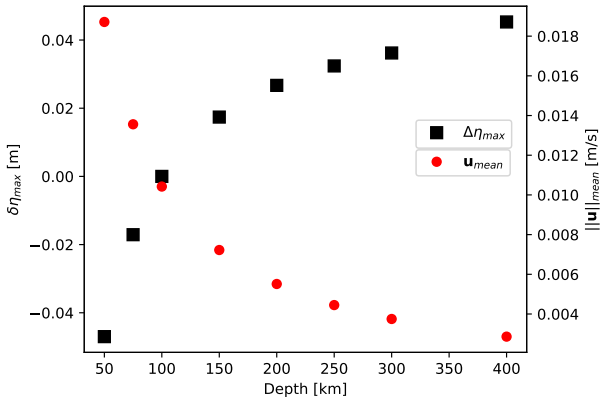

Fig. 6.14: Spatially and temporally averaged speed (circles) for various depths, and maximum variation between the associated surface elevation and the elevation of a 100 km deep ocean (squares). For the same depth variation, the elevation and speed variations are larger for an ocean shallower than 100 km than for a deeper ocean. The larger the depth difference, the larger the elevation and speed variations.

ficients are taken into account: 2.5×10^{-3} (the reference value for a free-surface ocean), 5×10^{-3} (the reference value for a subsurface ocean), and 7.5×10^{-3}.

Modifying the friction coefficient does not significantly impact the ocean surface elevation: the amphidromic points, the maximum elevation, and the spatial patterns are identical. The influence on the velocity field is more significant although small with respect to that of the other parameters. The larger the friction coefficient, the smaller the mean and maximum speeds. Tripling the coefficient results in a maximum and mean speed 5×10^{-4} m/s and 4×10^{-4} m/s slower, respectively. The velocity orientation can locally vary with the bottom friction. For instance, at perikron, the gyres centers are located slightly further from the equator for the largest friction studied (about 2° further west and 0.7° further north/south).

6.5.3 Influence of the ice shell

The factors A and B quantifying the elastic and viscous deformations of the ice shell are function of the shell rheology and sub-layers relative thickness. The latter being poorly constrained at present, a sensitivity analysis with respect to A and B is conducted. Besides the reference configuration studied in Section 6.4.1.2, seven configurations are studied: an elastic-like ($\delta = 0.1$) and a fluid-like ($\delta = 10$) bottom layer making 90% and 60% of the shell thickness, a critical bottom layer making 60% of the shell thickness, a viscous deformation corresponding to the reference case with the factor B being multiplied by 100, an ice shell whose sole impact consists of the top friction term, and an ice shell whose sole impact consists of the surface pressure term. These last two configurations are studied to separate the effect of the surface pressure from that of the bottom friction. The elevation and velocity fields predicted are compared to the reference configuration for a subsurface ocean (see Section 6.4.1.2).

As its name suggests, an ice shell with an elastic-like bottom layer results in a mostly elastic deformation of the ice shell as the viscous deformation tends toward zero as δ decreases. In our model, it results in increasing the surface pressure resulting from the horizontal gradient of the surface elevation. The impact of such an ice shell does not vary significantly with the relative thickness of the bottom layer. This behaviour was expected in the light of Figs. 2.8, 6.15: for $\delta \leq 0.1$, A does not vary with the thickness while B, although experiencing minor variations, is almost zero. Under this configuration, the ocean experiences a smaller surface elevation, at most 8.44 m, which is 0.17 m smaller than for the reference case (see Fig. 6.15(a)). The decrease results from the smaller range of the diurnal tidal component. A small phase lag with respect to the subsurface ocean is also observed. Other aspects of the elevation field such as the location of the amphidromic points and the centre of the tidal bulges/troughs are similar to those predicted in the reference case. This ice shell also slows down the flow more

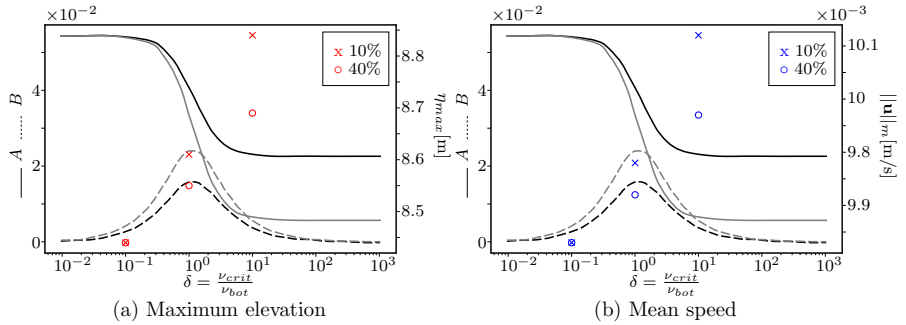

(a) Maximum elevation (b) Mean speed

Fig. 6.15: (a) Maximum elevation and (b) mean speed for six of the configurations implemented: elastic-like ($\delta = 0.1$), critical ($\delta = 1$), and fluid-like ($\delta = 10$) bottom layer with a top layer making 10% (crosses) or 40% (circles) of the shell thickness. The dashed and full lines represent the value of B and A coefficients for a 10% thick top layer (gray) and a 40% thick top layer (black), respectively. The smaller the viscosity of the bottom layer, the larger the elevation and speed.

significantly: the mean and maximum velocity are 2×10^{-4} m/s and 1.6×10^{-4} m/s slower than for the reference case (see Fig. 6.15(b)).

A fluid-like bottom layer also induces a mostly elastic deformation of the ice shell but reduces the surface pressure with respect to an elastic-like bottom layer. The thicker the bottom layer, the smaller A and the larger B. The former is constant with respect to δ and its variation with respect to the top layer thickness is much more significant than that of B as the latter tends toward 0 as δ increases (see Figs. 2.8, 6.15). The surface pressure being smaller than for the reference case, the maximum surface elevation and the speed are larger. The former increases by 0.23 m (resp. 0.09 m) for a top layer making 10% (resp. 40%) of the shell thickness while the mean and maximum speed are larger by 2.3×10^{-4} m/s and 1.4×10^{-4} m/s (resp. 8.8×10^{-5} m/s and 7×10^{-5} m/s) (see Fig. 6.15). The other aspects of the velocity and elevation fields remain unchanged with respect to the reference case.

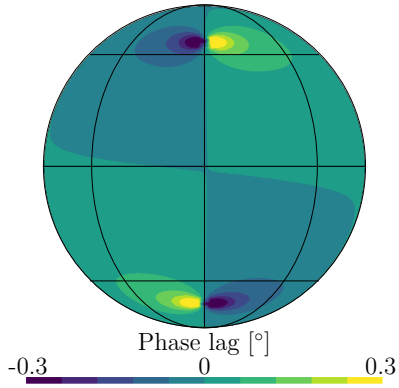

Fig. 6.16: Difference between the phase of the diurnal tidal component of the reference subsurface ocean and that of a similar ocean with a highly viscous shell lying over (i.e., B is 100 times larger than for the reference case). The maximum lag occurs near the amphidromic points of the diurnal component. The phase lag is negative/positive almost everywhere on a spherical octant and changes sign near their separation.

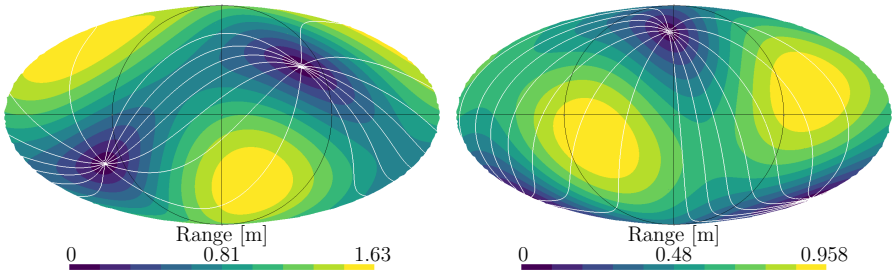

Fig. 6.17: Tidal range (in m) and phase (white lines, with a 22.5° spacing) of the tidal components whose associated range is the second (left panel, period of $\frac{1}{46}$ TD) and third (right panel, period of $\frac{1}{47}$ TD) largest (the largest being the diurnal) when the viscous part of the surface pressure is multiplied by 100. Both tidal components have two antipodal amphidromic points.

Slimming the viscoelastic bottom layer results in an increase of the elastic aspect of the deformation while diminishing its viscous aspect (i.e. A increases and B decreases). Such modifications of the surface pressure induce a decrease of the surface elevation and speed. The maximum elevation and speed decrease by 0.06 m (see Fig. 6.15) and 1×10^{-4}m/s, respectively. The other aspects of the elevation and velocity fields are not impacted. We also study the case of a highly viscous shell by multiplying B by 100 in order to separate the effects of the viscous deformation from those of the elastic deformation. In this case, the range of the diurnal tidal component remains unchanged with respect to the reference case but a phase lag of about $\pm0.3°$ is observed (see Fig. 6.16). The latter is maximum near the amphidromic points and is positive/negative over almost a whole spherical octant. The most significant variation of the elevation field consists in the appearance of high frequency oscillations. They result in a maximum elevation larger by 0.75 m and occurring 0.15 TD after apokron. Several tidal components are associated to these oscillations. Those that have the largest range (1.63 m and 0.958 m) have a period of $\frac{1}{46}$ and $\frac{1}{47}$ TD (see Fig. 6.17). The velocity field also undergoes significant variations. Although the velocity field consists of two gyres separated by a ring of high velocity flow, the gyres centre do not follow a sinusoidal motion but rather a helicoidal one around the equator. This back-an forth motion of the center is due to the small period oscillations of the elevation. It also results in centres located at higher latitudes than in the reference case (up to 12°). The magnitude of the velocity field is also impacted. The mean speed is slightly larger (by 9×10^{-5} m/s) while the maximum speed is significantly larger (by 2.7×10^{-3} m/s). We conclude that the viscous deformation does not impact the global behaviour of the diurnal motion but can generate high frequency oscillations impacting both the velocity and elevation fields.

An ice shell deforming as the ocean (i.e. the surface pressure term is nil) does not significantly modify the surface elevation in terms of amplitude or spatial patterns. The velocity field is simi-

lar to the one of a free surface ocean although the maximum and mean speed are slightly smaller, by 3×10^{-5} m/s and 3×10^{-4} m/s, respectively. In the opposite case of a friction-less ice shell, the surface elevation is similar to the one of a subsurface ocean, with a maximum elevation 0.28 m smaller than the maximum predicted for a free surface ocean. The velocity field is similar to that of a subsurface ocean but the maximum and mean speed are slightly larger, by 4×10^{-5} m/s and 4×10^{-4} m/s, respectively. We conclude that the impact of the friction on the velocity field is less significant than that of the ice shell and the latter impacts both the velocity and elevation fields.

6.6 Discussion

6.6.1 Deformation of the bottom of the ocean

Similarly to the ice shell at the top of the ocean, the bottom of the ocean deforms due to the tidal forcing, resulting in an attenuation of the forcing acting on the ocean. This effect can be modelled by means of an attenuation factor (similarly to what is done for the surface lakes and seas). The real parts of the Love numbers k_2 and h_2 are 0.12 and 0.221 (Hay and Matsuyama, 2017), resulting in an attenuation factor $\gamma_2 = 0.899$, which is close to unity. As shown in the previous chapters, in an enclosed domain without internal separation, multiplying the forcing by the attenuation factor results in decreasing the surface elevation and speed without modifying the spatial patterns. A numerical simulation is conducted for a subsurface ocean whose bottom deformation results in an attenuation of the forcing. The predicted elevation decreases, leading to a maximum elevation of 7.74 m (which is the value obtained by multiplying the maximum elevation predicted for the reference case by γ_2). The mean and maximum speed are also smaller, by 6×10^{-4} m/s and 9×10^{-4} m/s, respectively. The energy dissipated by friction within the ocean is therefore smaller, 2.4×10^{-4} W/m^2. Other aspects of

the elevation and velocity fields are not significantly modified by the attenuation factor. The elevation and speed predicted by our model should therefore be used as an upper bound.

6.6.2 Thermally driven flow

The temperature gradient resulting from the heat fluxes at the top and bottom of the ocean can generate a significant thermally driven flow. The latter interacts with the tidal flow, modifying significantly the flow orientation and locally increasing the speed and, hence, the heat production through viscous dissipation. The predicted temperature variation over the depth is small, which matches the results of Amit et al. (2019). In this chapter, we assume a uniform bottom heat flux while the latter is expected to vary significantly. Indeed, according to Choblet et al. (2017), the heat transfer trough the high pressure ice layer mainly consists of water transport in hot convective plume conduits. In the absence of tidal motion, such a bottom boundary condition induces narrow cylindrical chimneys which broaden over time until they become baroclinically unstable (Goodman and Lenferink, 2012). On Europa, the currents associated with these plumes can reach 5 cm/s (Goodman and Lenferink, 2012). The tidal motion would likely prevent the formation of purely vertical chimneys due to the horizontal transport associated with the tides[6] while the chimneys could locally modify the flow orientation and magnitude. Depending on the size of the hot convective plume conduit (and the resulting chimneys), the bottom heat flux could impact the lower ocean layers, locally modifying the liquid motion, or the whole ocean. The vertical transport of hot water from these plumes to the top ice shell could partially explain the variations of the surface heat flux. In order to study their impacts on the tidal motion, the spatial distribution as well as the characteristics of the water in the plume should be known.

[6]This assumption is not based on numerical results but on the observation of wind induced updraft rupture below cumulus: the horizontal wind velocity can tear apart the updraft, which results in isolated updraft bubbles.

Other phenomena which could have a significant impact on the flow are also neglected. The heat production by dissipation within the ocean as well as the latent heat flux are not taken into account in the ocean heat balance. Indeed, the melting/freezing processes could play a significant role by modifying locally the bathymetry. Such aspects should be implemented in the model in order to increase the accuracy. Nevertheless, this is not the goal of the present study which aims at evaluating the thermally driven flow with regards to the tidal one. Their interactions being significant, a more complex model should be build to construct a more realistic representation of the thermal aspect of our study but this is beyond the scope of this chapter.

6.6.3 Influence of the ocean depth, the friction, and the ice shell rheology

Several aspects of Titan's subsurface ocean are poorly constrained. Some of them, such as the liquid density, are not considered here, as their influence on barotropic phenomena is negligible, while others are interconnected, which makes it difficult to distinguish their impact from that of other parameters. Therefore, the influence of three major parameters is discussed while the others are disregarded. These parameters are the ocean depth, the mechanical behaviour of the ice shell lying at the top of the ocean, and the friction at the top and bottom of the ocean. The parametric studies are limited by the actual knowledge of the ocean. For instance, the depth is assumed to be constant although the top and bottom could be undulated due to spatial variations of the heat fluxes. Such limitations are unfortunately unavoidable as there are almost an infinity of realistic configurations.

The ocean depth has a significant influence on the liquid motion. The variations mainly consist of a phase lag of the surface elevation and modifications of the speed. The former and the latter respectively increases and decreases when the depth is increased. The phase lag could be explained by the influence of the ocean depth

on the phase speed of the gravity waves in shallow water. The latter is proportional to the square root of the depth. Modifying the depth therefore results in variation of the phase speed, which could explain the phase lag observed in the elevation field. In the case of a 50 km deep ocean, high frequency oscillations were predicted. One explanation could be that the high frequency oscillations occurring in deeper oceans are not captured by our model due to the time step. This assumption was tested by conducting a simulation with an export time step divided by 5 (i.e. 10^{-3} TD) for a 100 km deep ocean. No high frequency oscillation being observed, this explanation is ruled out. Another explanation could be that a normal mode of the ocean is excited. Indeed, the more shallow the ocean, the longer the natural period. The small period oscillations in a 50 km deep ocean could be due to a normal mode which would not be excited in deeper ocean due to its smaller natural period.

While the friction cannot be disregarded, multiplying/dividing the uniform friction coefficient by a factor 2 does not significantly modify the tidal motion in the subsurface ocean. The velocity orientation can locally change, due to the displacement of the gyres center, and the flow slightly slows down but the variations are small with respect to those observed when the depth or the shell mechanical behaviour are modified. A non uniform friction coefficient could locally impact the flow speed but the influence of the coefficient spatial variations is expected to be small and is therefore not studied.

The effect of the ice shell is similar for each of the configurations studied: it decreases the amplitude of the surface elevation and it slows down the flow without significantly modifying the global patterns of the elevation and velocity fields. Such differences make sense as the effects of the shell are modelled by modifying the surface pressure term and doubling the friction coefficient. Doubling the friction coefficient slows down the flow while the increase of the surface pressure slows down the flow and decreases the surface elevation. The elastic deformation of the ice shell increases the horizontal pressure gradient (which exists in the "classic" shallow

water equations, its effect is thus similar to increasing the mean gravitational acceleration) while the viscous deformation results in a smaller, 90° out-of-phase, surface pressure. Depending on the rheology and thickness of the bottom layer, the elevation decrease and flow slowing down is more or less significant (see Fig. 6.15): the larger A, the smaller the elevation and speed. The factor B has the same effect within the range corresponding to Fig.6.15. In order to highlight the effect of the viscous deformation, we conducted a simulation where B is multiplied by 100. In this case, the flow is speeded up, the elevation is larger and the spatial patterns of these fields are significantly different from those predicted in the reference case. These modifications are mainly due to the apparition of high frequency oscillations resulting from the viscous surface pressure that is out of phase with respect to the elevation field.

The ocean depth and the ice shell rheology both influence the tidal motion but in different ways: the speed varies more significantly with respect to the ocean depth while the shell deformation has a stronger impact on the amplitude of the surface elevation. Regarding the diurnal tidal component, the shell mainly impacts the range while the depth modifies the tidal phase of the component. A shallow ocean or a highly viscous ice shell could also result in the appearance of small period oscillations, modifying the global aspect of the elevation field and possibly increasing the maximum elevation.

In our study of the impact of the ice shell deformation, the shell is assumed to be made of two layers: an elastic top layer and a bottom layer which can be elastic-like, viscoelastic, or fluid-like, depending on its viscosity. Using a different rheology could slightly modify the results presented but this is taken into account by studying the impact of the shell deformation for significantly different configurations, which likely spans the rheology variations resulting from the use of another model. Our approach does not take into account the feedback effect of the ocean on the ice shell deformation. This could be circumvented by coupling an ocean model and a deformation model. While the impact of the ice shell

on the tidal motion is significant, the variations associated with the different shell mechanical behaviour implemented are small, except for a highly viscous shell. Therefore, we do not think a more elaborate approach is necessary as we consider our model to be well suited for a first approach of the tidal motion within the subsurface ocean –it allows evaluating the significance of the impact of the ice shell deformation on the liquid motion. However, we recognize that a more complex model should be developed if a high accuracy is requested. While the impact of improving the representation of the shell deformation on the tidal motion is expected to be small (if not insignificant), it could be interesting as part of a more elaborate study. Indeed, we assume a constant bathymetry and a smooth ice-water interface. These hypotheses are made because of the lack of information although such parameters are expected to have a significant impact on the tidal motion (especially the depth variations which could generate a Venturi effect[7]). In order to study such phenomena, a much more elaborate model should be built. It should take into account the surface heat fluxes, their spatial variations, and the crystallization/melting processes at the top and bottom of the ocean. The latter impact the deformation of the shell in a way that only a complex 3D model could apprehend. In order to model its impact on the ocean, a time-varying bathymetry should be implemented and the latent heat flux should be taken into account. Building such a model is beyond the scope of this thesis and could be the main topic of a PhD thesis, which could take advantage of the forthcoming JUpiter ICy moons Explorer (JUICE) mission. this mission will reach the Jovian system in 2030 and will study three icy moons housing a subsurface ocean (Europa, Ganymede and Callisto). This model could easily be applied to these moons. The data collected by JUICE could be used to improve the model, confirm (or disprove) our working hypotheses, and/or as a basis to construct the more elaborate model discussed above.

[7]The Venturi effect is an acceleration of the flow due to a constriction of a pipe. It can also be observed in natural environment on Earth such as in river rapids or mountain passes.

6.6.4 Energy dissipation by friction

The mean rate of energy dissipated by friction in the ocean over a tidal period is computed following the same approach as, e.g., Hay and Matsuyama (2017); Sears (1995): $\dot{E} = -\frac{1}{\Omega}\int_\Omega \frac{\rho c_D u^3}{H} \mathrm{d}\Omega$ where Ω is the volume of the domain, ρ is the liquid density, u is the speed, and c_D is the quadratic bottom friction coefficient. The resulting heat flux is then temporally averaged, leading to the mean rate of energy dissipation by friction over a tidal period (in $\mathrm{W/m^2}$).

Energy dissipation within icy satellites has been the subject of many studies (e.g. Tyler, 2008, 2014; Matsuyama, 2014; Matsuyama et al., 2018; Hay and Matsuyama, 2017, 2019). Unfortunately, either these authors computed the dissipation within the whole satellites or they paid attention to smaller depths at which resonance could occur, generating more heat through dissipation, which prevents us to compare numerical values. The global behaviour predicted by Hay and Matsuyama (2017) is also observed in our results: the amount of energy dissipated by friction decreases when the depth or the friction coefficient are increased. The mechanical behaviour of the ice shell lying above the ocean has a small effect on the energy dissipated by friction within the ocean: the mean rate varies by less than 13%. The ocean depth has a more significant influence with a dissipation rate 48 times larger for a 100 km deep ocean than for a 400 km deep ocean.

6.7 Conclusion

The existence of an ocean lying beneath Titan's icy surface is asserted by several observations and measurements (Rappaport et al., 2008; Béghin et al., 2010; Nimmo and Bills, 2010; Iess et al., 2012; Hemingway et al., 2013; Lefevre et al., 2014; Baland et al., 2011, 2014). This ocean has a substantial impact on the deformation of Titan and is a place where tidal energy is dissipated. Various studies focus on these aspects (see, e.g., Tyler, 2008, 2014; Matsuyama, 2014; Matsuyama et al., 2018; Hay and Matsuyama, 2017, 2019).

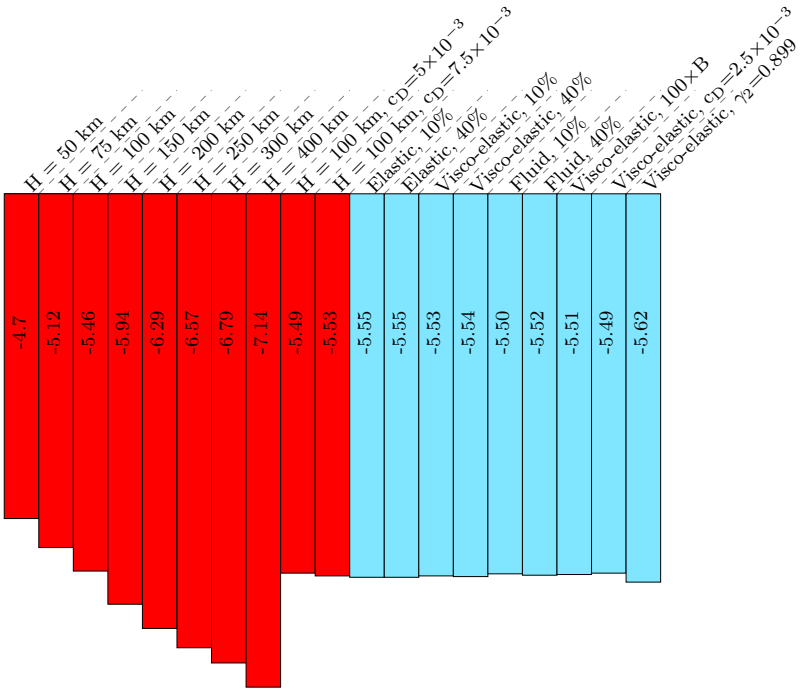

Fig. 6.18: Log_{10} of the mean rate of energy dissipation averaged over a tidal period [W/m^2] for each of the configurations studied. The free surface and subsurface configurations are filled in red/blue, respectively. The subsurface ocean depth is 100 km.

In this chapter, we studied the liquid motion within the global subsurface ocean using an Earth-based model, SLIM, which can solve the equations on a sphere and was adapted to the specific conditions of Titan. The 2D and 3D versions were used to predict the tides and the thermally driven flow, respectively. The mechanical behaviour of the ice shell and the depth of the ocean being poorly constrained, a sensitivity analysis with respect to these parameters was conducted.

Our model predicts an elevation field made of two troughs/bulges rotating around Titan and resulting in a diurnal tide whose max-

imum amplitude is 8.9 m. The associated depth-averaged velocity field consists of two gyres separated by an area of high speed flow. The centres of the gyres move westwards following a sinusoidal path centred on the equator and whose amplitude is small. Taking the ice shell lying above the ocean into account results in a smaller surface elevation and a slower tidal flow but does not modify the spatial patterns of these fields. The magnitude of the speed and elevation reduction depends on the mechanical behaviour of the ice shell. For instance, the impact of a fluid-like ice shell is less significant than that of a viscoelastic or elastic shell. The other poorly constrained parameter whose influence is studied is the ocean depth. The latter has a minor impact on the elevation field but increasing the ocean depth significantly slows down the tidal flow. These results suggest that, while the influence of the ice shell on the liquid motion is significant, the latter is less sensitive to the mechanical behaviour of the shell. Therefore, it is important to take into account the shell and to have a good estimation of the ocean depth to model the tidal motion.

The ocean experiences significant heating/cooling at its top and bottom. These heat fluxes have a significant impact on the flow, while the impact on the elevation is small in terms of magnitude. The resulting flow is significantly different from the tidally induced one: the gyres are located at higher latitudes and, in the case of a realistic surface heat flux, they rotate around the poles following a sinusoid centred on the 60° parallel. These results suggest a 2D model is efficient to model the tides of the subsurface ocean and study the influence of the depth and shell deformation but a 3D model is needed to study the liquid motion as the thermally driven flow is significant and strongly interacts with the tidal flow.

CHAPTER 7

Conclusions and perspectives

The astronomers' interest for Titan was raised by the observations of Voyager spacecrafts. Further explorations were conducted by means of Earth-based observation tools and the successful Cassini mission provided plentiful data whose analysis is an ongoing process. While this mission answered a variety of questions, crucial ones remain open. To this end, various exploration missions have been designed. One of them, Dragonfly (Lorenz et al., 2018), was recently selected by the NASA as part of its New Frontiers program while others are still under development and are proposed to several spatial agencies (Mitri et al., 2014a; Hartwig et al., 2016). Despite the numerous projects, new *in situ* data are not expected before at least 14 years. Indeed, Dragonfly, which is the most advanced project, is expected to be launched in 2026 and will land in 2034. Until then, Earth-based observations, data analysis by means of

enhanced algorithms, and numerical modelling are the only tools able to provide new pieces of information about Titan.

Exploration of Titan's liquid bodies

Titan is the only celestial body of the solar system, besides the Earth, housing significant surface liquid bodies. The latter played a key role in the apparition of life on our planet. It was thus instinctive to pay interest to the surface lakes and seas of Titan although the latter are filled with liquid hydrocarbons instead of water. The oceanography of Titan is still in its early stages due to the lack of data and observations, which leads to large uncertainties in the models predictions and prevents the scientists from validating their model(s) by comparison with *in situ* measurements. Unfortunately, pieces of information only available through numerical simulations are requested to design an exploration mission focusing on the surface lakes and seas. For instance, an *a priori* knowledge of the flow is a key feature in the design of an exploration mission. It is a chicken-and-egg problem. To circumvent this paradox, one has to proceed in stages. The first step consists in running numerical simulations of the flow in the surface lakes and seas using the scarce data available. Depending on the landing craft, different aspects of the liquid motion need to be known. For instance, the maximum flow speed is needed to design the engine of a motorised capsule while the orientation of the flow is useful to predict the path of a non-motorised capsule as a function of time and landing site and to select the latter such that the capsule does not beach within a short amount of time. The variation of the sea/lake surface elevation is a key parameter in order to ensure the capsule is able to be refloated from the beach, if it beaches on purpose at a given location. The influence of the poorly constrained parameters has to be assessed by means of sensitivity analyses. The results can then be used to design the selected operation mission taking into account the worst case scenario predicted by the sensitivity analyses. The data col-

lected by this exploration mission could be used to validate more accurately the models and improve them as well as our understanding of the physical mechanisms at play. The results of the improved models could then be used to help analysing the data collected or to design more complex exploration missions.

While there are proposals for exploration missions focusing on the surface lakes and seas, such missions are not expected to take place before years. Indeed, the surface liquid bodies are located in the high latitudes, mostly in the northern hemisphere. The last spring equinox in this hemisphere occurred on August 11, 2009. A year on Titan lasting about 29.5 years on Earth, the autumn equinox in the northern hemisphere will occur before the next exploration mission could reach Titan (which is expected to be in 2034). Direct to Earth communication with a lander being impossible at high latitudes during the winter (without an orbiter acting as a relay antenna), it was decided that the next exploration mission, DragonFly, would land in the equatorial region, as it does not include an orbiter. The main drawback of a single lander is that it explores a single location, which can be circumvented if the lander is mobile. Among the concepts presented in the literature, Lorenz (2000) proposed a helicopter but, a helicopter being mechanically complex, this idea was not very successful. Fortunately, technology developments in the last decades led to the advent of drones, which are much better suited for spatial exploration. The Dragonfly mission, which consists in sending a rotorcraft on Titan was recently selected by the NASA as part of its "New Frontiers" program. While it was first imagined granting the rotorcraft with amphibian capabilities, this idea was not pursued and it was decided to focus on operations on dry land (Lorenz et al., 2018). Dragonfly is expected to land at a location and season similar to the Huygens descent in 2005 to take advantage of the data collected by the probe. Once the drone is released from the entry system and parachute, it will take advantage of its mobility to scan the area and select the more favourable landing site. After Dragonfly safely landed, it will carry on small displacements and then flights of increasing range, dura-

tion, and height. The mission aims at improving our knowledge of the organic and methanogenic cycle on Titan and investigating the subsurface ocean and/or liquid reservoirs, particularly their evolution and interactions with the surface (Lorenz et al., 2018). To this end, Dragon fly will (Turtle et al., 2017)

- Identify the chemical components and processes producing biologically relevant compounds by sampling surface material and conducting analyses with a mass spectrometer;
- Analyse bulk elemental surface composition by means of a neutron-activated gamma-ray spectrometer;
- Provide measurement of the atmospheric and surface conditions as well as their diurnal and spatial variations with meteorology sensors;
- Characterise geologic features by imaging;
- Perform seismic studies to detect subsurface activity and structure;
- Measure atmospheric vertical profile near the surface;
- Provide aerial images of surface geology.

Several Jovian and Saturnian moons house a global subsurface ocean beneath their icy surface. Such subsurface oceans are interesting candidates as potential life-supporting areas. Unfortunately, the subsurface oceans are out of reach for common exploration missions although some aspects such as their density and depth can be inferred/modelled from the data collected. Different models are required to study the habitability of such oceans. Three main approaches exist: the "follow the energy", the "follow the water", and the "follow the nutriment" approaches (see, e.g., Lingam and Loeb, 2018). Those three approaches require an *a priori* knowledge of the liquid motion within the ocean, which can be provided by a hydrodynamic model.

While Dragonfly could provide data about Titan's subsurface ocean by performing seismic studies, the next advance regarding the subsurface oceans of icy moons will likely come from the JUpiter ICy moons Explorer (JUICE) mission which will be launched in 2022 and should start observing the Jovian moons in 2030. This mission will first orbit Jupiter, investigating Callisto and Europa and then orbit Ganymede. While the mission focuses on Jovian moons housing a subsurface ocean, it will also study other aspects of these natural satellites. Regarding Ganymede and, to a lesser extent, Callisto, JUICE will

- characterise the ocean layer and detect putative subsurface water reservoirs;
- study the physical properties of the icy crust;
- characterise the internal mass distribution, dynamics and evolution of the interiors.

JUICE will provide the first subsurface sounding of Europa and the minimal thickness of its icy crust over the most recently active regions.

The model used to study the liquid motion in Titan's global subsurface ocean could easily be modified to study the ocean of Callisto, Europa, and Ganymede. The data collected by JUICE could be used to better constrain the model's parameters regarding the Jovian moon and validate and/or improve our model. Our model is of little interest for the preparation of the mission as an orbiter does not need an *a prioiri* knowledge of the domain studied. Nevertheless, the model could be used in a retro-engineering approach: once the deformations of the surface are well constrained and the number of poorly constrained parameters is reduced, the model could be used to infer the missing parameters from the results. Parameters such as the ocean depth could not be inferred as their influence on the elevation is insignificant but others could more easily be constrained. For instance, the surface heat flux generates

a constant elevation which could be isolated from the temporally varying surface deformation measured. Conducting a great number of simulations for various boundary heat fluxes could provide a first approximation of the real boundary heat fluxes.

Numerical modelling

Numerical modelling allows virtually experiencing situations that cannot be observed and to study the impact of various parameters. It is therefore a powerful tool for scientists studying extra-terrestrial sciences for which data are scarce and observations occasional. Each model has its advantages and drawbacks. For instance, a full 3D hydrodynamic model coupled with a meso-scale atmospheric model is able to predict the surface flow which impacts the path of a capsule but it is very costly to use to conduct a sensitivity analysis with respect to the poorly constrained parameters. On the other hand, a 2D hydrodynamic model allows studying a wide range of parameters but only predicts the depth-averaged flow. The ideal tool to study a domain where the lack of data is significant is therefore a combination of these models. The less costly model should be used to study the impact of a wide range of parameters and build a database. Once the range of variation of each parameter is reduced by comparing the results with the observations, a more complex model should be used to predict more accurately the liquid motion. Depending on the domain and data, such models may not exist or the data may not be available to constrain the parameters based on the database.

My thesis in this context

The objective of this thesis was as follows:

> *Using the scarce available data and a numerical model to improve our knowledge of the motion of surface and*

subsurface liquid bodies of Titan, thereby helping design future exploration missions of this moon.

To this end, I adapted the Second generation Louvain-la-Neuve Ice ocean Model, SLIM, to extra-terrestrial conditions. The equations solved by the model were modified to take into account the impact of Titan's surface deformation on the liquid motion in the surface lakes and seas and in the subsurface ocean. Due to the lack of data, sensitivity analyses were conducted with respect to the poorly constrained parameters by means of the 2D version of SLIM. The 3D version was also modified to model the liquid motion on Titan. 3D simulations being significantly more costly, the model is used sparingly to study the interactions between the thermally driven flow and the tidal flow in the subsurface ocean (see Chapter 6) or is applied to a specific sub-domain such as Trevize Fretum, the strait linking Kraken and Ligeia Mare (see Vincent et al., 2017).

The liquid motion predicted in the subsurface ocean could be used by astrobiologists studying the habitability of such an ocean or to constrain the internal heat fluxes. Such applications are beyond the scope of this thesis and are therefore not further developed. Regarding the surface lakes and seas, one goal of the thesis was to provide the elevation variations and the tidal flow, which are key data for the design and planning of an exploration mission focusing on the surface liquid bodies. The lakes/seas surface elevation variations allow highlighting area(s) where the capsule could beach. The tidal flow, on the other hand, can be used to predict the path of a drifted capsule, to provide design constraints for the engine of a motorised capsule/submarine, and to schedule some aspects of the mission such as the crossing of the straits linking the basins of the northern seas. Indeed, it would be convenient to go through these straits when the tidal current is in the right direction to save energy. The Lagrangian particle tracker module (LPT) implemented in SLIM was used to predict the path of a drifted capsule. It could be modified to study the path of a motorised capsule by adding the acceleration resulting from the thrust in the cinematic equations.

This could be an asset to optimize the engine operation: using the latter by phase would save energy and reduce the fatigue stress. A modified version of the LPT could easily model the influence of the engine phases on the path, hence allowing conducting a sensitivity study in order to optimize the phases distribution such as the capsule follows a defined path.

Several aspects of SLIM were modified/improved as part of this thesis. The modified model used to study the surface lakes and seas could be used on Earth if the user provides the suitable parameters. There is no other application due to the absence of significant surface liquid bodies in the solar system. The model used to study the liquid motion in the subsurface ocean, on the other hand, could be easily modified to study the ocean of other icy moons housing a subsurface ocean (although particular attention should be paid to the aspect ratio for small moons such as Enceladus). Studying those oceans could be interesting in the context of the forthcoming JUICE mission. Numerical modifications of SLIM could also be useful for terrestrial applications. For instance, its ability to solve the equations on the sphere could be used to study domains where geographic projections are not well suited[1]. The post-processing tools developed have already been used by other members of the SLIM Team.

Various studies focusing on the surface lakes and seas were conducted in parallel with this thesis. My work differs by the high number of parameters taken into account as well as a better spatial representation of the nearshore areas by taking advantage of the geometrical flexibility of the unstructured grids. The internal structure of Titan and its ocean were also the main topic of studies conducted in parallel with this. My work focuses on the hydrodynamics of the ocean while most studies consider the ocean as a layer while studying the internal structure of Titan or pay interest to the dissipation in the ocean but not to the flow itself.

[1] In terrestrial domains, SLIM solves the equations on a flat domain which is obtained by geographic projection of the globe's surface.

Ontario Lacus

Ontario Lacus was the first lake studied as part of this thesis (see Chapters 3 and 4). This lake was selected as the first application for two reasons: two bathymetry maps were available and unexplained shoreline variations were observed. The tides were ruled out as an explanation shortly after the beginning of this thesis, which was confirmed by our results. The elevation field is similar to that predicted by Tokano (2010) while the velocity field significantly differs. This is due to the use of a complex bathymetry and the better spatial resolution of our simulations, which enhanced the representation of the coastline, resulting in a better capture of its effect on the flow. The normal modes of the lake were also studied, as a seiche could explain local but significant shoreline variations, and the lake response to arbitrary wind conditions was discussed.

The tides in Ontario Lacus cannot be observed by means of an orbiter. Indeed, the tidal range is much smaller than the vertical resolution of the state-of-the-art instruments. The shoreline variations induced by the tidal motion are also too small to be observed by a radar while Titan's atmosphere makes observation in the visible spectra harder. A spacecraft landing in the lake could easily provide temporal series of the surface elevation and velocity, an accurate bathymetry map as well as the liquid composition and atmospheric conditions. The temporal series of the surface elevation could be used to validate our numerical results (the diurnal signal should be isolated as other forcings could modify the elevation). The bathymetry map would decrease the uncertainties surrounding our results and the liquid composition and atmospheric conditions could be used to take into account additional forcings while studying the liquid motion in the lake. Unlike the tidal motion, the liquid motion associated with large scale normal modes could be observed by an orbiter, if they were resonantly forced. Indeed, the latter can result in high amplitude elevation variation, which could results in significant shoreline variations. The latter could be captured by an orbiter just as those observed by Cassini.

The numerical results can be used to constrain various aspects of a mission consisting in a capsule landing in the lake. For instance, in the light of the small tidal range, less than 0.06 m, beaching should be avoided as the tides could not refloat a beached capsule. The path of a drifted capsule as a function of time and sea landing site was studied by means of the LPT. As expected, the displacements induced by the tidal motion are small, less than 1 km over 3 Titan days (i.e. 1.5 months on Earth) except in the nearshore high speed areas where it can reach a few kilometers. A floating capsule should therefore be motorised to prevent beaching and to allow more significant displacements. In Ontario Lacus, the engine of the capsule should be designed while taking into account the wind forcing as the influence of the latter on the path could be more significant than that of the tidal motion.

The model in itself does not need to be improved to enhance our representation of the tidal motion in Ontario Lacus. Additional data allowing validating the results would be helpful but they are not expected before years. The major improvement that could be effective within a reasonable amount of time would be to couple SLIM3D with a meso-scale atmospheric model to study the air-sea interactions. Indeed, although the wind speed is weak regarding terrestrial standards (at most 10 m/s under stormy conditions), the larger atmosphere density and the smaller liquid density increase the influence of the wind, resulting in a surface stress of the same order of magnitude as on Earth. Two situations are of interest: the liquid motion under stormy conditions and under standard wind conditions. The former could be related to our study of the normal modes. If a mode with a recognizable pattern and a large amplitude develops, it could be observed by the next exploration mission. The liquid motion under standard wind conditions is useful as part of the creation and design of a lander. Due to the slow tidal motion, the wind could play a significant role in the drift of a capsule both by modifying the flow and by pushing the lander in a specific direction (this observation does not stand if the lander is a submarine). The driving effect of the wind on a capsule could be modelled by

adding the acceleration resulting from this force in the cinematic equations of the LPT. Using the velocity field predicted by the 3D model would be more accurate as the surface velocity can locally significantly differ from the depth averaged velocity. The particle tracker module being 2D, the surface velocity would be used by the latter instead of the depth averaged velocity.

Northern seas

The northern seas of Titan are another liquid area of high interest. The tidal motion and the liquid exchange between the two largest seas were studied by means of SLIM2D (see Chapter5). The comparison of our results with those of Tokano et al. (2014) is deemed satisfactory both in term of magnitude and spatial patterns. Solar glints at the northern mouth of the strait linking Kraken and Ligeia Maria were observed by Sotin et al. (2012). Turbulent eddies or high velocity flows could be responsible for these glints. Therefore, SLIM3D was briefly used to study this area using the sea surface elevation and depth averaged flow as boundary conditions (see Vincent et al. (2017)). The surface speed can locally reach 0.12 m/s and small gyres were observed but their impact on the sea surface roughness was not discussed. Numerical simulations of the liquid motion due to the density gradient (Tokano and Lorenz, 2016) and wind (Tokano and Lorenz, 2015) based on the predictions of a global circulation model can also be found in the literature.

An orbiter would not be well suited to observe the tidal motion as the height variations are small (especially with respect to the deformation of Titan's surface), although the horizontal variations between low and high tides could induce shoreline variations significant enough to be observed by a radar, depending on the morphology of the surroundings. A lander would be better suited for the same reasons as in Ontario Lacus. Nevertheless, it would be more interesting to send a lander in the northern seas as the later could constrain spatial variations of the atmospheric fields (surface temperature, air moisture, wind velocity . . .) on a much larger scale

than in Ontario Lacus and could provide a bathymetry for Kraken Mare and data about possible variations of the liquid composition between the basins.

The northern seas are a designated target for future exploration mission(s). Several proposals were published. At least two of them consist in sending a lander (a drifted capsule or a submarine) in the northern seas. An *a priori* knowledge of the tidal motion in theses seas is an asset for the design and planning of such missions. Although the tidal range is larger than in Ontario Lacus, it is still small and unable to refloat a beached capsule. The path of a drifted capsule as a function of time and landing site was studied by means of the LPT. The capsules landing offshore drift by less than 2 km over 3 Titan days (TD) while those landing in the straits can drift up to 80 km over the same period. Their paths, however, mainly consist of back and forth motion: capsules landing during a specific period are the only one which can reach the straits outlets without being driven back. Therefore a motorised capsule would be better suited as it could travel longer distance and avoid being trapped in the straits. Other forcings such as the wind could impact the path of the capsule. The effect of the wind pushing on the superstructure of the capsule could be taken into account by adding the acceleration resulting from this force in the cinematic equations of the LPT but the influence of the wind, density spatial variations, surface heat fluxes ... on the liquid motion should also be taken into account in the hydrodynamic model. Conducting a study of the liquid motion induced by the tides, atmospheric forcings, and density gradient is tricky as the timescale of these phenomena are significantly different while they are equally significant in terms of flow speed (at least in the middle of the seas according to Tokano and Lorenz (2015, 2016)). The best approach seems to consist in focusing on a specific area using an atmospheric mesoscale model to predict the wind and the surface boundary conditions for the temperature equation. The lateral boundary conditions could be given by SLIM2D and the results of Tokano and Lorenz (2015, 2016). The depth averaged velocity field has already been used

as boundary conditions for 3D modelling of sub-domains such as the straits linking the northern seas (see Vincent et al., 2017). An advantage of this approach would be that the LPT could use the surface velocity field instead of the depth-averaged velocity field to predict the displacements of a capsule. While these velocity fields are not expected to differ significantly regarding the tidal motion, this is no longer the case when baroclinic phenomena and wind forcing are taken into account. The straits linking the basins are also a key point for the design of a motorised capsule/submarine as the speed there is one order of magnitude larger than elsewhere in the northern seas. It will therefore constrain the engine of the capsule/submarine. An *a priori* knowledge of the velocity variation with respect to the depth in the straits would be an asset to design a submarine. Indeed, the velocity orientation and magnitude varies with the depth. Selecting the appropriate period and/or depth for a crossing would result in a significant energy saving and would decrease the maximum engine power needed.

It could also be interesting to take advantage of the developments of SLIM conducted in parallel with this thesis. Indeed, a member of the SLIM team, Thomas Dobbelaere, recently coupled SLIM with a wave model, SWAN (Simulating WAves Nearshore, `swanmodel.sourceforge.net/`, see Booij et al. (1997)). Studying the waves of the northern seas could be interesting both as part of the design of a lander and to explain phenomena such as the solar glints and the "Magic Islands". Indeed, the capsule should be stable enough to not capsize due to the regular swell and its structure should be sized to be able to resist the small shocks with the waves. Therefore, the waves height and energy should be quantified as they are useful quantities for the design of a capsule. Regarding the "Magic Islands", four explanations were initially proposed. The tides being ruled out, the remaining suspects are sediment in suspension, rising bubbles, and small waves. Due to the lack of information, it is not possible to study the sediment transport in the area of the "Magic Islands" and rising bubbles request a different model to be studied. The third explanation could be discussed

by means of a coupled SLIM-SWAN model. Such a model requires an *a priori* knowledge of the wind distribution during the period studied. The wind predicted by a mesoscale atmospheric model (or a GCM, depending on the domain studied) could be used as input without coupling the atmospheric model with the SLIM-SWAN model.

Possible connection(s) with a third basin south of Kraken Mare and with Punga mare could be taken into account in order to improve our model. Although no connection is visible on the Cassini images, Punga Mare is likely connected to the northern seas as its surface is on the same equipotential as those of Kraken and Ligeia Maria. Regarding the basin south of Kraken Mare, a connection appears on ISS images but not on the radar images. This basin was therefore disregarded as our study is based on radar images. These basins could however be linked to Ligeia and/or Kraken Maria by canals too small to be observed by Cassini, by a subsurface flow, or by swamps. Taking into account the connection with these basins could modify the tidal motion as the liquid exchanges between basins have a significant impact on the tidal phase (see Chapter 5). Nevertheless, conducting such a study without basic knowledge of the domain is pointless. Crucial parameters such as the horizontal dimensions of the canals/straits or an approximation of the volumetric flow rate are required to construct a realistic approximation of the domain.

Global ocean

The penultimate chapter of this thesis focuses on the liquid motion in the subsurface ocean of Titan. Studying the liquid motion in this ocean could seem to be of little interest as models predicting the deformation of Titan or the tidal dissipation are available. Nevertheless, studying the liquid motion can help ruling out or validating assumptions about the heat fluxes at the top and bottom of the ocean and the results could be useful for astrobiologists paying attention to the ocean as a life-supporting area.

The ice shell has a significant impact on the surface elevation and the velocity field. Its effect should therefore be taken into account by scientists paying interest to the ocean hydrodynamics. Nevertheless, while a fully coupled model could be used to improve our knowledge of the fluid-structure interactions, the further insight gained would be very limited due to the poorly constrained parameters. Such a model could detect a resonance phenomenon induced by the interactions but such phenomenon seems to appear only in unrealistically shallow ocean (see, e.g., Hay and Matsuyama, 2017; Tyler, 2014). Building such a model would be a giant with feet of clay as the accuracy gained would be rendered useless by the uncertainties in the parameters. The preliminary study also shows that the tidal and thermally driven flows strongly interacts. Taking into account disregarded phenomena such as the ice melting/water freezing (and the resulting bathymetry variations), a spatially varying bottom heat flux, and the heat produced by dissipation at the boundary and within the ocean would improve our understanding of the liquid motion within a subsurface ocean more significantly than coupling the model to study the interactions with the ice shell.

Conclusion

Using a modified version of SLIM, an Earth-based model for geophysical and environmental flows, I studied the tides of Titan's liquid bodies. This version of SLIM is able to solve the depth-averaged shallow water equations as well as the 3D hydrostatic equations under the Boussinesq approximations on flat as well as spherical extra-terrestrial domains. The global ocean of Titan lying beneath an ice shell, the hydrodynamics equations were modified to take into account the impact of the shell deformation on the liquid motion.

The tidal motion in the surface liquid bodies of Titan was studied in order to provide useful data for the forthcoming dedicated exploration mission(s) and in the hope of explaining phenomena

such as shoreline variations or "Magic Islands". The tidal motion in the surface lakes and seas of Titan is of little amplitude with respect to terrestrial standards. The surface elevation, although significantly varying depending on the lake/sea, is smaller than 0.4 m in the domains studied. The flow speed is $\mathcal{O}(10^{-2})$ m/s except in the straits linking the basins of the northern seas where it is one order of magnitude larger. The relatively weak tidal amplitude is due to the deformation of Titan's surface which damps the astronomical forcing acting on the surface lakes and seas. The same damping effect is observed on Earth, but at smaller scales. Indeed, the deformation of Titan's surface is much larger in terms of amplitude as the liquid layer is filled with water, instead of liquid metal on Earth, and the Young modulus of ice is one order of magnitude smaller than that of rocks. Therefore, the damping effect on Titan is much more significant: the attenuation factor is about 0.1 while it is about 0.7 on Earth. The various phenomena observed in the surface lakes and seas such as the shoreline variations of Ontario Lacus, the "Magic Islands" and the solar glints in the northern seas cannot be explained by the tidal motion. While excited normal mode(s) could be responsible for liquid motion whose amplitude is at least one order of magnitude larger than the tidal range in Ontario lacus, their natural period is such that only atmospheric forcings could resonantly force them. The numerical results were used to predict the path of drifted capsules. Based on the paths predicted for various landing sites and time, a motorised capsule seems better suited to avoid beaching or being trapped in small areas as well as for allowing significant displacements to take place. The results can also be used to constrain the engine of a capsule landing in the surface liquid bodies and to schedule the period at which a capsule should sail through a strait in order to take advantage of the flow orientation. The model can be used to study sub-domains more accurately or to predict the influence of various parameters on the liquid motion and/or the path of a capsule.

The simulations of the liquid motion within the global subsurface ocean show that the surface heat fluxes derived by Kvorka et al.

(2018) do not result in unrealistic liquid motion. The resulting flow strongly interact with the tidal motion, modifying significantly the velocity orientation while the surface elevation is only slightly modified. Although the predicted surface elevation corresponds to the observed deformation of Titan's surface, the results cannot be validated by comparison with data. The ice shell lying at the top of the ocean significantly impacts the tidal motion: it slows down the tidal flow and decreases the amplitude of the surface elevation by a few percentage points. If viscous deformation significantly larger than the one expected took place, the elevation and speed would be increased by the ice shell as high frequency oscillations would appear due to the 90° out of phase term of the surface pressure representing the viscous deformation.

Modelling the tides of Titan liquid bodies is a complex task as the lack of data prevents from validating the results and leads to poorly constrained parameters. I took advantage of the current state-of-the-art knowledge of Titan and a proven Earth-based model to build an image of Titan liquid tides while taking into account the remaining uncertainties. Extra-terrestrial exploration is a scientific field suffering from many stop's and go's due to the elapsed time between the missions. Each mission is a giant leap forward which can contradict the predictions based on the observations of the previous mission(s). For instance, based on Voyager spacecrafts observations, a deep ocean of liquid hydrocarbons was assumed to take place on Titan surface while Cassini mission showed that the surface lakes and seas covered only 1.3% of Titan's surface. Similarly, data from forthcoming exploration mission(s) could prove that Earth-based models are not suitable for modelling the liquid motion of Titan's liquid bodies or could infirm the values of the parameters used in this thesis.

This thesis is based on the data and observations collected by Cassini mission, which provided a clear outline of the surface lakes and seas shoreline, and bathymetry maps for some of them. Further insight were also gained in other aspects such as the composition of the liquid filling the lakes and seas, the internal structure of

Titan, and the atmospheric conditions. While some observations such as the lakes/seas shoreline are hardly questionable, others are. For instance, the bathymetry map of Ontario Lacus significantly varies depending on the method used to derive it. To address this problem, sensitivity analysis with respect to the poorly constrained parameters were conducted. I am reasonably confident about the results presented in this thesis as they compare well with those available in the literature. While the quantified values do vary with the parameters, several aspects such as the global patterns of the elevation and velocity fields are rather insensitive to the parameters; except in the northern seas where the liquid exchanges between the basins have a significant influence on the phase of the main tidal component, hence modifying the spatial and temporal variations of the elevation field.

Bibliography

Afanasyev, Y., Zhang, Y., 2018. Cyclonic circulation of Saturn′s atmosphere due to tilted convection. Nat. Geosci. 11, 164. doi:10.1038/s41561-018-0070-3.

Aharonson, O., Hayes, A., Lunine, J., Lorenz, R., Allison, M., Elachi, C., 2009. An asymmetric distribution of lakes on Titan as a possible consequence of orbital forcing. Nat. Geosci. 2, 851–854. doi:10.1038/ngeo698.

Altaf, M.U., Verlaan, M., Heemink, A.W., 2012. Efficient identification of uncertain parameters in a large-scale tidal model of the european continental shelf by proper orthogonal decomposition. Int. J. Numer. Meth. Fl. 68, 422–450. doi:10.1002/fld.2511.

Amit, H., Choblet, G., Tobie, G., Terra-Nova, F., Čadek, O., Bouffard, M., 2019. Cooling patterns in rotating thin spherical shells–application to Titan's subsurface ocean. Icarus , 113509doi:10.1016/j.icarus.2019.113509.

Anderson, E.J., Schwab, D.J., 2013. Predicting the oscillating bidirectional exchange flow in the straits of mackinac. J. Great Lakes Res. 39, 663–671. doi:10.1016/j.jglr.2013.09.001.

Arvelo, J., Lorenz, R.D., 2013. Plumbing the depths of Ligeia: Considerations for depth sounding in Titan's hydrocarbon seas. J. Acoust. Soc. Am. 134, 4335–4350. doi:10.1121/1.4824908.

Atreya, S.K., Adams, E.Y., Niemann, H.B., Demick-Montelara, J.E., Owen, T.C., Fulchignoni, M., Ferri, F., Wilson, E.H., 2006. Titan's methane cycle. Planet. Space. Sci. 54, 1177–1187. doi:10.1016/j.pss.2006.05.028.

Baland, R.M., Tobie, G., Lefèvre, A., Van Hoolst, T., 2014. Titan′s internal structure inferred from its gravity field, shape, and rotation state. Icarus 237, 29–41. doi:10.1016/j.icarus.2014.04.007.

Baland, R.M., Van Hoolst, T., Yseboodt, M., Karatekin, Ö., 2011. Titan′s obliquity as evidence of a subsurface ocean? Astron. Astrophys. 530, A141. doi:10.1051/0004-6361/201116578.

Baretta-Bekker, H.J., Duursma, E.K., Kuipers, B.R., 1998. Encyclopedia of Marine Sciences. Springer Science & Business Media.

Barnes, J.W., Brown, R.H., Soderblom, J.M., Soderblom, L.A., Jaumann, R., Jackson, B., Le Mouélic, S., Sotin, C., Buratti, B.J., Pitman, K.M., et al., 2009. Shoreline features of Titan's Ontario Lacus from Cassini/VIMS observations. Icarus 201, 217–225. doi:10.1016/j.icarus.2008.12.028.

Barr, A.C., Citron, R.I., Canup, R.M., 2010. Origin of a partially differentiated Titan. Icarus 209, 858–862. doi:10.1016/j.icarus.2010.05.028.

Béghin, C., Sotin, C., Hamelin, M., 2010. Titan's native ocean revealed beneath some 45 km of ice by a Schumann-like resonance. Comptes. Rendus. Geoscience 342, 425–433. doi:10.1016/j.crte.2010.03.003.

Bernard, P.E., Chevaugeon, N., Legat, V., Deleersnijder, E., Remacle, J.F., 2007. High-order h-adaptive discontinuous Galerkin methods for ocean modelling. Ocean Dyn. 57, 109–121. doi:10.1007/s10236-007-0127-0.

Bernard, P.E., Deleersnijder, E., Legat, V., Remacle, J.F., 2008. Dispersion analysis of discontinuous Galerkin schemes applied to Poincaré, Kelvin and Rossby waves. J. Sci. Comput. 34, 26–47. doi:10.1007/s10915-007-9156-6.

Beuthe, M., 2008. Thin elastic shells with variable thickness for lithospheric flexure of one-plate planets. Geophys. J. Int. 172, 817–841. doi:10.1111/j.1365-246X.2007.03671.x.

Beuthe, M., 2015a. Tides on Europa: The membrane paradigm. Icarus 248, 109–134. doi:10.1016/j.icarus.2014.10.027.

Beuthe, M., 2015b. Tidal Love numbers of membrane worlds: Europa, Titan, and Co. Icarus 57, 239–266. doi:10.1007/s10236-006-0093-y.

Beuthe, M., 2016. Crustal control of dissipative ocean tides in Enceladus and other icy moons. Icarus 280, 278–299. doi:10.1016/j.icarus.2016.08.009.

Birch, S., Hayes, A., Corlies, P., Stofan, E., Hofgartner, J., Lopes, R., Lorenz, R., Lunine, J., MacKenzie, S., Malaska, M., et al., 2018. Morphological evidence that titan's southern hemisphere basins are paleoseas. Icarus 310, 140–148. doi:10.1016/j.icarus.2017.12.016.

Blaise, S., Comblen, R., Legat, V., Remacle, J.F., Deleersnijder, E., Lambrechts, J., 2010. A discontinuous finite element baroclinic marine model on unstructured prismatic meshes. Ocean Dyn. 60, 1371–1393. doi:10.1007/s10236-010-0358-3.

Booij, N., Holthuijsen, L., Ris, R., 1997. The" swan" wave model for shallow water, in: Coastal Engineering 1996, pp. 668–676.

Box, G.E., Draper, N.R., 1987. Empirical model-building and response surfaces. John Wiley & Sons.

de Brauwere, A., Gourgue, O., de Brye, B., Servais, P., Ouattara, N.K., Deleersnijder, E., 2014. Integrated modelling of faecal contamination in a densely populated river–sea continuum (Scheldt River and Estuary). Sci. Tot. Environ. 468, 31–45. doi:10.1016/j.scitotenv.2013.08.019.

Brown, J.M., Norman, D.L., Amoudry, L.O., Souza, A.J., 2016. Impact of operational model nesting approaches and inherent errors for coastal simulations. Ocean Model. 107, 48–63. doi:10.1016/j.ocemod.2016.10.005.

Brown, R.H., Baines, K.H., Bellucci, G., Bibring, J.P., Buratti, B.J., Capaccioni, F., Cerroni, P., Clark, R.N., Coradini, A., Cruikshank, D.P., et al., 2004. The Cassini visual and infrared mapping spectrometer (VIMS) investigation, in: The Cassini-Huygens Mission. Springer, pp. 111–168. doi:10.1007/1-4020-3874-7_3.

Brown, R.H., Soderblom, L.A., Soderblom, J.M., Clark, R.N., Jaumann, R., Barnes, J.W., Sotin, C., Buratti, B., Baines, K.H., Nicholson, P.D., 2008. The identification of liquid ethane in Titan's Ontario Lacus. Nature 454, 607–610. doi:10.1038/nature07100.

Bryan, K., Cox, M.D., 1967. A numerical investigation of the oceanic general circulation. Tellus 19, 54–80. doi:10.1111/j.2153-3490.1967.tb01459.x.

de Brye, B., de Brauwere, A., Gourgue, O., Delhez, E.J., Deleersnijder, E., 2012. Water renewal timescales in the Scheldt Estuary. J. Marine Syst. 94, 74–86. doi:10.1016/j.jmarsys.2011.10.013.

Burchard, H., Bolding, K., Villarreal, M.R., 1999. GOTM, a general ocean turbulence model. Theory, implementation and test cases. Technical Report EUR 18745. European Commission.

Burr, D.M., Emery, J.P., Lorenz, R.D., Collins, G.C., Carling, P.A., 2006. Sediment transport by liquid surficial flow: Application to

Titan. Icarus 181, 235–242. doi:10.1016/j.icarus.2005.11.012.

Castillo-Rogez, J.C., Lunine, J.I., 2010. Evolution of Titan's rocky core constrained by Cassini observations. Geophy. Res. Lett. 37. doi:10.1029/2010GL044398.

Charnay, B., 2014. Dynamique troposphérique et évolution climatique de Titan et de la Terre primitive. Ph.D. thesis. Université Pierre et Marie Curie - Paris VI.

Charnay, B., Barth, E., Rafkin, S., Narteau, C., Lebonnois, S., Rodriguez, S., Du Pont, S.C., Lucas, A., 2015. Methane storms as a driver of Titan's dune orientation. Nat. Geosci. 8, 362. doi:10.1038/ngeo2406.

Chen, E., Glatzmaier, G., Nimmo, F., 2010. Modeling the dynamics of icy satellite subsurface oceans with focus on implications for spacecraft observables, in: Lunar and Planetary Science Conference, p. 1454.

Chen, E., Nimmo, F., Glatzmaier, G., 2014. Tidal heating in icy satellite oceans. Icarus 229, 11–30. doi:10.1016/j.icarus.2013.10.024.

Chen, W., 2011. Nonlinear inverse model for velocity estimation from an image sequence. J. Geophys. Res.-Oceans 116. doi:10.1029/2010JC006924.

Choblet, G., Tobie, G., Sotin, C., Kalousova, K., Grasset, O., 2017. Heat transport in the high-pressure ice mantle of large icy moons. Icarus 285, 252–262. doi:10.1016/j.icarus.2016.12.002.

Comblen, R., Blaise, S., Legat, V., Remacle, J.F., Deleersnijder, E., Lambrechts, J., 2010a. A discontinuous finite element baroclinic marine model on unstructured prismatic meshes. Ocean Dyn. 60, 1395–1414. doi:10.1007/s10236-010-0357-4.

Comblen, R., Lambrechts, J., Remacle, J.F., Legat, V., et al., 2010b. Practical evaluation of five partly discontinuous finite element pairs for the non-conservative shallow water equations. Int. J. Numer. Meth. Fl. 63, 701–724. doi:10.1002/fld.2094.

Comblen, R., Legrand, S., Deleersnijder, E., Legat, V., 2009. A finite element method for solving the shallow water equations on the sphere. Ocean Model. 28, 12–23. doi:10.1016/j.ocemod.2008.05.004.

Conroy, C.J., Kubatko, E.J., 2016. hp discontinuous Galerkin methods for the vertical extent of the water column in coastal settings part I: Barotropic forcing. J. Comput. Phys. 305, 1147–1171. doi:10.1016/j.jcp.2015.10.038.

Consolmagno, G.J., Lewis, J.S., 1978. The evolution of icy satellite interiors and surfaces. Icarus 34, 280–293. doi:10.1016/0019-1035(78)90168-9.

Cordier, D., Mousis, O., Lunine, J.I., Lavvas, P., Vuitton, V., 2009. An estimate of the chemical composition of Titan's lakes. Astrophys. J. Lett. 707, L128. doi:10.1088/0004-637X/707/2/L128.

Cordier, D., Mousis, O., Lunine, J.I., Lebonnois, S., Rannou, P., Lavvas, P., Lobo, L.Q., Ferreira, A.G.M., 2012. Titan's lakes chemical composition: sources of uncertainties and variability. Planet. Space. Sci. 61, 99–107. doi:10.1016/j.pss.2011.05.009.

Cornet, T., Bourgeois, O., Le Mouélic, S., Rodriguez, S., Lopez Gonzalez, T., Sotin, C., Tobie, G., Fleurant, C., Barnes, J.W., Brown, R.H., et al., 2012. Geomorphological significance of Ontario Lacus on Titan: Integrated interpretation of cassini VIMS, ISS and RADAR data and comparison with the Etosha Pan (Namibia). Icarus 218, 788–806. doi:10.1016/j.icarus.2012.01.013.

Cottini, V., Nixon, C.A., Jennings, D.E., de Kok, R., Teanby, N.A., Irwin, P.G., Flasar, F.M., 2012. Spatial and temporal variations in Titan's surface temperatures from Cassini CIRS observations. Planet. Space. Sci. 60, 62–71. doi:10.1016/j.pss.2011.03.015.

Coyette, A., Baland, R.M., Van Hoolst, T., 2018. Variations in rotation rate and polar motion of a non-hydrostatic Titan. Icarus 307, 83–105. doi:10.1016/j.icarus.2018.02.003.

Critchell, K., Lambrechts, J., 2016. Modelling accumulation of marine plastics in the coastal zone; what are the dominant physical processes? Estuar. Coast. Shelf S. 171, 111–122. doi:10.1016/j.ecss.2016.01.036.

Cushman-Roisin, B., Beckers, J.M., 2011. Introduction to geophysical fluid dynamics: physical and numerical aspects. II ed., Academic Press.

Danilov, S., 2012. Two finite-volume unstructured mesh models for large-scale ocean modeling. Ocean Model. 47, 14 – 25. doi:10.1016/j.ocemod.2012.01.004.

de Brauwere, A., de Brye, B., Servais, P., Passerat, J., Deleersnijder, E., 2011a. Modelling Escherichia coli concentrations in the tidal Scheldt river and estuary. Water Res. 45, 2724 – 2738. doi:10.1016/j.watres.2011.02.003.

de Brauwere, A., de Brye, B., Blaise, S., Deleersnijder, E., 2011b. Residence time, exposure time and connectivity in the Scheldt Estuary. J. Marine Syst. 84, 85–95. doi:10.1016/j.jmarsys.2010.10.001.

de Brye, B., de Brauwere, A., Gourgue, O., Kärnä, T., Lambrechts, J., Comblen, R., Deleersnijder, E., 2010. A finite-element, multi-scale model of the Scheldt tributaries, river, estuary and ROFI. Coastal Eng. 57, 850–863. doi:10.1016/j.coastaleng.2010.04.001.

de Brye, B., de Brauwere, A., Gourgue, O., Delhez, E., Deleersnijder, E., 2012. Water renewal timescales in the Scheldt Estuary. J. Marine Syst. 94, 74–86. doi:10.1016/j.jmarsys.2011.10.013.

de Brye, B., Schellen, S., Sassi, M., Vermeulen, B., Kärnä, T., Deleersnijder, E., Hoitink, T., 2011. Preliminary results of a finite-element, multi-scale model of the Mahakam Delta (Indonesia). Ocean Dyn. 61, 1107–1120. doi:10.1007/s10236-011-0410-y.

De Jong, M., Battjes, J., 2004. Low-frequency sea waves generated by atmospheric convection cells. J. Geophys. Res.-Oceans 109. doi:1029/2003JC001931.

De Vriend, H.J., 1991. Mathematical modelling and large-scale coastal behaviour: Part 1: physical processes. J. Hydraul. Res. 29, 727–740. doi:10.1080/00221689109498955.

Delandmeter, P., Lambrechts, J., Legat, V., Vallaeys, V., Naithani, J., Thiery, W., Remacle, J.F., Deleersnijder, E., 2018. A fully consistent and conservative vertically adaptive coordinate system for SLIM 3d v0.4 with an application to the thermocline oscillations of Lake Tanganyika. Geosci. Model Dev. 11, 1161–1179. doi:10.5194/gmd-11-1161-2018.

Delandmeter, P., Lambrechts, J., Marmorino, G.O., Legat, V., Wolanski, E., Remacle, J.F., Chen, W., Deleersnijder, E., 2017. Submesoscale tidal eddies in the wake of coral islands and reefs: satellite data and numerical modelling. Ocean Dyn. 67, 897–913. doi:10.1007/s10236-017-1066-z.

Delandmeter, P., Lewis, S.E., Lambrechts, J., Deleersnijder, E., Legat, V., Wolanski, E., 2015. The transport and fate of riverine fine sediment exported to a semi-open system. Estuar. Coast. Shelf S. 167, 336–346. doi:10.1016/j.ecss.2015.10.011.

Deleersnijder, E., 2018. LGCIV2056 Marine hydrodynamics.

Deleersnijder, E., 2019. From Leibniz integral rule to Reynolds' transport theorem. URL: http://hdl.handle.net/2078.1/221577.

Dermott, S.F., Sagan, C., 1995. Tidal effects of disconnected hydrocarbon seas on Titan. Nature 374, 238–240. doi:10.1038/374238a0.

Dhingra, R.D., Barnes, J.W., Yanites, B.J., Kirk, R.L., 2018. Large catchment area recharges Titan's Ontario Lacus. Icarus 299, 331–338. doi:10.1016/j.icarus.2017.08.009.

Drews, C., 2013. Using wind setdown and storm surge on Lake Erie to calibrate the air-sea drag coefficient. PloS ONE 8, e72510. doi:10.1371/journal.pone.0072510.

Dunaeva, A., Kronrod, V., Kuskov, O., 2016. Physico-chemical models of the internal structure of partially differentiated Titan. Geochem. Int.+ 54, 27–47. doi:10.1134/S0016702916010043.

Durante, D., Hemingway, D., Racioppa, P., Iess, L., Stevenson, D., 2019. Titan's gravity field and interior structure after cassini. Icarus 326, 123–132. doi:10.1016/j.icarus.2019.03.003.

Egbert, G.D., Ray, R.D., 2000. Significant dissipation of tidal energy in the deep ocean inferred from satellite altimeter data. Nature 405, 775–778. doi:10.1038/35015531.

Elachi, C., Allison, M.D., Borgarelli, L., Encrenaz, P., Im, E., Janssen, M.A., Johnson, W.T.K., Kirk, R.L., Lorenz, R.D., Lunine, J.I., et al., 2004. Radar: the Cassini Titan radar mapper. Space Sci. Rev. 115, 71–110. doi:10.1007/s11214-004-1438-9.

Flasar, F.M., Kunde, V.G., Abbas, M.M., Achterberg, R.K., Ade, P., Barucci, A., Bézard, B., Bjoraker, G.L., Brasunas, J.C., Calcutt, S., et al., 2004. Exploring the Saturn system in the thermal infrared: The composite infrared spectrometer, in: The

Cassini-Huygens Mission. Springer, pp. 169–297. doi:10.1007/1-4020-3874-7_4.

Fortes, A.D., 2012. Titan's internal structure and the evolutionary consequences. Planet. Space Sci. 60, 10–17. doi:10.1016/j.pss.2011.04.010.

Fortes, A.D., Grindrod, P.M., Trickett, S., Vočadlo, L., 2007. Ammonium sulfate on Titan: Possible origin and role in cryovolcanism. Icarus 188, 139–153. doi:10.1016/j.icarus.2006.11.002.

Friedson, A.J., West, R.A., Wilson, E.H., Oyafuso, F., Orton, G.S., 2009. A global climate model of Titan's atmosphere and surface. Planet. Space Sci. 57, 1931–1949. doi:10.1016/j.pss.2009.05.006.

Fringer, O.B., Dawson, C.N., He, R., Ralston, D.K., Zhang, Y.J., 2019. The future of coastal and estuarine modeling: Findings from a workshop. Ocean Model. , 101458doi:10.1016/j.ocemod.2019.101458.

Frys, C., Saint-Amand, A., Le Hénaff, M., Figueiredo, J., Kuba, A., Walker, B., Lambrechts, J., Vallaeys, V., Vincent, D., Hanert, E., 2020. Fine-scale coral connectivity pathways in the Florida Reef Tract: Implications for conservation and restoration. Front. Marine Sci. (submitted) submitted.

Fulchignoni, M., Ferri, F., Angrilli, F., Ball, A.J., Bar-Nun, A., Barucci, M.A., Bettanini, C., Bianchini, G., Borucki, W., Colombatti, G., et al., 2005. In situ measurements of the physical characteristics of Titan's environment. Nature 438, 785–791. doi:10.1038/nature04314.

Geuzaine, C., Remacle, J.F., 2009. Gmsh: A 3-d finite element mesh generator with built-in pre-and post-processing facilities. Int. J. Numer. Meth. in Eng. 79, 1309–1331. doi:10.1002/nme.2579.

Glein, C.R., Shock, E.L., 2013. A geochemical model of non-ideal solutions in the methane-ethane-propane-nitrogen-acetylene system on Titan. Geochim. Cosmochim. Ac. 115, 217–240. doi:10.1016/j.gca.2013.03.030.

Goodman, J.C., Lenferink, E., 2012. Numerical simulations of marine hydrothermal plumes for Europa and other icy worlds. Icarus 221, 970–983. doi:10.1016/j.icarus.2012.08.027.

Gordeev, R., Kagan, B., Polyakov, E., 1977. The effects of loading and self-attraction on global ocean tides: the model and the results of a numerical experiment. J. Phys. Oceanogr. 7, 161–170. doi:10.1175/1520-0485(1977)007<0161:TEOLAS>2.0.CO;2.

Gourgue, O., Baeyens, W., Chen, M., de Brauwere, A., de Brye, B., Deleersnijder, E., Elskens, M., Legat, V., 2013. A depth-averaged two-dimensional sediment transport model for environmental studies in the Scheldt Estuary and tidal river network. J. Marine Syst. 128, 27 – 39. doi:10.1016/j.jmarsys.2013.03.014.

Gourgue, O., Comblen, R., Lambrechts, J., Kärnä, T., Legat, V., Deleersnijder, E., 2009. A flux-limiting wetting–drying method for finite-element shallow-water models, with application to the Scheldt Estuary. Adv. Water Res. 32, 1726–1739. doi:10.1016/j.advwatres.2009.09.005.

Gourgue, O., Deleersnijder, E., Legat, V., Marchal, E., White, L., 2011. Free and forced thermocline oscillations in Lake Tanganyika. pp. 146–162. doi:10.1017/CBO9780511921414.011.

Gourgue, O., Deleersnijder, E., White, L., 2007. Toward a generic method for studying water renewal, with application to the epilimnion of Lake Tanganyika. Estuar. Coast. Shelf S. 74, 628–640. doi:10.1016/j.ecss.2007.05.009.

Griffith, C.A., Hall, J.L., Geballe, T.R., 2000. Detection of daily clouds on Titan. Science 290, 509–513. doi:10.1126/science.290.5491.509.

Griffith, C.A., Lora, J.M., Turner, J., Penteado, P.F., Brown, R.H., Tomasko, M.G., Doose, L., See, C., 2012. Possible tropical lakes on Titan from observations of dark terrain. Nature 486, 237. doi:10.1038/nature11165.

Hamblin, P., 1982. On the free surface oscillations of Lake Ontario. Limnol. Oceanogr. 27, 1039–1049. doi:/10.4319/lo.1982.27.6.1039.

Hanel, R., Conrath, B., Flasar, F.M., Kunde, V., Maguire, W., Pearl, J., Pirraglia, J., Samuelson, R., Herath, L., Allison, M., Cruikshank, D., Gautier, D., Gierasch, P., Horn, L., Koppany, R., 1981. Infrared observations of the saturnian system from Voyager-1. Science 212, 192–200. doi:10.1126/science.212.4491.192.

Hanert, E., Legat, V., Deleersnijder, E., 2003. A comparison of three finite elements to solve the linear shallow water equations. Ocean Model. 5, 17–35. doi:10.1016/S1463-5003(02)00012-4.

Hansen, W., 1956. Theorie zur Errechnung des Wasserstandes und der Strömungen in Randmeeren nebst Anwendungen. Tellus 8, 287–300.

Hartwig, J.W., Colozza, A., Lorenz, R.D., Oleson, S., Landis, G., Schmitz, P., Paul, M., Walsh, J., 2016. Exploring the depths of Kraken Mare–power, thermal analysis, and ballast control for the Saturn Titan submarine. Cryogenics 74, 31–46. doi:10.1016/j.cryogenics.2015.09.009.

Hay, H.C., Matsuyama, I., 2017. Numerically modelling tidal dissipation with bottom drag in the oceans of Titan and Enceladus. Icarus 281, 342–356. doi:10.1016/j.icarus.2016.09.022.

Hay, H.C., Matsuyama, I., 2019. Nonlinear tidal dissipation in the subsurface oceans of Enceladus and other icy satellites. Icarus 319, 68–85. doi:10.1016/j.icarus.2018.09.019.

Hayes, A.G., 2016. The lakes and seas of Titan. Annu. Rev. Earth Pl. Sc. 44. doi:10.1146/annurev-earth-060115-012247.

Hayes, A.G., Aharonson, O., Callahan, P., Elachi, C., Gim, Y., Kirk, R.L., Lewis, K., Lopes, R., Lorenz, R.D., Lunine, J.I., et al., 2008. Hydrocarbon lakes on Titan: Distribution and interaction with a porous regolith. Geophys. Res. Lett. 35. doi:10.1029/2008GL033409.

Hayes, A.G., Aharonson, O., Lunine, J.I., Kirk, R.L., Zebker, H.A., Wye, L.C., Lorenz, R.D., Turtle, E.P., Paillou, P., Mitri, G., et al., 2011. Transient surface liquid in Titan's polar regions from Cassini. Icarus 211, 655–671. doi:10.1016/j.icarus.2010.08.017.

Hayes, A.G., Birch, S.P.D., Dietrich, W.E., Howard, A.D., Kirk, R.L., Poggiali, V., Mastrogiuseppe, M., Michaelides, R.J., Corlies, P.M., Moore, J.M., Malaska, M.J., Mitchell, K.L., Lorenz, R.D., Wood, C.A., 2017. Topographic constraints on the evolution and connectivity of Titan's lacustrine basins. Geophys. Res. Lett. 44, 11,745–11,753. doi:10.1002/2017GL075468.

Hayes, A.G., Lorenz, R.D., Lunine, J.I., 2018. A post-cassini view of Titan's methane-based hydrologic cycle. Nat. Geosci. 11, 306–313. doi:10.1038/s41561-018-0103-y.

Hayes, A.G., Mastrogiuseppe, M., Lumine, J.I., Poggiali, V., Lorenz, R.D., Mitchell, K.M., Malaska, M.J., Le Gall, A., 2016. The bathymetry and composition of Titan′s lakes and seas, in: 47th Lunar and Planetary Science Conference, p. 1904.

Hayes, A.G., Michaelides, R.J., Turtle, E.P., Barnes, J.W., Soderblom, J.M., Masrtogiuseppe, M., Lorenz, R.D., Kirk, R.L., Lunine, J.I., 2014. The distribution and volume of Titan's hydrocarbon lakes and seas, in: Lunar and Planetary Institute Science Conference Abstracts, p. 2341.

Hayes, A.G., Wolf, A.S., Aharonson, O., Zebker, H., Lorenz, R.D., Kirk, R.L., Paillou, P., Lunine, J.I., Wye, L., Callahan, P., et al., 2010. Bathymetry and absorptivity of Titan's Ontario Lacus. J. Geophys. Res.-Planet. 115, E09009. doi:10.1029/2009JE003557.

Hemingway, D., Nimmo, F., Zebker, H., Iess, L., 2013. A rigid and weathered ice shell on Titan. Nature 500, 550–552. doi:10.1038/nature12400.

Hendershott, M.C., 1972. The effects of solid Earth deformation on global ocean tides. Geophys. J. Int. 29, 389–402. doi:10.1111/j.1365-246X.1972.tb06167.x.

Henry, R.F., Walters, R.A., 1993. Geometrically based, automatic generator for irregular triangular networks. Commun. Numer. Meth. En. 9, 555–566. doi:10.1002/cnm.1640090703.

Hervouet, J.M., 2007. Hydrodynamics of free surface flows: modelling with the finite element method. John Wiley & Sons.

Higdon, R.L., de Szoeke, R.A., 1997. Barotropic-Baroclinic Time Splitting for Ocean Circulation Modeling. J. Comput. Phys. 135, 30–53. doi:10.1006/jcph.1997.5733.

Hofgartner, J.D., Hayes, A.G., Lunine, J.I., Zebker, H., Lorenz, R.D., Malaska, M.J., Mastrogiuseppe, M., Notarnicola, C., Soderblom, J.M., 2016. Titan's "Magic Islands": Transient features in a hydrocarbon sea. Icarus 271, 338–349. doi:10.1016/j.icarus.2016.02.022.

Hofgartner, J.D., Hayes, A.G., Lunine, J.I., Zebker, H., Stiles, B.W., Sotin, C., Barnes, J.W., Turtle, E.P., Baines, K.H., Brown, R.H., et al., 2014. Transient features in a Titan sea. Nat. Geosci. 7, 493–496. doi:10.1038/ngeo2190.

Howarth, M.J., 2005. Hydrography of the Irish Sea. SEA6 Technical report. UK, Department of Trade and Industry offshore energy Strategic Assessment programme.

Hussmann, H., Choblet, G., Lainey, V., Matson, D.L., Sotin, C., Tobie, G., Van Hoolst, T., 2010. Implications of rotation, orbital states, energy sources, and heat transport for internal processes in icy satellites. Space sci. rev. 153, 317–348. doi:10.1007/s11214-010-9636-0.

Iess, L., Jacobson, R.A., Ducci, M., Stevenson, D.J., Lunine, J.I., Armstrong, J.W., Asmar, S.W., Racioppa, P., Rappaport, N.J., Tortora, P., 2012. The tides of Titan. Science 337, 457–459. doi:10.1126/science.1219631.

Jackett, D.R., McDougall, T.J., Feistel, R., Wright, D.G., Griffies, S.M., 2006. Algorithms for density, potential temperature, conservative temperature, and the freezing temperature of seawater. J. Atmos. Ocean. Tech. 23, 1709–1728. doi:10.1175/JTECH1946.1.

Jennings, D., Flasar, F., Kunde, V., Samuelson, R., Pearl, J., Nixon, C., Carlson, R., Mamoutkine, A., Brasunas, J., Guandique, E., et al., 2009. Titan's surface brightness temperatures. Astrophys. J. Lett. 691, L103. doi:10.1088/0004-637X/691/2/L103.

Jennings, D.E., Cottini, V., Nixon, C., Flasar, F., Kunde, V., Samuelson, R., Romani, P., Hesman, B., Carlson, R., Gorius, N., et al., 2011. Seasonal changes in Titan's surface temperatures. Astrophys. J. Lett. 737, L15. doi:10.1088/2041-8205/737/1/L15.

Jones, E., Oliphant, T., Peterson, P., et al., 2001. SciPy: Open source scientific tools for Python. URL: http://www.scipy.org/. [Online; accessed May 2018].

Kärnä, T., 2012. Development of a Baroclinic Discontinuous Galerkin Finite Element Model for Estuarine and Coastal Flows. Ph.D. thesis. UCLouvain.

Kärnä, T., De Brye, B., Gourgue, O., Lambrechts, J., Comblen, R., Legat, V., Deleersnijder, E., 2011. A fully implicit wetting-drying method for DG-FEM shallow water models, with an application to the Scheldt Estuary. Comput. Method Appl. M. 200, 509–524. doi:10.1016/j.cma.2010.07.001.

Kärnä, T., Kramer, S.C., Mitchell, L., Ham, D.A., Piggott, M.D., Baptista, A.M., 2018. Thetis coastal ocean model: discontinuous Galerkin discretization for the three-dimensional hydrostatic equations. Geosci. Model Dev. Discussions 2018, 1–36. doi:10.5194/gmd-2017-292.

Kärnä, T., Legat, V., Deleersnijder, E., 2013. A baroclinic discontinuous Galerkin finite element model for coastal flows. Ocean Model. 61, 1–20. doi:10.1016/j.ocemod.2012.09.009.

Kell, G.S., 1975. Density, thermal expansivity, and compressibility of liquid water from 0. deg. to 150. deg.. correlations and tables for atmospheric pressure and saturation reviewed and expressed on 1968 temperature scale. J. Chem. Eng. data 20, 97–105. doi:10.1021/je60064a005.

Kuiper, G.P., 1944. Titan: a satellite with an atmosphere. Astrophys. J. 100, 378. doi:10.1086/144679.

Kvorka, J., Čadek, O., Tobie, G., Choblet, G., 2018. Does Titan's long-wavelength topography contain information about subsurface ocean dynamics? Icarus 310, 149–164. doi:10.1016/j.icarus.2017.12.010.

Lambrechts, J., Comblen, R., Legat, V., Geuzaine, C., Remacle, J.F., 2008a. Multiscale mesh generation on the sphere. Ocean Dyn. 58, 461–473. doi:10.1007/s10236-008-0148-3.

Lambrechts, J., Hanert, E., Deleersnijder, E., Bernard, P.E., Legat, V., Remacle, J.F., Wolanski, E., 2008b. A multi-scale model of the hydrodynamics of the whole Great Barrier Reef. Estuar. Coast. Shelf S. 79, 143–151. doi:10.1016/j.ecss.2008.03.016.

Le, H.A., Dang, V.X.H., Lambrechts, J., Ortleb, S., Vallaeys, V., Vincent, D., Gratiot, N., Soares Frazao, S., Deleersnijder, E., 2018. A new wetting–drying algorithm integrated in slim, with an application to the tonle sap lake, mekong, in: European Geosciences Union General Assembly 2018, pp. EGU2018–8100–1.

Le, H.A., Lambrechts, J., Ortleb, S., Gratiot, N., Deleersnijder, E., Soares-Frazao, S., 2020. An implicit wetting-drying algorithm for the Discontinuous Galerkin method: Application to the Tonle Sap, Mekong river basin. Environ. Fluid Mech. in Press. doi:10.1007/s10652-019-09732-7.

Le Bars, Y., Vallaeys, V., Deleersnijder, E., Hanert, E., Carrere, L., Channelière, C., 2016. Unstructured-mesh modeling of the Congo river-to-sea continuum. Ocean Dyn. 66, 589–603. doi:10.1007/s10236-016-0939-x.

Le Gall, A., Malaska, M.J., Lorenz, R.D., Janssen, M.A., Tokano, T., Hayes, A.G., Mastrogiuseppe, M., Lunine, J.I., Veyssière, G., Encrenaz, P., et al., 2016. Composition, seasonal change and bathymetry of Ligeia Mare, Titan, derived from its microwave thermal emission. J. Geophys. Res.-Planet. 121, 233–251. doi:10.1002/2015JE004920.

Le Roux, D., Sène, A., Rostand, V., Hanert, E., 2005. On some spurious mode issues in shallow-water models using a linear algebra approach. Ocean Model. 10, 83–94. doi:10.1016/j.ocemod.2004.07.008.

LeBlond, P.H., Mysak, L.A., 1978. Chapter 3 Free Waves: Long Wavelengths, in: LeBlond, P.H., Mysak, L.A. (Eds.), Elsevier Oceanography Series. Elsevier. volume 20 of *Waves in the Ocean*, pp. 119–196. doi:10.1016/S0422-9894(08)70816-X.

Lebonnois, S., Burgalat, J., Rannou, P., Charnay, B., 2012. Titan global climate model: A new 3-dimensional version of the IPSL

Titan GCM. Icarus 218, 707–722. doi:10.1016/j.icarus.2011.11.032.

Lefevre, A., Tobie, G., Choblet, G., Čadek, O., 2014. Structure and dynamics of Titan′s outer icy shell constrained from Cassini data. Icarus 237, 16–28. doi:10.1016/j.icarus.2014.04.006.

Legrand, S., Deleersnijder, E., Hanert, E., Legat, V., Wolanski, E., 2006. High-resolution, unstructured meshes for hydrodynamic models of the Great Barrier Reef, Australia. Estuar. Coast. Shelf S. 68, 36–46. doi:10.1016/j.ecss.2005.08.017.

Legrand, S., Legat, V., Deleersnijder, E., 2000. Delaunay mesh generation for an unstructured-grid ocean general circulation model. Ocean Model. 2, 17–28. doi:10.1016/S1463-5003(00)00005-6.

Lingam, M., Loeb, A., 2018. Is extraterrestrial life suppressed on subsurface ocean worlds due to the paucity of bioessential elements? Astron. J. 156, 151. doi:10.3847/1538-3881/aada02.

Lorenz, R., Lunine, J., Neish, C., 2011. Cyanide soap? dissolved materials in Titan's seas. EPSC-DPS2011 6, 488.

Lorenz, R.D., 1994. Crater lakes on titan: Rings, horseshoes and bullseyes. Planet. Space Sci. 42, 1–4. doi:10.1016/0032-0633(94)90134-1.

Lorenz, R.D., 1996. Pillow lava on Titan: Expectations and constraints on cryovolcanic processes. Planet. Space Sci. 44, 1021–1028. doi:10.1016/0032-0633(95)00139-5.

Lorenz, R.D., 1997. Impacts and cratering on Titan: A pre-Cassini view. Planet. Space Sci. 45, 1009–1022. doi:10.1016/S0032-0633(97)00085-8.

Lorenz, R.D., 2000. Post-cassini exploration of titan: Science rationale and mission concepts. J. Brit. Inter. Soc. 53, 218–234.

Lorenz, R.D., 2013. Oceanography on Saturn's moon, Titan, in: Oceans-San Diego, 2013, IEEE. pp. 1–7.

Lorenz, R.D., 2014. The flushing of Ligeia: Composition variations across Titan's seas in a simple hydrological model. Geophys. Res. Lett. 41, 5764–5770. doi:10.1002/2014GL061133.

Lorenz, R.D., Kirk, R.L., Hayes, A.G., Anderson, Y.Z., Lunine, J.I., Tokano, T., Turtle, E.P., Malaska, M.J., Soderblom, J.M., Lucas, A., et al., 2014. A radar map of Titan seas: Tidal dissipation and ocean mixing through the throat of Kraken. Icarus 237, 9–15. doi:10.1016/j.icarus.2014.04.005.

Lorenz, R.D., Newman, C., Lunine, J.I., 2010. Threshold of wave generation on Titan's lakes and seas: Effect of viscosity and implications for Cassini observations. Icarus 207, 932–937. doi:10.1016/j.icarus.2009.12.004.

Lorenz, R.D., Tokano, T., Newman, C.E., 2012. Winds and tides of Ligeia Mare, with application to the drift of the proposed time TiME (Titan Mare Explorer) capsule. Planet. Space Sci. 60, 72–85. doi:10.1016/j.pss.2010.12.009.

Lorenz, R.D., Turtle, E.P., Barnes, J.W., Trainer, M.G., Adams, D.S., Hibbard, K.E., Sheldon, C.Z., Zacny, K., Peplowski, P.N., Lawrence, D.J., et al., 2018. Dragonfly: a rotorcraft lander concept for scientific exploration at Titan. J. Hopkins APL Tech. D. .

Lunine, J.I., Hayes, A., Aharonson, O., Mitri, G., Lorenz, R., Stofan, E., Wall, S., Elachi, C., Cassini Radar Team, et al., 2009. Evidence for liquid in Ontario Lacus (Titan) from Cassini-observed changes, in: AAS/Division for Planetary Sciences Meeting Abstracts# 41.

Lunine, J.I., Stevenson, D.J., 1987. Clathrate and ammonia hydrates at high pressure: Application to the origin of methane on Titan. Icarus 70, 61–77. doi:10.1016/0019-1035(87)90075-3.

Luspay-Kuti, A., Chevrier, V., Cordier, D., Rivera-Valentin, E., Singh, S., Wagner, A., Wasiak, F., 2015. Experimental constraints on the composition and dynamics of Titan's polar lakes. Earth Planet. Sc. Lett. 410, 75–83. doi:10.1016/j.epsl.2014.11.023.

Manor-Chapman, E., 2013. Cassini Solstice Mission overview and science results, in: 2013 IEEE Aerospace Conference, pp. 1–13. doi:10.1109/AERO.2013.6496923.

Marshall, J., Adcroft, A., Hill, C., Perelman, L., Heisey, C., 1997. A finite-volume, incompressible Navier Stokes model for studies of the ocean on parallel computers. J. Geophys. Res.-Oceans 102, 5753–5766. doi:10.1029/96JC02775.

Mastrogiuseppe, M., Hayes, A., Poggiali, V., Seu, R., Lunine, J.I., Hofgartner, J., 2016. Radar sounding using the Cassini altimeter: Waveform modeling and Monte Carlo approach for data inversion of observations of Titan's seas. IEEE T Geosci. Remote 54, 5646–5656. doi:10.1109/TGRS.2016.256342.

Mastrogiuseppe, M., Hayes, A.G., Poggiali, V., Lunine, J.I., Lorenz, R., Seu, R., Le Gall, A., Notarnicola, C., Mitchell, K.L., Malaska, M., et al., 2018a. Bathymetry and composition of Titan's Ontario Lacus derived from Monte Carlo-based waveform inversion of Cassini RADAR altimetry data. Icarus 300, 203–209. doi:10.1016/j.icarus.2017.09.009.

Mastrogiuseppe, M., Poggiali, V., Hayes, A., Lunine, J., Seu, R., Achille, G.D., Lorenz, R., 2018b. Cassini radar observation of Punga Mare and environs: Bathymetry and composition. Earth Planet. Sc. Lett. 496, 89 – 95. doi:https://doi.org/10.1016/j.epsl.2018.05.033.

Mastrogiuseppe, M., Poggiali, V., Hayes, A.G., Lorenz, R.D., Lunine, J.I., Picardi, G., Seu, R., Flamini, E., Mitri, G., Notarnicola, C., et al., 2014. The bathymetry of a Titan sea. Geophys. Res. Lett. 41, 1432–1437. doi:10.1002/2013GL058618.

Matsuyama, I., 2014. Tidal dissipation in the oceans of icy satellites. Icarus 242, 11–18. doi:10.1016/j.icarus.2014.07.005.

Matsuyama, I., Beuthe, M., Hay, H.C., Nimmo, F., Kamata, S., 2018. Ocean tidal heating in icy satellites with solid shells. Icarus 312, 208–230. doi:/10.1016/j.icarus.2018.04.013.

McEwen, A., Turtle, E., Perry, J., Dawson, D., Fussner, S., Collins, G., Porco, C., Johnson, T., Soderblom, L., 2005. Mapping and monitoring the surface of Titan, in: Bulletin of the American Astronomical Society, p. 739.

Merian, J., 1828. Ueber die Bewegung tropfbarer Flüssigkeiten in Gefässen [On the motion of drippable liquids in containers]. Ph.D. thesis. PhD thesis, Basel, Schweighauser.

Meriggiola, R., Iess, L., Stiles, B.W., Lunine, J.I., Mitri, G., 2016. The rotational dynamics of Titan from Cassini RADAR images. Icarus 275, 183–192. doi:10.1016/j.icarus.2016.01.019.

Misiura, K., Czechowski, L., 2015. Numerical modelling of sedimentary structures in rivers on Earth and Titan. Geol. Q. 59, 565–580. doi:10.7306/gq.1236.

Mitchell, J.L., Ádámkovics, M., Caballero, R., Turtle, E.P., 2011. Locally enhanced precipitation organized by planetary-scale waves on Titan. Nat. Geosci. 4, 589–592. doi:10.1038/ngeo1219.

Mitchell, K.L., Barmatz, M.B., Jamieson, C.S., Lorenz, R.D., Lunine, J.I., 2015. Laboratory measurements of cryogenic liquid alkane microwave absorptivity and implications for the composition of Ligeia Mare, Titan. Geophys. Res. Lett. 42, 1340–1345. doi:10.1002/2014GL059475.

Mitri, G., Coustenis, A., Fanchini, G., Hayes, A.G., Iess, L., Khurana, K., Lebreton, J.P., Lopes, R.M., Lorenz, R.D., Meriggiola, R., et al., 2014a. The exploration of Titan with an orbiter and a

lake probe. Planet. Space Sci. 104, 78–92. doi:10.1016/j.pss.2014.07.009.

Mitri, G., Meriggiola, R., Hayes, A., Lefevre, A., Tobie, G., Genova, A., Lunine, J.I., Zebker, H., 2014b. Shape, topography, gravity anomalies and tidal deformation of Titan. Icarus 236, 169 – 177. doi:10.1016/j.icarus.2014.03.018.

Munk, W.H., 1950. On the wind-driven ocean circulation. J. Meteorol. 7, 80–93.

Newman, C.E., Lee, C., Lian, Y., Richardson, M.I., Toigo, A.D., 2011. Stratospheric superrotation in the TitanWRF model. Icarus 213, 636–654. doi:10.1016/j.icarus.2011.03.025.

Newman, C.E., Richardson, M.I., Lian, Y., Lee, C., 2016. Simulating Titan's methane cycle with the TitanWRF general circulation model. Icarus 267, 106–134. doi:10.1016/j.icarus.2015.11.028.

Niemann, H.B., Atreya, S.K., Bauer, S.J., Carignan, G.R., Demick, J.E., Frost, R.L., Gautier, D., Haberman, J.A., Harpold, D.N., Hunten, D.M., et al., 2005. The abundances of constituents of Titan's atmosphere from the GCMS instrument on the Huygens probe. Nature 438, 779–784. doi:10.1038/nature04122.

Nimmo, F., 2004. What is the Young's modulus of ice?, in: Workshop on Europa's Icy Shell, Lunar and Planetary Institute, Houston. Abstract #7005.

Nimmo, F., Bills, B.G., 2010. Shell thickness variations and the long-wavelength topography of Titan. Icarus 208, 896–904. doi:10.1016/j.icarus.2010.02.020.

NOAA, 2014. Do the Great Lakes have tides ? http://oceanservice.noaa.gov/facts/gltides.html. Accessed: 2015-08-21.

Okubo, A., 1971. Oceanic diffusion diagrams. Deep-Sea Res. 18, 789–802. doi:TODDO.

Orosei, R., Lauro, S., Pettinelli, E., Cicchetti, A., Coradini, M., Cosciotti, B., Di Paolo, F., Flamini, E., Mattei, E., Pajola, M., et al., 2018. Radar evidence of subglacial liquid water on Mars. Science , eaar7268doi:10.1126/science.aar7268.

Otto, L., Zimmerman, J., Furnes, G., Mork, M., Saetre, R., Becker, G., 1990. Review of the physical oceanography of the North Sea. Neth. J. Sea Res. 26, 161–238. doi:10.1016/0077-7579(90)90091-T.

O'Rourke, J.G., Stevenson, D.J., 2014. Stability of ice/rock mixtures with application to a partially differentiated titan. Icarus 227, 67–77. doi:10.1016/j.icarus.2013.09.010.

Pacanowski, R., Philander, S., 1981. Parameterization of vertical mixing in numerical models of tropical oceans. J. Phys. Oceanogr. 11, 1443–1451. doi:TODDO.

Pham Van, C., de Brye, B., Deleersnijder, E., Hoitink, A.J.F., Sassi, M., Spinewine, B., Hidayat, H., Soares-Frazão, S., 2016. Simulations of the flow in the Mahakam river–lake–delta system, Indonesia. Environ. Fluid Mech. 16, 603–633. doi:10.1007/s10652-016-9445-4.

Poggiali, V., Mastrogiuseppe, M., Hayes, A.G., Seu, R., Birch, S.P.D., Lorenz, R.D., Grima, C., Hofgartner, J.D., 2016. Liquid-filled canyons on Titan. Geophys. Res. Lett. 43, 7887–7894. doi:10.1002/2016GL069679.

Porco, C.C., Baker, E., Barbara, J., Beurle, K., Brahic, A., Burns, J.A., Charnoz, S., Cooper, N., Dawson, D.D., Del Genio, A.D., et al., 2005. Imaging of Titan from the Cassini spacecraft. Nature 434, 159. doi:10.1038/nature03436.

Porco, C.C., West, R.A., Squyres, S., Mcewen, A., Thomas, P., Murray, C.D., Delgenio, A., Ingersoll, A.P., Johnson, T.V., Neukum, G., et al., 2004. Cassini imaging science: Instrument characteristics and anticipated scientific investigations at Saturn. Space Sci. Rev. 115, 363–497. doi:10.1007/s11214-004-1456-7.

Rappaport, N.J., Iess, L., Wahr, J., Lunine, J.I., Armstrong, J.W., Asmar, S.W., Tortora, P., Di Benedetto, M., Racioppa, P., 2008. Can Cassini detect a subsurface ocean in Titan from gravity measurements? Icarus 194, 711–720. doi:10.1016/j.icarus.2007.11.024.

Remacle, J.F., Lambrechts, J., 2018. Fast and robust mesh generation on the sphere—application to coastal domains. Comput. Aided Design 103, 14–23. doi:10.1016/j.cad.2018.03.002.

Ringler, T., Petersen, M., Higdon, R.L., Jacobsen, D., Jones, P.W., Maltrud, M., 2013. A multi-resolution approach to global ocean modeling. Ocean Model. 69, 211–232. doi:10.1016/j.ocemod.2013.04.010.

Rodriguez, S., Le Mouélic, S., Rannou, P., Sotin, C., Brown, R., 2013. Six years of continuous observation of Titan cloud activity with Cassini/VIMS, in: SF2A-2013: Proceedings of the Annual meeting of the French Society of Astronomy and Astrophysics, pp. 71–74.

Sagan, C., Dermott, S.F., 1982. The tide in the seas of Titan. Nature 300, 731–733. doi:10.1038/300731a0.

Samuelson, R.E., Hanel, R.A., Kunde, V.G., Maguire, W.C., 1981. Mean molecular weight and hydrogen abundance of Titan's atmosphere. Nature 292, 688–693.

Sauter, S., Wittum, G., 1992. A multigrid method for the computation of eigenmodes of closed water basins. Impact Comput. Sci. Eng. 4, 124–152. doi:10.1016/0899-8248(92)90019-5.

Schneider, T., Graves, S., Schaller, E., Brown, M., 2012. Polar methane accumulation and rainstorms on Titan from simulations of the methane cycle. Nature 481, 58–61. doi:10.1038/nature10666.

Sears, W.D., 1995. Tidal dissipation in oceans on Titan. Icarus 113, 39–56. doi:10.1006/icar.1995.1004.

Seny, B., Lambrechts, J., Comblen, R., Legat, V., Remacle, J.F., 2013. Multirate time stepping for accelerating explicit discontinuous Galerkin computations with application to geophysical flows. Int. J. Numer. Meth. Fl. 71, 41–64. doi:10.1002/fld.3646.

Seny, B., Lambrechts, J., Toulorge, T., Legat, V., Remacle, J.F., 2014. An efficient parallel implementation of explicit multirate Runge–Kutta schemes for discontinuous Galerkin computations. J. Comput. Phys. 256, 135–160. doi:10.1016/j.jcp.2013.07.041.

Smagorinsky, J., 1963. General circulation experiments with the primitive equations: I. the basic experiment. Mon. Weather Rev. 91, 99–164. doi:10.1175/1520-0493(1963)091<0099:GCEWTP>2.3.CO;2.

Soderlund, K., Schmidt, B., Wicht, J., Blankenship, D., 2014. Ocean-driven heating of Europa's icy shell at low latitudes. Nature Geosci. 7, 16. doi:10.1038/ngeo2021.

Sohl, F., Hussmann, H., Schwentker, B., Spohn, T., Lorenz, R.D., 2003. Interior structure models and tidal Love numbers of Titan. J. Geophys. Res.-Planet. 108. doi:10.10029/2003JE002044.

Sohl, F., Sears, W.D., Lorenz, R.D., 1995. Tidal dissipation on Titan. Icarus 115, 278–294. doi:10.1006/icar.1995.1097.

Sohl, F., Solomonidou, A., Wagner, F.W., Coustenis, A., Hussmann, H., Schulze-Makuch, D., 2014. Structural and tidal mod-

els of Titan and inferences on cryovolcanism. J. Geophys. Res.-Planet. 119, 1013–1036. doi:10.1002/2013JE004512.

Sotin, C., Hayes, A.G., Malaska, M.J., Nimmo, F., Trainer, M., Mastrogiuseppe, M., Soderblom, J.M., Tortora, P., Hofgartner, J.D., Aharonson, O., Barnes, J.W., Hodyss, R., Iess, L., Kirk, R.L., Lavvas, P., Lorenz, R.D., Lunine, J.I., Mazarico, E., McEwen, A.S., Neish, C., Nixon, C.A., Turtle, E.P., Vuitton, V., Yelle, R., 2017. Oceanus: A new frontiers orbiter to study Titan's potential habitability, in: 48th Lunar and Planetary Science Conference, p. 2306.

Sotin, C., Lawrence, K.J., Reinhardt, B., Barnes, J.W., Brown, R.H., Hayes, A.G., Le Mouélic, S., Rodriguez, S., Soderblom, J.M., Soderblom, L.A., et al., 2012. Observations of Titan′s northern lakes at 5μm: Implications for the organic cycle and geology. Icarus 221, 768–786. doi:10.1016/j.icarus.2012.08.017.

Soto, A., Rafkin, S., 2015. Mesoscale Circulations over Titan's Lakes, in: EGU General Assembly Conference Abstracts, p. 6146.

Stofan, E., Lunine, J., Lorenz, R., Kirk, R., Aharonson, O., Hayes, A., Lucas, A., Turtle, E., Wall, S., Wood, C., 2012. Shorelines of Ligeia Mare, Titan, pp. 1556–.

Stofan, E.R., Elachi, C., Lunine, J.I., Lorenz, R.D., Stiles, B., Mitchell, K.L., Ostro, S., Soderblom, L., Wood, C., Zebker, H., et al., 2007. The lakes of Titan. Nature 445, 61–64. doi:10.1038/nature05438.

Stommel, H., 1948. The westward intensification of wind-driven ocean currents. Eos, T. Am. Geophy. U. 29, 202–206. doi:10.1029/TR029i002p00202.

Tan, S.P., Kargel, J.S., Jennings, D.E., Mastrogiuseppe, M., Adidharma, H., Marion, G.M., 2015. Titan's liquids: Exotic behavior

and its implications on global fluid circulation. Icarus 250, 64–75. doi:10.1016/j.icarus.2014.11.029.

Tan, S.P., Kargel, J.S., Marion, G.M., 2013. Titan's atmosphere and surface liquid: New calculation using statistical associating fluid theory. Icarus 222, 53–72. doi:10.1016/j.icarus.2012.10.032.

Thomas, C.J., Lambrechts, J., Wolanski, E., Traag, V.A., Blondel, V.D., Deleersnijder, E., Hanert, E., 2014. Numerical modelling and graph theory tools to study ecological connectivity in the Great Barrier Reef. Ecol. Model. 272, 160–174. doi:10.1016/j.ecolmodel.2013.10.002.

Tobie, G., Gautier, D., Hersant, F., 2012. Titan's bulk composition constrained by Cassini-Huygens: implication for internal outgassing. Astrophys. J. 752, 125. doi:10.1088/0004-637X/752/2/12.

Tobie, G., Lunine, J.I., Sotin, C., 2006. Episodic outgassing as the origin of atmospheric methane on Titan. Nature 440, 61–64. doi:10.1038/nature04497.

Tokano, T., 2008. Dune-forming winds on Titan and the influence of topography. Icarus 194, 243–262. doi:10.1016/j.icarus.2007.10.007.

Tokano, T., 2009. Impact of seas/lakes on polar meteorology of Titan: Simulation by a coupled GCM-Sea model. Icarus 204, 619–636. doi:10.1016/j.icarus.2009.07.032.

Tokano, T., 2010. Simulation of tides in hydrocarbon lakes on Saturn's moon Titan. Ocean Dyn. 60, 803–817. doi:10.1007/s10236-010-0285-3.

Tokano, T., Lorenz, R.D., 2015. Wind-driven circulation in Titan's seas. J. Geophys. Res.-Planet. 120, 20–23. doi:10.1002/2014JE004751.

Tokano, T., Lorenz, R.D., 2016. Sun-stirred Kraken Mare: Circulation in Titan′s seas induced by solar heating and methane precipitation. Icarus 270, 67–84. doi:10.1016/j.icarus.2015.08.033.

Tokano, T., Lorenz, R.D., Van Hoolst, T., 2014. Numerical simulation of tides and oceanic angular momentum of Titan′s hydrocarbon seas. Icarus 242, 188–201. doi:10.1016/j.icarus.2014.08.021.

Toon, O.B., McKay, C.P., Courtin, R., Ackerman, T.P., 1988. Methane rain on Titan. Icarus 75, 255–284. doi:10.1016/0019-1035(88)90005-X.

Tseng, Q., Duchemin-Pelletier, E., Deshiere, A., Balland, M., Guillou, H., Filhol, O., Théry, M., 2012. Spatial organization of the extracellular matrix regulates cell–cell junction positioning. P. Natl. Acad. Sci. 109, 1506–1511. doi:10.1073/pnas.1106377109.

Turtle, E., Barnes, J., Trainer, M., Lorenz, R., Hibbard, K., Adams, D., Bedini, P., Langelaan, J., Zacny, K., 2017. Dragonfly: In situ exploration of Titan's prebiotic organic chemistry and habitability, in: European Planetary Science Congress, pp. EPSC2017–349–4.

Turtle, E., Perry, J., Barbara, J., Del Genio, A., Rodriguez, S., Le Mouélic, S., Sotin, C., Lora, J., Faulk, S., Corlies, P., et al., 2018. Titan's meteorology over the Cassini mission: Evidence for extensive subsurface methane reservoirs. Geophys. Res. Lett. 45, 5320–5328. doi:10.1029/2018GL078170.

Turtle, E.P., Perry, J.E., Hayes, A.G., McEwen, A.S., 2011. Shoreline retreat at Titan's Ontario Lacus and Arrakis Planitia from Cassini imaging science subsystem observations. Icarus 212, 957–959. doi:10.1016/j.icarus.2011.02.005.

Tyler, R.H., 2008. Strong ocean tidal flow and heating on moons of the outer planets. Nature 456, 770–772. doi:10.1038/nature07571.

Tyler, R.H., 2014. Comparative estimates of the heat generated by ocean tides on icy satellites in the outer Solar System. Icarus 243, 358–385. doi:10.1016/j.icarus.2014.08.037.

Vallaeys, V., 2018. Discontinuous Galerkin finite element modelling of estuarine and plume dynamics. Ph.D. thesis. UCLouvain.

Vallaeys, V., Kärnä, T., Delandmeter, P., Lambrechts, J., Baptista, A.M., Deleersnijder, E., Hanert, E., 2018. Discontinuous galerkin modeling of the columbia river's coupled estuary-plume dynamics. Ocean Model. 124, 111–124.

Vallaeys, V., Lambrechts, J., Delandmeter, P., Pätsch, J., Spitzy, A., Hanert, E., Deleersnijder, E., 2020. Understanding the circulation in the deep, micro-tidal and strongly stratified Congo River ROFI. Ocean Model. submitted.

Van, C.P., Gourgue, O., Sassi, M., Hoitink, A., Deleersnijder, E., Soares-Frazão, S., 2016. Modelling fine-grained sediment transport in the Mahakam land–sea continuum, Indonesia. J. hydro-environ. res. 13, 103–120. doi:10.1016/j.jher.2015.04.005.

Vance, S., Goodman, J., 2009. Oceanography of an ice-covered moon. Europa .

Ventura, B., Notarnicola, C., Casarano, D., Posa, F., Hayes, A.G., Wye, L., 2012. Electromagnetic models and inversion techniques for Titan's Ontario Lacus depth estimation from Cassini RADAR data. Icarus 221, 960–969. doi:10.1016/j.icarus.2012.09.011.

Vienne, A., Duriez, L., 1991. A general theory of motion for the eight major satellites of Saturn. II-Short-period perturbations. Astron. Astrophys. 246, 619–633.

Vienne, A., Duriez, L., 1992. A general theory of motion for the eight major satellites of Saturn. III-Long-period perturbations. Astron. Astrophys. 257, 331–352.

Vienne, A., Duriez, L., 1995. TASS1. 6: Ephemerides of the major Saturnian satellites. Astron. Astrophys. 297, 588.

Vincent, D., Karatekin, O., Dehant, V., Deleersnijder, E., 2017. Study of liquid exchanges between titan seas kraken mare and ligeai mare, in: European Geosciences Union General Assembly 2017, pp. EGU2017–855.

Vincent, D., Karatekin, Ö., Lambrechts, J., Lorenz, R.D., Dehant, V., Deleersnijder, É., 2018. A numerical study of tides in Titan's northern seas, Kraken and Ligeia Maria. Icarus 310, 105–126. doi:10.1016/j.icarus.2017.12.018.

Vincent, D., Karatekin, Ö., Vallaeys, V., Hayes, A.G., Mastrogiuseppe, M., Notarnicola, C., Dehant, V., Deleersnijder, E., 2016. Numerical study of tides in Ontario Lacus, a hydrocarbon lake on the surface of the Saturnian moon Titan. Ocean Dyn. 66, 461–482. doi:10.1007/s10236-016-0926-2.

Vincent, D., Lambrechts, J., Karatekin, Ö., Van Hoolst, T., Tyler, R.H., Dehant, V., Deleersnijder, E., 2019. Normal modes and resonance in ontario lacus: a hydrocarbon lake of titan. Ocean Dyn. , 1–12doi:10.1007/s10236-019-01290-2.

Volkov, V.A., 2002. Polar seas oceanography: an integrated case study of the Kara Sea. Springer Science & Business Media. doi:10.1029/2004EO080011.

Wahr, J., Selvans, Z.A., Mullen, M.E., Barr, A.C., Collins, G.C., Selvans, M.M., Pappalardo, R.T., 2009. Modeling stresses on satellites due to nonsynchronous rotation and orbital eccentricity using gravitational potential theory. Icarus 200, 188–206. doi:10.1016/j.icarus.2008.11.002.

Wall, S., Hayes, A.G., Bristow, C., Lorenz, R.D., Stofan, E.R., Lunine, J.I., Le Gall, A., Janssen, M., Lopes, R., Wye, L., et al., 2010. Active shoreline of Ontario Lacus, Titan: A morphological

study of the lake and its surroundings. Geophys. Res. Lett. 37, L05202. doi:10.1029/2009GL041821.

Wang, Q., Danilov, S., Schröter, J., 2008. Finite element ocean circulation model based on triangular prismatic elements, with application in studying the effect of topography representation. J. Geophys. Res.-Oceans 113. doi:10.1029/2007JC004482.

Webb, D., 2013. On the shelf resonances of the English Channel and Irish Sea. Ocean Sci. 9, 731–744. doi:10.5194/os-9-731-2013.

Wenzel, H.G., 1997. Tide-generating potential for the Earth, in: Tidal phenomena. Springer, pp. 9–26. doi:10.1007/BFb0011455.

White, L., Deleersnijder, E., Legat, V., 2008a. A three-dimensional unstructured mesh finite element shallow-water model, with application to the flows around an island and in a wind-driven, elongated basin. Ocean Model. 22, 26–47. doi:10.1016/j.ocemod.2008.01.001.

White, L., Legat, V., Deleersnijder, E., 2008b. Tracer conservation for three-dimensional, finite-element, free-surface, ocean modeling on moving prismatic meshes. Month. weather rev. 136, 420–442. doi:10.1175/2007MWR2137.1.

Williamson, D.L., Drake, J.B., Hack, J.J., Jakob, R., Swarztrauber, P.N., 1992. A standard test set for numerical approximations to the shallow water equations in spherical geometry. J. Comput. Phys. 102, 211–224. doi:10.1016/S0021-9991(05)80016-6.

Zebker, H.A., Stiles, B., Hensley, S., Lorenz, R., Kirk, R.L., Lunine, J., 2009. Size and shape of Saturn's moon Titan. Science 324, 921–923. doi:10.1126/science.1168905.

Zhang, Y., Baptista, A.M., 2008. SELFE: a semi-implicit Eulerian–Lagrangian finite-element model for cross-scale ocean circulation. Ocean model. 21, 71–96. doi:10.1016/j.ocemod.2007.11.005.